UNIVERSIDAD DE GRANADA

CONSEJO SUPERIOR DE INVESTIGACIONES CIENTÍFICAS

Departamento de Mineralogía y Petrología

Instituto Andaluz de Ciencias de la Tierra

Petrogenesis of the ultramafic and mafic rocks from the Mayarí-Baracoa Ophiolitic Belt and the spatially-related volcanism (eastern Cuba)

Petrogénesis de las rocas ultramáficas y máficas del Cinturón Ofiolítico Mayarí-Baracoa y del volcanismo asociado (Cuba oriental)

Claudio Marchesi

Ph.D. Thesis

Tesis Doctoral

Editor: Editorial de la Universidad de Granada
Autor: Claudio Marchesi
D.L.: Gr. 2163 - 2006
ISBN: 978-84-338-4196-4

Claudio Marchesi

PETROGENESIS OF THE ULTRAMAFIC AND MAFIC ROCKS FROM THE MAYARÍ-BARACOA OPHIOLITIC BELT AND THE SPATIALLY-RELATED VOLCANISM (EASTERN CUBA)

PETROGÉNESIS DE LAS ROCAS ULTRAMÁFICAS Y MÁFICAS DEL CINTURÓN OFIOLÍTICO MAYARÍ-BARACOA Y DEL VOLCANISMO ASOCIADO (CUBA ORIENTAL)

Ph.D. Thesis

Tesis Doctoral

Advisors

Directores

Fernando Gervilla Linares

Carlos Jesús Garrido Marín

Departamento de Mineralogía y Petrología
Universidad de Granada

Instituto Andaluz de Ciencias de la Tierra
CSIC-Universidad de Granada

AGRADECIMIENTOS

Escribo estas líneas al final de cuatro años de trabajo para agradecer principalmente a las personas que han contribuido a la realización de mi tesis doctoral en la Universidad de Granada. Ante todo quiero aprovechar esta ocasión para dar una pequeña señal de gratitud hacía España y su gente que me ha recibido de manera muy acogedora y con quienes me he sentido muy a gusto. El trato amable recibido por los granadinos se ha visto alterado solamente en ocasiones muy puntuales y a raíz de episodios objetivamente escabrosos, como el reiterado embotellamiento de aceite de producción española (más concretamente andaluza) y su posterior exportación por parte de empresas italianas, y sobre todo el inolvidable codazo de Tassotti a Luís Enrique en los cuartos de final del mundial de fútbol de 1994.

En primer lugar, quiero dar las gracias a mis dos directores de tesis, Fernando Gervilla Linares y Carlos Jesús Garrido Marín, por la posibilidad que me han brindado de realizar este trabajo de investigación y la fundamental ayuda recibida a lo largo de estos años. Valoro mucho además la relación amigable y la estima (espero recíproca) que se han instaurado entre nosotros durante estos años de colaboración.

Agradezco a mi familia que me ha apoyado en el proyecto de seguir con la investigación en Ciencias de la Tierra aunque haya tenido que soportar una prolongada lejanía.

Le doy las gracias a todo el personal del Departamento de Mineralogía y Petrología de la Universidad de Granada y del Instituto Andaluz de Ciencias de la Tierra, y en especial a sus directores respectivos Miguel Ortega Huertas y Andrés Maldonado, por la colaboración y la disponibilidad demostradas a lo largo de estos años. Quiero también agradecer a los investigadores y técnicos que han trabajado conmigo durante mis estancias en el Departament de Cristal·lografia, Mineralogia i Dipòsits Minerals de la Universidad de Barcelona y en el Institut des Sciences de la Terre de l'Environnement et de l'Espace de Montpellier. Estoy particularmente agradecido a Joaquín Proenza, Xavier Llovet, Marguerite Godard, Patrick Monié, Olivier Bruguier, Beatrice Galland y Simone Pourtales. Mi especial gratitud a Delphine Bosch que ha sido más que una directora de trabajo a lo largo de mis últimas estancias en Montpellier, en concreto durante un momento personal bastante difícil. Por supuesto no quiero olvidarme de los geólogos del Instituto Superior Minero-Metalúrgico de Moa y de la empresa Geominera de Oriente

(Santiago de Cuba) que han hecho posible la realización de dos campañas de muestreo en Cuba y que además me han permitido vivir una experiencia muy enriquecedora. Quiero expresar mi agradecimiento especialmente a Jesús Blanco-Moreno, Antonio Rodríguez-Vega, Roberto Díaz-Martínez, José Batista-Rodríguez, Silva Pereira, Waldo Lavaut y Rubén Ruiz.

Quiero también destacar la confianza y el apoyo recibidos por parte de María Teresa Gómez-Pugnaire de la Universidad de Granada y de Bernardo Cesare de la Universidad de Padua quienes hicieron posible el comienzo de mi actividad investigadora en Granada.

Un gran abrazo a todos mis compañeros, becarios o precarios de naturaleza varia, del programa de Ciencias de la Tierra de la Universidad de Granada con quienes me lo he pasado fenomenal y con quienes espero hayan todavía muchas ocasiones para echar una (¿?) caña: Fermín, Alpiste, Franci, Concha, Julia, David, José Maria, Iñaki, Ana, Antonio A., José Mari (el Chiquitillo), Rocío, Maja, Vicente, José Alberto, Vincenzo, Idael, Antonio P., Luisa, Encarni, Pedro A., Pedro M., Isa M., Isa A., Javi, Patricia.

Un saludo a mis otros amigos de Granada y un sentido gracias por su apoyo: Coco (quien en cierta manera es mi versión andaluza), Lidia (quien me alimentó en Londres), Che (aunque se haya escaqueado de la salsa), Alicia (y su bizcocho), Antonio T. (quien sufre conmigo por el Inter de Milán), Antonio A.V. y su esposa Ade (lañez), Jose (y su método de tomar puntería), Silvia, Juanma, Santiago, Shaila, Teresa, Cedric, Giulia, Pilar, Raquel, Fermín (II), Luigi, Migue, Africa, Carol, Tuty, Silvia G. (la gitana de la Valpolicella), Silvana, Ade D.P., Edwards.

Un recuerdo especial para mis amigos italianos (o similares): Paolo (el pursel, con quien todavía queda pendiente Venezuela y mucho más), Bea, Elena I., Andrea (Zanasi pequeño), Giovanni (Zanasi grande), Paolo Z., Vale, Carlone, Elena G., Andrea R., Fax, Ghianda, Nora, Marco, Rosa, Giorgios, Laura M., Paloma, Ilaria, Livia, Cecchi, Laura L., Riccardo, Stefano, Ausch.

Quiero agradecer también a mis amigos becarios de Montpellier por los buenos momentos pasados juntos: Ingrid, Bruno, Remi, Marianne, Julie.

Granada, noviembre de 2006

ABSTRACT

The Moa-Baracoa and Mayarí-Cristal massifs (eastern Cuba) are two ophiolitic complexes mainly composed of harzburgite tectonites and minor dunites, cut by mafic and ultramafic dykes. The Moa-Baracoa massif exhibits a well-developed Moho transition zone, with gabbroic sills and impregnated clinopyroxene- and plagioclase-bearing dunites, and an incomplete crustal section made up of layered gabbros. In contrast, both the Moho transition zone and the plutonic crustal unit are absent in the Mayarí-Cristal massif. The volcanic rocks of the Morel and Quibiján Formations are in tectonic contact with the Moa Baracoa massif, whereas the Mayarí-Cristal mantle peridotites are spatially-related with the Téneme volcanic rocks.

Harzburgite tectonites from these massifs are very refractory in terms of modal compositions (clinopyroxene < 1 vol.%), whole rock major element (Al_2O_3 content on anhydrous basis is 0.37-1.11 wt% and 0.14-0.70 wt% in Moa-Baracoa and Mayarí-Cristal, respectively) and heavy rare earth element contents ($0.06 < Yb_{(N)} < 0.2$, normalized to chondrite composition). Their modal and geochemical signatures imply that Moa-Baracoa and Mayarí-Cristal harzburgites are residues after high degrees (20-30%) of partial melting under intermediate fO_2 conditions (-1 < QFM < 1). The relative enrichment of Th, Nb, Ta and light rare earth elements in peridotites is due to re-equilibration of melting residues with percolating melts. Dunites originated by interaction of harzburgite tectonites with orthopyroxene-undersaturated melts in two different settings. In Moa-Baracoa massif, dunites formed by melt/rock reaction close to the paleo-Moho; dunites acted as focused channels for melt flow in the Moho transition zone and were occasionally impregnated by basaltic liquids. Dunites in Mayarí-Cristal massif are likely related to mantle-melt reaction during melt extraction into dunite channels deeper in the mantle. Peridotites lost on average 6 wt% of relative MgO by intense seafloor weathering.

Mineral chemistry and whole rock geochemical compositions of gabbroic sills, dykes and layered gabbros from the Moho transition zone and crustal section of the Moa-Baracoa massif show evidence that they are cumulates from parental melts generated deeper in the mantle. Rare earth element contents and Mg-numbers of melts in equilibrium with these cumulitic gabbros coincide with those of the Morel back-arc basalts. On the other hand, no geochemical relation has been inferred between the melt in

equilibrium with the studied segregate from Mayarí-Cristal and the Téneme arc volcanic rocks.

The Upper Cretaceous igneous suites spatially-related with the Moa-Baracoa and Mayarí-Cristal massifs record different subduction-related igneous styles that are now juxtaposed in complex field relations. I classify these suites in three main geochemical groups. Group 1 (Morel-type volcanic rocks) consists of tholeiitic basalts and rare basaltic andesites that exhibit N-MORB-like compositions similar to those found in back-arc basin basalts (TiO_2 = 1.2-2.9 wt%; $La/Yb_{(N)}$ = 0.7-0.9, normalized to chondrite composition; and Th/Nb = 0.06-0.08). They are characterized by high initial ε_{Nd} (9.1-11.1), and slightly radiogenic $^{207}Pb/^{204}Pb$ (15.49-15.51) and $^{208}Pb/^{204}Pb$ (37.65-37.74) ratios. Group 2 are subvolcanic basalts and rare basaltic andesitic dykes that intrude the residual mantle peridotites of the Moa-Baracoa and Mayarí-Cristal massifs mainly in the Guamuta-Loma de la Bandera region. These dykes exhibit major and trace element compositions similar to island arc tholeiites (IAT) (TiO_2 = 0.7-1.4 wt%; $La/Yb_{(N)}$ = 0.6-0.9, normalized to chondrite composition; and Th/Nb = 0.06-0.69) and have initial ε_{Nd} (9.6-11.0) similar to Group 1, but have, in general, more radiogenic $^{207}Pb/^{204}Pb$ (15.46-15.60) and $^{208}Pb/^{204}Pb$ (37.74-38.25) isotope ratios. Group 3 is composed of low-Ti (TiO_2 = 0.3-0.9 wt%) basaltic to dacitic volcanic rocks, minor basaltic andesitic dykes and dioritic intrusive rocks from the Quibiján and Téneme Formations that show a major element calcalkaline line of descent. Their light rare earth element-enriched patterns ($La/Yb_{(N)}$ = 1.1-5.0, normalized to chondrite composition) and high Th/Nb (0.35-1.51) ratios, coupled with variable but relatively low initial ε_{Nd} (2.7-9.4) and radiogenic $^{87}Sr/^{86}Sr$ (0.70339-0.70531), $^{207}Pb/^{204}Pb$ (15.53-15.62) and $^{208}Pb/^{204}Pb$ (37.94-38.39) isotope ratios prove an unambiguous subduction-related character for Group 3 samples. These three igneous groups formed by variable degrees of melting (< 5-35%) of depleted spinel lherzolite at depths of less than 85 km. The mantle source was more depleted for Groups 2 and 3 than for Group 1.

The trace element and radiogenic isotope compositions of primitive Group 3 volcanic rocks from the Quibiján Formation are manifestly bimodal. One subgroup of samples is characterized by relatively low Ta/Yb (0.02-0.03) and Th/La (0.10-0.13), slightly subchondritic Nb/Ta (13.5-17.3), and high initial $^{206}Pb/^{204}Pb$ (18.57-18.62) and ε_{Nd} (7.6-9.4); on the other hand, the rest of the Quibiján primitive lavas shows greater Ta/Yb (0.07-0.11) and Th/La (0.23-0.31) ratios, highly subchondritic Nb/Ta (7.7-8.9), coupled with lower initial $^{206}Pb/^{204}Pb$ (18.24-18.29) and ε_{Nd} (3.4-5.5). These two signatures were induced by two distinct subduction components that imposed their Nb/Ta fractionations to the mantle source of Group 3. In the first case the dehydration and/or melting of

Cretaceous Atlantic marine sediments in the subducting slab may have caused the fractionation of Nb from Ta, and the slab-derived component might have then mixed in small percentages (< 1%) with the depleted sub-arc mantle overprinting its primary Nb/Ta ratio. In the second case, the highly subchondritic Nb/Ta that characterized the slab-derived fluids and/or melts was not created in the subduction zone but was inherited from the recycled continental sediments. Pb isotopic data indicate that this slab component derived from the dehydration and/or melting of North-American continental material and may have then mixed in small proportions (< 1%) with the mantle wedge beneath the Cuban paleo-arc.

The results of this study indicate that the Mayarí-Baracoa Ophiolitic Belt formed at an original back-arc spreading centre. The Moa-Baracoa massif represents a portion of MORB-like lithosphere located nearby a back-arc spreading ridge, and the Mayarí-Cristal massif represents a portion of transitional (MORB to IAT) mantle located closer to the paleo-volcanic arc than Moa-Baracoa. The variability in the source depletion and imprint of a subduction component recorded in the Cretaceous magmatism of eastern Cuba may reflect across arc different settings of the magmatic activity. In this context Morel-type volcanic rocks (Group 1) were probably extruded at a back-arc ridge and were part of the Moa-Baracoa lithospheric section. On the other hand, the Guamuta-Loma de la Bandera island arc tholeiitic dykes (Group 2) were generated closer to the paleo-volcanic arc than the Morel volcanic rocks in a setting that probably coincided with that of the Mayarí-Cristal massif. Finally, the Quibiján-Téneme calcalkaline rocks (Group 3) likely record the magmatic activity produced at the volcanic front of the paleo-island arc. The involvement of Atlantic and North American sediments in the Cretaceous magmatism from eastern Cuba indicates that the Proto-Caribbean (North American-Proto Atlantic) lithosphere was subducting beneath the Greater Antilles arc in Late Cretaceous (pre-Campanian) time. This conclusion supports geotectonic models proposing the onset of south-westward dipping subduction beneath the Great Caribbean arc in the Aptian.

RESUMEN AMPLIADO

INTRODUCCIÓN

El conocimiento de la estructura y composición de la litosfera oceánica se ha adquirido principalmente a través de: 1) estudios geofísicos de sus propiedades sísmicas, magnéticas, gravitatorias y de flujo de calor; 2) perforaciones y dragas del fondo marino; 3) afloramientos en zonas submarinas de fracturación y en correspondencia de ventanas tectónicas; 4) estudios de porciones de litosfera oceánica obducidas en la corteza (complejos ofiolíticos).

La estructura general de la litosfera oceánica está compuesta, de base a techo, por: 1) rocas ultramáficas del manto; 2) rocas gabróicas con diferente textura (~ 3-5 km de espesor); 3) un complejo de diques sub-paralelos de diabasas (~ 1-2 km de espesor); 4) lavas basálticas con estructura en almohadilla (~ 1-2 km de espesor); 5) sedimentos pelágicos (p.e. Penrose Conference Participants 1972; Mutter y Mutter 1993; Karson et al. 2002). Las áreas de corteza oceánica con un espesor elevado (10-30 km) constituyen los llamados plateaux oceánicos (p.e. Mahoney et al. 1993; Gladczenko et al. 1997; Eldholm y Coffin 2000; Hauff et al. 2000; Weis et al. 2001; Kerr et al. 2003). La nueva litosfera oceánica se crea en los límites de placa divergentes. El modelo generalmente aceptado para su origen (p.e Klein 2003) prevé que la separación de las placas litosféricas en las dorsales oceánicas provoca la subida del manto subyacente. La fusión adiabática del manto empieza a la profundidad donde éste cruza el solidus de la peridotita fértil cuya composición modal inicial generalmente es: 50-60 vol.% de olivino; 20-30 vol.% de ortopiroxeno; 15-20 vol.% de clinopiroxeno; 0-5 vol.% de espinela (si la presión es ~ 1-2.5 GPa) o granate (si la presión es > 2.5 GPa) (Walter 2003). Los fundidos ascendentes interactúan con los residuos de la fusión parcial y se focalizan hacia el centro de expansión oceánica (Kelemen et al. 1992, 1995). Los magmas así concentrados forman una lente de ~ 50-100 m de espesor localizada por debajo del eje de la dorsal oceánica en la que cristalizan y se enfrían las rocas gabróicas de la corteza. Las fuerzas extensivas asociadas a la expansión oceánica crean periódicamente un camino favorable a la inyección de diques de diabasa y, finalmente, los fundidos pueden extruir en el fondo oceánico.

La extracción de magmas de composición predominantemente basáltica es el principal proceso que controla la composición mineralógica y química del manto litosférico oceánico. La presión, la temperatura, la composición inicial del manto, la tasa de fusión, la porosidad residual y el grado de equilibrio entre los fundidos y la roca encajante son los principales factores que controlan la composición de los magmas y de los residuos de fusión. Una vez creada, la litosfera oceánica es alejada del centro de expansión oceánica, acumula sedimentos marinos conforme aumenta su edad, y es finalmente consumida en las zonas de subducción donde se recicla en el manto astenosférico después de haber sido sometida a procesos metamórficos de alta presión (p.e. Isacks et al. 1968; McKenzie 1969; Green 1972). La subducción de litosfera oceánica provoca la actividad magmática en los arcos volcánicos continentales e insulares como consecuencia de la fusión de la cuña mantélica que subyace al arco y que se ve afectada por la influencia de fluidos/fundidos/líquidos supercríticos procedentes del material que subduce.

En general los magmas generados en las zonas de subducción presentan mayores contenidos en SiO_2 y menores contenidos en FeOt y TiO_2 que los generados en las dorsales medio-oceánicas (MORB) (p.e. Kelemen et al. 2003a). Además, los magmas de arco están generalmente enriquecidos en elementos traza altamente incompatibles en el manto como Cs, Rb, Ba, Th, U, elementos de las tierras raras ligeras (LREE), Pb y Sr; este enriquecimiento está generalmente asociado a los agentes derivados de la deshidratación/fusión de la placa que subduce. El Nb y el Ta presentan características peculiares en los magmas generados en los límites de placa convergentes, ya que tales magmas están relativamente empobrecidos en estos dos elementos en comparación con el Th, el U y los LREE. Como consecuencia, la presencia de razones Nb/U relativamente bajas (Hofmann et al. 1986) o de razones Th/Nb y Th/Ta relativamente altas (Plank 2005) han sido utilizadas de manera satisfactoria para distinguir entre magmas tipo MORB u OIB y magmas de arco volcánico. La contribución de los agentes procedentes de la placa que subduce a la fuente de los fundidos generados en las zonas de subducción influye también sobre la composición isotópica de estos fundidos. En particular los magmas de arco generalmente presentan razones $^{143}Nd/^{144}Nd$ más bajas y $^{87}Sr/^{86}Sr$, $^{206}Pb/^{204}Pb$, $^{207}Pb/^{204}Pb$, y $^{208}Pb/^{204}Pb$ más altas que los MORB por efecto de la contaminación de su fuente mantélica por parte de material de origen cortical.

Las ofiolitas representan porciones de antigua litosfera oceánica obducidas por encima de terrenos continentales (Penrose Conference Participants 1972). Los complejos ofiolíticos mejor preservados del mundo se encuentran en Omán (Ofiolita de Semail), Chipre (Ofiolita de Troodos), Papa-Nueva Guinea (Ofiolita de Papua) y Canadá (Ofiolita

de Bay of Islands). Las ofiolitas pueden estar constituidas por escamas litosféricas de varios kilómetros de espesor o por una melange tectónica de diferentes unidades que representa una secuencia litosférica incompleta (p.e. Coleman 1977; Gass et al. 1984, Nicolas 1989; Parson et al. 1992; Ishiwatari et al. 1994; Vissers y Nicolas 1995; Dilek et al. 2000). Las litologías de la porción mantélica de las ofiolitas pueden variar entre peridotitas moderadamente refractarias (lherzolitas) y harzburgitas altamente refractarias. Estas litologías constituyen comúnmente las unidades más profundas de la secuencia mantélica, mientras que la zona de transición entre el manto y la corteza oceánica presenta una composición principalmente dunítica. El ambiente de formación de algunas ofiolitas ha sido intensamente debatido, especialmente para los complejos que presentan una porción mantélica fuertemente refractaria. En particular para estas ofiolitas el debate se ha centrado en si las altas tasas de fusión parcial alcanzadas por las peridotitas mantélicas están relacionadas con un ambiente de dorsal oceánica de alta velocidad de expansión (p.e. Coleman 1977; Boudier y Nicolas 1985; Nicolas 1989), o con un ambiente de supra-subducción (p.e. Pearce et al. 1981, 1984; Ishiwatari et al. 1994; Shervais 2001; Stern 2004).

En la región del Caribe afloran numerosos complejos ofiolíticos y varias series de rocas ígneas. Las series magmáticas en este área presentan tres estilos geoquímicos principales (Donnelly y Rogers 1980; Donnelly et al. 1990): 1) series de tipo MORB-OIB, de edad Jurasico-Cretácico Superior, generalmente asociadas al plateau de la placa del Caribe o a la corteza oceánica de la placa Proto-Caribeña (Atlántica); 2) rocas volcánicas y plutonicas, de edad Cretácico-Holoceno, asociadas a actividad magmática en zonas de subducción y que generalmente presentan composiciones de tipo toleita de arco (IAT) o calcoalcalina; 3) basaltos alcalinos, de edad Terciario-Holoceno, relacionados con una actividad tectónica de tipo rifting. En particular, en la isla de Cuba se encuentra el denominado “Cinturón Ofiolítico Septentrional” el cual está formado por una serie de complejos ultramáficos y máficos que afloran de este a oeste en la porción norte de la isla (Iturralde-Vinent 1989, 1994, 1996a, 1998); además gran parte de la isla está constituida por terrenos ígneos y metamórficos relacionados con una o más zonas de subducción (p.e. Iturralde-Vinent 1996a; Kerr et al. 1999; García-Casco et al. 2002; Blein et al. 2003; Schneider et al. 2004).

Este estudio tiene como objetivos la caracterización litológica, estructural, petrológica y geoquímica de las rocas ultramáficas y máficas que constituyen el Cinturón Ofiolítico Mayarí-Baracoa, el complejo más oriental entre los que conforman el Cinturón Ofiolítico Septentrional de Cuba. En esta memoria, además, están incluidos los

resultados de mi investigación sobre la petrogenesis de las formaciones magmáticas cretácicas de Cuba oriental. Estas series están relacionadas espacialmente con los macizos ofiolíticos de Moa-Baracoa y Mayarí-Cristal, pero sus relaciones petrológicas con los mismos no han sido completamente aclaradas hasta ahora. Los resultados presentados en esta tesis doctoral tienen particular interés en el contexto de los estudios dedicados a la evolución geodinámica del Caribe y, más en general, contribuyen a un mejor conocimiento de los procesos relacionados con la alta tasa de fusión del manto en un ambiente de supra-subducción y del comportamiento geoquímico de diferentes elementos en traza (en particular el Nb y el Ta) en dicho ambiente.

CONTEXTO GEOLÓGICO

El Cinturón Ofiolítico Mayarí-Baracoa aflora en la parte más oriental del Cinturón Ofiolítico Septentrional de Cuba, el cual está constituido por una serie de complejos ultramáficos, plutónicos, volcánicos y sedimentarios intensamente fallados. El Cinturón Ofiolítico pertenece al Substrato Plegado de Cuba, una unidad orogénica formada por escamas tectónicas deformadas y metamorfizadas que se emplazaron a lo largo del Cretácico Superior-Eoceno Superior, durante la colisión de la porción occidental del arco de las Antillas Mayores con la plataforma continental de las Bahamas (Iturralde-Vinent 1994, 1996a, 1998).

La evolución tectónica de la región del Caribe es compleja y los investigadores no han alcanzado todavía un grado suficiente de consenso sobre un único modelo geodinámico capaz de integrar todas las observaciones geológicas disponibles en este área (p.e. Draper y Dengo 1990; Morris et al. 1990; Iturralde-Vinent 1998; James 2006; Iturralde-Vinent y Lidiak 2006). Se acepta generalmente que la corteza oceánica de la placa Proto-Caribeña se formó durante el Jurasico Medio-Cretácico Inferior, por efecto del rifting continental y de la sucesiva apertura de una cuenca oceánica entre los continentes Norteamericano y Suramericano (Gondwana) (Ross y Scotese 1988; Morris et al. 1990; Pindell y Barrett 1990; Sawyer et al. 1991; Meschede y Frish 1998; Mann 1999). En el Cretácico Inferior empezó en la región del Caribe una fase tectónica caracterizada por la subducción de las placas Proto-Caribeña y/o Caribeña. Las ofiolitas del Cinturón Ofiolítico Septentrional de Cuba se han relacionado generalmente con esta fase y se han interpretado, alternativamente: como porciones de litosfera oceánica Proto-Caribeña procedentes de una cuenca marginal de retro-arco (Iturralde-Vinent 1994, 1996b, 1998), como testigos de la litosfera oceánica del Proto-Caribe que subducía por debajo de la placa del Caribe, o como remanentes de la litosfera de la parte frontal del arco generados en el paleo-margen de la placa del Caribe (Pindell y Barrett 1990; Pindell 1994). El

número y la polaridad de los arcos volcánicos activos en la región caribeña durante el Cretácico son cuestiones sujetas a debate (p.e. Iturralde-Vinent 1994, 1998; Pindell 1994; Kerr et al. 1999). Otros dos temas importantes que siguen siendo fuente de discusión entre los investigadores son el origen Pacifico (p.e. Malfait y Dinkelman 1972; Ross y Scotese 1988; Pindell y Barrett 1990) o inter-Americano (Atlántico) (p.e. Aubouin et al. 1982; Donnelly 1989; Meschede y Frisch 1998; James 2006) de la placa del Caribe, y la edad de inversión de la polaridad de la subducción de noreste a suroeste en el arco de las Antillas Mayores (Aptiense *versus* Campaniense) (p.e. Burke 1988; Lebron y Perfit 1993, 1994; Pindell 1994; Draper et al. 1996; Kerr et al. 1998, 2003; Pindell et al. 2006). En el Paleógeno una nueva zona de subducción estuvo activa en la región del Caribe. En Cuba este arco volcánico está representado por las rocas volcáno-sedimentarias que afloran en la Sierra Maestra (Cuba oriental) (Cobiella 1988; Cazañas et al. 1998; Kysar-Mattietti 2001; Rojas-Agramonte et al. 2006). Después del Paleógeno, la actividad de la subducción se desplazó hacia el este por efecto de un sistema de fallas de desgarre (p.e. Falla de Oriente) y hoy en día está representada por el arco de la Antillas Menores.

En Cuba oriental, la actividad magmática cretácica dio lugar a tres formaciones volcánicas principales: la Formación Téneme, la Formación Quibiján y la Formación Santo Domingo (Quintas 1988a, 1989; Iturralde-Vinent 1996a, c, d; Gyarmati et al. 1998; Kerr et al. 1999). Solamente existe un estudio geoquímico exhaustivo de las rocas volcánicas de la Formación Téneme, las cuales han sido clasificadas como toleitas de arco de isla relacionadas con una zona de subducción incipiente (Proenza et al. 2006). Las peridotitas del macizo de Mayarí-Cristal están en contacto tectónico con las rocas de la Formación Téneme y normalmente yacen encima de ellas. La Formación Téneme está constituida principalmente por basaltos masivos, andesitas basálticas, andesitas y escasas dacitas, intercalados con tufitas, areniscas tufiticas y calizas de edad Turoniense-Coniaciense Inferior (Iturralde-Vinent et al. 2006). En la región sureste de la localidad tipo las rocas volcánicas de la Formación Téneme están cortadas por las rocas intrusivas de composición diorítica del pluton de Río Grande.

La Formación Quibiján está en contacto tectónico con las rocas del macizo ofiolítico de Moa-Baracoa y con las rocas metamórficas del Complejo del Purial (Quintas 1987, 1988a). Esta formación está compuesta principalmente por basaltos masivos porfíricos, ricos en amígdalas rellenas de cuarzo y clorita, andesitas basálticas y escasas andesitas, intercalados con silex y rocas tufiticas. Iturralde-Vinent et al. (2006) propusieron una edad Albiense-Turoniense para la Formación Quibiján basándose en la correlación con rocas similares en Cuba central. Los basaltos y andesitas basálticas con

estructura en almohadilla procedentes de la localidad de Morel fueron incluidos originalmente en la Formación Quibiján y fueron clasificados como toleitas relacionadas con un ambiente de trasera de arco (Kerr et al. 1999). Sin embargo, como se demuestra en el Capitulo 5 de esta memoria, estas rocas de edad Turoniense-Coniaciense (Iturralde-Vinent et al. 2006) presentan una signatura geoquímica distinta de las rocas de la Formación Quibiján y su inclusión en esta formación es por consecuencia incorrecta.

La Formación Santo Domingo está constituida por rocas volcáno-sedimentarias de edad Turoniense-Campaniense (Iturralde-Vinent et al. 2006) que presumiblemente yacen encima de la Formación Quibiján (Quintas 1987, 1988b). La secuencia litológica de la Formación Santo Domingo definida en su localidad tipo presenta un espesor superior a los 1200 metros y está constituida principalmente por tobas, rocas tufiticas, y sills andesíticos intercalados con calizas (Iturralde-Vinent 1976, 1977). Hasta la fecha no se han realizado estudios geoquímicos detallados sobre estas rocas; sin embargo los datos de elementos mayores disponibles indican que las mismas son de afinidad calcoalcalina (Gyarmati et al. 1998).

TÉCNICAS ANALÍTICAS

Para este estudio he seleccionado 119 muestras representativas de las principales litologías que constituyen el Cinturón Ofiolítico Mayarí-Baracoa y las series magmáticas Cretácicas relacionadas espacialmente con estos macizos ofiolíticos. Las composiciones en elementos mayores de los minerales han sido analizadas por Microsonda Electrónica (EPMA) en los Serveis Cientificotècnics (SCT) de la Universidad de Barcelona o en el Institut des Sciences de la Terre, de l'Environnement et de l'Espace de Montpellier (ISTEEM, Francia) utilizando, respectivamente, un equipo CAMECA SX 50 y CAMECA SX 100. El voltaje de aceleración aplicado ha sido de 20 kV y la corriente sobre la muestra de 15 nA (en el SCT) y 10 nA (en el ISTEEM), excepto para los análisis de espinela en peridotitas para los que se ha utilizado una corriente de 20 nA. Las concentraciones elementales han sido analizadas con un tiempo de contaje de 10 segundos en el SCT (excepto para el Ni y el V, 30 segundos) y 30 segundos en el ISTEEM (excepto para el Mn y el Fe, 20 segundos).

Para realizar los análisis de la composición de la roca total, se han eliminado previamente las venas de inyección secundarias y la superficie de alteración arcillosa de las peridotitas. Las rocas se han triturado moliendo y pulverizando grandes cantidades de muestra (> 3 kg) en un molino de mandíbulas y, posteriormente, en un mortero eléctrico de ágata. Los elementos mayores y menores de transición (Sc, V, Cr y Ni) se han

analizado por Florescencia de Rayos X (XRF) en la Universidad del País Vasco, en el Centro de Instrumentación Científica de la Universidad de Granada, o en el GeoAnalytical Lab de la Washington State University (Estados Unidos) utilizando respectivamente un equipo PHILIPS PW 1510, PHILIPS PW 1404/10 y ThermoARL Advant XP+. Las rocas pulverizadas se mezclaron con tetraborato de litio ($Li_2B_4O_7$) y se fundieron para obtener perlas de fusión que posteriormente se montaron en el equipo para el análisis.

Los elementos traza (Li, Co, Rb, Sr, Y, Zr, Nb, Cs, Ba, elementos de las tierras raras, Hf, Ta, Pb, Th y U) en la roca total se analizaron por Espectrometría de Masas sobre Plasma Inductivamente Acoplado (ICP-MS) utilizando un equipo VG-PQ2 Turbo+ en el ISTEEM o un equipo HP 4500+ en el GeoAnalytical Lab de la Washington State University. En el ISTEEM, las rocas pulverizadas se disolvieron con HF y $HClO_4$ siguiendo el método de Ionov et al. (1992). Para evitar efectos de memoria en los análisis de Nb y Ta, las concentraciones de estos dos elementos se determinaron respectivamente a través de Zr y Hf como estándar interno. Los limites de detección obtenidos a partir de los blancos químicos analizados durante varios años en el ISTEEM se encuentran en Ionov et al. (1992) y Garrido et al. (2000). Para las peridotitas con contenidos en elementos incompatibles extremadamente bajos se realizaron varios análisis de duplicados. Una estimación de la precisión de los análisis se realizó utilizando tres medidas para cada elemento y calculando la desviación estándar del análisis (σ_s) a partir de las desviaciones estándares de las medidas en la muestra (σ_s), en el blanco instrumental (σ_i) y en el blanco químico (σ_p): $\sigma_s = \sqrt{\sigma_i^2 + \sigma_p^2 + \sigma_s^2}$ (véase también Godard et al. 2000). El análisis fue descartado si la σ_s relativa era mayor del 80% del valor promedio. Las composiciones de los estándares internacionales (PCC-1, UB-(N), BHVO-1, ROA-1 y BIR) analizados en el ISTEEM juntos con las muestras evidencian un buen acuerdo con los valores publicados para estos materiales de referencia (Govindaraju 1994). La reproducibilidad de los análisis de estos materiales es superior al 80% para UB-(N), BHVO-1 y BIR, y varía entre el 60 y el 98% para PCC-1 y ROA-1. En el GeoAnalytical Lab la roca pulverizada se mezcló con tetraborato de litio ($Li_2B_4O_7$) y a continuación se procedió a su fusión. Una alícuota de las perlas de fusión así obtenidas fue posteriormente molida y disuelta en HF, HNO_3 y $HClO_4$, siguiendo el método de Crock y Lichte (1982). Durante cada sesión se analizaron un blanco químico y tres estándares internos del laboratorio. Las concentraciones promedio de los estándares internacionales analizados en el GeoAnalytical Lab muestran una buena coincidencia con los valores de referencia publicados para estos materiales (Govindaraju 1994). La reproducibilidad de

los análisis de elementos trazas en este laboratorio a lo largo de 3 años es superior al 90%.

Los elementos traza en clinopiroxeno y plagioclasa de las rocas ígneas se analizaron mediante Espectrometría de Masas con Ablación por Láser sobre Plasma Inductivamente Acoplado (LA-ICP-MS). Los análisis se realizaron en el ISTEEM sobre láminas pulidas de espesor alrededor de 150 µ utilizando un espectrómetro de masas VG-PQ2 Turbo+ acoplado con un láser de 193 nm de longitud de onda. El tiempo de contaje de los elementos fue de 2 minutos para los blancos químicos y de 1 minuto para las muestras. El láser operó sobre un área de 77 µ de diámetro con una densidad de energía de 15 J/cm^2 y a una frecuencia de 5 Hz. El ^{30}Si o el ^{43}Ca fueron utilizados como estándares internos y las concentraciones de cada elemento fueron calibradas según los valores de referencia para el vidrio riolítico NIST 610.

Los isótopos radiogénicos de Nd, Sr y Pb se analizaron en la roca total y en separados de clinopiroxeno y plagioclasa para un grupo seleccionado de muestras. Los isótopos de Nd y Pb se analizaron por Espectrometría de Masas Multi-Colector sobre Plasma Inductivamente Acoplado (MC-ICP-MS) en la Ecole Normale Supérieure de Lyon (Francia) utilizando un equipo P54 Fisons o NuPlasma 500. Los análisis de isótopos de Sr se realizaron por Espectrometría de Masas con fuente de Ionización Térmica (TIMS) en el Laboratoire Géosciences Azur de la Université de Nice-Sophia Antipolis (Francia) utilizando un equipo CAMECA TSN 206, o en el LABOGIS del Centre Universitaire de Formation et de Recherche de Nîmes (Francia) utilizando un espectrómetro de masas ThermoFinnigan Triton T1. Previamente, se llevaron a cabo las separaciones químicas de los elementos por cromatografía líquida en el laboratorio de separaciones del ISTEEM utilizando reagentes ultra-puros. Las muestras fueron disueltas inicialmente mediante ataque acido con HNO_3 y HF. El Pb fue separado utilizando la resina AG1-X8 por elución de HBr y HCl. A continuación se extrajeron el Nd y el Sr siguiendo un método modificado de Pin et al. (1994) por elución de HCl y HNO_3.

PETROGÉNESIS DE LAS ROCAS ULTRAMÁFICAS Y MÁFICAS DEL CINTURÓN OFIOLÍTICO MAYARÍ-BARACOA

El Cinturón Ofiolítico Mayarí-Baracoa (Cuba oriental) es un cuerpo pseudo-tabular de ~170 km de largo y 10-30 km de ancho que presenta un espesor promedio de ~3.5 km. Este complejo ofiolítico está constituido por dos macizos intensamente fallados: el macizo de Moa-Baracoa, que aflora en la región oriental del área de estudio, y el macizo de Mayarí-Cristal, que se encuentra en la región occidental (Proenza et al. 1999a, b). Los

dos complejos ofiolíticos están constituidos principalmente por harzburgitas con textura de tectonitas y menores cantidades de dunitas que presentan una orientación sub-paralela a la foliación de las harzburgitas. A menudo las dunitas incluyen cuerpos podiformes de cromita de varios metros de espesor. Tanto las harzburgitas como las dunitas están cortadas por diques máficos (gabros olivinicos a veces con textura pegmatítica, diabasas, troctolitas) y ultramáficos (piroxenitas, wehrlitas con plagioclasa). El macizo de Moa-Baracoa presenta una zona de transición manto/corteza (Moho transition zone) bien desarrollada, con sills gabróicos (gabros olivinicos, troctolitas) y dunitas ocasionalmente impregnadas por fundidos basálticos. En el macizo de Moa-Baracoa se observa también una unidad cortical incompleta de ~ 300 m de espesor, formada principalmente por gabros olivinicos con escaso ortopiroxeno; estos gabros presentan un marcado bandeado modal inducido por la variación de las proporciones volumétricas de clinopiroxeno y olivino con respecto a las de plagioclasa. Por el contrario, en el macizo de Mayarí-Cristal no se observan ni la zona de transición manto/corteza ni la unidad cortical plutónica. Ninguno de los macizos presenta afloramientos de la unidad de gabros isotrópicos, ni del complejo de diques paralelos típicos de la secuencia ofiolítica convencional (p.e. Nicolas 1989). Sin embargo, es conveniente señalar que las rocas volcánicas de las Formaciones Morel y Quibiján están en contacto tectónico con el macizo de Moa-Baracoa, y que las peridotitas del macizo de Mayarí-Cristal están relacionadas espacialmente con las rocas volcánicas pertenecientes a la Formación Téneme.

Las harzburgitas con textura de tectonitas procedentes de los macizos de Moa-Baracoa y Mayarí-Cristal son extremadamente refractarias en términos de abundancias modales (clinopiroxeno < 1 vol.%) y de la composición de la roca total en elementos mayores (contenido en peso en Al_2O_3 en base anhidra = 0.37-1.11% en Moa-Baracoa y 0.14-0.70% en Mayarí-Cristal), elementos de las tierras raras pesadas ($0.06 < Yb_{(N)} < 0.2$, normalizado a la composición del condrito), y elementos traza incompatibles (concentraciones normalizadas a la composición del manto primitivo que varían entre 0.001 y 0.3). Sus signaturas modales y geoquímicas indican que las harzburgitas del Cinturón Ofiolítico Mayarí-Baracoa son rocas mantélicas residuales, generadas mediante altas tasas de fusión parcial (20-30%), la cual tuvo lugar principalmente en condiciones de fugacidad de oxigeno intermedias (fO_2: -1 < QFM < 1). En particular, las peridotitas procedentes de la región meridional del macizo de Mayarí-Cristal registran tasas de fusión más intensas y condiciones de fugacidad de oxigeno ligeramente más altas que las de las otras muestras. Las peridotitas del Cinturón Ofiolítico Mayarí-Baracoa presentan contenidos en algunos elementos traza altamente incompatibles en el manto (Th, Nb, Ta,

elementos de las tierras raras ligeras) relativamente elevados que no reflejan el intenso grado de fusión parcial sufrido por estas rocas. El enriquecimiento relativo en estos elementos es debido al reequilibrio de los residuos de la fusión parcial con fundidos ascendentes que percolaron por el manto.

Las dunitas que afloran en el Cinturón Ofiolítico Mayarí-Baracoa se originaron por interacción de las harzburgitas con fundidos subsaturados en ortopiroxeno en dos escenarios diferentes. En el macizo de Moa-Baracoa las dunitas se formaron por reacción entre las rocas mantélicas y los fundidos percolantes en proximidad de la paleo-Moho. Las dunitas actuaron como canales preferenciales para el flujo poroso focalizado de fundidos basálticos en la zona de transición manto/corteza y fueron ocasionalmente impregnadas por tales fundidos que cristalizaron clinopiroxeno y plagioclasa; por efecto de este proceso las dunitas impregnadas presentan un mayor contenido en Al_2O_3, TiO_2, y elementos traza incompatibles. Las dunitas del macizo de Mayarí-Cristal están probablemente relacionadas con reacciones entre el manto y los fundidos intersticiales en una región más profunda del manto durante la extracción de fundidos en los canales duniticos. Estas dunitas presentan una composición de la espinela [número de Cr = Cr/(Cr+Al) = 0.53-0.75] característica de un ambiente de supra-subducción.

Las peridotitas del Cinturón Ofiolítico Mayarí-Baracoa perdieron, en promedio, el 6% relativo en peso de MgO por efecto de la intensa alteración que sufrieron en el fondo marino. Este proceso ha provocado un aparente enriquecimiento en SiO_2,y en menor medida en FeO_{total}, en estas rocas.

Las composiciones minerales y de roca total de los sills y diques gabróicos que se encuentran en la zona de transición manto/corteza y de los gabros bandeados de la unidad cortical del macizo de Moa-Baracoa indican que estas rocas son acumulados máficos generados a partir de magmas parentales formados a mayor profundidad en el manto. Las concentraciones de elementos de las tierras raras en los fundidos en equilibrio con estos gabros han sido calculadas a partir de la composición de la roca total y de las abundancias modales según el método de Bédard (1994); los análisis adicionales de elementos traza en el clinopiroxeno de dos gabros cumuliticos de la unidad cortical del macizo de Moa-Baracoa han proporcionado resultados coincidentes con aquellos obtenidos por este método. Los espectros de tierras raras de los fundidos en equilibrio con los acumulados máficos del Cinturón Ofiolítico Mayarí-Baracoa son de tipo MORB ($La/Yb_{(N)}$ = 0.5-0.9; $Ce/Sm_{(N)}$ = 0.6-1.0, normalizados a la composición del condrito). Estos espectros y los números de Mg [100 x $MgO/(MgO+FeO_{total})$ en concentración molar] calculados para los fundidos en equilibrio con el olivino de los gabros de Moa-Baracoa

coinciden con los valores propios de las rocas volcánicas de la Formación Morel. Por otro lado, las rocas volcánicas de la Formación Téneme presentan espectros de tierras raras claramente enriquecidos en elementos de las tierras raras ligeras que no coinciden con el espectro del fundido en equilibrio con el micro-gabro de Mayarí-Cristal analizado en este estudio. Se puede por lo tanto concluir que las rocas volcánicas de la Formación Morel representan los productos de cristalización de los fundidos derivados de la fraccionación de los acumulados gabróicos del macizo de Moa-Baracoa. Por el contrario, no se han encontrado relaciones geoquímicas entre la muestra estudiada de los diques cumuliticos que cortan las peridotitas del macizo de Mayarí-Cristal y las rocas volcánicas de la Formación Téneme.

PETROGÉNESIS DEL MAGMATISMO CRETÁCICO EN CUBA ORIENTAL

Las series magmáticas de edad Cretácico Superior que están relacionadas espacialmente con los macizos ofiolíticos de Moa-Baracoa y Mayarí-Cristal presentan diferentes signaturas geoquímicas asociadas a una zona de subducción. En el presente estudio estas series se han clasificado en tres grupos principales, diferenciados según sus composiciones geoquímicas. El Grupo 1 (rocas afines a la Formación Morel) está formado por basaltos toleíticos y escasas andesitas basálticas que presentan una signatura geoquímica de tipo MORB, similar a los basaltos cristalizados en una cuenca de trasera de arco (TiO_2 = 1.2-2.9% en peso; $La/Yb_{(N)}$ = 0.7-0.9, normalizado a la composición del condrito; Th/Nb = 0.06-0.08). Estas rocas se caracterizan por presentar altos valores iniciales de ε_{Nd} (9.1-11.1), y razones isotópicas $^{207}Pb/^{204}Pb$ (15.49-15.51) y $^{208}Pb/^{204}Pb$ (37.65-37.74) levemente radiogénicas.

El Grupo 2 está constituido por diques de composición basáltica y raramente andesítico-basáltica que intruyen a las peridotitas residuales del Cinturón Ofiolítico Mayarí-Baracoa, especialmente en el área de Guamuta-Loma de la Bandera (macizo de Mayarí-Cristal). Estos diques presentan una composición en elementos mayores y traza afín a la de las toleitas de arco (TiO_2 = 0.7-1.4% en peso; $La/Yb_{(N)}$ = 0.6-0.9, normalizado a la composición del condrito; Th/Nb = 0.06-0.69). Los valores iniciales de ε_{Nd} (9.6-11.0) de estos diques son similares a los del Grupo 1, pero en general sus razones isotópicas $^{207}Pb/^{204}Pb$ (15.46-15.60) y $^{208}Pb/^{204}Pb$ (37.74-38.25) son más radiogénicas. La datación mediante el método Ar-Ar de un separado de hornblenda indica una edad intrusiva mínima de 88.6 ± 3.5 Ma para los diques del Grupo 2.

El Grupo 3 está constituido por rocas volcánicas pobres en Ti (TiO_2 = 0.3-0.9% en peso) de composición variable entre basáltica y dacítica, y, en menor medida, diques

basálticos andesíticos y rocas intrusivas dioríticas pertenecientes a las Formaciones Téneme y Quibiján. Estas series presentan una afinidad calcoalcalina sobre la base de su composición en elementos mayores. Las rocas ígneas del Grupo 3 están claramente asociadas a una zona de subducción como demuestran su enriquecimiento relativo en elementos de las tierras raras ligeras ($La/Yb_{(N)}$ = 1.1-5.0, normalizado a la composición del condrito), sus altas razones Th/Nb (0.35-1.51), junto con sus valores iniciales de ε_{Nd} variables pero relativamente bajos (2.7-9.4) y sus valores relativamente radiogénicos de $^{87}Sr/^{86}Sr$ (0.70339-0.70531), $^{207}Pb/^{204}Pb$ (15.53-15.62) y $^{208}Pb/^{204}Pb$ (37.94-38.39).

Para deducir la tasa de fusión parcial sufrida por las fuentes mantélicas del magmatismo Cretácico de Cuba oriental y obtener indicaciones sobre la profundidad a la que tuvo lugar la fusión, se ha realizado una modelización de los contenidos en elementos de las tierras raras medianas (en particular Dy) y de los elementos de las tierras raras pesadas (en particular Lu) en los producto de fusión parcial de una lherzolita con espinela y de una lherzolita con granate. Los resultados obtenidos indican que los tres grupos magmáticos identificados en Cuba oriental se formaron por diferentes tasas de fusión parcial (< 5-35%) de una lherzolita con espinela variablemente empobrecida. La ausencia de granate en la fuente mantélica indica que la fusión se produjo principalmente a profundidades inferiores a 85 km. Los resultados de la modelización en las rocas más primitivas de cada serie, asociados a los valores de sus razones Ta/Yb, indican que las fuentes de los Grupos 2 y 3 tenían una composición variable entre la del manto empobrecido fuente de los MORB (DMM) y la de un manto levemente más empobrecido (D-DMM); por otro lado la signatura geoquímica de los volcánicos del Grupo 1 indica que estas rocas derivaron de una fuente ligeramente más enriquecida (próxima a la composición E-DMM) que la de las otras series magmáticas.

La composición en elementos traza e isótopos radiogénicos de Pb y Nd de las rocas volcánicas más primitivas del Grupo 3 es claramente bimodal. Parte de las muestras se caracteriza por presentar razones Ta/Yb (0.02-0.03) y Th/La (0.10-0.13) relativamente bajas, razones Nb/Ta (13.5-17.3) ligeramente sub-condríticas, y valores iniciales de $^{206}Pb/^{204}Pb$ (18.57-18.62) y ε_{Nd} (7.6-9.4) relativamente altos; por otro lado el resto de las lavas más primitivas del Grupo 3 presenta valores mayores de Ta/Yb (0.07-0.11) y Th/La (0.23-0.31), razones Nb/Ta (7.7-8.9) altamente sub-condríticas, y valores iniciales inferiores de $^{206}Pb/^{204}Pb$ (18.24-18.29) y ε_{Nd} (3.4-5.5). Estas signaturas no se pueden explicar por los procesos normales de fusión parcial de un manto tipo MORB, sino que fueron inducidas por dos componentes de subducción distintos; estos componentes impusieron sus valores fraccionados de la razón Nb/Ta a la fuente

mantélica del Grupo 3. Para el primer sub-grupo, la deshidratación/fusión, en la placa subducente, de meta-sedimentos Cretácicos marinos procedentes del Océano Atlántico pudo haber causado la fraccionación de Nb y Ta; el agente derivado de este proceso pudo haberse mezclado en pequeñas proporciones (< 1%) con el manto altamente empobrecido subyacente al arco y haber sobreimpreso su razón Nb/Ta original. Para el segundo sub-grupo, la razón Nb/Ta altamente sub-condrítica que caracterizaba los fluidos/fundidos derivados de la placa que subducía no fue generada en la zona de subducción, sino que fue heredada de los meta-sedimentos continentales reciclados. Los datos de isótopos radiogénicos, especialmente de Pb, indican que el agente derivado de la placa subducente se originó, en este caso, por deshidratación/fusión de sedimentos continentales procedentes del continente Norteamericano. Este fluido/fundido se mezcló posteriormente, en pequeños porcentajes (< 1%), con la cuña mantélica subyacente al paleo-arco cubano, e impuso una nueva signatura geoquímica a la fuente de parte del Grupo 3 y, en menor medida, del Grupo 2.

MARCO GEODINÁMICO DE LA ACTIVIDAD MAGMÁTICA REGISTRADA EN EL CINTURÓN OFIOLÍTICO MAYARÍ-BARACOA Y EN LAS SERIES ÍGNEAS CRETÁCICAS ASOCIADAS

Las peridotitas de los macizos ofiolíticos de Moa-Baracoa y Mayarí-Cristal presentan composiciones minerales y de la roca total coincidentes con las secciones mantélicas procedentes de un ambiente tanto de dorsal oceánica como de supra-subducción. Sin embargo, las condiciones de fugacidad de oxigeno que acompañaron la fusión parcial de estas peridotitas coinciden con los valores más oxidantes propios de un ambiente de dorsal oceánica (fO_2: -3 < QFM < 0, según Lee et al. 2003). Esta observación sustenta una localización en una cuenca de trasera de arco con una ligera signatura de supra-subducción para el centro de expansión oceánica donde se formó la litosfera del Cinturón Ofiolítico Mayarí-Baracoa. Para el macizo de Mayarí-Cristal, un ambiente original de supra-subducción está ulteriormente sustentado por la composición de la espinela en las dunitas, que indica que estas rocas se formaron por interacción de las tectonitas mantélicas con fundidos toleíticos de arco de isla. Además, las relaciones cogenéticas deducidas entre los gabros cumulíticos del macizo de Moa-Baracoa y los volcánicos de la Formación Morel, interpretados en este estudio y por Kerr et al. (1999) como toleiitas originadas en una cuenca de trasera de arco, confirman un ambiente de supra-subducción para el origen de la litosfera oceánica que constituye el Cinturón Ofiolítico Mayarí-Baracoa.

Los macizos ofiolíticos de Moa-Baracoa y Mayarí-Cristal presentan características diferentes tanto en términos de sus secuencias litológicas cómo de la composición de los minerales y de la roca total. Estas diferencias indican que los dos macizos no formaron parte de una única secuencia litosférica sino que estaban localizados en dos ambiente geodinámicos distintos. El macizo de Moa-Baracoa representaría una porción de litosfera de tipo MORB originalmente situada cerca de una dorsal de retro-arco, mientras que el macizo de Mayarí-Cristal está constituido por una secuencia mantélica transicional (MORB-IAT) situada originalmente más cerca del frente del arco volcánico que la litosfera representada por el macizo de Moa-Baracoa.

La variabilidad en el grado de empobrecimiento y en la influencia de un componente de subducción registrada por las fuentes del magmatismo Cretácico en Cuba oriental puede reflejar diferentes ambientes geodinámicos de la actividad magmática que posiblemente estaban alineados en dirección perpendicular al frente volcánico. En este contexto las rocas volcánicas afines a la Formación Morel (Grupo 1) pudieron haber extruido en una dorsal oceánica de trasera de arco y pasaron a formar parte de la secuencia litosférica representada por el macizo de Moa-Baracoa. Por otro lado, los diques intrusivos con afinidad de toleitas de arco, que afloran especialmente en el área de Guamuta-Loma de la Bandera (Grupo 2), fueron generados más cerca del paleo-arco volcánico que las rocas de la Formación Morel en un ambiente geodinámico probablemente coincidente con la porción litosferica del macizo de Mayarí-Cristal. Las rocas calcoalcalinas de las Formaciones Téneme y Quibiján (Grupo 3) registran la actividad magmática generada en el frente volcánico del antiguo paleo-arco cubano. La influencia de sedimentos procedentes del Océano Atlántico y del continente Norteamericano en la composición de las fuentes del magmatismo Cretácico en Cuba oriental indica que la litosfera de la placa Proto-Caribeña (Norteamericana-Proto Atlántica) estaba subduciendo debajo del paleo-arco de las Antillas Mayores en el Cretácico Superior (Pre-Campaniense). Esta conclusión sustenta los modelos de la evolución geodinámica del Caribe que proponen que la subducción en sentido suroeste, debajo del arco de las Antillas Mayores, empezó en el Aptiense.

CONTENTS

1. INTRODUCTION

1. INTRODUCTION

1.1. SOME BASIC CONCEPTS

I think that at the beginning of this study it is useful to introduce some fundamental geological concepts although presented in a very elementary definition.

The Earth crust and the strong outer layer of the upper mantle are different in mineralogy but very similar mechanically and they define the lithosphere (~ 50-300 km thick), the portion of the Earth that reacts to many stresses as an elastic solid. On the other hand the asthenosphere, extending in the upper mantle below the base of the lithosphere, is by comparison a weak layer that deforms by creep (e.g. Barrell 1914; Le Pichon et al. 1973; Condie 1997).

Physical and chemical differences exist between the continental and oceanic lithosphere. Geophysical and petrological studies have provided evidence that the crust and the lithospheric mantle under the continents are thicker than in oceanic plates (e.g. Jordan 1975). The nature of the crust represents the main compositional difference between the two types of lithosphere and consequently determines their distinct densities. The continental crust has an average bulk composition that can be defined as intermediate or andesitic (Taylor and McLennan 1985 and references therein) whereas the oceanic crust is viewed as dominantly basaltic (e.g. Penrose Conference Participants 1972) and denser.

Sampling the upper mantle is obviously problematic. Investigations on cratonic or off-craton continental mantle lithosphere have been mainly focused on ultramafic xenoliths enclosed in kimberlitic or alkalic basalt lavas and on orogenic lherzolite massifs (review in Walter 2003); on the other hand, the abyssal peridotites collected in dredge hauls and as drill cores from the oceanic seafloor are believed to represent the modern oceanic lithospheric mantle (Bodinier and Godard 2003 and references therein). In terms of modal and major element compositions the subcontinental mantle xenoliths are generally richer in orthopyroxene and show higher bulk Mg# [100 x molar MgO/(MgO+FeOt); where FeOt is total Fe] and SiO_2 contents than the oceanic mantle peridotites (e.g. Boyd 1989; Herzberg 2004). This signature is usually interpreted as evidence that the xenoliths collected from the subcontinental mantle are residues of melt extraction at higher average pressures than the oceanic abyssal peridotites (e.g. Walter 2003). Furthermore, the

continental mantle lithosphere is generally viewed as a reservoir enriched in incompatible trace elements compared to the oceanic mantle (McDonough 1990).

1.2. THE OCEANIC LITHOSPHERE

Our knowledge of the structure and composition of the oceanic lithosphere comes from four main sources: 1) geophysical studies of its seismic, magnetic, gravitational and heat flow properties; 2) drilling and dredging of the oceanic seafloor; 3) exposures at submarine fracture zones and tectonic windows; 4) studies of portions of oceanic lithosphere that have been obducted onto the land (ophiolite complexes).

The general structure of the oceanic lithosphere is composed, from top to bottom, by: 1) pelagic sediments; 2) basaltic pillow lavas (~ 1-2 km thick); 3) a basaltic sheeted dyke complex (~ 1-2 km thick); 4) gabbroic rocks of diverse textures (~ 3-5 km thick); and 5) ultramafic mantle rocks (Fig. 1.1) (e.g. Penrose Conference Participants 1972; Mutter and Mutter 1993; Karson et al. 2002). Areas of anomalously (10-30 km) thick oceanic crust constitute the so-called oceanic plateaus (e.g. Mahoney et al. 1993; Gladczenko et al. 1997; Eldholm and Coffin 2000; Hauff et al. 2000; Weis et al. 2001; Kerr et al. 2003).

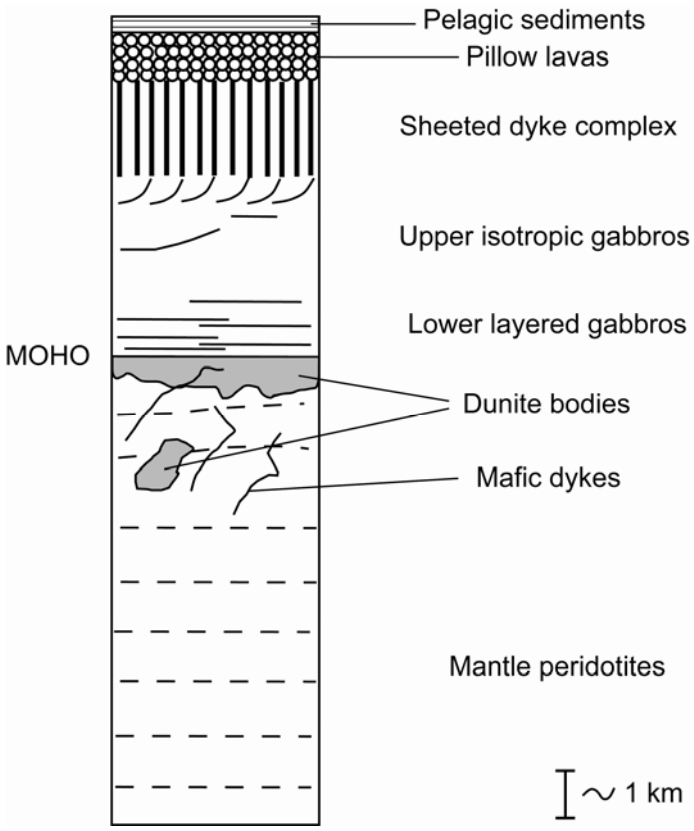

Figure 1.1 Schematic section of common oceanic lithosphere, after Boudier and Nicolas (1985).

New oceanic lithosphere is created at divergent plate boundaries (ocean ridges or spreading centers). The generally accepted model for its genesis (e.g. Klein 2003 and references therein) implies that the plate separation at ocean ridges causes the asthenospheric mantle below to rise. Adiabatic melting of decompressing mantle starts at the depth where it intersects the solidus of fertile peridotite and ends as result of conductive cooling to the seafloor. Ascending magmas interact with previous melting residues and are focused toward the spreading centre (Kelemen et al. 1992; 1995). Pooled melt replenishes a mush (crystals + melt) zone under the ridge and forms a thin (50-100 m) lens where cooling and crystallization of gabbroic rocks take place. Such melt lenses are believed to be present for long periods at fast-spreading ridges (spreading rate = 6-8 cm/yr), but they are transient at ridges with slow-spreading rate (1-2 cm/yr). In consequence the crust at slow-spreading ridges is thin and mantle lithosphere can tectonically be exposed at the seafloor (Cannat et al. 1997; Escartin and Cannat 1999). Extensive forces associated with seafloor spreading periodically create a pathway favorable for dyke injection and the magma can eventually erupt on the ocean floor.

The extraction of predominantly basaltic melts is the main process that controls the mineralogical and chemical compositions of the oceanic lithospheric mantle. Dick and Bullen (1984), Dick (1989), Bonatti and Michael (1989), Johnson et al. (1990) proved that oceanic abyssal peridotites are the complementary residues of the mid-ocean ridge basalts (MORB) generally after 5-25% melt extraction. Pressure, temperature, initial bulk composition of the mantle, melting degrees, residual porosity and extent of equilibration between migrating magmas and wall rocks are the main variables that control the composition of melts and residues. The modal assemblage of fertile mantle peridotite is mainly constituted by olivine (50-60 vol.%), orthopyroxene (20-30 vol.%), clinopyroxene (15-20 vol.%) and a pressure-dependant aluminous mineral. At the solidus temperature, plagioclase is the stable phase at pressure less than ~ 1 GPa, giving way to spinel (~ 1-2.5 GPa) and garnet (> 2.5 GPa) (e.g. Walter 2003); however, melting in the plagioclase stability field is physically unlikely (Niu 2004). Melt extraction can be modeled as either a batch process, wherein a given amount of melt equilibrates with the residue at a prescribed pressure and temperature (e.g. Ribe 1985), or as a fractional process in which an infinitesimal amount of melt is extracted and isolated from the residue without re-equilibration (Johnson et al. 1990). In nature a spectrum from batch to fractional melting likely exists and mixtures of polybaric near-fractional and batch melting better describe the melting processes beneath the mid-ocean ridges (Asimow 1999). As effect of melt extraction, modal and chemical compositions of the mantle residues continuously change as minerals are consumed or crystallized during melting and elements are incorporated

into the melt. Melting of spinel lherzolite generally consumes pyroxene and spinel and leads to olivine crystallization in the residue (Kinzler and Grove 1992; Baker and Stolper 1994; Niu 1997), whereas at higher pressures olivine, clinopyroxene and garnet are the main melting phases (Walter 1998; Presnall et al. 2002).

Once created, the oceanic lithosphere is transported off-axis to each side of the spreading center, accumulating sediment at the top as it ages, and is ultimately consumed at subduction zones (convergent plate boundaries) where it returns in a modified form to the asthenospheric mantle (e.g. Isacks et al. 1968; McKenzie 1969; Green 1972). Subduction causes volcanic arc magmatism as result of the flux-related and decompression melting of the subarc mantle that is affected by addition of H_2O and other fluxes (by fluids/melts/supercritical liquids) from the subducting material (e.g. Armstrong 1968, 1981; Hawkesworth et al. 1979; Chase 1981; Gill 1981; Hawkesworth et al. 1991; Elliott 2003). The generally higher contents in aqueous fluids induce the supra-subduction peridotites to usually record higher melting degrees and fO_2 values than the oceanic ridge mantle (Brandon and Draper 1996; Parkinson and Pearce 1998; Pearce et al. 2000; Lee et al. 2003). The compositions of arc-related volcanic and plutonic rocks also reflect the processes occurring in their mantle source and are strongly influenced by the signatures of two main reservoirs: a) the pre-subduction mantle wedge beneath the arc and b) the mobile phase created by the prograde dehydration/melting of the subducting slab (e.g. Kay 1980; McCulloch and Gamble 1991; Hawkesworth et al. 1991, 1993; Pearce and Peate 1995). As result of these processes the composition of the crust generated at convergent plate boundaries is remarkably similar to the average continental crust (e.g. Kelemen et al. 2003a; Plank 2005).

1.3. MAIN COMPOSITIONAL DIFFERENCES BETWEEN OCEAN RIDGE AND SUBDUCTION-RELATED IGNEOUS ROCKS

The geochemical characteristics of mid-ocean ridge and arc lavas have been recently compared by Kelemen et al. (2003a). In general arc magmas show higher SiO_2 and lower FeOt and TiO_2 contents than MORB at similar stages of differentiation. Olivine, clinopyroxene and plagioclase start to be fractionated from MOR-melts at the primitive stages of differentiation thus leading to a steady increase in FeOt and TiO_2 and decrease in Al_2O_3 (tholeiitic trend); on the other hand, FeOt, TiO_2 and Al_2O_3 abundances increase during the evolution of primitive arc melts (Mg# > 50) and after generally decrease as result of delayed fractionations of Fe-Ti oxides and plagioclase (calcalkaline trend). These different evolutionary trends are ascribed to a variable role of higher pressure crystal

fractionation and higher H_2O content of the parental melts in calcalkaline relative to tholeiitic series (e.g. Grove and Kinzler 1986).

MOR- and arc magmas in general differ not only in terms of major element evolutionary trends but also for their contents in incompatible trace elements. Cs, Rb, Ba, Th and U are enriched in most arc lavas relative to MORB, along with light rare earth elements (LREE), Pb and Sr. On the other hand, middle- and heavy-REE, which are slightly less incompatible than LREE in the common mantle assemblage, are generally depleted in arc magmas. The possible sources of enrichment in highly incompatible trace elements are commonly related to the agent(s) extracted from the subducting slab, i.e. the aqueous fluids/hydrous melts/supercritical liquids derived from the subducting metasediments, (altered) metabasalts and/or partially serpentinized mantle peridotites (e.g. Peacock et al. 1994; Schmidt and Poli 1998, 2003; Garrido et al. 2005; Kessel et al. 2005). These fluxes could act in the arc setting upon a mantle wedge with a composition similar to the enriched sources inferred for the ocean island basalts (OIB), or on a MORB-mantle depleted by melt extraction beneath a mid-ocean and/or a back arc spreading center (McCulloch and Gamble 1991; Woodhead et al. 1993; Elliott 2003; Plank 2005).

Nb and Ta show a peculiar behaviour in subduction-related settings compared to other trace elements with similar high incompatibility, as they are relatively more depleted in arc magmas than Th, U and LREE. So, for instance relatively low Nb/U (Hofmann et al. 1986) and high Th/Nb and Th/Ta ratios (Plank 2005) have been successfully used to discriminate between arc magmas and both MORB and OIB. This feature has been ascribed to different processes that generally involve the role of Fe-Ti oxides and/or amphibole in the petrogenesis of subduction-related magmas (e.g. Green 1995; Tiepolo et al. 2001; Kelemen et al. 2003a; Schmidt et al. 2004).

The slab contribution to the mantle wedge beneath the arcs also affects the radiogenic isotope composition of the subduction-related melts. In particular arc magmas overlap MORB in terms of Sr-Nd isotope systematic but they generally trend toward higher $^{87}Sr/^{86}Sr$ and lower $^{143}Nd/^{144}Nd$ (ε_{Nd}) ratios than MORB. This is generally ascribed to the contamination of their sources with material ascending from the subducting oceanic crust (metasediments and/or metabasalts) that overprints the isotopic signature of the mantle wedge (e.g. Weaver et al. 1986; Hawkesworth et al. 1993; Elliott 2003 and references therein). Pb radiogenic isotope ratios ($^{206}Pb/^{204}Pb$, $^{207}Pb/^{204}Pb$, $^{208}Pb/^{204}Pb$) display similar tendencies, as arc lavas overlap MORB values but commonly point toward more radiogenic compositions generally coincident with those of local subducting

sediments and/or (altered) oceanic igneous crust (e.g. White and Dupré 1986; Plank and Langmuir 1998; Elliott 2003).

1.4. OPHIOLITES

Ophiolites represent slivers of ancient oceanic lithosphere obducted onto continental crust (Penrose Conference Participants 1972). More than 70 ophiolites have been described throughout all the major orogenic belts of the world and they represent a unique opportunity to study the structure and composition of the oceanic crust and upper mantle. Semail ophiolite in Oman, Troodos ophiolite in Cyprus, Papua ophiolite in Papua-New Guinea, and Bay of Islands ophiolite in Canada are the best known examples. Ophiolite may occur as a thrust sheet of variable thickness or as a tectonic mixture of fragments that displays an incomplete or dismembered lithospheric section (e.g. Coleman 1977; Gass et al. 1984, Nicolas 1989; Parson et al. 1992; Ishiwatari et al. 1994; Vissers and Nicolas 1995; Dilek et al. 2000).

The lithological sequence in ophiolites (Fig. 1.1) is frequently overlain by oceanic sedimentary rocks such as bedded radiolarites, cherts, mudstones, limestones, and greywacke sandstones. The igneous crustal section (volcanics, sheeted dykes and mafic plutonics) generally consists of altered patchy basaltic and gabbroic rocks. Ophiolitic volcanics and dykes display MORB-like, island arc tholeiitic, boninitic and calcalkaline compositions. Crustal plutonics can be usually distinguished into upper isotropic gabbros directly underlying the sheeted dyke complex and lower gabbros with marked modal layering (e.g. Pallister and Hopson 1981; Kelemen et al. 1998 and references therein). Cumulitic mafic rocks are common in ophiolitic crust and occur also as sills or dykes that intrude the underlying mantle peridotite (e.g. Boudier and Nicolas 1995; Korenaga and Kelemen 1997; Kelemen et al. 1997a).

Lithologies in ophiolitic mantle section vary between mildly refractory peridotites dominated by lherzolites (such in Internal Ligurides ophiolite, Italy) and strongly refractory harzburgites (like in Oman ophiolite) (Boudier and Nicolas 1985; Ishiwatari 1985). This variability can be ascribed to different melting degrees recorded by the lithospheric mantle (e.g. Bodinier and Godard 2003 and references therein). From top to bottom the mantle section in ophiolites is in general constituted by the following two main units that can display different thickness and degrees of serpentinization: 1) a dominantly dunitic Moho transition zone (MTZ) where dunites can be interlayered with pyroxenites and gabbroic sills and are often impregnated by melt-derived crystal segregates of clinopyroxene and plagioclase (Nicolas and Prinzhofer 1983; Boudier and Nicolas 1995); 2) a main lherzolitic

or harzburgitic section including a variety of dunite bodies, mafic layers and dykes (e.g. Nicolas and Jackson 1972; Quick 1981; Lippard et al. 1986; Boudier and Nicolas 1988; Suhr 1992; Rampone et al. 1996). Ophiolitic mantle peridotites generally show porphyroclastic and subordinate equigranular textures (Mercier and Nicolas 1975) and record high temperature (> 1200 ºC) deformation related to the asthenospheric mantle flow (e.g. Ceuleneer and Rabinowicz 1992).

The original tectonic setting of several ophiolites has been widely debated especially for the complexes that display a highly depleted mantle section (e.g. Miyashiro 1973; Boudier and Nicolas 1985; Moores et al. 2000). While there is consensus to ascribe the refractory composition of the ophiolitic harzburgites to a high degree of melt extraction, the opinions diverge on whether this process is achieved by decompression melting at intermediate to fast-spreading ridges (e.g. Coleman 1977; Boudier and Nicolas 1985; Nicolas 1989), or by dominantly hydrous melting in supra-subduction mantle wedges (e.g. Pearce et al. 1981, 1984; Ishiwatari et al. 1994; Shervais 2001; Beccaluva et al. 2004; Stern 2004). Suggested supra-subduction settings include back-arc ocean basins, axial arc and forearc settings (e.g. Robertson 2002, 2004).

1.5. IGNEOUS AND OPHIOLITIC ROCKS IN CUBA

In the Jurassic to Recent evolution of the Caribbean two main tectonic phases can be identified. First, Proto-Caribbean oceanic basin opened as result of drift between North America and Gondwana (South America); afterwards a collisional phase led to the development of several volcanic arc systems and the consumption of the Proto-Caribbean (Atlantic) and/or Caribbean (Atlantic or Pacific) oceanic lithosphere (e.g. Pindell and Barrett 1990; Meschede and Frisch 1998; Kerr et al. 1999). As result of this geological evolution several ophiolitic massifs are present in the Caribbean region (Fig. 1.2) (e.g. Lewis et al. 2006) and igneous rocks nowadays constitute the thick floor of the Caribbean basin and numerous terrains emplaced on land.

Three major igneous sequences are commonly recognized in the volcanic and plutonic records of the modern Caribbean (Donnelly and Rogers 1980; Donnelly et al. 1990). Two magmatic suites are unrelated to subduction and are constituted by: 1) Jurassic to Upper Cretaceous, mainly Turonian, magmatic rocks dominated by oceanic basalts (MORB and OIB) (Sinton et al. 1998; Révillon et al. 2000; Kerr et al. 2003) generally associated with putative ophiolite sequences or recovered on the oceanic floor, and interpreted as portions of the Caribbean-Colombian oceanic plateau (Kerr et al. 1997a, b; Lapierre et al. 1999, 2000; Mamberti et al. 2003 and references therein), or

pieces of the Proto-Caribbean (Atlantic) oceanic crust (Donnelly et al. 1990; Kerr et al. 1997a); and by 2) middle Tertiary to Holocene alkaline basalt suites related to rifting tectonics. The third type of Caribbean igneous sequences is constituted by subduction-related volcanic and plutonic rocks associated with the development of the Greater Antilles (Cuba, Jamaica, Hispaniola, Puerto Rico and Virgin Islands) and Lesser Antilles (from Saba in the north to Grenada in the south) island arcs spanning from the Early Cretaceous to Holocene. This subduction-related magmatism comprises Lower Cretaceous island arc tholeiitic (IAT) series and many Cenomanian-Holocene calcalkaline and minor high-K series. The IAT and the calcalkaline series are generally interpreted as recording the early and mature stages of development in the Greater Antilles island arc(s), respectively (Donnelly et al. 1990). The change from IAT to calcalkaline magmatism is thought to reflect a gradual transition related to the temporal evolution of the arc(s) (Kerr et al. 2003), or an abrupt switch of magmatism due to polarity reversal of subduction (Lebron and Perfit 1993, 1994; Draper et al. 1996). In the Greater Antilles arc the calcalkaline igneous activity continued until the Eocene and it is still active in the Lesser Antilles arc.

Figure 1.2 Geographic locations of ophiolitic massifs (green) in northern Caribbean. Black box indicates the Mayarí-Baracoa Ophiolitic Belt, subject of this study. Modified from Wadge et al. (1984).

A large portion of the Cuban accretionary complex is constituted by subduction-related igneous and metamorphic terrains (e.g. Iturralde-Vinent 1996a; Kerr et al. 1999; García-Casco et al. 2002; Blein et al. 2003; Schneider et al. 2004), whereas the occurrence of remnants of the Caribbean-Colombian oceanic plateau and Proto-Caribbean oceanic crust is much more reduced and has been suggested only in the northwestern region of the island (Kerr et al. 1999). Arc-related plutonic bodies are not widespread in Cuba and mainly outcrop in central and southern regions. Kerr et al. (1999)

proposed the existence of two pre-Albian intra-oceanic subduction zones recorded in the Cretaceous Cuban volcanics: one primitive boninitic arc and one tholeiitic arc that subsequently evolved to calcalkaline-alkaline arc in the Albian-Campanian. After the demise of the Cretaceous arc in Late Campanian, several sedimentary basins mainly filled with greywacke and limestone sections (e.g. Iturralde-Vinent 1996a). During the Paleogene a new island arc system developed in the Caribbean realm and in Cuba it is essentially represented by the volcano-sedimentary and plutonic rocks cropping out in the Sierra Maestra range (e.g. Kysar-Mattietti 2001; Rojas-Agramonte et al. 2006). After the Paleogene the subduction activity shifted to the eastern Caribbean zone due to strike slip fault systems (e.g. Oriente fault) and it is nowadays located in the Lesser Antilles arc.

In Cuba several ophiolitic massifs form the so-called “Northern Cuban Ophiolite Belt” constituted by dismembered mafic-ultramafic bodies cropping out along an east-west trend in the northern portion of the island (Fig. 1.2) (Iturralde-Vinent 1989, 1994, 1996a, 1998 and references therein). Cuban ophiolites show a generally incomplete lithospheric section constituted by strongly dislocated tectonic slides locally metamorphosed and mixed with different rock complexes. Highly serpentinized peridotites and mafic volcanics are dominant. These ophiolites represent portions of oceanic lithosphere obducted onto the North American continental paleomargin owing to the collision between the paleo-Greater Antilles island arc and the Florida-Bahamas platform. Cuban ophiolites are generally interpreted as oceanic Proto-Caribbean lithospheric slabs (Iturralde-Vinent 1994), or forearc lithosphere built on the Pacific-Caribbean paleomargin (Pindell and Barrett 1990; Pindell 1994). However, in spite of their importance in the context of the geodynamic evolution of the Caribbean, the structure, petrology and geochemistry of Cuban ophiolites are scarcely documented. In particular, detailed structural studies and geochemical data on major, trace element and isotopic compositions of whole rocks and minerals from residual peridotites, ophiolitic gabbros and tectonically-related volcanics are specially required.

1.6. GOALS OF THIS STUDY

This study is aimed to characterize the lithological, structural, petrological and geochemical signatures of the ultramafic and mafic rocks that constitute the Mayarí-Baracoa Ophiolitic Belt, the easternmost and largest massif of the Northern Cuban Ophiolite Belt (Fig. 1.2). Furthermore, I have also examined the petrological and geochemical signatures of different Cretaceous igneous suites (volcanics, intrusive dykes and plutonics) spatially-related with the Mayarí-Baracoa ophiolitic complex but whose petrological link with the ophiolites had not been so far clarified.

Geochemical data on residual peridotites, ophiolite gabbros and tectonically-related volcanics will be used to infer the degrees of melting underwent by mantle rocks, constrain the interaction processes between migrating magmas and mantle wall rocks, examine key geodynamic issues such as the genetic link between ophiolite plutonics and the spatially-related volcanics, and clarify the supra-subduction, back-arc and/or mid-ocean spreading-ridge nature of the ophiolitic massifs. Moreover, this study is the first to report major and trace element compositions, as well as Nd, Sr and Pb radiogenic isotope ratios and geochronological data, for whole rocks and minerals from the different Cretaceous igneous suites that outcrop in the study region. I will show that these data are important to constrain the subduction polarity of the Greater Antilles paleo-arc in Late Cretaceous and to better characterize the distinct styles of magmatism recorded in eastern Cuba in the frame of the Caribbean plate tectonics.

The results presented here are not only of interest in the context of studies on the geodynamic evolution of the Caribbean realm, but also, and more generally, they contribute to a better understanding of the processes devoted to high degrees of mantle melting at convergent plate boundaries, and shed light to the important subject of how the high-field strength elements (HFSE), in particular Nb and Ta, behave in subduction zones.

In order to achieve these goals I present and discuss the following data for a comprehensive set of samples from the Mayarí-Baracoa Ophiolitic Belt and the spatially-related Cretaceous igneous suites (Morel, Téneme, Quibiján Formations and Guamuta-Loma de la Bandera dykes):

1) Field observations from two campaigns carried out in 2002 and 2004;

2) Electron Probe Microanalyses (EPMA) of major elements in minerals;

3) X-Ray Fluorescence (XRF) analyses of major and minor transition elements (Sc, V, Cr and Ni) in whole rocks;

4) Inductively Coupled Plasma-Mass Spectrometry (ICP-MS) analyses of trace elements in whole rocks;

5) Laser Ablation Inductively Coupled Plasma-Mass Spectrometry (LA-ICP-MS) trace element analyses of minerals;

6) Nd, Sr and Pb radiogenic isotopic ratios measured in whole rocks and mineral separates by Multi-Collector Inductively Coupled Plasma-Mass Spectrometry (MC-ICP-MS) and Thermal Ionisation Mass Spectrometry (TIMS);

7) Step-heating laser probe Ar-Ar isotope analysis on amphibole separate.

1.7. OUTLINE OF THE THESIS

The following sections of this treatise are respectively concerned to:

- *Chapter 2. Geological Setting.* Geographical and geological description of the modern Caribbean region; geological evolution of the Caribbean since the Jurassic with emphasis on the main geodynamic issues still open to debate; synthesis of the geology of Cuba with details on the eastern area of the island.
- *Chapter 3. Analytical Techniques.* For each analytical method: description of sample processing; analytical conditions; treatment of the data; evaluation of the precision and accuracy of the analyses.
- *Chapter 4. Petrogenesis of the ultramafic and mafic rocks from the Mayarí-Baracoa Ophiolitic Belt.* Field relations and petrographic description of the main lithological units constituting the ophiolitic massifs; sampling; mineral chemistry; whole rock geochemistry; discussion and interpretation of the data. The results presented in this chapter have been published in the paper by: Claudio Marchesi, Carlos J. Garrido, Marguerite Godard, Joaquín A. Proenza, Fernando Gervilla, Jesús Blanco-Moreno (2006): *Petrogenesis of highly depleted peridotites and gabbroic rocks from the Mayarí-Baracoa Ophiolitic Belt (eastern Cuba)*. Contributions to Mineralogy and Petrology 151, 717-736.
- *Chapter 5. Petrogenesis of the Cretaceous magmatism in eastern Cuba.* Sampling and petrographic description of the main igneous suites spatially-related with the Mayarí-Baracoa Ophiolitic Belt; whole rock geochemistry; Nd-Sr-Pb radiogenic isotopic compositions; Ar-Ar geochronology; discussion and interpretation of the data. The results presented in this chapter have been submitted for publication in *Journal of Petrology* in the paper by: Claudio Marchesi, Carlos J. Garrido, Delphine Bosch, Joaquín A. Proenza, Fernando Gervilla, Patrick Monié, Antonio Rodríguez-Vega: *Geochemistry of the Cretaceous Magmatism in Eastern Cuba: Implications for Nb-Ta Behaviour in Subduction Zones and Recycling of North American Continental Sediments at the Western Greater Antilles Paleo-arc*.
- *Chapter 6. Geodynamic setting of the magmatic activity recorded in the Mayarí-Baracoa Ophiolitic Belt and the spatially-related Cretaceous igneous suites.* Tectonic setting of the Mayarí-Cristal and Moa-Baracoa ophiolitic massifs; geochemical classification of the Cretaceous igneous rocks from eastern Cuba in the frame of the Caribbean magmatic suites; tectonic setting of the magmatic activity recorded by the Cretaceous igneous suites from eastern Cuba; subduction polarity of the Greater

Antilles paleo-arc in Late Cretaceous; implications for geotectonic models proposed for the Caribbean realm.

- *Chapter 7. Conclusions - Conclusiones.*
- *References.*
- *Appendixes.* Tables with major, trace element and Nd-Sr-Pb isotopic compositions of minerals and whole rock for the studied samples.

2. GEOLOGICAL SETTING

2. GEOLOGICAL SETTING

2.1. INTRODUCTION

Cuba is the biggest and westernmost of the Greater Antilles and borders the Gulf of Mexico and the North American continent (North), the Florida-Bahamas platform and the Atlantic Ocean (East), the Caribbean Sea (South), the Yucatán Basin and Central America (West). The Cuban archipelago is formed by the island of Cuba (104 945 km²), the Island of Pines (or Island of Youth) (2200 km²) and around 4200 keys and islands of small size. The geographical limits of the country are between the ~19º 49' and the ~23º 17' north latitude and between the ~74º 07' and the ~84º 57' west longitude. The island of Cuba has a length (Northwest-Southeast) of ~1250 km and a width (North-South) that varies between ~32 and 210 km. Cuba is mainly a flat country as around 75% of its surface is formed by plains (altitude < 100 m above sea level) that alternate with 3 main mountain ranges located in the occident, center and east of the island, respectively: the Sierra Guaniguánico (Pinar del Rio province), the Guamauhaya (Escambray) Range (Cienfuegos, Santa Clara and Sancti Spiritus provinces) and the Sierra Maestra (Guantánamo, Santiago de Cuba and Granma provinces). Pico Turquino in Sierra Maestra is the highest peak of the island with 1974 meters above sea level.

2.2. THE MODERN CARIBBEAN

Cuba is nowadays incorporated in the North American Plate but till the Middle-Late Eocene was an integrating part of the Caribbean Plate (e.g. Draper and Barros 1994; Iturralde-Vinent 1994, 1996a). The modern central Caribbean is a lithospheric plate mainly consisting of an anomalously (up to 20 km) thick oceanic plateau (e.g. Donnelly 1994; Kerr et al. 2003) situated between the North and South American continents. Several deep water regions are present in the Caribbean Sea: the Yucatán Basin, the Cayman Trough, the Colombian Basin, the Venezuelan Basin and the Grenada Basin (Fig. 2.1). They are separated by more or less linear ridges and rises: the Cayman Ridge, the Nicaraguan Rise, the Beata Ridge and the Aves Ridge, respectively (e.g. Case et al. 1990; Holcombe et al. 1990; Draper et al. 1994).

At present the Caribbean Plate is moving eastwards with respect to both North and South America at a rate of about 1-4 cm/yr (Mann et al. 1990 and references therein).

These movements are distributed on several active fault zones at the northern and southern plate boundaries producing seismic areas about 200 km wide. The Caribbean northern plate boundary is marked by the Motagua-Polochic fault zone in Central America that extends eastward in the Swan Island and Oriente left-lateral transform faults (Fig. 2.1) (e.g. Lewis and Draper 1990). A left lateral step-over in the boundary between the Caribbean and North America has resulted in a crustal-scale pull-apart basin, the Cayman Trough, in which a 100 km long spreading ridge segment has been developed (Fig. 2.1) (e.g. Holcombe et al. 1990). The boundary between the Caribbean and the South American plates coincides with the northern Venezuelan Orogenic Belt (Caribbean Mountain System, Netherlands and Venezuelan Antilles) which is an area of intense deformation and accretion generally related to right-lateral strike-slip faults (Fig. 2.1) (Molnar and Sykes 1969; Bellizzia and Dengo 1990; Mann et al. 1990 and references therein).

Figure 2.1 Geological provinces of the Caribbean region with the location of modern plate boundaries and major tectonic elements. Modified from Calais et al. (1992) and Draper et al. (1994).

The eastward movement of the Caribbean Plate has resulted in the subduction of the Atlantic oceanic lithosphere beneath the eastern margin of the Caribbean producing the Lesser Antilles island arc system (e.g. Maury et al. 1990; Macdonald et al. 2000).

Eastward motion of the Nazca and Cocos Plates with respect to the Caribbean and North America produces the subduction of these plates beneath the western margin of the Caribbean, i.e. beneath Central America (Fig. 2.1) (e.g. Ladd et al. 1990; McCann and Pennington 1990).

2.3. GEOLOGICAL EVOLUTION OF THE CARIBBEAN

The plate tectonic evolution of the Caribbean is complex and investigators have not yet come to a consensus on a geodynamic model capable of integrating the different geologic observations available in this region (e.g. reviews in Draper and Dengo 1990; Morris et al. 1990; Iturralde-Vinent 1998; James 2006; Iturralde-Vinent and Lidiak 2006). It is widely accepted that the Proto-Caribbean oceanic crust was originated in Middle Jurassic-Early Cretaceous during continental rifting and ensuing opening of an oceanic basin between the North and South America (Gondwana) continents (Fig. 2.2) (e.g. Ross and Scotese 1988; Morris et al. 1990; Pindell and Barrett 1990; Sawyer et al. 1991; Meschede and Frish 1998; Mann 1999). In southern and eastern U.S.A. this phase reactivated pre-existing thrust faults of the Alleghanian Orogen and led to deposition of terrestrial red beds in extensive graben belts (Rodgers 1984). Further south, rift-related volcanism occurred and Florida-Bahamas basins were filled with evaporitic sediments that correlate with contemporary salt deposits in western Africa (Fig. 2.2) (Jansa and Weidmann 1982).

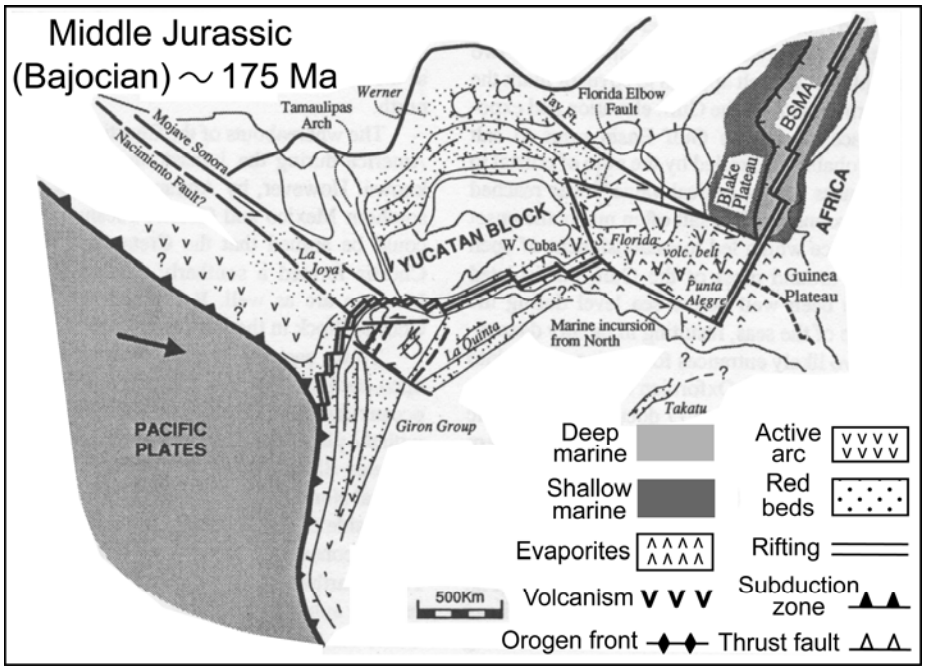

Figure 2.2 Middle Jurassic (Bajocian) paleogeographic reconstruction of the Caribbean realm, from Pindell (1994).

During the Late Jurassic-Early Cretaceous, seafloor spreading occurred in the Gulf of Mexico and the Proto-Caribbean Sea continued to open between Yucatán and Venezuela as an arm of the Central North Atlantic Ocean. West of the Proto-Caribbean area a main intra-oceanic westward facing island arc developed as result of subduction of the Pacific (Farallon) lithosphere beneath the Proto-Caribbean and marked the onset of the Greater Antilles island arc (Fig. 2.3). The number of subduction zones active during this phase and their relative polarity are open to debate as some authors (e.g. Iturralde-Vinent 1994, 1998; Draper and Barros 1994; Kerr et al. 1999) propose that different arc system(s) were present further east in the Proto-Caribbean realm.

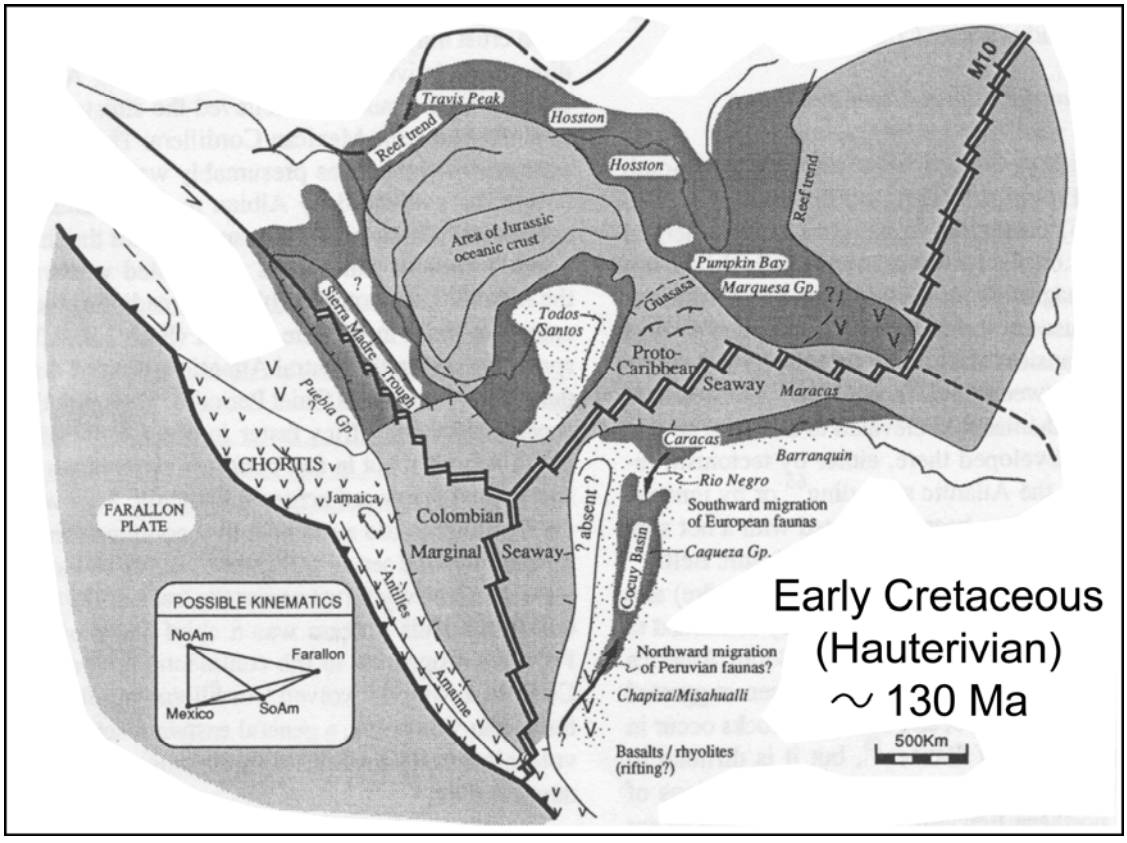

Figure 2.3 Early Cretaceous (Hauterivian) paleogeographic reconstruction of the Caribbean realm, from Pindell (1994). Legend as in Figure 2.2.

Another important point of recurring controversy in the models of the Caribbean tectonic evolution is the age (principally Aptian *vs* Campanian) of subduction reversal from northeast to southwest dipping slab in the Greater Antilles island arc system (Mattson 1979; Burke 1988; Duncan and Hargraves 1984; Lebron and Perfit 1993, 1994; Pindell 1994; Draper et al. 1996; Kerr et al. 1998, 2003; Pindell and Kennan 2001; Lewis et al. 2002; Kesler et al. 2005; García-Casco et al. 2006; Pindell et al. 2006). According to the

authors that propose the Aptian-Albian flipping of subduction (Fig. 2.4) this event probably occurred as result of the Mid-Cretaceous increase of spreading rate in the Central Atlantic (e.g. Pindell 1994; Pindell et al. 2006). On the other hand, researchers that set the polarity reversal in the Campanian generally relate it to the failed subduction of the thick buoyant Caribbean oceanic plateau in the Greater Antilles arc system (e.g. Burke 1988; Kerr et al. 1998, 2003).

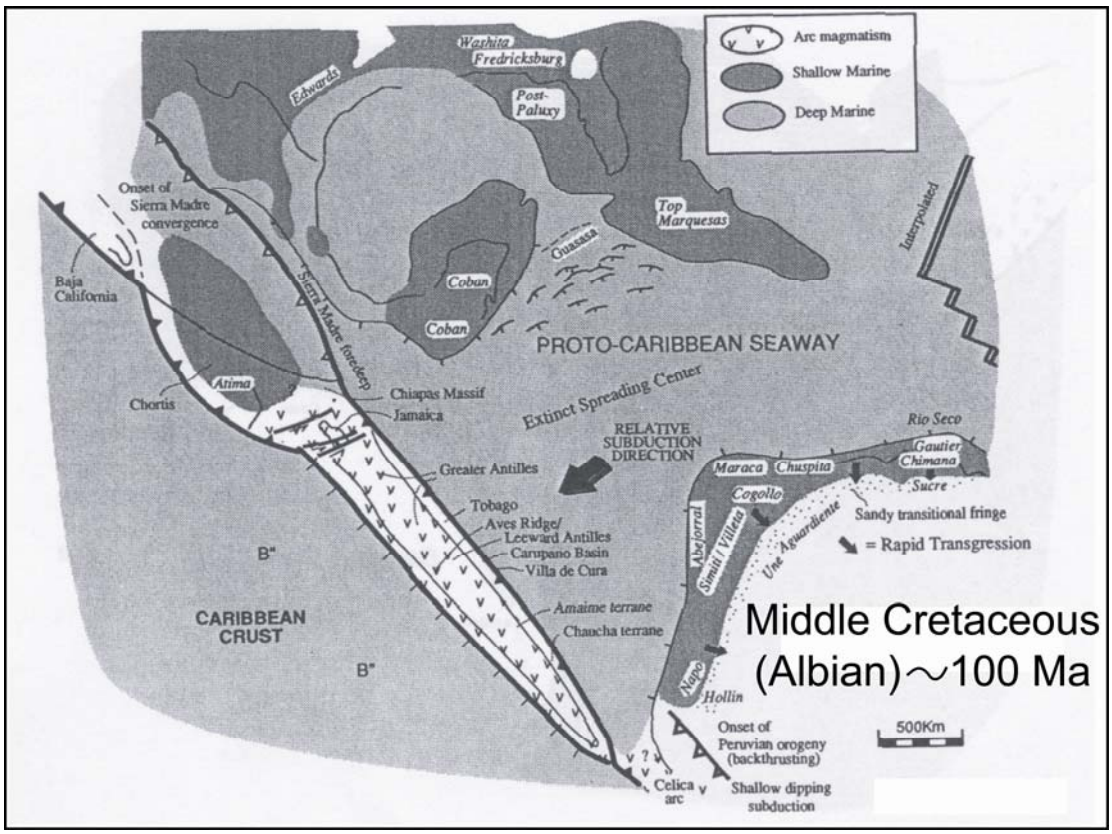

Figure 2.4 Middle Cretaceous (Albian) paleogeographic reconstruction of the Caribbean realm, from Pindell (1994). Legend as in Figure 2.2.

Thus, if an Aptian-Albian flip of the dipping slab polarity is assumed, the Late Albian-Eocene magmatic activity in the Caribbean realm is consequence of subduction of the Proto-Caribbean oceanic lithosphere beneath the Greater Antilles arc at the eastern margin of the Caribbean (Fig. 2.5).

At this stage the models of the Caribbean tectonic evolution diverge again in two essentially different groups: 1) the “Pacific” models that propose a Late Cretaceous (mainly Turonian-Campanian) origin of the Caribbean thick oceanic lithosphere in the Pacific region and its eastward drift towards the present position between North and South America (Wilson 1966; Malfait and Dinkelman 1972; Pindell and Dewey 1982; Duncan

and Hargraves 1984; Ross and Scotese 1988; Pindell 1985, 1994; Pindell and Barrett 1990; Mann 1999; Pindell et al. 2006); and 2) the “inter-American” models that support the formation of the Caribbean thick oceanic crust by seafloor spreading between Yucatán and South America and limited eastward migration (Fig. 2.6) (Ball et al. 1969; Aubouin et al. 1982; Anderson and Schmidt 1983; Donnelly 1989; Iturralde-Vinent 1994, 1996a; Meschede and Frisch 1998; James 2006; Giunta et al. 2006). In the first case the thick crust of the Caribbean-Colombian oceanic plateau is related to Galápagos or other Pacific plumes (Kerr et al. 1997a, b, 2002; Sinton et al. 1998; Lapierre et al. 1999, 2000; Révillon et al. 2000; Mamberti et al. 2003) whereas in the second it is likely linked to the Cretaceous superplume event in the Atlantic (Cox 1991; Larson 1991).

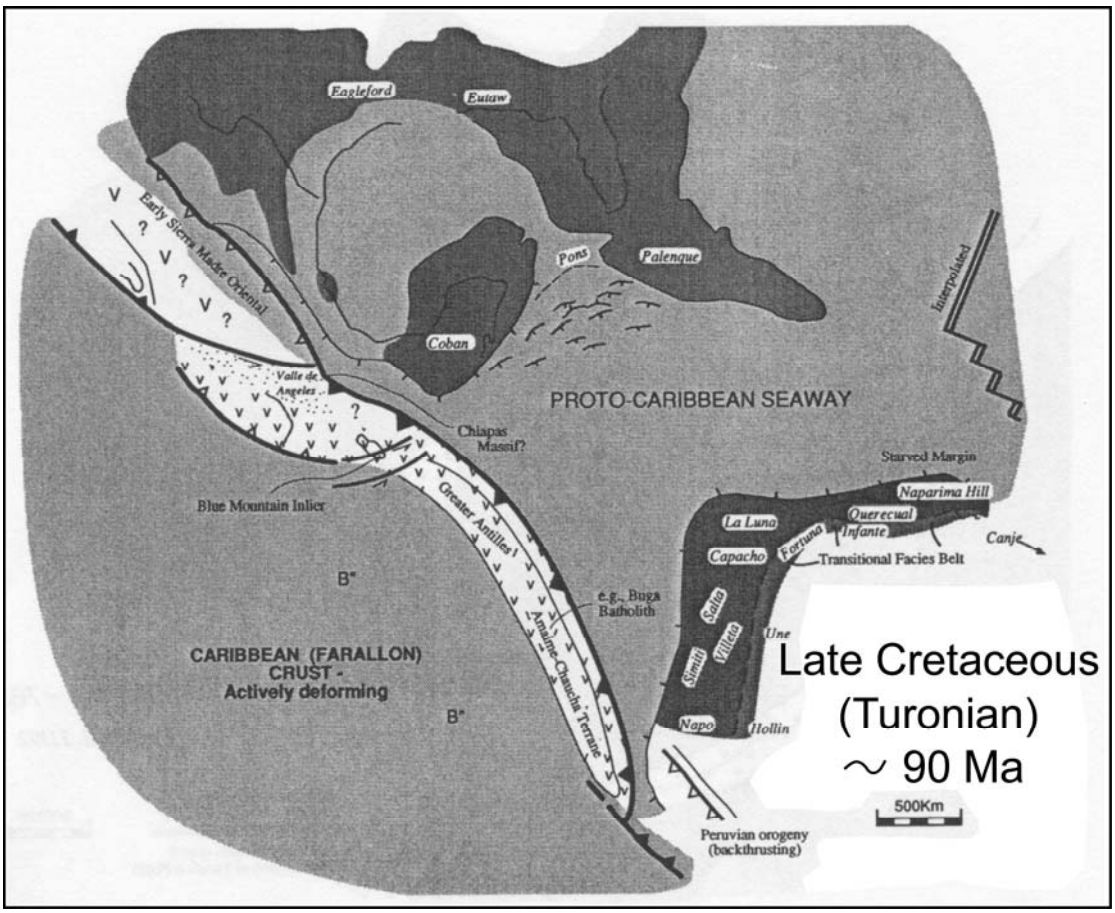

Figure 2.5 Late Cretaceous (Turonian) paleogeographic reconstruction of the Caribbean realm, from Pindell (1994). Legend as in Figure 2.2.

Probably in Early Campanian the Pacific lithosphere began to subduct eastward at the new Costa Rica-Panama arc system thus defining the western margin of the Caribbean Plate (Fig 2.7a). The Caribbean proceeded to move east-northeast at about 3 cm/yr and consequently the Greater Antilles island arc collided with the Florida-Bahamas

platform in the Paleocene-Late Eocene. Cuba terrains were thus incorporated in the North American Plate and eastward migration of the Caribbean relative to North America continued along a new plate boundary system (Fig 2.7b) (e.g. Lewis and Draper 1990; Pindell and Barrett 1990; Meschede and Frisch 1998).

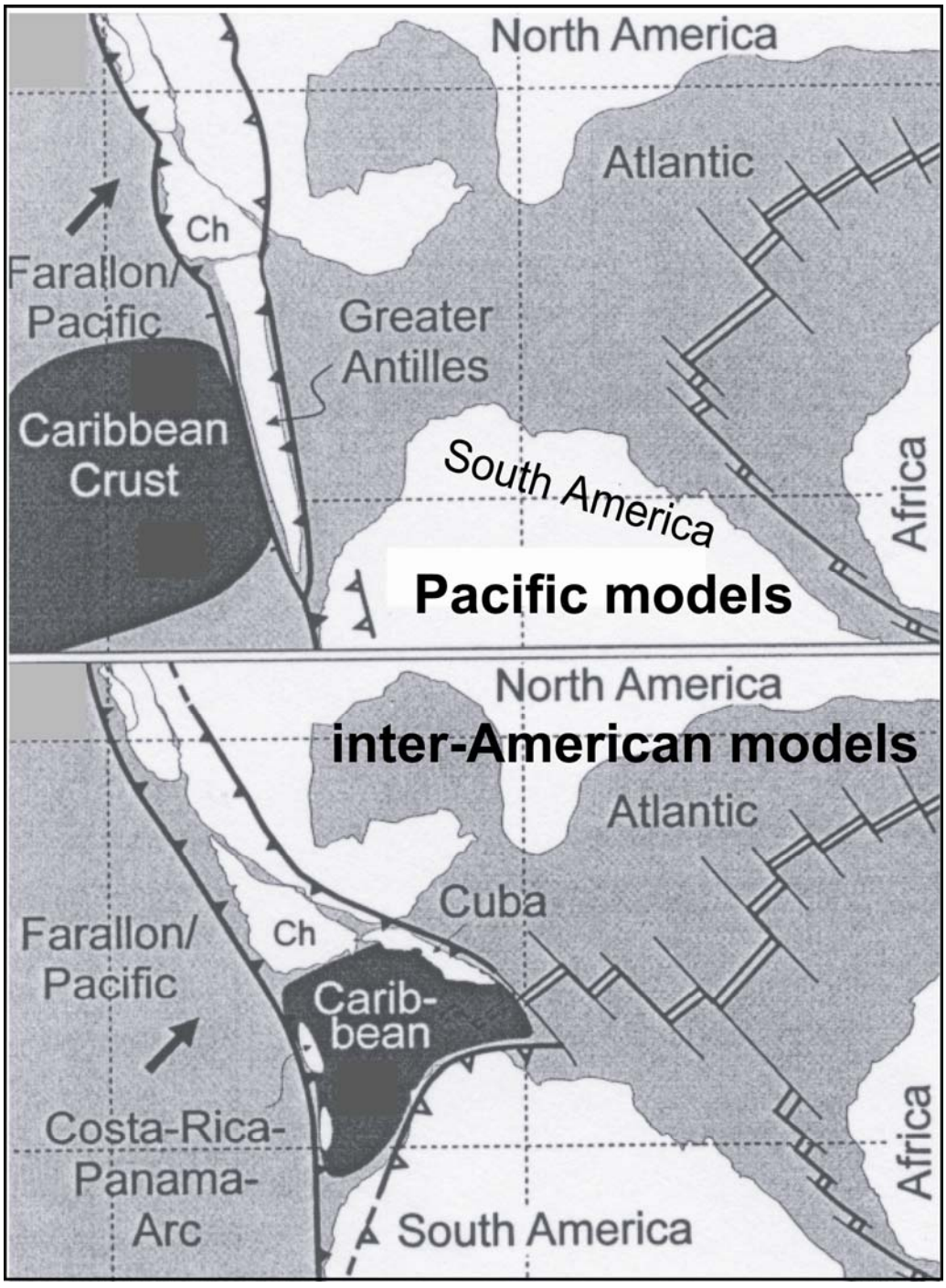

Figure 2.6 Palinspastic Late Cretaceous reconstructions according to the two main groups of models for the generation of the Caribbean lithosphere: Pacific models (up) and inter-American models (low). From Meschede and Frisch (1998).

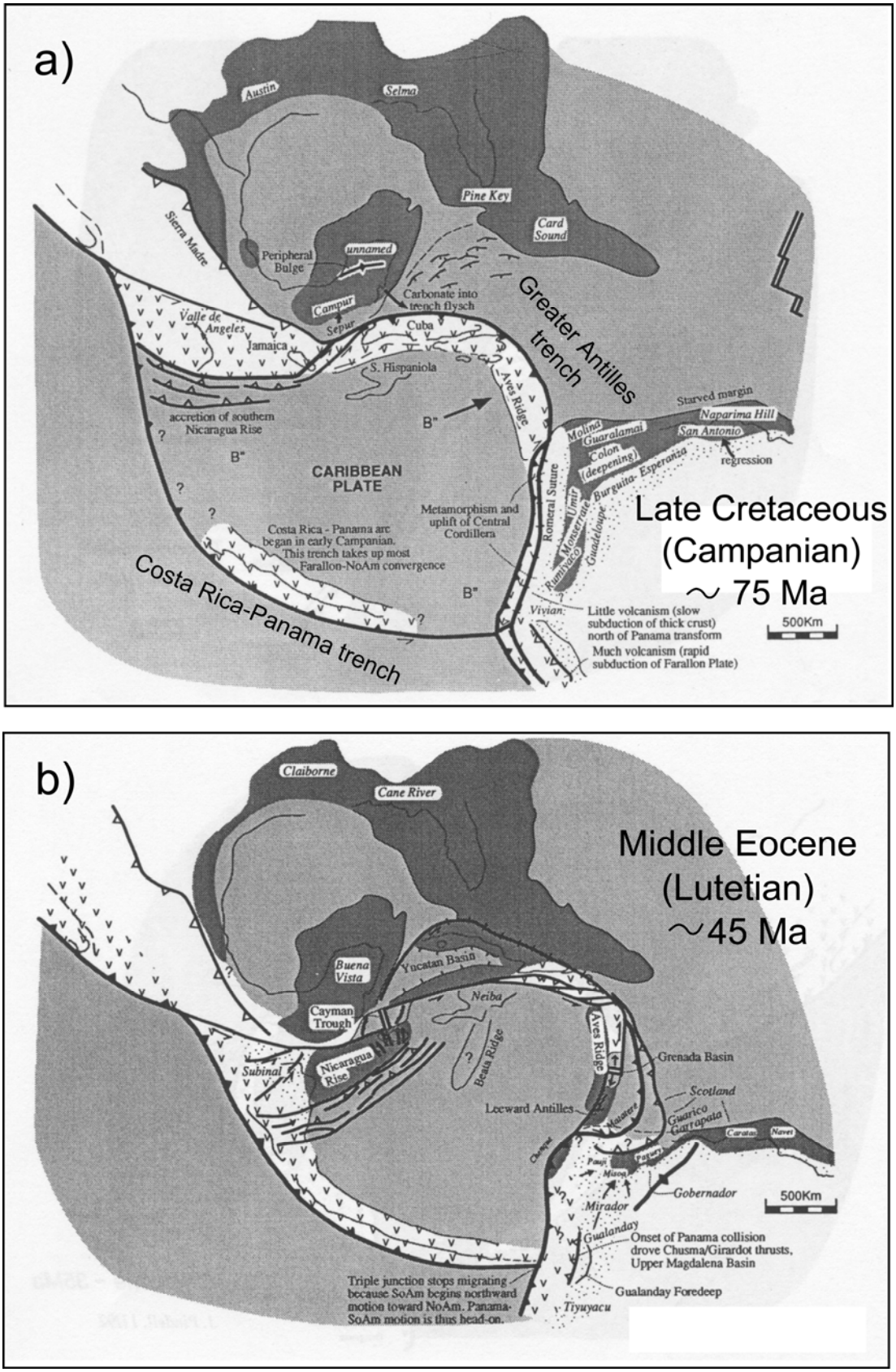

Figure 2.7 a) Late Cretaceous (Campanian) and b) Middle Eocene (Lutetian) paleogeographic reconstructions of the Caribbean realm, from Pindell (1994). Legend as in Figure 2.2.

The Oriente Fault became the main locus of motion since the Late Oligocene and caused the separation of Cuba from Hispaniola. The Cayman Trough nucleated as a pull-apart basin between Yucatán and Jamaica and post-Eocene subduction beneath the Caribbean Plate continued in the Lesser Antilles arc system (Fig. 2.8). Finally, the relative convergence of North and South America towards the Caribbean Plate since the Miocene caused an intense phase of compression still active in the region (e.g. McCann and Pennington 1990).

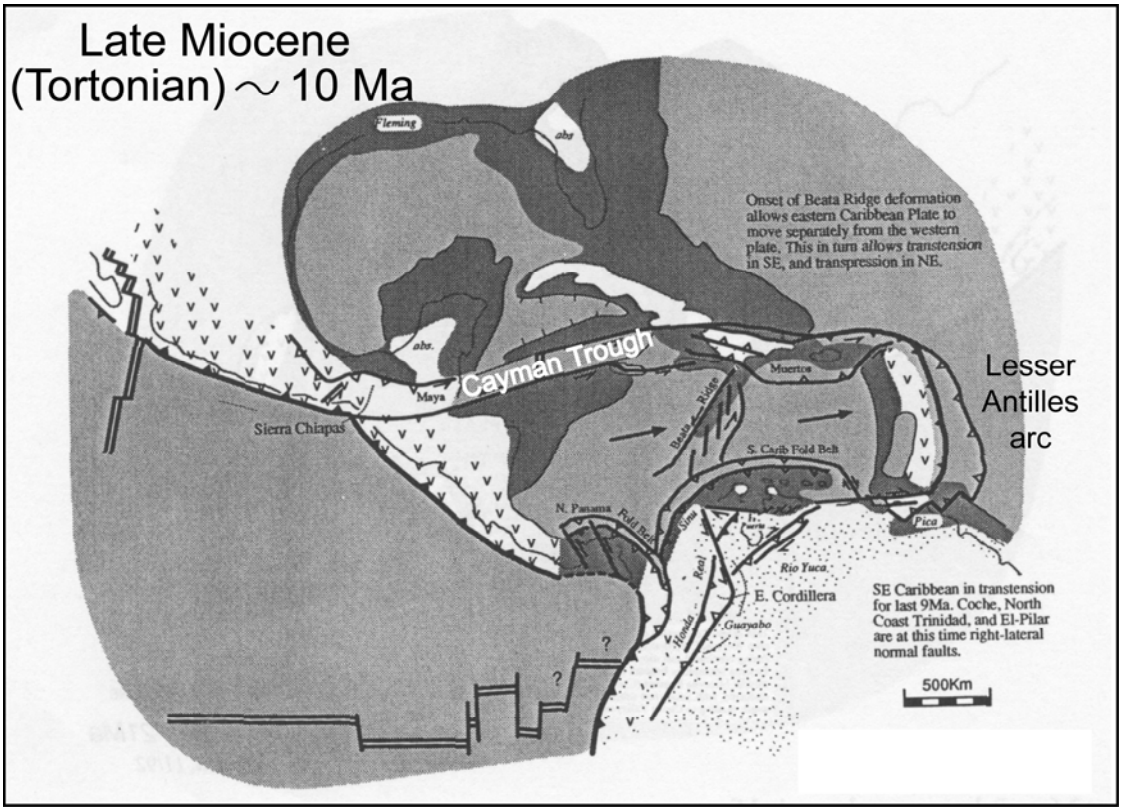

Figure 2.8 Late Miocene (Tortonian) paleogeographic reconstruction of the Caribbean realm, from Pindell (1994). Legend as in Figure 2.2.

2.4. SYNTHESIS OF THE CUBAN GEOLOGY

In this section I will follow the description of the Cuban geology made by Iturralde-Vinent (1994, 1996a, 1998) who recognized two main structural units in Cuba, named the foldbelt and the neo-autochthon, respectively. The foldbelt is made up of deformed and metamorphosed tectonic nappes accreted in the Late Cretaceous-Late Eocene during the northward collision of the western Greater Antilles island arc with the Florida-Bahamas continental platform. This orogenic belt consists of Jurassic to Late Eocene passive continental margin (the Florida-Bahamas platform and the so-called South-western

terrains) and oceanic units (the Northern Cuban Ophiolite Belt, the Cretaceous and the Paleogene island arcs) (Fig. 2.9). The neo-autochthon is composed of Late Eocene to Quaternary slightly deformed carbonate and clastic sedimentary rocks that rest discordantly over the foldbelt units (Fig 2.9). These materials were deposited in several basins mainly controlled by oscillatory vertical movements probably related to transpression along the northern margin of the Caribbean Plate (Iturralde-Vinent 1991; Draper and Barros 1994).

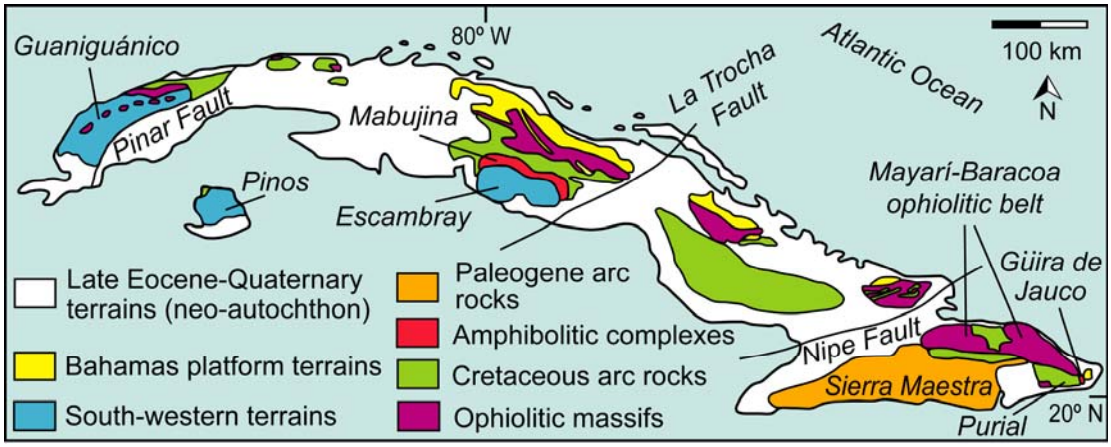

Figure 2.9 Geological sketch map of Cuba according to the subdivision in the geological units identified by Iturralde-Vinent (1994).

2.4.1. The continental units of the Cuban foldbelt

Jurassic-Cretaceous rocks related to the Florida-Bahamas platform crop out along the northern half of Cuba (Fig. 2.9). They are mainly constituted by shallow-water limestones, dolomites and minor evaporites, cherts and deep-water sedimentary rocks. Different facies belts broadly oriented parallelly to the coast can been distinguished form NE to SW: shelf facies, slope deposits and deep-water basin rocks (Khudoley and Meyerhoff 1971; Pardo 1975; Roque Marrero and Iturralde-Vinent 1987; Pushcharovsky 1988; Pushcharovsky et al 1989). After the Maastrichtian the carbonate platform was overlain by Paleocene-Upper Eocene olistostromic and flyschoid sequences partially derived from ophiolitic and Cretaceous volcanic rocks thus recording the north-eastward movement of these terranes approaching the southern edge of the basin.

The South-western terrains (Guaniguánico, Pinos and Escambray; Fig. 2.9) are lithostratigraphic composite units constituted by Jurassic-Cretaceous continental margin sedimentary rocks (conglomerates, sandstones, shales and limestones), and minor ophiolitic (serpentinites, gabbros) and volcanic (pillow basalts) material commonly affected

by very low grade to high-P metamorphism (Somin and Millán 1981; Millán and Somin 1985; Draper and Barros 1994; Millán 1996; Auzende et al. 2002; Schneider et al. 2004; Stanek et al. 2006). Pinos terrain experienced a partly different evolution compared to Guaniguánico and Escambray as it records high grade conditions of metamorphism and partial hydrous melting of metapelites (García-Casco et al. 2001). Several complex stages of folding and thrusting are found in the South-western terrains and have been generally related to their rotation during the emplacement. The stratigraphical similarities among the Guaniguánico, Pinos and Escambray sequences suggest that they belong to the same paleogeographic realm; however their original position has been matter of debate since their provenance from the Bahamas platform, South America, Chortis and Yucatán blocks has been alternatively proposed (Khudoley and Meyerhoff 1971; Pushcharovsky et al. 1989; Iturralde-Vinent 1996a; García-Casco et al. 2001; Pindell and Kennan 2001).

2.4.2. The oceanic units of the Cuban foldbelt

2.4.2.1. The Northern Cuban Ophiolite Belt

The Cuban Ophiolite Belt outcrops in the northern half of the island (Fig. 2.9) and is constituted by a ~ 1000 km long set of strongly faulted ultramafic, plutonic, volcanic and sedimentary melange complexes (Fonseca et al. 1985; 1992; Iturralde-Vinent 1989, 1994, 1996b; Millán 1996; Andó et al. 1996; Proenza et al. 1999a, b; García-Casco et al. 2002, 2006). From Northwest to Southeast, the main ophiolitic massifs described in the island are: Cajálbana, Mariel-La Habana-Matanzas, Las Villas, Camagüey, Holguín and Mayarí-Baracoa (e.g. Iturralde-Vinent 1994, 1996b; Cobiella-Reguera 2005; Lewis et al. 2006). The tectonic position of the single Cuban ophiolitic massifs varies in the different regions of the island, as they show different structural relations in particular with the Cretaceous arc rocks (Iturralde-Vinent 1989; Pushcharovsky et al. 1989). From top to bottom, the reconstructed ophiolitic section generally includes radiolarites, limestones and shales that are underlain by Cretaceous (Hauterivian-Coniacian) volcanic and plutonic rocks and lower serpentinized mantle peridotites. Ophiolite volcanics are mainly amygdaloidal basalts and minor basaltic andesites that crop out as massive flows or pillow lavas and are usually affected by seafloor and subaerial intense alterations. The presence of the diabase sheeted dyke complex in Cuban ophiolites is uncertain as field descriptions are generally ambiguous on this topic (e.g. Andó et al. 1996; Iturralde-Vinent 1996b). The exposed crustal plutonic section is commonly several hundred meters thick and generally consists of layered and minor isotropic gabbroic rocks. Olivine gabbro with cumulate texture is the main lithological type but rare gabbro-dioritic bodies have also been

described (Ríos and Cobiella 1984; Andó et al. 1996). The transitional zone between the crustal and mantle units is commonly made up of (melt-impregnated) dunite layers, locally cut by cumulitic mafic (microgabbro, troctolite, norite) and ultramafic (websterite, wehrlite, hornblendite) dykes. The lower mantle section is constituted by highly serpentinized harzburgitic tectonites, minor lherzolites and intercalated dunitic layers up to several meters thick. Podiform chromitite bodies are common in the Cuban ophiolitic mantle section and they are considered the largest deposits of chromite in the Caribbean region (Murashko and Lavandero 1989; Kesler et al. 1990; Proenza et al. 1999b, 2001; Gervilla et al. 2005). The contacts between the lithological units described above are usually tectonic and the primary lithostratigraphic sequence can be inverted. Cuban ophiolites are generally interpreted as oceanic lithosphere slabs either from a Proto-Caribbean back-arc marginal basin (Iturralde-Vinent 1994, 1996b, 1998), remnants of the Proto-Caribbean oceanic lithosphere subducting beneath the Pacific-Caribbean Plate, or forearc lithosphere built on the Pacific-Caribbean paleomargin (Pindell and Barrett 1990; Pindell 1994).

2.4.2.2. The Cretaceous island arc

Cretaceous (Aptian-Campanian) arc volcanic and minor plutonic and pyroclastic rocks are widespread in Cuba and represent the westernmost part of the extinct Greater Antilles island arc. Cretaceous subduction-related terrains are particularly common in central, south central and eastern Cuba (Fig. 2.9); in the latter region they were partially affected by a high-P metamorphic event recorded in the Purial Complex. Cretaceous volcanics are mainly basalts, basaltic andesites and andesites with tholeiitic, calcalkaline and alkaline affinities and are locally interbedded with tuffs and volcano-sedimentary deposits (Meyerhoff and Hatten 1968; Khudoley and Meyerhoff 1971; Iturralde-Vinent 1976, 1977; 1996a; Díaz de Villalvilla and Dilla 1985; Iturralde-Vinent et al. 1989). Two main unconformities are present within the Cretaceous volcanoclastic sequence, one of Albian and another of Santonian age (Iturralde-Vinent 1994). These unconformities can be correlated with analogue structures in many Caribbean terrains. The largest Cretaceous arc-related (gabbroid to granitoid) plutons in Cuba crop out in the Camagüey area and are mainly of Campanian age (Pérez et al. 1986; Pushcharovsky 1988; Iturralde-Vinent et al. 1989; Hall et al. 2004). The petrological relations of Cretaceous arc volcanics and plutonics with the partially contemporaneous ophiolitic rocks as well as with the Güira de Jauco and Mabujina amphibolitic complexes (Fig. 2.9) are not completely clear; the latter have been interpreted as remnants of the pre-Albian arc basement (Somin and Millán 1981; Iturralde-Vinent 1989; 1994, 1996b; Draper and Barros 1994; Millán 1996) but this

view has been recently contested (Blein et al. 2003). Cretaceous arc terrains are tectonically in contact with the units of the Florida-Bahamas platform, the South-western terrains, the Northern Ophiolite Belt and the Paleogene arc. Based on the geochemistry of Cretaceous Cuban volcanics, Kerr et al. (1999) proposed the existence of two pre-Albian subduction zones in the Caribbean realm: one northeast facing (Neocomian-Aptian) arc mainly composed of boninites and related to a subduction zone within the Proto-Caribbean Plate; and one southwest facing arc constituted by island arc tholeiites and (Albian-Campanian) calcalkaline-alkaline volcanics associated with the subduction of the Pacific-Caribbean Plate beneath the Proto-Caribbean.

2.4.2.3. The Paleogene island arc and the piggy-back basins

Paleocene to Middle Eocene island arc suites are well known in eastern Cuba (Sierra Maestra Mountains) (Fig. 2.9) and are mainly constituted by volcanic and pyroclastic rocks locally intruded by granodiorite and granite plutons (Iturralde-Vinent 1976, 1977, 1990; Cobiella et al. 1977; Pérez et al. 1983; Cobiella 1988). These units will be briefly described in the following section. Minor Paleogene pyroclastic deposits have also been found in Camagüey and northern Oriente provinces. Several piggy-back sedimentary basins can be recognized in the Late Cretaceous-Oligocene terranes in Cuba and record the demise of the magmatic activity in the island and its collision with the North American continental margin. These basins were filled with sandstones, conglomerates, marls and limestones partially-derived from the deformed material of the Northern Ophiolitic Belt, the Cretaceous and the Paleogene island arcs.

2.5. GEOLOGY OF EASTERN CUBA

The geological province of eastern Cuba extends southeast to the Nipe Fault (Fig 2.9) (Draper and Barros 1994; Iturralde-Vinent 1994, 1998, 2003). This domain differs from the other regions of the island as here the rocks related to the Cuban Cretaceous island arc were partially metamorphosed (Purial Complex). Moreover, the largest exposures of the Cuban Paleogene volcanic and plutonic rocks crop out in this region. The main structural units recognized in eastern Cuba are (Fig. 2.10) (Cobiella et al. 1977; Iturralde-Vinent 1994, 1998): 1) the Asunción massif; 2) the Güira de Jauco amphibolitic complex; 3) several ophiolite-related terrains (the Mayarí-Cristal and Moa-Baracoa massifs) including serpentinitic melanges that contain high-P metamorphic rocks (the La Corea Melange and the Sierra del Convento massif); 4) (meta)volcanic and volcano-sedimentary rocks related to the Cretaceous island arc(s); 5) Late Campanian-Danian olistostromic sequences (Micara and La Picota Formations); 6) volcanic and volcanoclastic rocks related to the

Paleogene island arc; 7) Middle Eocene-Oligocene sedimentary material deposited in piggy-back basins; 8) post-Oligocene sedimentary rocks (neo-autochthon).

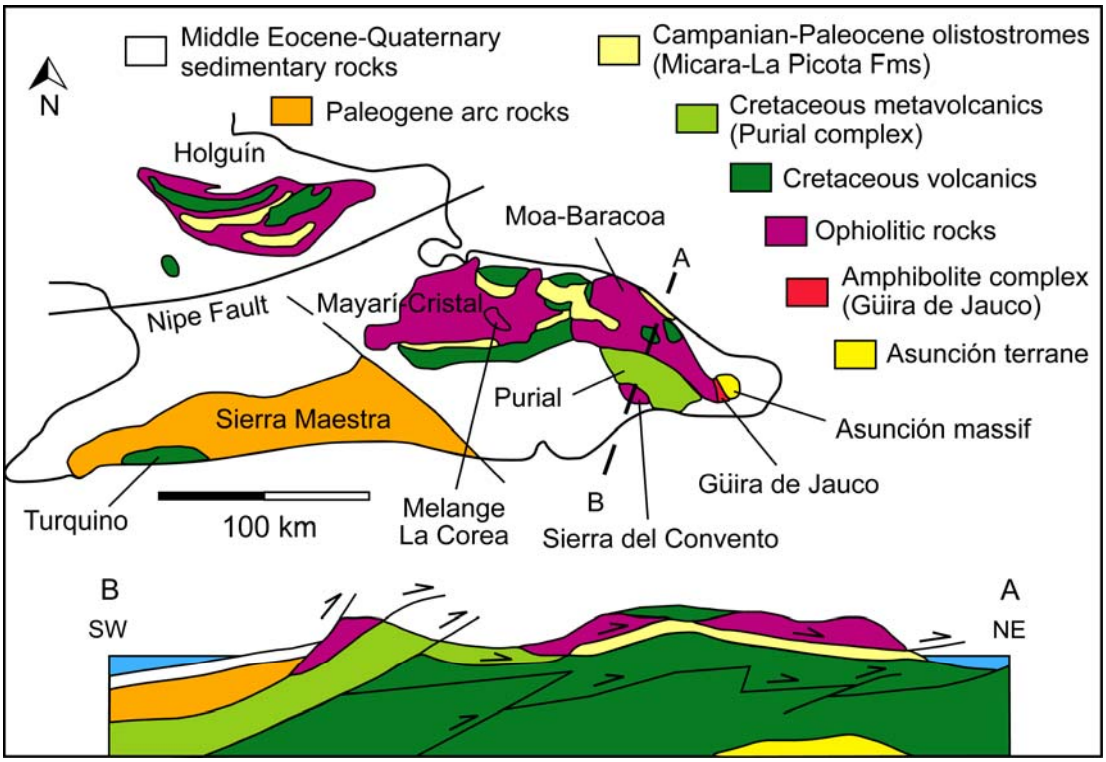

Figure 2.10 Schematic geological map and cross section of eastern Cuba. Modified from Iturralde-Vinent (1994).

In eastern Cuba the rocks associated with the continental units of the Cuban foldbelt are represented by the Asunción massif (Fig 2.10) that is made up of two Late Jurassic-Early Cretaceous lithostratigraphic units: 1) the Sierra Verde Formation constituted by high-P quartzites and graphitic schists; and 2) the Asunción Formation mainly composed of limestones and (dolomitic) marbles (Millán and Somin 1985). These formations have been correlated with similar rocks outcropping in northern Hispaniola (Iturralde-Vinent 1994, 1996a; Lewis and Draper 1990).

The two largest complexes of the Northern Cuban Ophiolite Belt outcrop in eastern Cuba: the Mayarí-Cristal (to the west) and the Moa-Baracoa (to the east) massifs (Fig 2.10). As a whole, they constitute a pseudo-tabular body 170 km long and 10 to 30 km wide that is principally made up of mantle harzburgites and minor dunites, (ultra)mafic sills and dykes that intrude the mantle section mainly in the Moho transition zone, and crustal layered gabbroic rocks. The lithological, structural, petrological and geochemical signatures of these massifs are among the aims of this study and will be discussed in

details in Chapter 4. Two serpentinitic melanges have been associated in eastern Cuba to the Northern Ophiolite Belt: the La Corea Melange and the Sierra del Convento massif (Fig 2.10) (Iturralde-Vinent 1996b; Millán 1996; García-Casco et al. 2006). The La Corea Melange is located in the southern region of the Sierra de Cristal and is tectonically overlain by the Mayarí-Cristal ophiolitic rocks. The Sierra del Convento massif is situated south to the Moa-Baracoa massif and is thrusted over the metavolcanic rocks of the Sierra del Purial complex. According to García-Casco (2005) and García-Casco et al. (2006), the Sierra del Convento terrain is mainly characterized by high-T basic metamorphic rocks (epidote-garnet amphibolites) and leucocratic (trondhjemitic) bodies interpreted as remnants of partial melting of the subducted oceanic crust. Minor lithologies are glaucophanitic and chloritic schists, quartzites, metapelites and rare eclogites (Boiteau et al. 1972; Cobiella et al. 1977; Somin and Millán 1981; Millán and Somin 1985; Quintas 1989; Somin et al. 1992; Millán 1996; Lázaro 2004). Available geochronological data indicate 66-125 and 82-116 Ma for the metamorphic events recorded in the La Corea and Sierra del Convento terrains, respectively (Somin and Millán 1981; Somin et al. 1992; Iturralde-Vinent 1996b; Millán 1996).

In eastern Cuba three main volcanic formations record the Cretaceous magmatic activity: the Téneme, Quibiján and the Santo Domingo Formations (Quintas 1988a, 1989; Iturralde-Vinent 1996a, c, d; Gyarmati et al. 1998; Kerr et al. 1999). The Téneme Formation is mainly constituted by massive basalts, basaltic andesites, andesites and minor dacites (Proenza et al. 2006), interbedded with tuffs, tuffaceous sandstones and limestones of Turonian-Lower Coniacian age (Iturralde-Vinent et al. 2006). These volcanics are tectonically overlain by the peridotites of the Mayarí-Cristal ophiolitic massif and by Upper Cretaceous-Paleogene sedimentary rocks (Fig. 2.11). In the southeastern portion of the type locality, the intrusive rocks of the Río Grande pluton (89.7 ± 0.5 Ma in age, Proenza et al. 2006) cut the Téneme volcanics.

The Quibiján Formation is constituted by massive, porphyritic and quartz-chlorite filled amygdaloidal basalts, basaltic andesites and minor andesites, interbedded with cherts and fine-grained tuffaceous rocks (Quintas 1987, 1988a). Iturralde-Vinent et al. (2006) propose an Albian-Turonian age for the Quibiján Formation on the basis of a tentative correlation with similar rocks from central Cuba. The Quibiján volcanics are tectonically overlain by the Purial Complex and by the Moa-Baracoa ophiolitic rocks (Fig. 2.12) (Quintas 1987, 1988a). The Purial Complex mainly consists of igneous rocks with island arc tholeiitic affinity (Proenza et al., unpublished data) partially metamorphosed in the greenschist and blueschist facies in Late Cretaceous (75 ± 5 Ma, Somin et al. 1992;

Iturralde-Vinent et al. 2006). The main lithologies recognized in this massif are garnet-amphibolites, serpentinites, gabbros, marbles and sericite schists (Boiteau et al. 1972; Somin and Millán 1981; Millán 1996); most of the protoliths consist of lavas, tuffs, volcanogenic-sedimentary rocks and minor limestones.

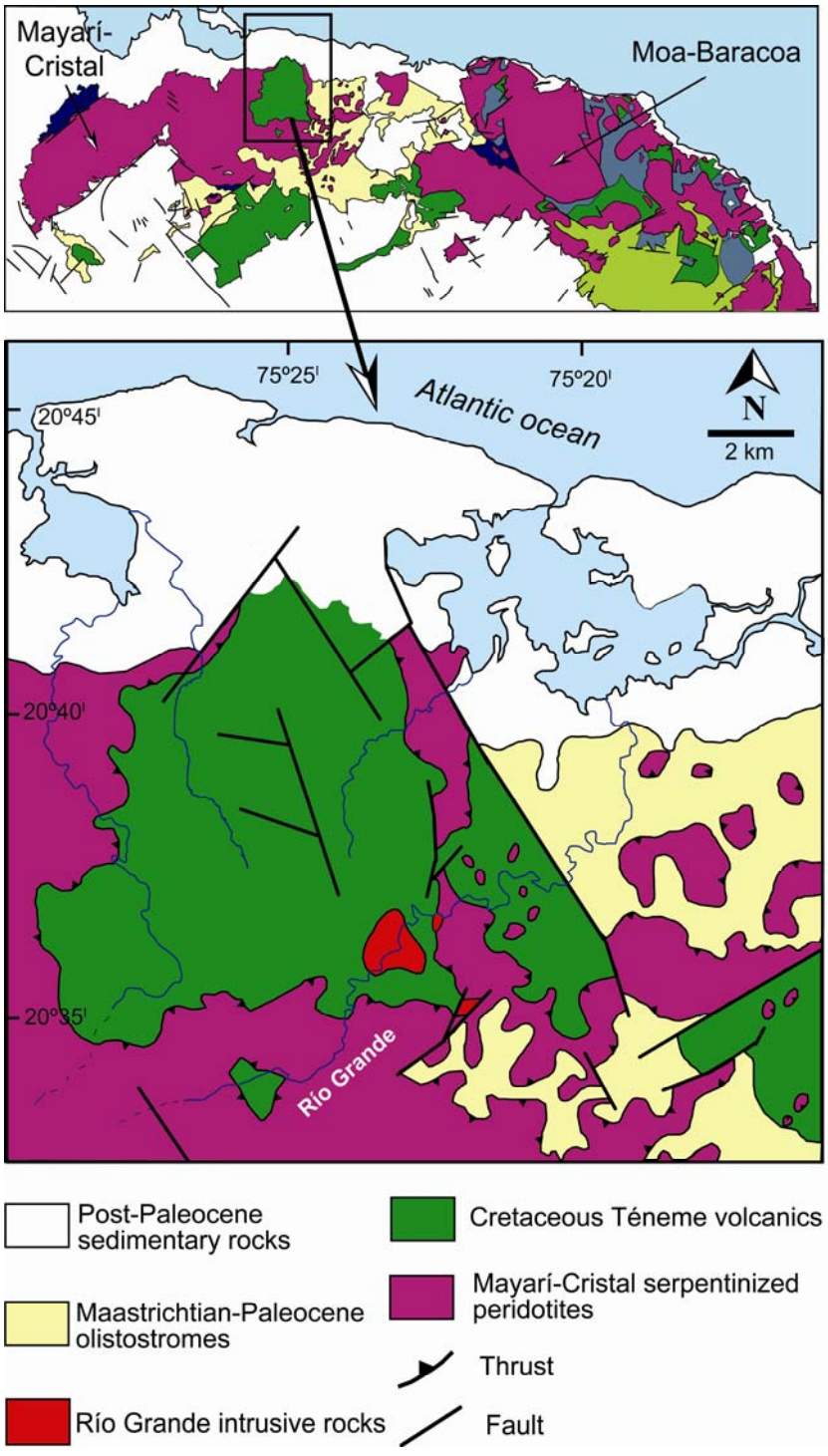

Figure 2.11 Geological map of the Téneme Formation type locality, from Proenza et al. (2006). Black box indicates the enlarged area.

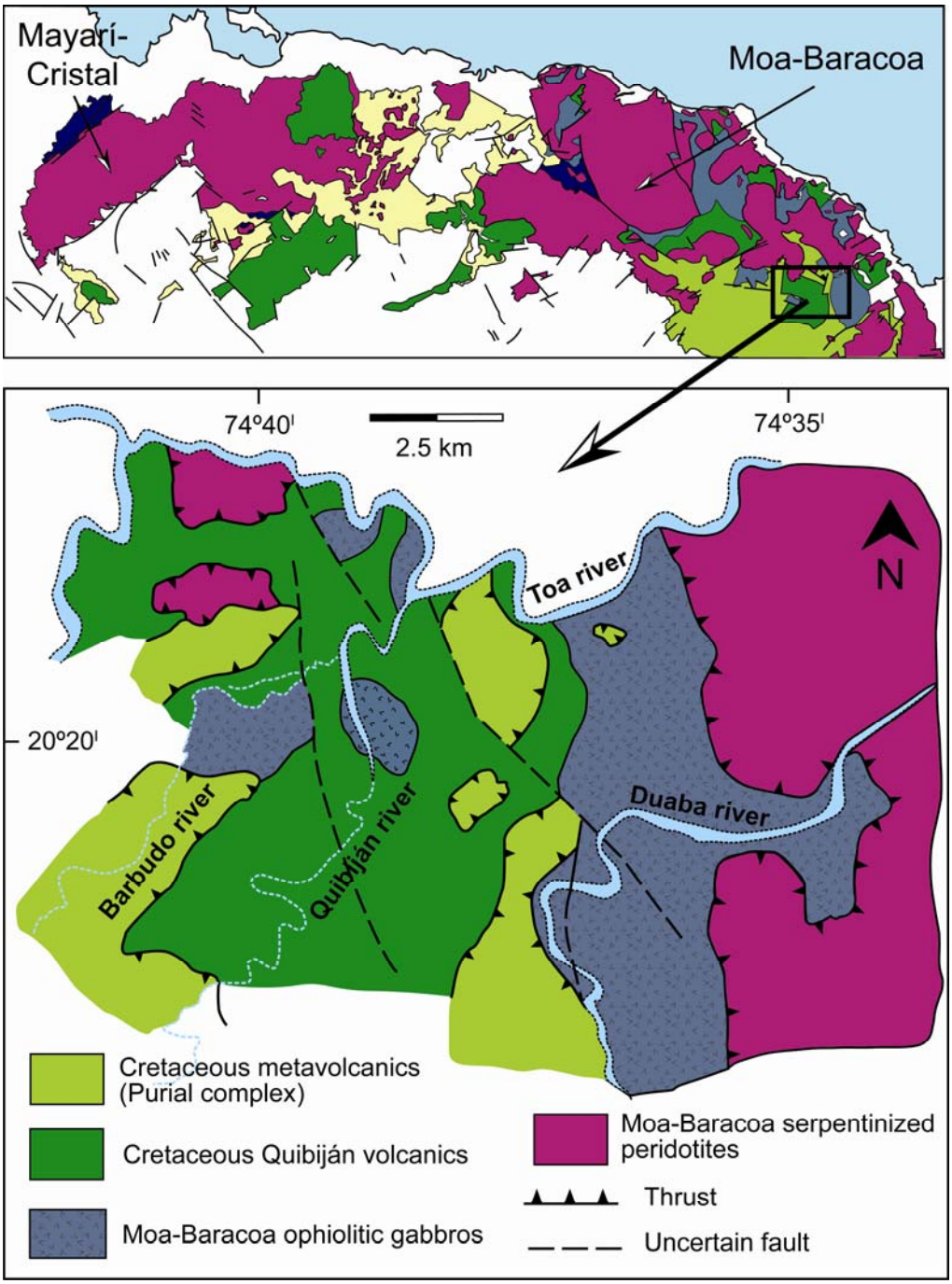

Figure 2.12 Geological map of the Quibiján Formation type locality, from Quintas (1988a). Black box indicates the enlarged area.

The Turonian-Coniacian pillow basalts and basaltic andesites from the locality of Morel (Fig. 2.13) have been previously included in the Quibiján Formation and classified as back-arc tholeiites (Kerr et al. 1999). As I will argue in Chapter 5, however, different suites initially assigned to the Quibiján Formation show dissimilar geochemical signatures and their classification in a single volcanic formation is thus inappropriate (see also Proenza et al. 2006).

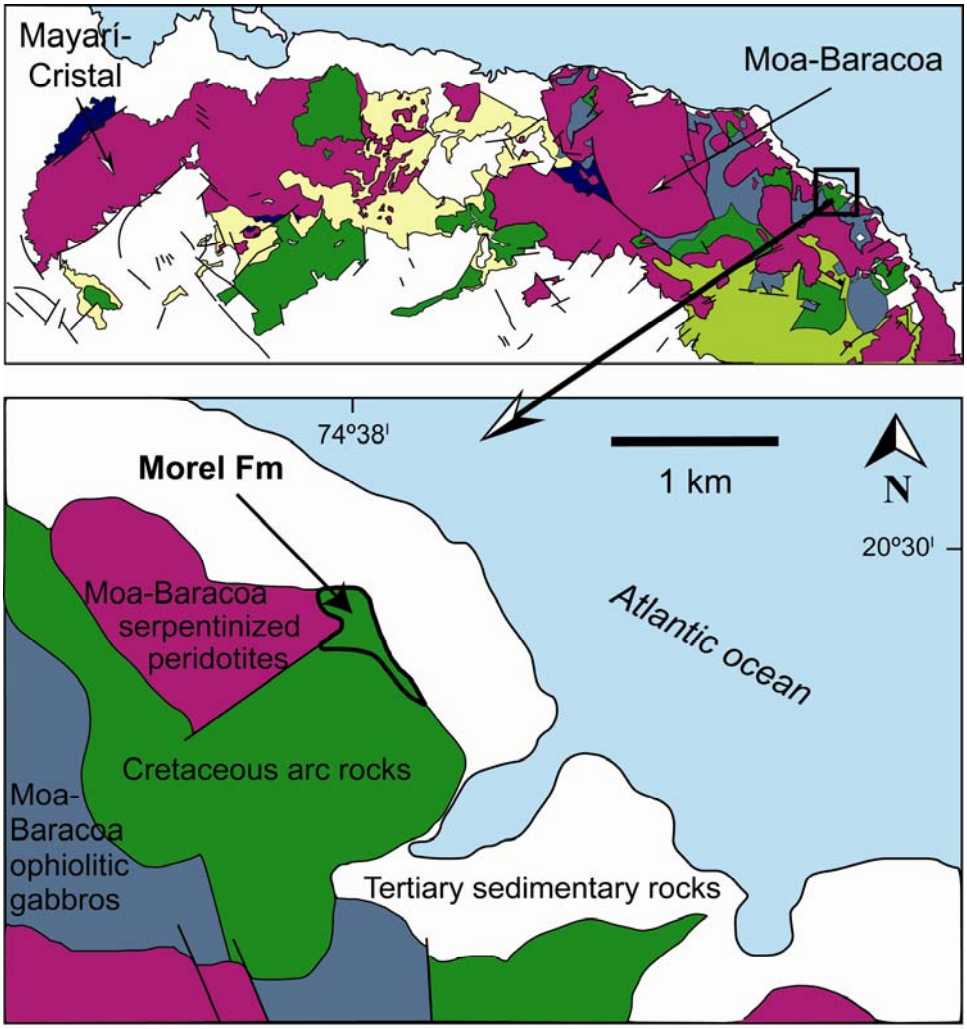

Figure 2.13 Geological map of the Morel Formation type locality, from Iturralde-Vinent et al. (2006). Black box indicates the enlarged area.

The Santo Domingo Formation is a volcano-sedimentary unit that consists of tuffs, tuffaceous rocks and minor sills of porphyritic andesites, interbedded with scarce lavas and limestone beds of Turonian-Campanian age (Iturralde-Vinent 1976, 1977; Iturralde-Vinent et al. 2006). The Santo Domingo sequence is more than 1200 m thick and presumably overlies the Quibiján and Morel extrusives (Quintas 1987, 1988b; Proenza and Carralero 1994). Up to date, no detailed geochemical studies have been performed to characterize the Santo Domingo Formation. On the basis of major element geochemistry, Gyarmati et al. (1998) suggested a calcalkaline affinity for these rocks.

Several sedimentary piggy back-basins formed in Late Campanian-Paleocene during the emplacement of the Cuban ophiolites and the Cretaceous igneous terranes onto the southern boundary of the Florida-Bahamas platform (Iturralde-Vinent 1976, 1977; Somin and Millán 1981; Millán and Somin 1985; Quintas 1988b, 1989; Draper and Barros

1994; Millán 1996). In eastern Cuba this phase is recorded by the olistostromic and melange sequences of the Micara and La Picota Formations (Fig. 2.10) that include blocks derived from the ophiolitic massifs. These terrains are of Maastrichtian age and record the obduction of the Mayarí-Baracoa Ophiolitic Belt (Cobiella 1978; Iturralde-Vinent 2003; Cobiella-Reguera 2002, 2005; Iturralde-Vinent et al. 2006). On the other hand, in the Paleocene terrains of eastern Cuba there are no evidence of significant displacement of ophiolitic-related nappes; this implies that the ophiolite emplacement in eastern Cuba ceased before than in the other regions of the Northern Cuban Ophiolite Belt (for which occurred in the Eocene, Cobiella-Reguera 2005). As result of the collision between the Greater Antilles island arc and the Florida-Bahamas platform the structure of eastern Cuba is nowadays constituted by several NE verging imbricated thrust-sheets (Fig. 2.10) (e.g. Iturralde-Vinent 1976, 1977; Cobiella 1978).

The Paleogene (Thanetian-Early Middle Eocene) volcanic activity in eastern Cuba is mainly represented by the El Cobre Group, a > 4 km thick sequence of volcanic and volcanoclastic rocks with intercalations of epiclastic materials and fossiliferous limestones (Jakus 1983; Cobiella 1988; Pushcharovsky 1988; Quintas et al. 1994; Iturralde-Vinent 1996e, 1998; Cazañas et al. 1998; Kysar-Mattietti 2001; Rojas-Agramonte et al. 2006). The El Cobre volcanic sequence is composed of low- K island arc tholeiitic lavas (basalts, andesites, dacites and rhyolites) (Cazañas et al. 1998; Kysar-Mattietti 2001; Rojas-Agramonte et al. 2006), pyroclastic flows, minor subvolcanic sills and related feeder dykes. During the final stages of the magmatic activity, the volcanic section was intruded by low- to medium-K calcalkaline granitoid plutons (sienites, monzodiorites, diorites, granodiorites, tonalites, plagiogranites and granites). Iturralde-Vinent (1996e; 1998) interpreted the El Cobre Group as formed in the axial zone of the volcanic arc. These igneous rocks can be correlated with contemporaneous mainly volcanic units in Hispaniola, Puerto Rico, Nicaraguan Rise, Aves and Cayman Ridges, thus attesting a post-Cretaceous magmatic activity at the scale of the Caribbean realm (Lewis and Draper 1990; Donnelly et al. 1990). In Cuba this magmatism is considered unrelated with the Cretaceous arc as the Maastrichtian-Lower Danian units in the island are characterized by the absence of volcanism record.

After the demise of the Paleogene arc a generation of post-volcanic sedimentary basins developed in Middle Eocene-Oligocene and was mainly filled with thick sections of limestones, marls and sandstones (Quintas 1989; Quintas and Blanco-Moreno 1993). The Late Eocene to Recent evolution of eastern Cuba is recorded by the neo-autochthon sedimentary sequences that were deposited discordantly over the foldbelt terranes. This

material is mainly made up of limestones, marls and sandstones related to the North America continental platform (Quintas 1989).

3. ANALYTICAL TECHNIQUES

3. ANALYTICAL TECHNIQUES

This study is based on the major, trace element and Nd-Sr-Pb radiogenic isotopic compositions of whole rocks and minerals of the main lithological types from the Mayarí-Baracoa Ophiolitic Belt and the spatially-related Cretaceous igneous suites. The database is constituted by 119 specimens selected from a larger sampling from different localities in eastern Cuba. Mineral assemblages and textures of the samples were at first studied in standard (~ 30 μm) polished thin sections by transmitted-light optical microscopy. Petrographic observations were exploited to select the most suitable samples for the subsequent geochemical analyses.

3.1. ELECTRON PROBE MICROANALYSES (EPMA)

Major element compositions of minerals in mantle peridotites and gabbroic rocks from the Mayarí-Baracoa Ophiolitic Belt were obtained by Electron Probe Microanalyses (EPMA) in ~ 30 μm thick sections using a CAMECA SX-50 instrument at the Serveis Cientificotècnics of the Universitat de Barcelona (Spain). Excitation voltage was 20 kV and beam current 15 nA, except for analyses of Cr-rich spinel in peridotites for which a current of 20 nA was preferred. Most elements were measured with a counting time of 10 s, except for Ni and V (30 s). The standards used for element calibrations were orthoclase (Si, Al), periclase (Mg), wollastonite (Ca), albite (Na), rhodonite (Mn), rutile (Ti), hematite (Fe), chromite (Cr), NiO (Ni) and metallic V (V). Kα lines of Ca, Ti, and Cr were measured by a spectrometer equipped with a PET crystal, Kα of Mg, Al, and Na by a TAP-equipped spectrometer, Kα of Mn, Fe, Ni and V by a LIF-equipped spectrometer, and Kα of Si by a second TAP-equipped spectrometer.

Minerals of igneous rocks spatially-related with ophiolites were analyzed on ~ 150 μm thick polished sections using a CAMECA SX-100 instrument at ISTEEM (Institut des Sciences de la Terre, de l'Environnement et de l'Espace de Montpellier, CNRS-Université Montpellier II, Montpellier, France). Analytical conditions were 20 kV accelerating voltage and 10 nA beam current. All the elements were measured with counting time of 30 s, except for Mn and Fe (20 s). The standards used for element calibrations were natural or synthetic quartz (Si), corundum (Al), orthoclase (K), forsterite (Mg), wollastonite (Ca), albite (Na), rhodonite (Mn), rutile (Ti) and hematite (Fe).

3.2. PREPARATION OF WHOLE ROCK POWDERS

Samples (usually > 3 kg) were processed at the rock crushing laboratory of the Departamento de Mineralogía y Petrología, Universidad de Granada (Spain). After the removal of the altered surface and secondary veins by a diamond saw, rock specimens were cut in cubic pieces with side-length ~ 4 cm and subsequently put in an ultrasonic water bath for ~ 30 minutes. Once dried, the cubes were repeatedly smashed in a steel jaw crusher and quartered several times by a riffle-splitter up to achieve a (~ 50 g) representative sample aliquot. Whole rock powders (< 2 μm grained) were obtained by pulverizing these aliquots in an agate ring mill for about 20-45 minutes depending on the nature of the sample (Fig. 3.1). The dust extraction system of the laboratory was constantly operating during grinding. After each single sample processing the entire rock milling equipment was carefully cleaned by compressed air, alcohol and quartz chips in order to avoid any contamination among the specimens. Each sample powder was stored in two distinct clean vials respectively for X-Ray Fluorescence (XRF) and Inductively Coupled Plasma-Mass Spectrometry (ICP-MS) analyses. The material left after the quartering was conserved in sealed clean plastic bags or jars for subsequent mineral separation of clinopyroxene in mantle peridotites and clinopyroxene, plagioclase and amphibole in selected igneous rocks.

3.3. X-RAY FLUORESCENCE (XRF)

3.3.1. Analyses of ultramafic and mafic rocks from the Mayarí-Baracoa Ophiolitic Belt

Whole rock major and minor transition elements (V, Cr and Ni) in mantle peridotites and gabbroic rocks from the Mayarí-Baracoa Ophiolitic Belt were analysed by WD X-Ray Fluorescence (XRF) at the Universidad del País Vasco (Spain) by a PHILIPS PW 1510 instrument, and at the Centro de Instrumentación Científica (CIC) of the Universidad de Granada (Spain) by a PHILIPS Magix Pro PW-2440 instrument equipped with six analyzer crystals (LiF200, LiF220, Ge, PE, PX1, PX2) using standard sample preparation and analytical procedures. Whole rock powders were mixed with a lithium tetraborate ($Li_2B_4O_7$)/metaborate ($LiBO_2$) flux and fused in a platinum-gold alloy crucible in a muffle furnace for 20-40 minutes. The resultant glass disk was excited with a rhodium anode tube operating at 3 or 4 KW. Usual detection limits are 0.01 wt% for major elements and 1-5 ppm for trace elements. Loss on ignition (LOI) was directly determined only on several samples at CIC by drying 0.5 g of whole rock powder at 110 ºC and placing it in a furnace at 1000 ºC for 1 hour.

Figure 3.1: Equipment utilized for the preparation of whole rock powders: a) Diamond saw; b) Jaw crusher; c) Riffle-splitter; d) Pulverizer agate mill.

3.3.2. Analyses of Cretaceous igneous rocks from eastern Cuba

Whole rock major and minor transition elements (Sc, V, Cr and Ni) in Cretaceous igneous rocks spatially-associated with ophiolites were analysed by a ThermoARL Advant XP+ sequential XRF spectrometer at the GeoAnalytical Lab facilities of the Washington State University (WA, USA). Fresh chips of the whole rock powder were handpicked and (~ 28

g) ground in a swing mill with tungsten carbide surfaces for 2 minutes. Handpicking of fresh chips after the use of steel hammers and steel jaw crusher should prevent significant Fe, Cr and Ni contamination, which resides mainly in the finer dust. Tungsten carbide mills usually cause contamination with W, Nb, Ta and Co so these elements were not analyzed by XRF. 3.5 g of the sample powder was weighed into a plastic mixing jar with 7.0 g of pure lithium tetraborate ($Li_2B_4O_7$) flux (2:1 flux:rock) and, assisted by an enclosed plastic ball, mixed for ten minutes. The mixed powders were emptied into graphite crucibles that were placed on a silica tray and loaded into a muffle furnace only large enough to contain the tray. Fusion took 5 minutes from the time the preheated furnace returned to its normal 1000 ºC after loading. The silica plate and graphite crucibles were then removed from the oven and allowed to cool. Each bead was reground in the swing mill for 35 seconds, the glass powder then replaced in the graphite crucibles and refused for 5 minutes. Following the second fusion, the cooled beads were labeled with an engraver, then their lower flat surface was ground on 600 silicon carbide grit and finished briefly on a glass plate (600 grit with alcohol) to remove any metal from the grinding wheel and to provide a smooth flat analysis surface. The glass beads were then washed in an ultrasonic cleaner, rinsed in alcohol and wiped dry, being so ready to be loaded into the XRF spectrometer. A rhodium target was run at 50 kV and 50 mA with full vacuum and a 25 mm mask for all elements and all samples. The intensities for all elements were corrected automatically for line interference and absorption effects due to all the other elements using the fundamental parameter method. Two in-house standard beads (BCR-P and GSP-1) run between every 28 unknown samples were used as internal standards. Further details on the analytical procedure can be found in Johnson et al. (1999).

3.4. INDUCTIVELY COUPLED PLASMA-MASS SPECTROMETRY (ICP-MS)

3.4.1. Analyses of ultramafic and mafic rocks from the Mayarí-Baracoa Ophiolitic Belt

Whole rock trace elements (Li, Co, Rb, Sr, Zr, Nb, Cs, rare earth elements, Hf, Ta, Th and U) in ophiolitic mantle peridotites and mafic rocks from the Mayarí-Baracoa Ophiolitic Belt were analysed at ISTEEM by a VG-PQ2 Turbo+ Inductively Coupled Plasma-Mass Spectrometer (ICP-MS).

3.4.1.1. Dissolution of the samples

Sample powders were digested in clean Teflon Savillex® vessels previously washed in two distinct baths of pure HNO_3 diluted in triple distilled water and left on a hotplate for

about one week. Each beaker was then filled with 2.5 ml HNO_3, 0.5 ml $HClO_4$ and 1 ml HF, kept on the hotplate for 48 hours, rinsed several times with distilled water and dried. The vessels were then ready to be loaded with 100 mg of sample powder.

The powders were first attacked with 1 ml $HClO_4$ and 2.5 ml HF for 24 hours at about 125 ºC. After the complete evaporation of the reagents a second chemical attack was conducted with 0.5 ml $HClO_4$ and 1 ml HF. Powders were then left on hotplate for 24 hours and the acids were evaporated at about 165 ºC. Finally, three subsequent evaporations of 0.5 ml and 0.25 ml (twice) of $HClO_4$ at about 200 ºC were performed up to achieve the complete dryness of the residues. The samples were then ready to be loaded into the ICP-MS instrument. Further details on the procedure followed at ISTEEM for chemical dissolution of whole rock powders (in particular for ultramafic rocks) can be found in Ionov et al. (1992).

3.4.1.2. Analytical procedure

The introduction of the samples in the ICP-MS instrument was done in the liquid modality. Slightly before the beginning of the analytical sessions, the sample residues were dissolved in a mixture of distilled water, pure HNO_3 and aqueous solution of In and Bi up to 1:1000 final dilution. For the analyses of minor transition elements (Li, Co) the dissolution factor was 4000.

The measurement procedure consisted of the following analytical steps: a) one 3%vol. HNO_3 solution (i.e. the instrumental blank, used to determine the baseline signal); b) 2 procedural blanks (in order to evaluate the contamination during the dissolution process); c) 4 or 5 samples run in the presumed sequence of increasing trace element concentrations; d) 5 calibration solutions of known compositions that permit to convert the intensity of the signal in counts per second to the corresponding ppb concentration for each element in the unknowns; e) a second group of 4 or 5 samples; f) 2 or 3 international standards (PCC-1, UB-(N), BHVO, ROA-1 or BIR). Each measurement was an average of 3 runs; the uptake time was 45 s and the counting time 80 s for each run. A rinsing 5%vol. HNO_3 solution was used for 180 s at the end of each measurement. The instrumental bias during the entire analytical session was monitored by the signal of the known concentration (10 ppb) of In and Bi in the aqueous solution added to the samples.

3.4.1.3. Treatment of the data

The analyses of the calibration solutions permitted to correct the sample concentrations in several elements (Eu, Gd, Tb, Dy, Ho, Er, Tm, Yb, Lu, Hf and Ta) for isobaric

interferences with oxides or hydroxides present in the plasma during the analytical sessions. To avoid memory effects due to the intake of concentrated Nb-Ta solutions in the instrument, Nb and Ta contents were determined by using Zr and Hf, respectively, as internal standards. This technique is an implementation to ICP-MS analysis of the method described by Jochum et al. (1990) for the determination of Nb and Ta by spark-source mass spectrometry.

Because of the extremely low concentrations of some incompatible trace elements in most peridotites I took special care in their analyses. The assessment of the analysis precision of a given element was made (see also Godard et al. 2000) using 3-run measurements in the same solution and estimating the absolute standard deviation (σ_s) from the standard deviations of the sample (σ_s), instrumental (σ_i) and procedural blanks (σ_p) measurements as: $\sigma_s = \sqrt{\sigma_i^2 + \sigma_p^2 + \sigma_s^2}$. The analysis was discarded when σ_s > 80% of the mean. In addition, duplicate analyses were performed for several highly depleted samples. Tables 3.1 and 3.2 show respectively the compositions of the procedural blanks and the reference samples (PCC-1, UB-(N), BHVO-1, ROA-1 and BIR) analyzed as unknowns during the analytical runs. The concentrations of the international standards show good agreement with working values for these reference materials (Govindaraju 1994). For the analyzed elements, reproducibility of the international standards is better than 20% for UB-(N), BHVO-1 and BIR, and within 5-40% for PCC-1 and ROA-1. Detection limits obtained by long-term (several years) analyses of chemical blanks at ISTEEM can be found in Ionov et al. (1992) and Garrido et al. (2000).

3.4.2. Analyses of Cretaceous igneous rocks from eastern Cuba

Whole rock trace elements (Rb, Sr, Y, Zr, Nb, Cs, Ba, rare earth elements, Hf, Ta, Pb, Th and U) in igneous rocks spatially-associated with the Mayarí-Baracoa Ophiolitic Belt were analysed at the GeoAnalytical Lab of the Washington State University (WA, USA) by a HP 4500+ quadrupole ICP-MS.

3.4.2.1. Sample digestion

Sample powders were dissolved following a digestion technique adapted from Crock and Lichte (1982). Samples were first ground in an iron bowl in a shatterbox swing mill. Two grams of this powder was then mixed with an equal amount of lithium tetraborate ($Li_2B_4O_7$) flux, placed into a carbon crucible and fused in a 1000 ºC muffle furnace for 30 minutes. The resulting fusion beads were briefly ground again in the shatterbox and 250 mg of these powders were dissolved on a hotplate at 110 ºC, using 6 ml HF, 2 ml HNO_3, and 2

ml $HClO_4$ in a Teflon vial. The samples were then evaporated to dryness, followed by an additional evaporation with 2 ml $HClO_4$ at about 165°C to convert insoluble fluorides to soluble perchlorates.

Table 3.1 Trace element contents of procedural blanks at ISTEEM

Day session	3/02/03	3/02/03	3/02/03	10/02/03	10/02/03	11/02/03	11/02/03	11/02/03	17/02/03	17/02/03	17/02/03
Li (ppm)	*bdl*	0.003	*bdl*	*bdl*	*bdl*	0.2	0.2	0.2	*bdl*	*bdl*	*bdl*
Co	0.1	0.01	*bdl*	*bdl*	0.003	0.1	0.1	0.1	*bdl*	*bdl*	*bdl*
Rb	0.001	0.002	0.0002	0.0003	0.0001	0.001	0.002	0.01	0.005	*bdl*	*bdl*
Sr	0.05	0.1	0.09	0.05	0.05	0.03	0.03	0.04	0.04	0.04	0.02
Zr	0.01	0.01	0.01	0.02	0.02	0.01	0.01	0.01	0.02	0.01	0.02
Nb	*bdl*	0.0005	0.0003	0.004	0.004	0.0008	0.0008	0.0004	*bdl*	*bdl*	*bdl*
Cs	0.0008	*bdl*	0.00003	0.00007	0.0001	0.0002	0.00008	0.0004	0.0001	0.0003	0.0007
La	0.001	0.001	0.0002	0.002	0.001	0.005	0.002	0.003	0.001	0.002	0.0009
Ce	0.002	0.001	0.0003	0.001	0.001	0.001	0.002	0.002	0.001	0.0004	0.0005
Nd	0.002	0.0003	0.002	0.001	0.002	0.0003	0.0003	0.001	0.002	*bdl*	0.001
Sm	0.0005	*bdl*	*bdl*	0.0007	0.0005	0.0002	0.0002	0.0003	0.002	0.0003	0.0003
Eu	0.0002	0.0001	0.0003	0.0002	0.0001	0.0001	0.0001	*bdl*	0.0003	0.0002	0.0001
Gd	*bdl*	0.0001	0.0005	0.0002	0.0003	*bdl*	*bdl*	*bdl*	*bdl*	0.0002	*bdl*
Tb	0.00003	*bdl*	0.00005	0.00005	0.00004	*bdl*	0.0001	*bdl*	0.00001	0.00002	*bdl*
Dy	0.0005	0.0006	0.0008	*bdl*	0.0002	0.0002	0.0004	*bdl*	*bdl*	*bdl*	0.0002
Ho	0.00006	0.00005	0.00004	0.00008	0.00006	0.00004	*bdl*	*bdl*	*bdl*	0.00005	0.0001
Er	0.0002	0.0001	*bdl*	0.00002	0.0002	0.0002	0.00008	0.0001	*bdl*	0.00008	0.00007
Tm	0.00005	*bdl*	*bdl*	*bdl*	0.00003	*bdl*	0.00002	*bdl*	*bdl*	*bdl*	*bdl*
Yb	0.00009	*bdl*	*bdl*	0.00002	0.0001	0.0002	0.0002	*bdl*	0.0002	*bdl*	0.00005
Lu	0.00001	0.00003	*bdl*	0.00003	0.00003	0.000001	0.00001	0.00005	*bdl*	*bdl*	0.00007
Hf	0.0003	0.00005	0.00004	0.001	0.001	0.0003	0.0003	*bdl*	0.00002	0.0004	0.0005
Ta	0.00006	0.00006	0.00002	0.00005	0.0002	0.0002	0.0001	*bdl*	*bdl*	*bdl*	*bdl*
Th	0.0001	0.00008	0.00007	0.0003	0.0003	0.0007	0.0006	0.0001	*bdl*	0.0002	0.0002
U	0.00007	0.00009	*bdl*	0.00017	0.00022	0.00029	0.00015	*bdl*	0.00006	*bdl*	*bdl*

Day session	18/2/03	18/2/03	16/10/03	16/10/03	16/10/03	16/10/03	17/10/03	17/10/03	17/10/03	17/10/03
Li (ppm)	*bdl*	*bdl*	*bdl*	*bdl*	*bdl*	*bdl*	*bdl*	*bdl*	*bdl*	*bdl*
Co	*bdl*	0.1	0.02	0.001	0.016	0.001	0.003	0.02	0.003	0.02
Rb	0.003	0.001	0.001	0.003	0.001	0.002	0.001	0.001	0.002	0.002
Sr	0.03	0.04	0.003	0.004	0.002	0.002	0.01	0.01	0.01	0.01
Zr	0.01	0.01	0.004	0.003	0.01	0.005	0.01	0.01	0.01	0.01
Nb	0.0002	*bdl*	0.0001	*bdl*	0.0004	*bdl*	0.0003	0.0005	0.0004	0.0004
Cs	0.0005	0.0005	*bdl*	0.0001	*bdl*	*bdl*	0.0001	0.0001	*bdl*	0.0003
La	0.0007	0.004	0.0003	0.0006	0.0009	0.001	0.001	0.002	0.001	0.003
Ce	0.001	0.0001	0.0002	0.0001	0.0005	0.0001	0.0003	0.001	0.0005	0.001
Nd	*bdl*	0.0001	0.001	0.0003	0.0005	0.00005	0.001	0.002	*bdl*	0.001
Sm	0.001	0.001	0.0001	0.00001	0.0002	0.0002	0.00004	0.0002	*bdl*	*bdl*
Eu	*bdl*	0.0004	0.00001	0.00004	0.0001	*bdl*	*bdl*	0.0001	*bdl*	*bdl*
Gd	*bdl*	0.0004	0.0003	0.0007	*bdl*	0.0001	0.0002	0.0004	*bdl*	0.0001
Tb	0.00002	0.00009	*bdl*	0.00009	*bdl*	*bdl*	0.00001	0.00006	*bdl*	*bdl*
Dy	0.0001	0.0001	0.0002	0.0003	*bdl*	*bdl*	0.0003	0.0009	0.0007	0.002
Ho	0.00005	*bdl*	*bdl*	*bdl*	*bdl*	*bdl*	0.00003	*bdl*	0.00003	0.00005
Er	*bdl*	*bdl*	*bdl*	0.0003	*bdl*	*bdl*	0.0004	0.0001	*bdl*	*bdl*
Tm	*bdl*	0.00003	0.00004	0.00007	*bdl*	*bdl*	0.00002	0.000002	*bdl*	*bdl*
Yb	0.00006	0.00004	*bdl*	*bdl*	*bdl*	*bdl*	0.00007	0.00009	0.0002	0.0001
Lu	*bdl*	0.00007	0.0001	0.0001	0.00004	0.00004	0.000004	*bdl*	*bdl*	*bdl*
Hf	0.0007	0.0004	0.0002	0.0003	*bdl*	*bdl*	0.00009	0.0003	0.0002	*bdl*
Ta	0.0001	*bdl*	0.00003	0.00001	*bdl*	*bdl*	*bdl*	0.00005	0.00007	0.00005
Th	0.00002	*bdl*	0.0002	0.0002	0.00002	*bdl*	0.00003	0.0004	*bdl*	0.00002
U	*bdl*	*bdl*	0.0002	0.0004	0.00008	0.0002	0.0001	0.0002	0.0002	0.0004

bdl = below detection limit

Table 3.2 Trace element contents of international reference samples analysed at ISTEEM as unknowns

Standard run	**PCC-1**	*RSD*	**UB-(N)**	*RSD*	**BHVO-1**	*RSD*	**ROA-1**	*RSD*	**BIR**	*RSD*
	n = 3	*(%)*	n = 11	(%)	n = 8	*(%)*	n = 5	*(%)*	n = 2	*(%)*
Li (ppm)	0.9	*4*	24	*7*	4.1	*11*	4.2	*11*	2.4	*1*
Co	112	*8*	96	*5*	42	*4*	70	*18*	50	*7*
Rb	0.073	*10*	3.4	*5*	9	*4*	0.65	*3*	0.19	*3*
Sr	0.400	*5*	7.8	*4*	352	*7*	36.7	*2*	73	*9*
Zr	0.145	*15*	3.6	*7*	165	*5*	38.2	*3*	14	*6*
Nb	0.0274	*5*	0.057	*14*	18	*3*	0.069	*19*	0.61	*1*
Cs	0.008	*5*	11	*4*	0.10	*6*	0.24	*4*	0.005	*8*
La	0.033	*6*	0.33	*4*	15	*2*	1.01	*4*	0.66	*1*
Ce	0.051	*5*	0.83	*5*	39	*2*	4.13	*3*	1.9	*1*
Nd	0.028	*9*	0.63	*6*	26	*4*	4.60	*4*	2.4	*2*
Sm	0.015	*23*	0.218	*5*	6.1	*3*	1.60	*3*	1.1	*2*
Eu	0.003	*26*	0.081	*6*	2.1	*5*	0.62	*4*	0.54	*1*
Gd	0.011	*16*	0.33	*5*	6.4	*4*	2.22	*3*	1.9	*2*
Tb	0.0018	*19*	0.062	*5*	1.0	*5*	0.384	*3*	0.37	*2*
Dy	0.0207	*19*	0.46	*6*	5.8	*5*	2.65	*3*	2.8	*3*
Ho	0.0048	*12*	0.101	*6*	1.1	*6*	0.55	*4*	0.61	*2*
Er	0.0159	*12*	0.298	*4*	2.6	*5*	1.53	*3*	1.8	*2*
Tm	0.0032	*15*	0.045	*6*	0.34	*5*	0.218	*3*	0.26	*2*
Yb	0.026	*8*	0.299	*5*	2.0	*5*	1.39	*3*	1.7	*1*
Lu	0.0061	*9*	0.05	*6*	0.30	*6*	0.223	*3*	0.27	*2*
Hf	0.0078	*33*	0.135	*6*	4.7	*7*	1.32	*5*	0.64	*2*
Ta	0.003	*34*	0.019	*16*	1.2	*8*	0.017	*9*	0.040	*1*
Th	0.013	*10*	0.069	*15*	1.3	*7*	0.009	*11*	0.035	*1*
U	0.0084	*19*	0.058	*13*	0.44	*9*	0.004	*39*	0.012	*10*

PCC-1 = Dunite; UB-(N) = Serpentinite; BHVO-1 = Basalt; ROA-1 = Websterite; BIR = Basalt. Values are average contents of "n" analyses of a given reference sample. RSD% are the variation coefficient in percentage. At least one reference sample was measured as unknown in each analytical run.

The combined fusion/dissolution procedure implemented at the WSU GeoAnalytical Lab ensures the complete dissolution of zircons and other refractory phases, while removing silica and boron as matrix elements by volatilizing them as gaseous fluorides.

3.4.2.2. Analytical procedure

3 ml HNO_3, 8 drops H_2O_2, 5 drops HF and an internal standard of In, Re and Ru were added to the samples which then were diluted up to 60 ml final volume (1:240 final dilution). The instrumentation consisted of a quadrupole ICP-MS equipped with an all Teflon PFA nebulizer and a quartz Scott-type spray chamber maintained at 2 ºC. Samples were introduced into the argon plasma at 1 ml/minute using a peristaltic pump and a Cetac ASX-510 automatic sampler. Plasma was powered at 1250 W. Under these conditions MO+/M+ (the proportion of metal ions forming oxides) is minimized. Once inside the vacuum region, the positive ion beam was extracted from the expanding jet, focused, offset by 1 cm to remove photons and residual neutrals, and then re-focused into a unit mass resolution quadrupole mass filter. The instrument was run in "multi-element" mode averaging 10 repeats of 0.5 s per element for a total integrated count time of 5 s per element. Detection by the electron multiplier was by pulse counting at low beam

intensities and by current integration at high beam intensities (> 3.0 MHz). Unknown samples were run in sets of 17. One procedural blank and two samples each of the 3 in-house rock standards BCR-P, GMP-01 and MON-01 were run with each batch, totaling 24 standard and unknown samples per batch.

3.4.2.3. Treatment of the data

The three in-house standards were calibrated against 17 international reference samples (e.g. BCR-1, BIR-1, BHVO-1, W-2, G-2). Raw intensities were corrected for oxide and isobaric interferences and for instrumental drift using the In, Re and Ru internal standard (after Doherty 1989). Calibration curves for each element were then constructed from the six (2x3) standard samples and single procedural blank by plotting reference values against the corrected intensities. Concentrations for the unknown samples were then computed from this curve. The detection limits and the reproducibility of the analyses at the WSU GeoAnalytical Lab are illustrated in Table 3.3, which also includes the average concentrations of 3 international standards (mafic volcanic rocks) analyzed at the WSU GeoAnalytical Lab for one year and their reference compositions (Govindaraju 1994).

Table 3.3 Detection limits, reproducibility and average concentrations of international standards run as unknowns for one year at the WSU GeoAnalytical Lab

	WSU detection limits	**Reproducibilty**		**International standards**					
		TED basalt		**BIR-1 basalt**		**BHVO-1 basalt**		**AGV-1 andesite**	
		WSU (n = 54) (2000-2003)	RSD (%)	WSU 1994	Govindaraju 1994	WSU 1994	Govindaraju 1994	WSU 1994	Govindaraju 1994
Rb (ppm)	0.057	4.06	8	0.66	0.25	10.1	11	68.95	67.30
Sr	0.115	208	2	108	108	394	403	665	662
Y	0.015	28.9	2	16.7	16.0	27.94	27.6	20.9	20.0
Nb	0.018	2.64	4	0.83	0.60	17.61	19	13.95	15.00
Cs	0.014	0.10	9	0.05	0.01	0.12	0.13	1.47	1.28
Ba	0.258	71.2	2	7.77	7.00	133	139	1216	1226
La	0.007	4.18	3	0.89	0.62	15.7	15.8	40	38
Ce	0.012	9.84	2	2.04	1.95	37.1	39.0	71	67
Pr	0.009	1.57	2	0.45	0.38	5.52	5.70	8.95	7.60
Nd	0.045	8.19	2	2.47	2.50	25.3	25.2	33	33
Sm	0.014	2.99	2	1.13	1.10	6.20	6.20	5.91	5.90
Eu	0.010	1.17	2	0.55	0.54	2.12	2.06	1.62	1.64
Gd	0.026	3.96	2	1.95	1.85	6.27	6.40	5.01	5.00
Tb	0.007	0.75	2	0.38	0.36	0.96	0.96	0.68	0.70
Dy	0.024	5.03	1	2.54	2.50	5.19	5.20	3.52	3.60
Ho	0.006	1.10	2	0.54	0.57	0.93	0.99	0.65	0.67
Er	0.021	3.11	2	1.61	1.70	2.41	2.40	1.75	1.70
Tm	0.006	0.46	2	0.25	0.26	0.34	0.33	0.26	0.34
Yb	0.023	2.89	1	1.66	1.65	2.02	2.02	1.69	1.72
Lu	0.007	0.46	2	0.26	0.26	0.28	0.29	0.26	0.27
Hf	0.032	1.87	2	0.62	0.60	4.34	4.38	5.10	5.10
Ta	0.014	0.17	6	0.08	0.04	1.25	1.23	0.93	0.90
Pb	0.204	0.87	8	*n.av.*	3.0	*n.av.*	2.6	*n.av.*	36
Th	0.009	0.40	8	0.08	0.03	1.25	1.08	6.62	6.50
U	0.014	0.14	7	0.02	0.01	0.39	0.42	1.86	1.92

n.av. = not available

3.5. LASER ABLATION INDUCTIVELY COUPLED PLASMA-MASS SPECTROMETRY (LA-ICP-MS)

In situ trace element analyses of clinopyroxene and plagioclase in ophiolitic gabbros from the Moa-Baracoa massif, and mafic volcanics and subplutonic dykes spatially-related with ophiolites were carried out by Laser Ablation Inductively Coupled Plasma-Mass Spectrometry (LA-ICP-MS) in ~ 150 μm thick polished sections. Analyses were performed at ISTEEM (Institut des Sciences de la Terre, de l'Environnement et de l'Espace de Montpellier, CNRS-Université Montpellier II, Montpellier, France) using a VG-PQ2 Turbo+ ICP-MS, coupled with a Geolas (Microlas) automated platform housing a 193 nm Compex 102 laser from LambdaPhysik.

After EPMA analyses, thick sections were cleaned with alcohol to remove carbon coating, dried under nitrogen and introduced into the ablation cell. Analyses were conducted using an in-house modified ablation cell of ca. 30 cm^3, which resulted in a shorter washout time and an improved sensitivity compared to the initial larger ablation cell. Ablation experiments were conducted in He atmosphere, which enhances sensitivity and reduces inter-element fractionation (Gunther and Heinrich 1999). The laser was fired using an energy density of 15 J/cm^2 at a frequency of 5 Hz and a spot size of 77 μm. This resulted in a sensitivity of ca. 4000 cps/ppm for In based on measurements on the NIST 610 certified reference material. The drilling rate was ~ 0.15 μm/pulse which resulted in crater depths of ~ 45 μm under the analytical conditions described above. The ablation was monitored by a video camera coupled to an optic microscopy set on the sample. The helium gas and particles from the sample were then mixed with Ar before entering the plasma. The measurement procedure consisted of the following steps: a) one analysis of the instrumental blank; b) one analysis of the NIST 610 rhyolitic glass; c) a second analysis of the instrumental blank; d) analyses of three or five unknowns; e) a third analysis of the instrumental blank; f) a second analysis of the NIST 610 rhyolitic glass; g) a fourth analysis of the instrumental blank. Signals were acquired in Time Resolved Acquisition (TRA), devoting 2 minutes for the blanks and 1 minute for measurement of the analytes. Data were obtained in the peak jumping mode using 1 point per peak and each element was measured using an equal dwell time of 10.24 ms. Oxide level, measured using the ThO/Th ratio, was below 0.3%. ^{30}Si or ^{43}Ca were used as internal standard and analyte concentrations were calibrated against the NIST 610 certified reference material. Data were subsequently reduced using the GLITTER software and a linear fit to ratio. This procedure typically resulted in a precision of 5 to 10% (RSD %) for the great majority of the analytes.

3.6. MULTI-COLLECTOR INDUCTIVELY COUPLED PLASMA-MASS SPECTROMETRY (MC-ICP-MS) AND THERMAL IONISATION MASS SPECTROMETRY (TIMS)

Pb (^{206}Pb, ^{207}Pb, ^{208}Pb /^{204}Pb) and Nd ($^{143}Nd/^{144}Nd$) radiogenic isotopic ratios were measured in whole rocks and in clinopyroxene and plagioclase concentrates by a P54 Fisons Multi-Collector Inductively Coupled Plasma-Mass Spectrometer (MC-ICP-MS) or a NuPlasma 500 MC-ICP-MS at the Ecole Normale Supérieure de Lyon (France). Sr radiogenic isotopic ratios ($^{87}Sr/^{86}Sr$) were measured by a CAMECA TSN 206 Thermal Ionisation Mass Spectrometer (TIMS) at the Laboratoire Géosciences Azur of the Université de Nice-Sophia Antipolis (France) and by a ThermoFinnigan Triton T1 MC-TIMS at the LABOGIS of the Centre Universitaire de Formation et de Recherche de Nîmes (France). Analyses were focused on the Cretaceous igneous suites spatially-related to the Mayarí-Baracoa Ophiolitic Belt and subordinately on the ophiolitic gabbros from the Moa-Baracoa massif.

3.6.1. Mineral separation

Sample chips from the jaw crusher were ground for few seconds by a steel ring mill to reduce their size before sieving. 6 grain fractions were separated: < 100 μm, 100-200 μm 200-300 μm, 300-425 μm, 425-1000 μm, and > 1000 μm. After each single sample processing the sieves were carefully cleaned by compressed air, plastic brush, metallic needle, ultrasonic cleaner and alcohol in order to remove any grain trapped in the meshes. The 100-200 μm fractions were then processed by wet gravity-shaking separation in a Wilfley® Concentrating Table followed by magnetic separation in a Frantz® isodynamic device (Fig. 3.2). Clean mineral concentrates were handpicked in alcohol under a binocular microscope in order to remove mixed and altered grains. However, the pervasive presence of fine intergrowths of clinopyroxene and plagioclase in mafic volcanics made it extremely difficult to obtain optically pure mineral concentrates. To improve mineral quality, hand-picked separates were ultrasonically washed in diluted 2.5N HCl, kept on hotplate at about 60 ºC for ten minutes, and rinsed several times with ultra-pure water. However, in many instances, the final separates contained mixed grains.

3.6.2. Pb, Nd and Sr chromatographic extractions

3.6.2.1. Cleaning of the equipment

The material utilized at the ISTEEM clean room isotopic laboratory during the chemical separations was carefully treated in order to limit the contamination of the samples. All the

reagents were Merck® Suprapur acids distilled three times by sub-boiling. Water was purified by a Millipore Milliq Element Elix3 device with electric resistance > 18.3 MΩ. The mouthpieces of pipette and the tubes were washed in several one-day baths of hot HCl 30% and HNO_3 30% and rinsed with ultra-pure water. Previously to be charged with samples, Teflon beakers were firstly cleaned with acetone, then filled with concentrated HNO_3 and put in ultrasonic cleaner for several minutes. After rinsing with ultra-pure water, the beakers were submerged in three HNO_3 diluted solutions, left on the hotplate during 24 hours for each bath, and carefully rinsed. Finally, the vessels were washed in two baths of double distilled HCl 6.4N and ultra-pure water, kept on the hotplate during one day for each bath, rinsed and dried.

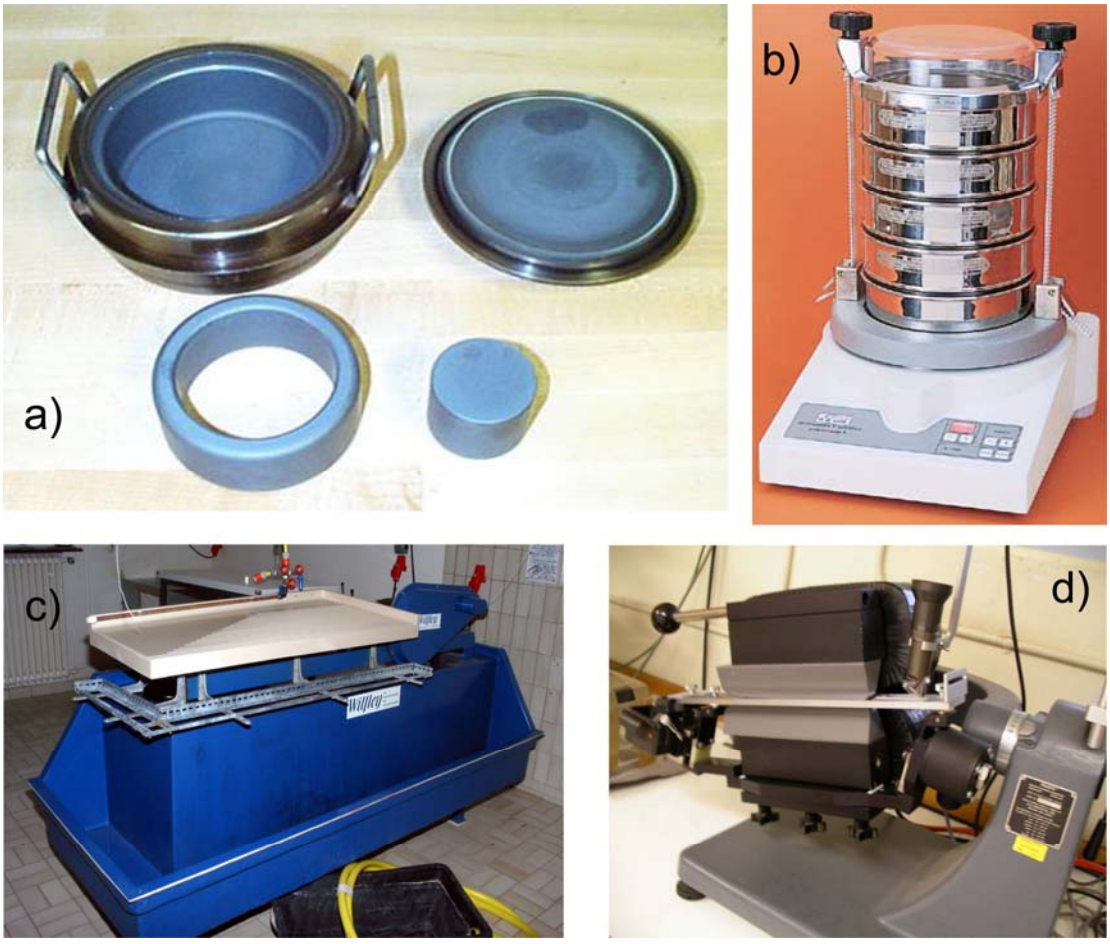

Figure 3.2: Standard tools for mineral concentration: a) Milling steel rings; b) Sieve shaker; c) Wilfley® Concentrating Table; d) Frantz® isodynamic separator.

3.6.2.2. Sample dissolution

The sample processing was continuously carried out on over-pressurized laminar vertical flow hoods to prevent external contamination. Clean digestion vessels were loaded with

approximately 400-1000 mg of whole rock or 200 mg of mineral separate. The calculation of the weight to be dissolved depends on the Pb, Nd and Sr contents in the sample. To obtain highly precise isotopic results, a minimum abundance of 400 ng is necessary for each element to be analyzed; however, the quantity of the sample that can be processed should not be > 1 g in order to prevent matrix effects during the chemical separations. Samples were digested with 2 ml HNO_3 13N and 2 ml HF 48% for at least 48 hours at about 120 ºC. After evaporation, 2 ml HNO_3 13N was added to the residues, kept at approximately 90 ºC for 24 hours and then evaporated.

3.6.2.3. Pb extraction by liquid chromatography

0.5 ml HBr 8N was firstly added to the samples which were kept at 70 ºC for 3-4 hours, moved in ultrasonic bath and then evaporated. Afterwards, 0.8 ml HBr 0.5N was added to the residues that were left in ultrasonic cleaner for several minutes. Sample solutions were then transferred to tubes and centrifuged for approximately 10 minutes. Pb extraction was done in Teflon columns using the AG1-X8 anion exchange resin (Fig. 3.3). The introduction of the resin was preceded and followed by three washing cycles with alternate HCl 6N and ultra-pure water. 1 ml HBr 0.5N was then added to the resin and after its percolation a vessel was placed below the columns. One sample solution was then carefully introduced in each column and samples were leached three times with 1 ml HBr 0.5N. The leaching solution was recuperated in the vessels and evaporated for subsequent Sr and rare earth elements pre-concentration. Pb was finally extracted from the samples adding 1 ml HCl 6N that was evaporated on the hotplate. Average total Pb in procedural blanks was < 50 pg.

3.6.2.4. Sr and rare earth elements (REE) pre-concentration

Sr and rare earth elements (REE) pre-concentration was done using the AGW 50-X8 cationic exchange resin firstly washed by four cycles of alternate ultra-pure water and HCl 6N. 0.5 ml HCl 6N was introduced in the beakers, kept on the hotplate for ~ 30 minutes and after evaporated. 2 ml HCl 1.5N was then added to the samples that were moved by ultrasounds, transferred to tubes and centrifuged for approximately 10 minutes. 4 ml HCl 1.5N was subsequently added to the resin and after its percolation a sample solution was carefully introduced in each Teflon column. Samples were therefore leached with 6 ml HCl 1.5N and 4 ml HCl 2.5N in order to extract the major elements. After this stage, a vial was placed below each column to recuperate the alkali and alkaline earth elements (e.g. K, Rb, Sr, Ba) by leaching twice with 4 ml HCl 2.5N that was finally evaporated on hotplate. 2

ml HCl 4N was afterwards introduced in the columns. REE were finally recuperated in a second beaker by the elution and subsequent evaporation of 7.5 ml HCl 6N.

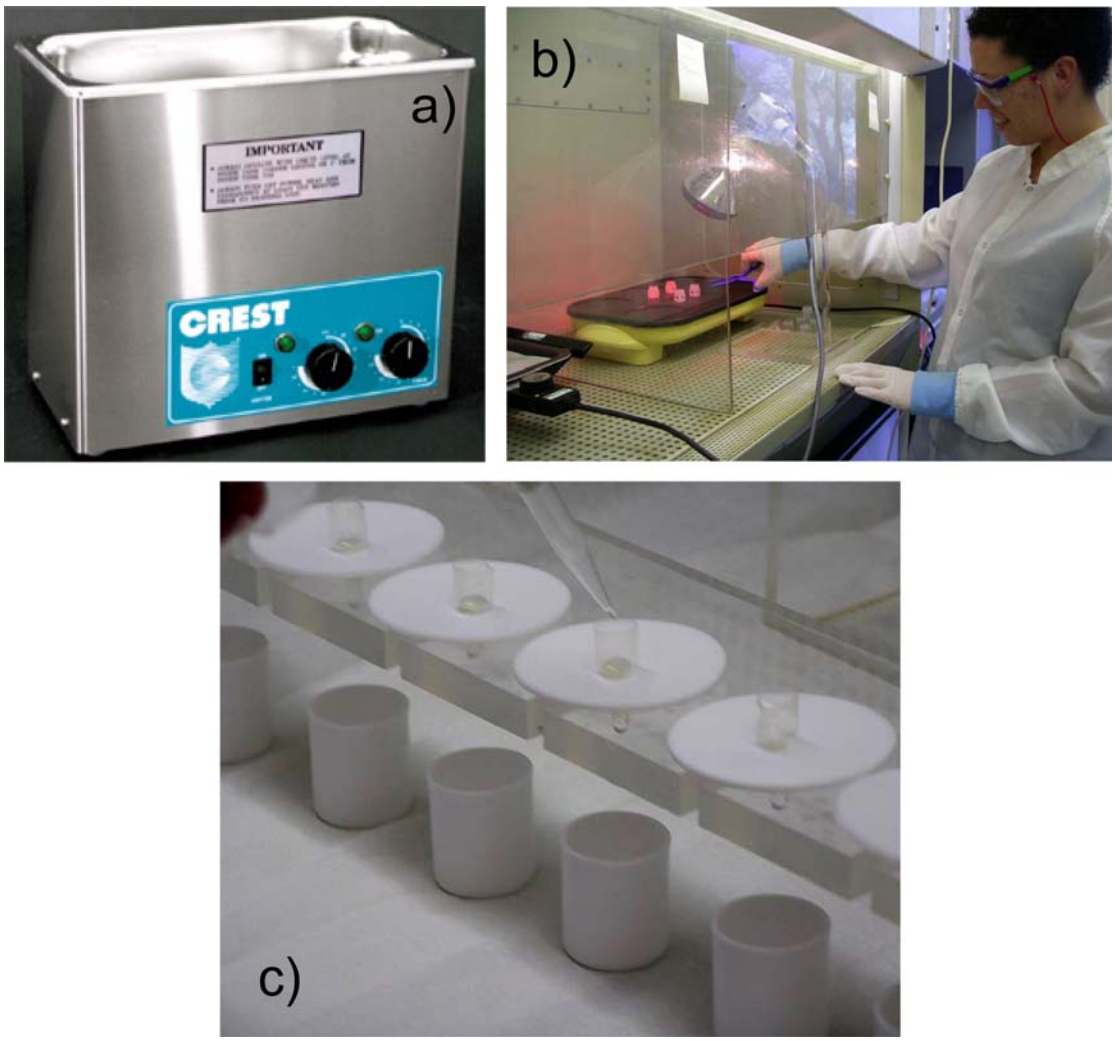

Figure 3.3: Standard equipment for chemical ion-exchange chromatographic liquid separation: a) Ultrasonic cleaner; b) Hotplate on over-pressurized laminar vertical flow hood; c) Teflon columns and beakers. Photos in b) and c) by V. Bennett, ANU, Canberra (Australia)

3.6.2.5. Sr extraction by liquid chromatography

Sr separation was done using the Eichrom Sr.Spec exchange resin following an extraction chromatographic method modified from Pin et al. (1994). 2 ml HNO_3 2N was introduced in the beakers and the sample solutions were then moved by ultrasounds, transferred to tubes and centrifuged for approximately 10 minutes. The resin was firstly washed by six cycles of alternate HCl 6N and HNO_3 0.05N and conditioned with 3 ml HNO_3 2N. A sample solution was then carefully introduced in each Teflon column. K and Rb were firstly extracted by leaching twice with 1 ml HNO_3 2N, followed by Ba that was eluted with 3 ml HNO_3 7N and 0.5 ml HNO_3 3N. Sr was then recuperated adding 6 ml HNO_3 0.05N

that was subsequently evaporated on hotplate. Average total Sr in procedural blanks was < 70 pg.

3.6.2.6. Nd extraction by liquid chromatography

Nd was separated from the other REE by employing the organic acid HDEHP fixed on the surface of microscopic Teflon balls (diameter ~ tens μm) set on silica columns. 0.5 ml HCl 0.3N was put in the beakers and the sample solutions were then moved by ultrasounds. Teflon balls were conditioned with 3 ml HCl 0.3N and after its percolation a sample solution was carefully introduced in each column. A variable volume of HCl 0.3N (ranging between 3.1 and 4.3 ml according to the calibration of each column) was added to firstly elute the LREE (La, Ce, Pr); Nd was subsequently recuperated by leaching with a second variable volume of HCl 0.3N (from 3.2 to 6.3 ml) that was finally evaporated. The Teflon balls were washed by the percolation of 8 ml HCl 6N. Average total Nd in procedural blanks was < 30 pg.

3.6.3. Multi-Collector Inductively Coupled Plasma-Mass Spectrometry (MC-ICP-MS) analyses of Pb and Nd radiogenic isotopic ratios

For the isotopic Multi-Collector Inductively Coupled Plasma-Mass Spectrometry (MC-ICP-MS) analyses of Pb, samples were dissolved in ~ 0.75-1 ml HNO_3 0.05N containing 50 μg/l of Tl (following the normalization method of White et al. 2000), kept some minutes on hotplate, moved by ultrasounds and transferred in a tube. The analyses took place in free aspiration and each one consisted of 3 batches of 20 runs. Two rinsing solutions of 3%vol. HNO_3 and HNO_3 0.05N were used at the end of every measurement. During the entire Pb analytical sessions, each batch of two samples was bracketed by NBS 981 standard splits. All the $^{206}Pb/^{204}Pb$, $^{207}Pb/^{204}Pb$ and $^{208}Pb/^{204}Pb$ ratios measured in the standard during the analytical sessions are listed in Table 3.4. After the analyses, an external correction was applied to the standard according to the values reported by Todt et al. (1996). Pb isotopic ratios of the samples are at most affected by errors on the third decimal (10^{-3}).

For the MC-ICP-MS analyses of Nd radiogenic isotopic ratios, the measurements followed the method described by Luais et al. (1997). Samples were dissolved in ~ 0.75-1 ml HNO_3 0.05N, kept some minutes on hotplate, moved by ultrasounds and transferred in a tube. During the entire analytical sessions 2 samples were bracketed between the Lyon in-house standard diluted in HNO_3 0.05N (Nd concentration = 120 ppb). The values of $^{143}Nd/^{144}Nd$ ratio (average = 0.512137 ± 44 (2σ), n = 42) measured in the standard during

the analytical sessions are listed in Table 3.4. Nd isotopic ratios of the samples are at most affected by errors on the fifth decimal (10^{-5}).

Table 3.4 Radiogenic isotopic ratios of standards run during the MC-ICP-MS and TIMS analytical sessions (Pb: NBS 981; Nd: Lyon in-house standard; Sr: NBS 987)

$^{206}Pb/^{204}Pb$	±	$^{207}Pb/^{204}Pb$	±	$^{208}Pb/^{204}Pb$	±	$^{143}Nd/^{144}Nd$	±	$^{87}Sr/^{86}Sr$	±
P54 Fisons		**P54 Fisons**		**P54 Fisons**		**P54 Fisons**		**CAMECA TSN**	
16.9440	6.E-04	15.4833	6.E-04	36.668	2.E-03	0.51215	1E-05	0.71027	2.E-05
16.9437	9.E-04	15.482	1.E-03	36.663	3.E-03	0.51214	2E-05	**TRITON T1**	
16.9424	8.E-04	15.4801	7.E-04	36.656	2.E-03	0.51215	2E-05	0.710262	6.E-06
16.9413	9.E-04	15.4790	9.E-04	36.653	2.E-03	0.51214	1E-05	0.710267	4.E-06
16.9442	8.E-04	15.4799	8.E-04	36.657	2.E-03	0.51217	1E-05	0.710246	5.E-06
16.9462	8.E-04	15.4826	8.E-04	36.663	2.E-03	0.51216	1E-05	0.710254	5.E-06
16.9451	9.E-04	15.4810	9.E-04	36.660	3.E-03	0.51211	1E-05		
16.9422	9.E-04	15.4779	7.E-04	36.652	2.E-03	0.51209	2E-05		
16.9474	8.E-04	15.482	1.E-03	36.665	3.E-03	0.51213	1E-05		
16.9472	9.E-04	15.481	1.E-03	36.661	3.E-03	0.51216	2E-05		
16.9430	8.E-04	15.4788	9.E-04	36.658	2.E-03	0.51211	1E-05		
16.9463	7.E-04	15.4791	8.E-04	36.658	2.E-03	0.51214	2E-05		
16.9457	7.E-04	15.4787	6.E-04	36.654	2.E-03	0.51213	1E-05		
16.9444	7.E-04	15.477	1.E-03	36.649	3.E-03	0.51211	1E-05		
16.9428	8.E-04	15.4745	7.E-04	36.645	2.E-03	0.51212	1E-05		
16.9456	8.E-04	15.477	1.E-03	36.655	3.E-03	0.51215	2E-05		
16.9427	9.E-04	15.4754	9.E-04	36.647	3.E-03	0.51221	1E-05		
16.9452	7.E-04	15.4790	8.E-04	36.660	2.E-03	**NuPlasma**			
16.9469	8.E-04	15.4780	9.E-04	36.654	2.E-03	0.512123	3.E-06		
16.946	1.E-03	15.477	1.E-03	36.648	3.E-03	0.512116	2.E-06		
16.9479	8.E-04	15.4788	9.E-04	36.654	2.E-03	0.512134	3.E-06		
16.9447	9.E-04	15.4773	7.E-04	36.652	2.E-03	0.512121	3.E-06		
16.9449	9.E-04	15.4770	9.E-04	36.661	2.E-03	0.512128	3.E-06		
16.9449	8.E-04	15.4784	9.E-04	36.654	3.E-03	0.512121	2.E-06		
NuPlasma		**NuPlasma**		**NuPlasma**		0.512116	3.E-06		
16.93349	9E-05	15.48824	7E-05	36.6872	5E-04	0.512120	3.E-06		
16.93284	8E-05	15.48741	7E-05	36.6861	5E-04	0.512112	2.E-06		
16.93548	7E-05	15.49066	6E-05	36.6960	4E-04	0.512115	2.E-06		
16.93430	6E-05	15.48900	5E-05	36.6923	3E-04	0.512126	3.E-06		
16.93558	6E-05	15.49030	5E-05	36.6960	4E-04	0.512116	3.E-06		
16.93537	7E-05	15.49014	7E-05	36.6945	4E-04	0.512112	3.E-06		
16.93380	6E-05	15.48825	6E-05	36.6896	4E-04	0.512146	2.E-06		
16.93308	7E-05	15.48701	7E-05	36.6861	4E-04	0.512152	3.E-06		
16.93346	7E-05	15.48733	7E-05	36.6875	4E-04	0.512151	2.E-06		
16.9348	1E-04	15.489	1E-04	36.6936	6E-04	0.512159	2.E-06		
16.93464	9E-05	15.48892	8E-05	36.6934	6E-04	0.512148	2.E-06		
16.93274	9E-05	15.48689	8E-05	36.6851	5E-04	0.512157	3.E-06		
16.93584	7E-05	15.48954	7E-05	36.6967	4E-04	0.512173	3.E-06		
16.93353	7E-05	15.48770	7E-05	36.6889	5E-04	0.512150	3.E-06		
16.9322	1E-04	15.48703	9E-05	36.6845	6E-04	0.512158	3.E-06		
16.93789	7E-05	15.49449	7E-05	36.7089	5E-04	0.512137	5.E-06		
16.93915	9E-05	15.49513	9E-05	36.7061	8E-04	0.512141	4.E-06		
16.93829	7E-05	15.49453	8E-05	36.7092	5E-04	0.512141	5.E-06		

3.6.4. Thermal Ionisation Mass Spectrometry (TIMS) analyses of Sr radiogenic isotopic ratios

For the Sr isotopic analyses by Thermal Ionisation Mass Spectrometry (TIMS), samples were firstly dissolved in 2 µl HNO_3 0.1N and carefully placed on a Re filament (Fig. 3.4). The deposition of the sample solution on the filament was preceded and followed by the

evaporation of 2 µl $TaCl_5$ that regulates the emission of Sr during the analysis. During the analytical sessions, filaments were heated in 3 steps up to ~ 1460 ºC before the onset of the analysis that consisted of 5 cycles of 15 runs each. $^{87}Sr/^{86}Sr$ ratios were corrected for mass discrimination by normalizing to $^{86}Sr/^{88}Sr = 0.1194$ and for interference with ^{87}Rb by measuring ^{85}Rb. The standard NBS 987 (average $^{87}Sr/^{86}Sr = 0.710260 \pm 20$, n = 5, Table 3.4) was run at the beginning of each analytical session. Sr isotopic ratios of the samples are at most affected by errors on the fifth decimal (10^{-5}).

Figure 3.4: Re electric filaments for deposition and loading of samples in TIMS. Photo by V. Bennett, ANU, Canberra (Australia).

3.7. Ar-MASS SPECTROMETRY

Ar-mass spectrometry was performed on amphibole concentrate of one mafic subplutonic dyke that intrudes the Mayarí-Cristal peridotite. After separation and washing with acetone, alcohol and distilled water in ultrasonic bath, amphibole single (500-1000 µm) grains were irradiated for 48 hours in the McMaster nuclear centre (Canada) together with several MMHb (hornblende) reference grains (Samson and Alexandre 1987). Single crystal ^{40}Ar-^{39}Ar measurements were carried out at ISTEEM (Institut des Sciences de la

Terre, de l'Environnement et de l'Espace de Montpellier, CNRS-Université Montpellier II, Montpellier, France) using the step heating procedure. The analytical equipment consisted of a continuous Lexel 3500 6 W argon-ion laser equipped with a programmable beam shutter, optics for laser beam focusing, a CCD camera used to monitor the experiments, a 300cc extraction-cleanup line and a MAP 215–250 mass spectrometer with a Nier ion source and a Johnston MM1 electron multiplier. Minerals were placed in drilled cores and exposed to the laser beam during 30 s for each of the 9 steps. Released Ar was separated from the other gases by trapping in a sector of the extraction-cleanup line provided with active coal cooled by liquid nitrogen. Blanks were monitored every two experiments. Each step analysis consisted of 8-run measurements and lasted approximately 20 minutes. Conventional isotope corrections were applied, including blanks, mass discrimination, radioactive decay of ^{37}Ar and ^{39}Ar and irradiation-induced mass interferences. Errors and isochron ages were calculated after McDougall and Harrison (1988) and York (1969), respectively.

4. PETROGENESIS OF THE ULTRAMAFIC AND MAFIC ROCKS FROM THE MAYARÍ-BARACOA OPHIOLITIC BELT

4. PETROGENESIS OF THE ULTRAMAFIC AND MAFIC ROCKS FROM THE MAYARÍ-BARACOA OPHIOLITIC BELT

4.1. MAYARÍ-BARACOA OPHIOLITIC BELT: FIELD RELATIONS AND PETROGRAPHY

The Mayarí-Baracoa Ophiolitic Belt (MBOB) is a pseudotabular, strongly faulted, mafic-ultramafic massif occurring in eastern Cuba (Fig. 4.1a). The MBOB is ca. 170 km long, 10 to 30 km wide and 3.5 km thick on average. The MBOB comprises two different massifs (Proenza et al. 1999a, b): the Moa-Baracoa massif to the east and the Mayarí-Cristal massif to the west (Fig. 4.1a). The MBOB is thrusted over volcanic and sedimentary rocks of Cretaceous age. Moa-Baracoa peridotites and gabbroic rocks are in tectonic contact with Quibiján and Morel volcanics (Fig. 4.1a, 2.12, 2.13) of Albian-Early Coniacian age (Iturralde-Vinent et al. 2006), whereas the easternmost part of the Mayarí-Cristal massif is thrusted over the Téneme extrusives (Fig. 4.1a, 2.11) which are partially isochronous with the Quibiján and Morel volcanism (Iturralde-Vinent et al. 2006). Field evidence indicates that the final emplacement of the MBOB occurred during the Maastrichtian (Cobiella-Reguera 2002, 2005; Iturralde-Vinent 2003). Locally some olistostromic units (i.e. the Micara and La Picota Formations) are intercalated between the ophiolites and the Cretaceous volcanic rocks (Iturralde-Vinent 1994, 1998, 2003; Cobiella-Reguera 2002). Upward, the MBOB is occasionally in contact with undeformed rocks of the Paleogene arc or it is covered by post-Upper Eocene sandstones and siltstones (Iturralde-Vinent 1996a).

4.1.1. The Moa-Baracoa massif

The Moa-Baracoa massif is made up of a section (> 2.2 km thick) of mantle tectonite harzburgite with subordinate dunite, and a Moho transition zone (MTZ) overlain by layered gabbros of the lower oceanic crust (ca. 500 m thick). All outcropping sections of the Moa-Baracoa massif lack exposures of isotropic gabbros and diabase sheeted-dyke complexes archetypical of the conventional ophiolite sequence (Nicolas 1989 and references therein). This is most likely due to tectonic omission as in some localities layered gabbros are directly overlain by tectonically discordant pillow lavas and radiolarites (30-40 m thick). In the field studies I did not find continuous sections from tectonite to layered gabbro owing to poor exposure in the tropical forest and/or pervasive faulting. The field description below corresponds to observations in good exposures of different sections of the massif

cropping out in the localities of Quemado del Negro (crustal layered gabbros), Amores, Mercedita Mine (MTZ sills and dykes), Cayo Guam and Yamaniguey (harzburgite tectonites, MTZ dunites, gabbro sills and dykes) (Fig. 4.1a). Despite poor exposure, the regional mapping indicates that the presence of a MTZ is a regular feature at the scale of the Moa-Baracoa massif, and it points to a lithological section as portrait in Figure 4.1b.

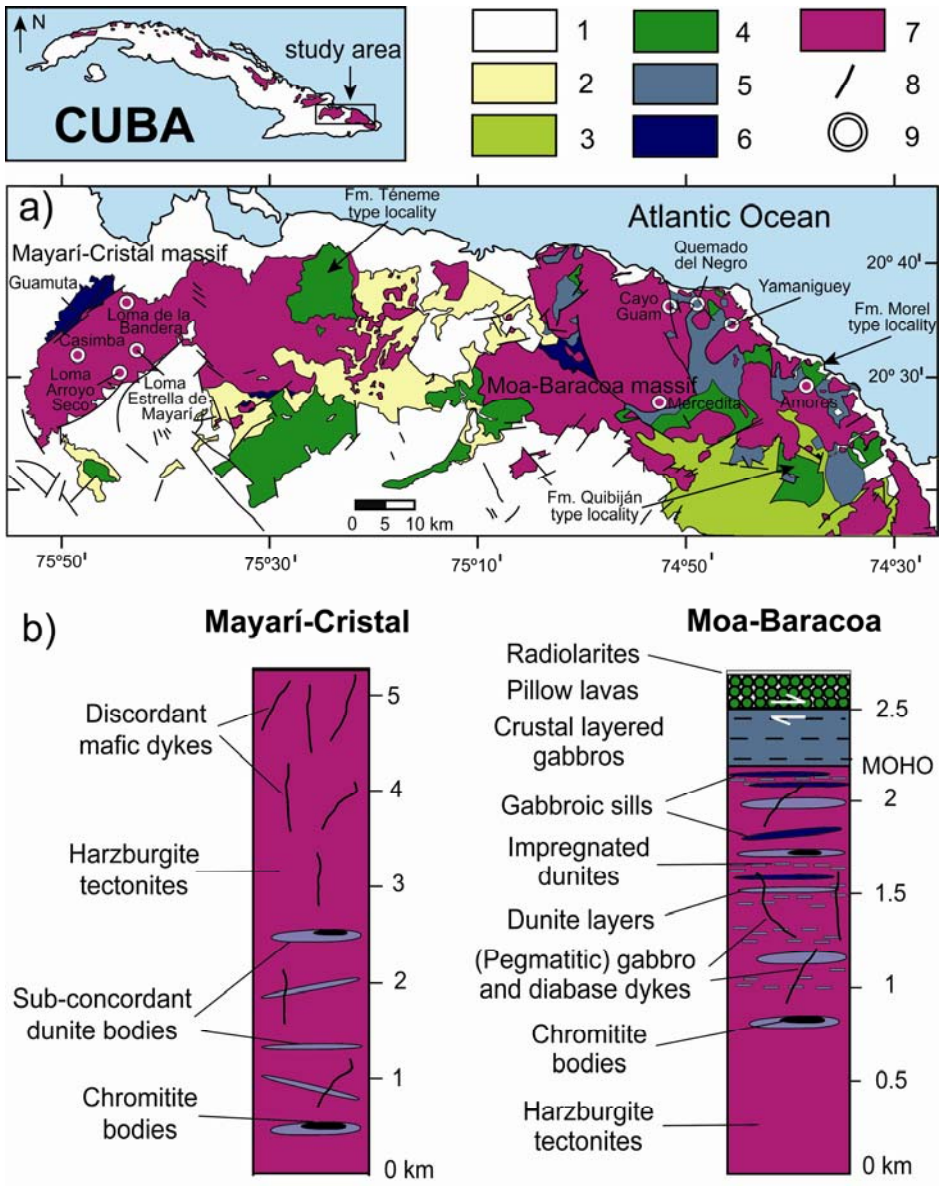

Figure 4.1 a) Geological map of the Mayarí-Baracoa Ophiolitic Belt with location of studied samples (white circles). 1 = Paleogene-Quaternary sedimentary and volcanic rocks; 2 = Ophiolitic and metamorphic melanges (La Picota and La Corea Fms.); 3 = Metamorphosed Cretaceous igneous and sedimentary rocks (Purial Complex); 4 = Cretaceous volcanic and minor plutonic rocks; 5 = Ophiolitic plutonic gabbroic rocks; 6 = Microgabbro dykes; 7 = Serpentinized peridotites locally intruded by mafic dykes; 8 = Faults; 9 = Sample locations. Inset: Geographic location of massifs constituting the Northern Cuban Ophiolite Belt (Iturralde-Vinent 1998); black box indicates the Mayarí-Baracoa Ophiolitic Belt. b) Schematic lithostratigraphic columns of Mayarí-Cristal and Moa-Baracoa massifs.

The Moa-Baracoa mantle section displays a penetrative NNW dipping foliation. Harzburgite tectonite is locally cut by gabbro dykes and minor pegmatitic gabbro, diabase, pyroxenite, troctolite and wehrlite, which are increasingly abundant near the Moho transition zone (Proenza et al. 1999a). I calculated the primary mode of peridotites (Fig. 4.2) by computer-assisted point counting on large sections following procedures of Dick et al. (1984) for highly altered abyssal peridotites. Point-counting and petrographic observations show that MBOB harzburgites lack clinopyroxene, except for tiny clinopyroxene exolutions in orthopyroxene. The absence of clinopyroxene was confirmed by careful checking under binocular microscope of different mineral separate fractions obtained by magnetic separation on large sample amounts.

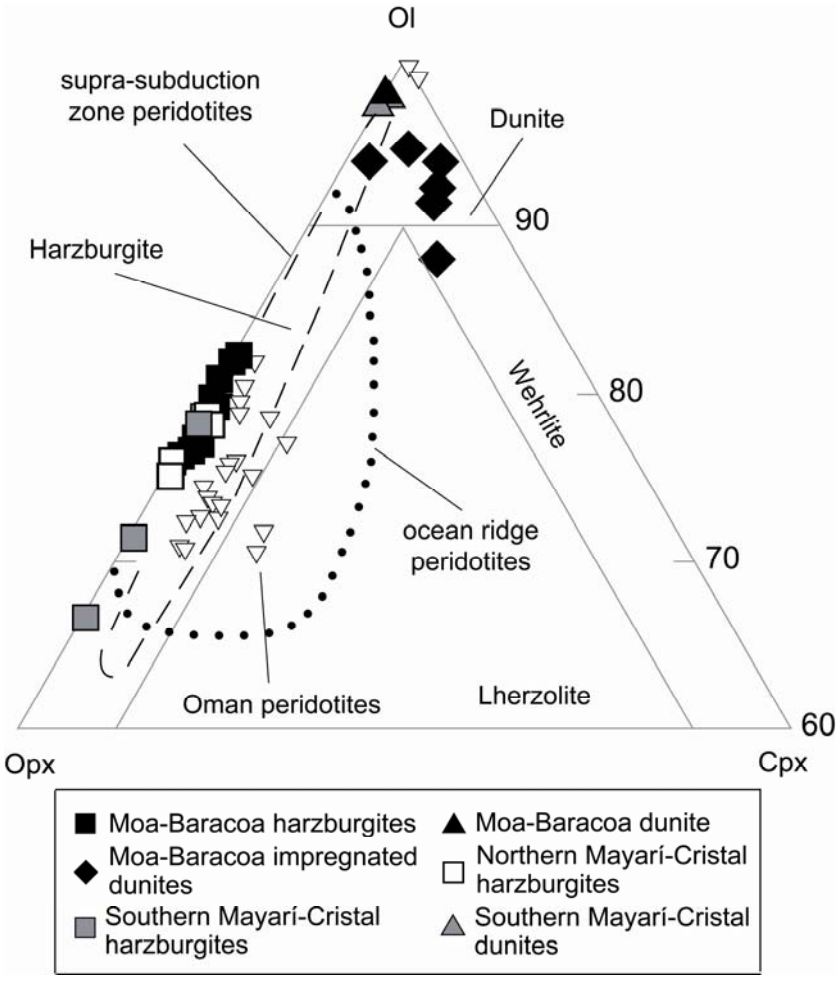

Figure 4.2 Modal compositions of Mayarí-Baracoa ultramafic rocks compared to those of peridotites from different tectonic settings. Black squares: Moa-Baracoa harzburgites; black triangle: Moa-Baracoa dunite; black diamonds: Moa-Baracoa impregnated dunites; white squares: Northern Mayarí-Cristal harzburgites; dark-grey squares: Southern Mayarí-Cristal harzburgites; dark-grey triangles: Southern Mayarí-Cristal dunites; white triangles down: Oman ophiolite peridotites (Godard et al. 2000); dotted line: ocean ridge peridotites (Dick 1989); dashed line: supra-subduction zone peridotites (Parkinson and Pearce 1998).

Moa-Baracoa harzburgites display the common porphyroclastic texture of ophiolite tectonites characterized by 1-4 mm olivine and orthopyroxene up to 1.5 cm long (Fig. 4.3a). The matrix consists of 200-500 μm polygonal olivine and orthopyroxene and minor xenomorphic Cr-rich spinel. The Moho transition zone is characterized by harzburgite and sub-concordant dunite showing sharp contacts with harzburgite (Fig. 4.3b). In terms of their clinopyroxene modal content, I differentiate two types of dunite: *dunite* (*sensu stricto*) and clinopyroxene-plagioclase rich dunite that I will refer hereafter to as *"impregnated dunite"* (Fig. 4.3c). Dunites show porphyroclastic or equigranular (~ 1 mm) textures made up of weakly deformed olivine, very rare orthopyroxene and anhedral to euhedral spinel. Impregnated dunites occur within MTZ dunite as centimetric, clinopyroxene- and plagioclase-rich patches that modally correspond to plagioclase-dunites and plagioclase-wehrlites (Fig. 4.2). Plagioclase (totally altered to phyllosilicates) is texturally associated with subhedral 2-3 mm clinopyroxene and fine grained spinel, forming interstitial clusters between olivine (Fig. 4.3d). Spinel also occurs in euhedral grains intergranular between olivine and rare orthopyroxene.

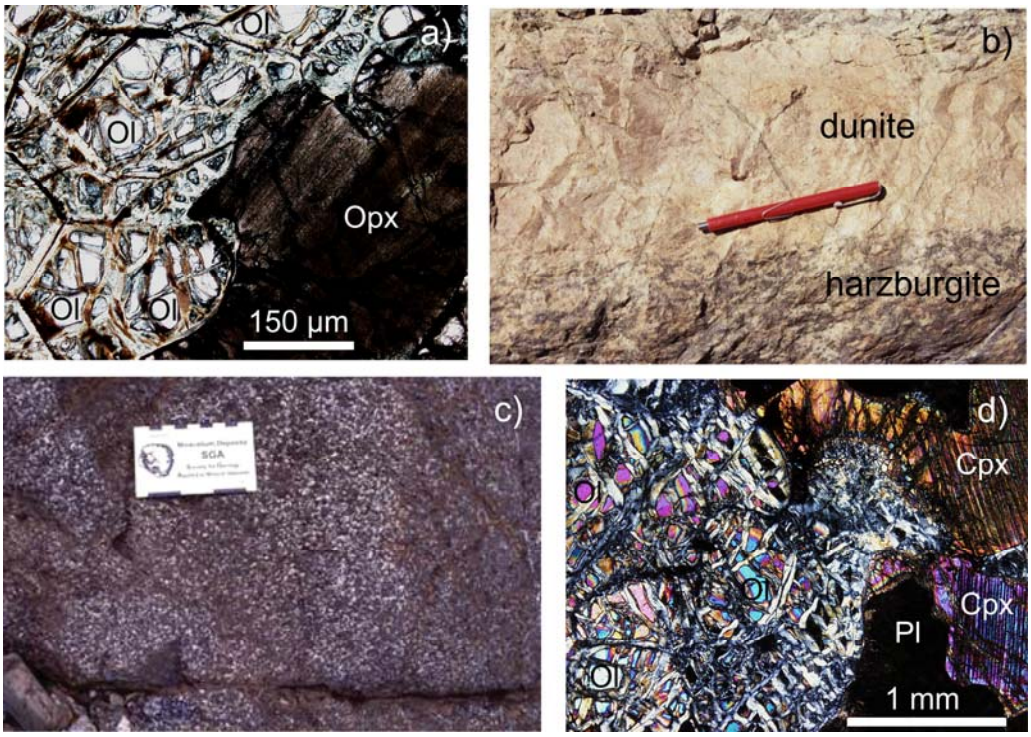

Figure 4.3 a) Porphyroclastic texture of Mayarí-Baracoa harzburgite constituted by 200-500 μm serpentinized olivine (Ol) in the matrix and millimetric olivine and orthopyroxene (Opx) grains (bastite); b) dunite *sensu stricto* in the Mayarí-Baracoa Ophiolite Belt showing sharp boundaries with enclosing harzburgite; c) "impregnated" dunite in the Moho transition zone of the Moa-Baracoa massif, rich in clinopyroxene-plagioclase clusters (light spots); d) patches of clinopyroxene (Cpx) and plagioclase (Pl) trapped in impregnated dunite owing to melt percolation. Olivine and clinopyroxene show intense serpentinization and plagioclase is completely altered to an aggregate of dark phyllosilicates. Crossed nicols.

In terms of field occurrence, Moa-Baracoa impregnated dunites are similar to impregnated dunites described in the Moho transition zone of the Oman ophiolite (Godard et al. 2000; Jousselin and Nicolas 2000; Koga et al. 2001), although such dunites are also common in some orogenic and abyssal peridotite exposures (Bodinier and Godard 2003). Such impregnated dunites testify "refertilization" processes due to pervasive interaction of the mantle with basaltic melts (e.g. Hellebrand et al. 2002; Bodinier and Godard 2003).

Modal abundances of gabbroic rocks (Fig. 4.4) were determined by mass balance between whole rock and single mineral compositions.

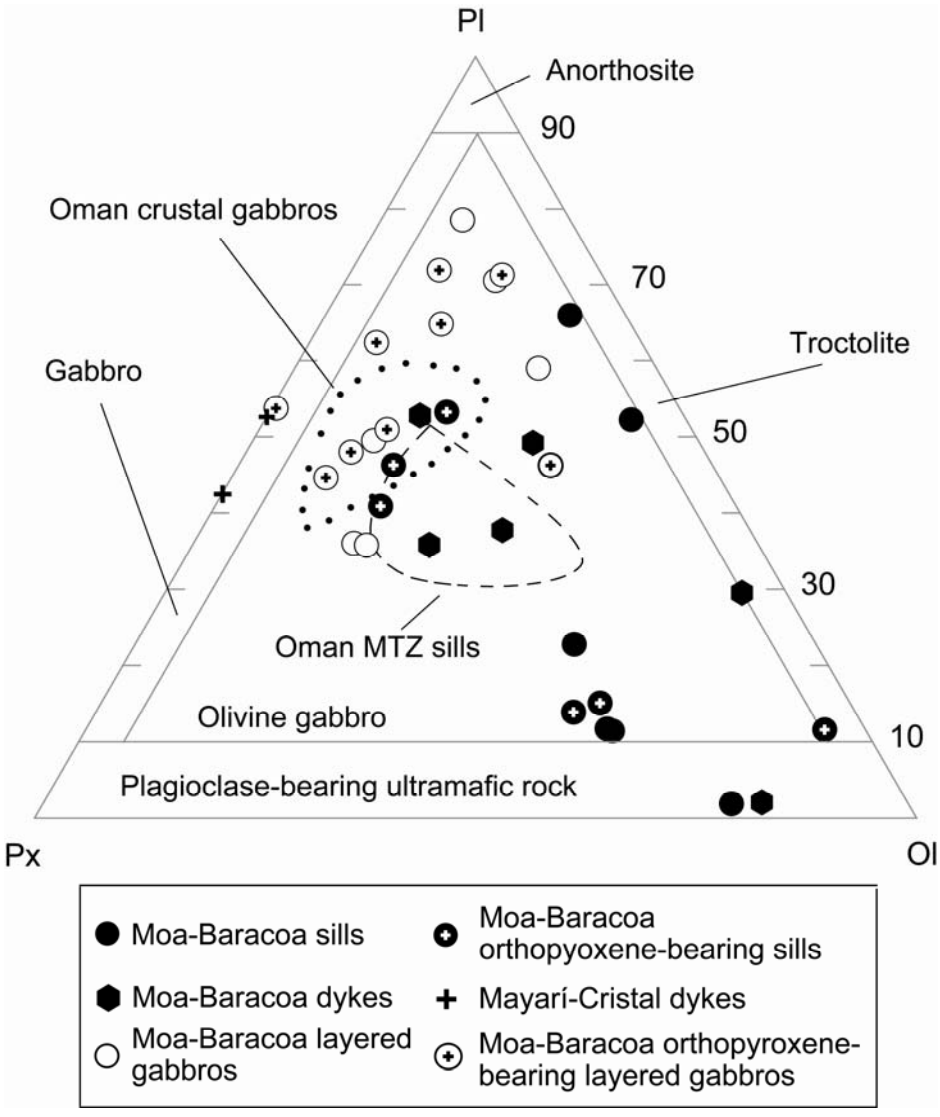

Figure 4.4 Modal compositions of Mayarí-Baracoa sills, dykes and layered gabbros. Black circles: Moa-Baracoa sills; black-crossed circles: Moa-Baracoa orthopyroxene-bearing sills; black hexagons: Moa-Baracoa dykes; crosses: Mayarí-Cristal dykes; white circles: Moa-Baracoa layered gabbros; white-crossed circles: Moa-Baracoa orthopyroxene-bearing layered gabbros; dashed line: Oman MTZ ophiolite sills (Korenaga and Kelemen 1997); dotted line: Oman ophiolite lower and middle crustal gabbros (Kelemen and Garrido, unpublished data).

Olivine gabbro and minor troctolite and plagioclase-bearing ultramafic dykes have been observed mainly in the Moho transition zone (Fig. 4.4, 4.5a). Olivine gabbro dykes display highly variable grain size (from ~ 1 mm up to several decimetres in pegmatitic samples) and degrees of alteration. Plagioclase grains are often altered to an aggregate of sericite + epidote or chlorite. Both clinopyroxene and olivine show deformation kink bands in pegmatitic samples. Titanite has occasionally been observed as alteration product.

Another particularity of the Moho transition zone is the presence of gabbroic sills (several meters thick) (Fig. 4.5b) showing misty gradations to the enclosing Moho transition zone dunites due to variation of the plagioclase/mafic mineral (clinopyroxene + olivine) modal ratio. Gabbroic sills show a wide modal variation ranging from olivine (orthopyroxene) gabbros similar to crustal layered gabbros, to troctolites to plagioclase-bearing peridotites (Fig. 4.4). This modal variability mainly reflects high olivine contents in samples with diffuse transitions to enclosing dunites at the hand-specimen scale. Moa-Baracoa gabbro sills resemble those described in the Moho transition zone of the Oman ophiolite and interpreted as relics of magmas lenses in the Moho transition zone of fast-spreading mid-ocean ridges (e.g. Boudier and Nicolas 1995; Korenaga and Kelemen 1997). Clinopyroxene in gabbroic sills is 1-5 mm in size and occasionally shows exsolved lamellae of orthopyroxene. <1-2 mm plagioclase grains are interstitial between clinopyroxene and olivine or included within clinopyroxene. Gabbro sills are in general slightly altered, as olivine, and to a lesser extent, clinopyroxene are occasionally affected by a moderate degree of serpentinization; on the other hand plagioclase is often transformed to an aggregate of sericite + epidote. Secondary magnetite, as product of olivine serpentinization, is the only oxide present.

Crustal layered gabbros are composed of olivine gabbros and minor gabbros that are in part orthopyroxene-bearing (Fig. 4.4). The great variability of modal plagioclase is due to a sampling bias related to uneven plagioclase/mafic mineral ratios in the samples. Modal layering (Fig. 4.5c), defined by variations of the mafic mineral/plagioclase ratio, is oriented N30°E dipping 30-50°NW and is broadly parallel to the regional harzburgite tectonite foliation. The contact between the different mafic rocks is transitional. Olivine (0.3-2 mm in size) is dispersed between dominant plagioclase and clinopyroxene (Fig. 4.5d). Clinopyroxene occurs either as 0.7-2 mm anhedral grains or as poikilitic crystals (~ 3 mm) occasionally with exsolved orthopyroxene lamellae. On the basis of textural observations, plagioclase began to crystallize prior to clinopyroxene in these gabbroic rocks.

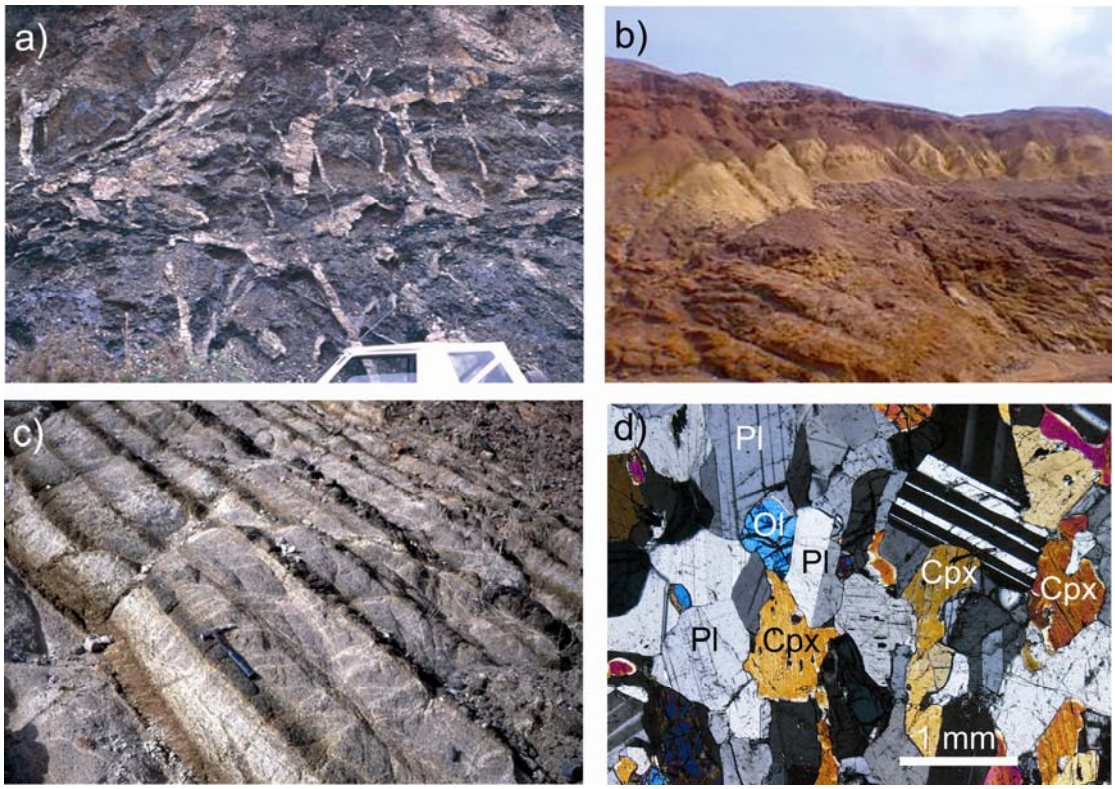

Figure 4.5 a) Intrusive mafic dykes cutting the peridotites in the Moho transition zone of the Moa-Baracoa massif; b) several meters thick gabbroic sill (strongly weathered) intruded in tropical laterite (Moa-Baracoa massif); c) layered crustal gabbros in the Moa-Baracoa massif showing variations of the mafic mineral (clinopyroxene + olivine)/plagioclase modal ratio; d) common texture of crustal gabbros from the Moa-Baracoa massif with minor olivine grains dispersed between dominant plagioclase (Pl) and clinopyroxene (Cpx). Crossed nicols.

4.1.2. The Mayarí–Cristal massif

The Mayarí-Cristal massif is essentially a peridotite massif (> 5 km thick) made up of harzburgite tectonite hosting minor sub-concordant dunite layers and subordinate discordant microgabbro dykes (Fig. 4.1b). Detailed mapping shows the absence of a Moho transition zone and plutonic crustal section. Previous investigators have described the existence of a sheeted-dyke complex in the northwestern part of the massif (Guamuta locality) (Fig. 4.1a). My reconnaissance studies indicate that this complex is a subvolcanic formation made up of massive microgabbros in tectonic contact with harzburgite or occasionally intruding them and does not represent the sheeted-dyke complex characteristic of the customary ophiolitic sequence.

Mayarí-Cristal harzburgites display porphyroclastic texture. They are clinopyroxene-poor and generally have higher orthopyroxene/olivine ratios than Moa-Baracoa harzburgites (Fig. 4.2).

In terms of field occurrence, I differentiate two domains in the western part of the Mayarí-Cristal massif:

1) A northern domain mainly constituted by harzburgite tectonites with a variable (25-55°) NE-SW foliation dipping NW. Dunites are scarce in this region. This domain is characterized by the presence of swarms of microgabbros discordant to the enclosing harzburgite tectonites. Microgabbro dykes are gabbros and minor hornblende-bearing gabbros (Fig. 4.4), with highly variable thickness (from ca. 5 cm to 10 m), and maximum grain size equal to ~ 1 mm decreasing toward the harzburgite wall-rocks. This indicates that, conversely to Moa-Baracoa gabbros, Mayarí-Cristal microgabbro dykes intruded in a relatively cold oceanic mantle lithosphere. Because of the lack of a plutonic crustal section and a Moho transition zone, along with the occurrence of microgabbros intruding tectonites, the northern domain of the Mayarí region resembles the ultramafic exposures described at slow-spreading oceanic ridges, as for the mid-Atlantic ridge (Bonatti et al. 1971; Cannat et al. 1997) and the Mariana Trough (Ohara et al. 2002).

2) A southern domain mainly composed of harzburgite tectonites with a NE-SW oriented foliation dipping 25-60° NW. In this domain highly serpentinized dunites are widespread and generally occur as irregular patches or sub-concordant layers (< 1 m thick) within harzburgite tectonites (Fig. 4.3b). I have also observed thicker dunite bodies (1-3 m) hosting chromitite lenses. As in Moa-Baracoa, the contact between dunites and harzburgite tectonites is sharp. Dunite displays porphyroclastic or equigranular (~ 400 μm grain size) texture. In most of the harzburgites the only phase which is not completely altered is the Cr-rich spinel.

4.1.3. Secondary alteration of the Mayarí-Baracoa peridotites

A general feature of peridotites from the Mayarí-Baracoa Ophiolitic Belt is that they are highly altered. The main alteration type is due to serpentinization. Available stable isotope data indicate that serpentinization occurred by ingression of seawater during the oceanic stage of MBOB peridotites (Proenza et al. 2003). Moa-Baracoa peridotites show variable degrees of serpentinization ranging from 60 to 90 vol.% in most samples, and serpentinization in Mayarí-Cristal peridotites is pervasive especially in those from the southern domain. The imprints of serpentinite alteration on MBOB peridotites are the transformation of olivine to lizardite-magnetite assemblages displaying mesh (Fig. 4.6) and rare non-pseudomorphic textures, and the alteration of orthopyroxene to pseudomorphic (bastite) (Fig. 4.3a) and non-pseudomorphic serpentine and, locally, to talc. Conversely, spinel is virtually fresh in all samples and only exhibits thin rims of

ferrichromite. In addition to serpentine-group minerals, clay minerals were also detected by X-Ray diffraction in most of the samples. Finally, MBOB peridotites usually display a thick reddish crust of sub-aerial iron oxide and clay minerals owing to tropical weathering, and minor carbonate veins. The studied samples lack pervasive talc alteration.

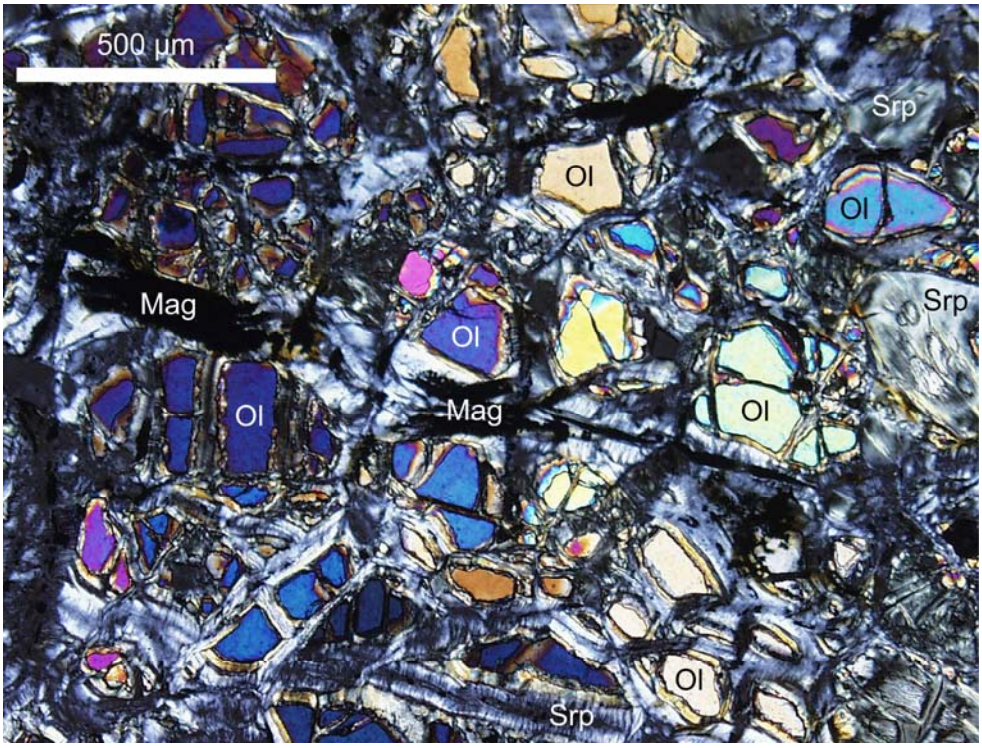

Figure 4.6 Pseudomorphic mesh texture in dunite from the Mayarí-Cristal southern massif. Olivine shows intense transformation to serpentine (Srp)-magnetite (Mag) assemblages Crossed nicols.

4.2. SAMPLING

For this study I selected 62 samples that are representative of the main lithological types of the Mayarí-Baracoa Ophiolitic Belt. The location of the selected specimens is depicted in Figure 4.1a. I took particular care in collecting mantle rocks far from chromite ore deposits in order to exclude samples potentially affected by magmatic processes related to ore genesis. Peridotite samples (n = 16) from the Moa-Baracoa massif are 9 harzburgites, 1 dunite and 6 impregnated dunites from the Cayo Guam and Yamaniguey localities. Gabbroic samples (n = 33) from the Moa-Baracoa massif comprise: different types of gabbros (n = 15) from the crustal section in Quemado del Negro; sills of olivine gabbros (n = 10), troctolite (n = 1) and werhlite (n = 1) in the Moho transition zone from Yamaniguey, Cayo Guam, Mercedita and Amores localities; and intrusive dykes of olivine gabbros (n = 4), troctolite (n = 1) and werhlite (n = 1) in the Moho transition zone from

Cayo Guam and Mercedita sections. Samples from the Northern Mayarí-Cristal massif encompass 4 harzburgites and 2 gabbroic dykes from Loma de la Bandera. Samples of dunite are not available because of the virtual absence of this lithotype in the Northern Mayarí-Crystal massif. Peridotites from the Southern Mayarí-Crystal massif are 4 harzburgites and 3 sub-concordant dunites from Loma Estrella de Mayarí, Loma Arroyo Seco and Casimba sections.

4.3. MINERAL CHEMISTRY

Mineral compositions of the different lithotypes are given in tables of Appendix 1 at the end of this study.

4.3.1. Peridotites

In Moa-Baracoa harzburgite, the Mg# [100·Mg/(Mg+Fe^{2+})] of olivine and the Cr# [Cr/(Cr+Al)] of spinel vary between 90.3-90.9 (Fig. 4.7a) and 0.45-0.55 (Fig. 4.7b), respectively. Orthopyroxene has an average Mg# = 91.0 and Al_2O_3 = 2.4 wt%. Mg# of olivine in Moa-Baracoa dunite (90.7-91.5) is slightly higher than that of harzburgite, whereas Cr# of spinel is similar (0.51-0.52). Moa-Baracoa impregnated dunite has olivine with lower Mg# (88.7-90.0) and spinel with slightly higher Cr# (up to 0.59) than the other peridotites from the Moa-Baracoa massif; spinel also shows significant enrichment in FeO and mainly in TiO_2 (1.3-2.0 wt%) (Fig. 4.7d, e). Secondary clinopyroxene in impregnated dunite exhibits Mg# ranging from 88.6 to 91.6, and average Al_2O_3 = 3.5 wt% and TiO_2 = 1.3 wt%.

Owing to pervasive serpentinization, I was unable to analyze olivine and orthopyroxene in Mayarí-Cristal harzburgites. Spinel exhibits generally higher Cr# (from 0.53 to 0.67) (Fig. 4.7b) than that from Moa-Baracoa harzburgite in particular in the southern tectonites, where it is also enriched in FeO (Fig. 4.7d). The Mg# of olivine in Mayarí-Cristal dunites ranges from 91.9 to 92.4 (Fig. 4.7a); spinel displays Cr# that varies between 0.59-0.75 (Fig. 4.7b) and TiO_2 (average value = 0.12 wt%) notably higher than in peridotites from the other regions of the MBOB (Fig. 4.7e).

The range of olivine Mg# in MBOB peridotites overlaps that of both ocean ridge and supra-subduction zone peridotites (Fig. 4.7a) and more generally fits in the data commonly reported for mantle rocks. This is also true for the Cr# of spinel except for the high values displayed by peridotites from the Southern Mayarí-Cristal massif that are characteristic only of spinel from supra-subduction settings (Fig. 4.7b) (Pearce et al. 2000).

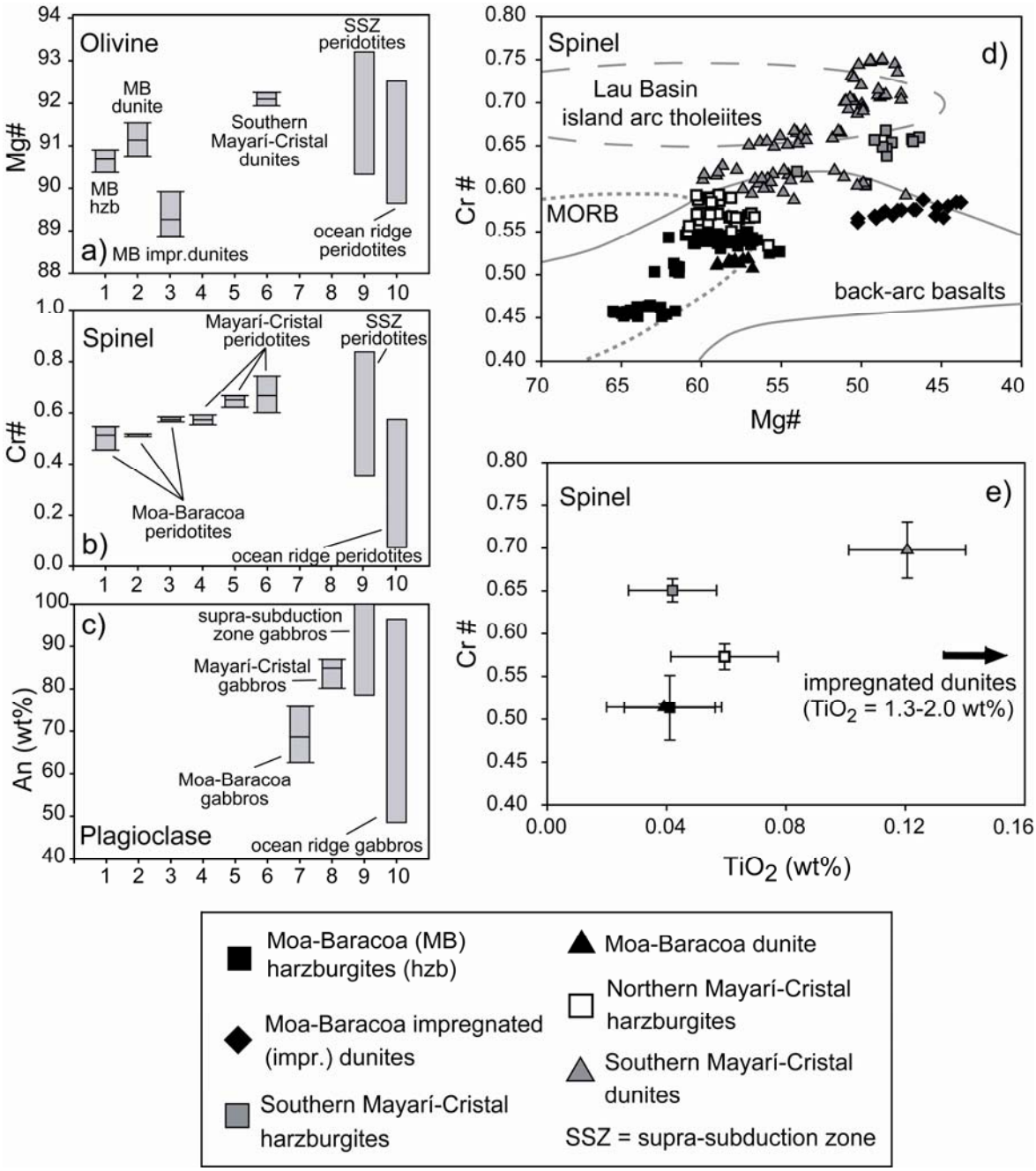

Figure 4.7 a) Mg# ranges of olivine from MBOB peridotites; b) Cr# ranges of chromian spinel from MBOB peridotites; c) Anorthite content (wt%) of plagioclase from MBOB gabbros. Horizontal bar within columns marks the average value. 1 = Moa-Baracoa (MB) harzburgites (hzb); 2 = Moa-Baracoa dunite; 3 = Moa-Baracoa impregnated (impr.) dunites; 4 = Mayarí-Cristal northern harzburgites; 5 = Mayarí-Cristal southern harzburgites; 6 = Mayarí-Cristal southern dunites; 7 = Moa-Baracoa gabbros; 8 = Mayarí-Cristal gabbro dykes; 9 = supra-subduction zone (SSZ) peridotite or gabbro (in c); 10 = ocean ridge peridotite or gabbro (in c). Data of columns 9 and 10 are from Pearce et al. (2000) and Beard (1986) (in c), and references therein. d) Cr# *vs* Mg# of chromian spinel from MBOB mantle peridotites. Fields for MORB, back-arc basalts and Lau basin island arc tholeiites are from Metzger et al. (2002), and references therein. e) Average Cr# *vs* average TiO_2 (wt%) content of chromian spinel from MBOB mantle peridotites; bars represent standard deviations from average values. Symbols as in Figure 4.2.

4.3.2. Gabbros

Olivine, orthopyroxene and clinopyroxene in gabbroic rocks from the Moa-Baracoa massif exhibit Mg# values (74.0-82.6 in olivine, 77.4-82.7 in orthopyroxene and 78.8-91.7 in clinopyroxene) comparable to similar ophiolitic (e.g. Korenaga and Kelemen 1997) and oceanic gabbroic rocks. Anorthite (An) content in plagioclase varies between 63-71, 68-70 and 67-76 wt% in sills, dykes and crustal layered gabbros, respectively (Fig. 4.7c).

Clinopyroxene in mafic dykes from the Mayarí-Cristal northern domain exhibits a Mg# average value = 81.2. Plagioclase is remarkably richer in Ca (An_{80-87}) compared to Moa-Baracoa gabbroic rocks (Fig. 4.7c).

The anorthite content of plagioclase in Moa-Baracoa gabbros is characteristic of gabbros crystallized at ocean spreading centres (An = 48-97 wt%, according to Beard 1986), whereas that of plagioclase from Mayarí-Cristal gabbro dyke is compatible with both ocean ridge and arc setting (An = 78-100 wt%, according to Beard 1986) (Fig. 4.7c).

4.4. WHOLE ROCK GEOCHEMISTRY

Whole rock compositions of the studied samples are given in tables of Appendix 2.

4.4.1. Peridotites

The analysed major oxide totals of the Mayarí-Baracoa peridotites range from 82 to 95 wt% indicating significant addition of volatile components during alteration. Owing to the lack of mineral analyses for all mineral phases, I was unable to reconstruct the major element whole rock compositions combining modes and mineral chemistry as customarily done for abyssal peridotites(1) (e.g. Dick 1989; Niu et al. 1997; Baker and Beckett 1998; Asimow 1999).

MBOB peridotites show low Al_2O_3 contents (< 1.2 anhydrous wt%) and are highly refractory mantle rocks (Fig. 4.8a, b, c); in particular, the southern Mayarí-Cristal samples exhibit the lowest Al_2O_3 abundances (Fig. 4.8d, e, f). SiO_2 and (to a lesser extent) FeOt contents are higher than values usually reported for oceanic peridotites (Fig. 4.8a, b). As generally noted for mantle tectonites (e.g. Bodinier and Godard 2003) the Al_2O_3 content of MBOB peridotites is correlated with TiO_2 (Fig. 4.8f) and Yb (Fig. 4.9). Impregnated dunites plot out of these trends most likely owing to peridotite refertilization.

(1) Primary whole rock compositions of peridotites can be reconstructed exploiting the mineral modes converted to weight fractions (f_j) and the mineral analyses by the following formula:

$Ox_i^{wr} = \Sigma^n_{j=1} f_j \cdot Ox_i^j$ where the subscript "i" refers to oxides and "j" refers to mineral phases

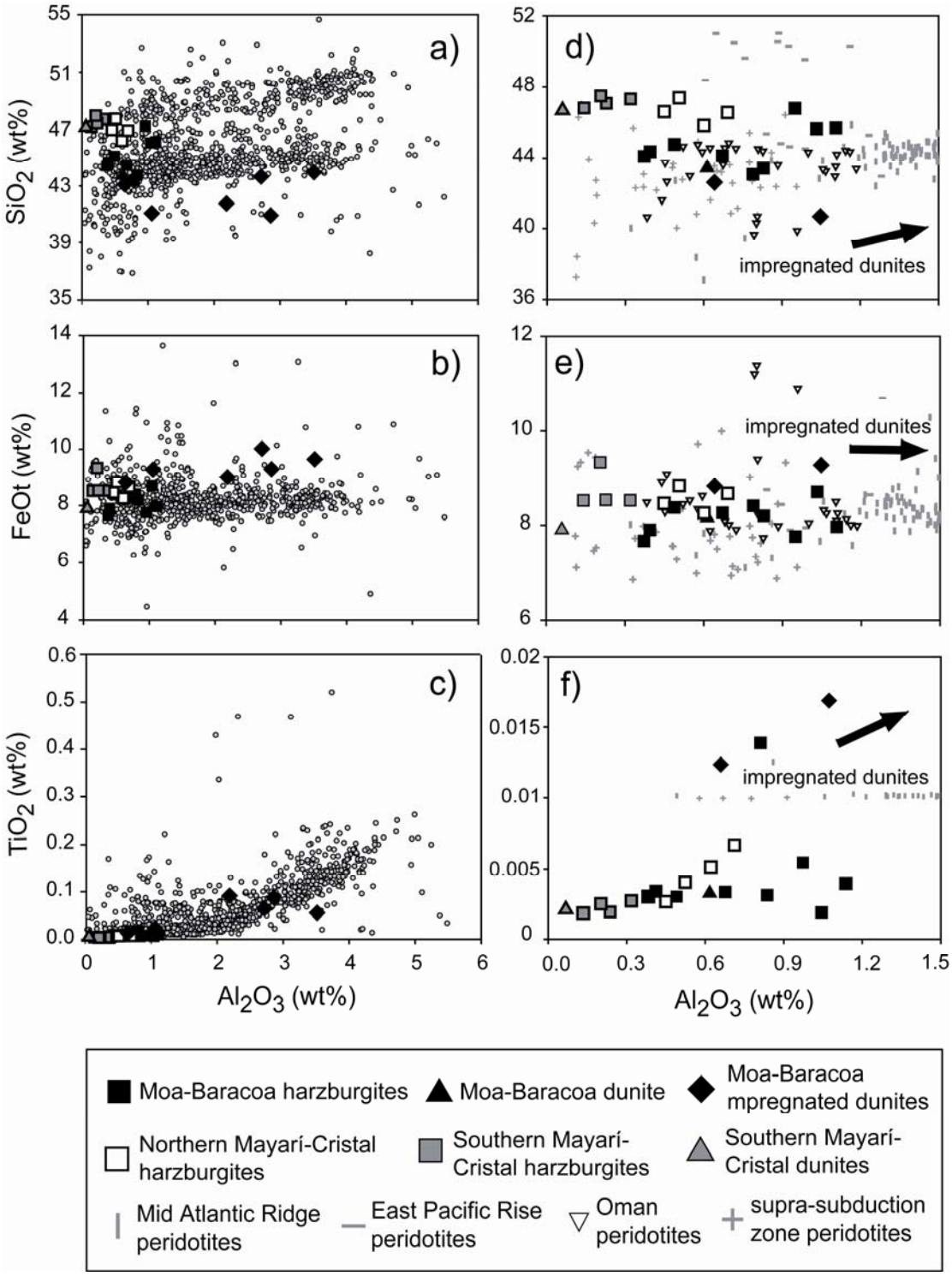

Figure 4.8 Whole rock abundances of Al_2O_3 *vs* SiO_2 (a), FeOt (b), and TiO_2 (c) in Mayarí-Baracoa ultramafics and published data (grey circles) for peridotites from different tectonic settings (Bodinier and Godard 2003, and references therein). d), e), f) Enlarged area of previous plots in order to display MBOB data in more details. All data on anhydrous basis in wt%. Symbols for MBOB ultramafics as in Figure 4.2. Vertical bars: Mid Atlantic Ridge peridotites (Bonatti et al. 1971; Shibata and Thompson 1986; Casey 1997). Horizontal bars: East Pacific Rise peridotites (Constantin 1995; Niu and Hékinian 1997). White triangles down: Oman ophiolite peridotites (Godard et al. 2000). Crosses: supra-subduction zone peridotites (Parkinson and Pearce 1998; Pearce et al. 2000).

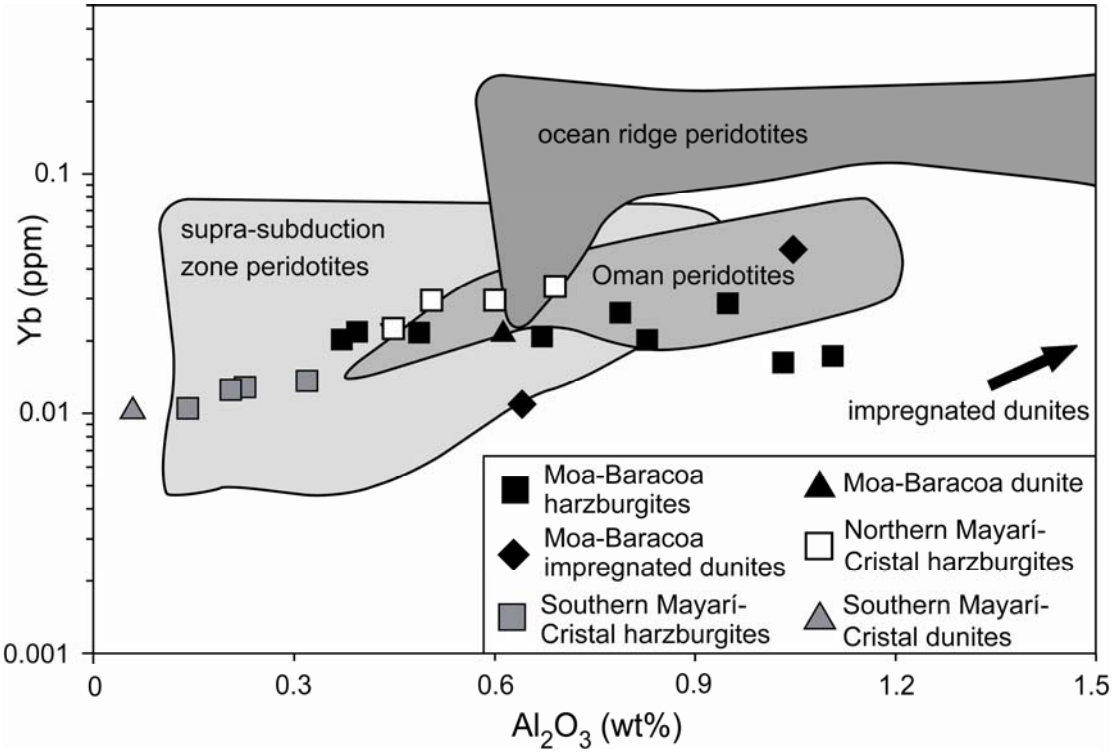

Figure 4.9 Yb (ppm) *vs* Al_2O_3 (anhydrous wt%) whole rock contents of Mayarí-Baracoa peridotites. Published data are displayed for comparison: supra-subduction zone peridotite field from Parkinson and Pearce (1998) and Pearce et al. (2000); Oman ophiolite peridotite field from Godard et al. (2000); ocean ridge peridotite field from Bonatti et al. (1971), Shibata and Thompson (1986), Casey (1997), Constantin (1995), Niu and Hékinian (1997). Symbols for Mayarí-Baracoa ultramafics as in Figure 4.2.

The chondrite-normalized rare earth element (REE) patterns of the MBOB ultramafics are displayed in Figure 4.10. The rock/chondrite REE concentrations for the peridotites are very low, ranging between 0.002-0.05 and 0.005-0.3 for LREE and HREE respectively. The patterns have strikingly homogenous HREE contents and are characterized by relatively flat LREE and steep HREE fractionated segments. These REE patterns are similar to those of supra-subduction peridotites from Izu-Bonin-Mariana forearc (Parkinson and Pearce 1998) (Fig. 4.10a, b) and to those of the most depleted harzburgites from Oman ophiolite (Godard et al. 2000). The peridotites from the Mayarí-Cristal southern domain are depleted in MREE and HREE compared to the northern one, whereas those from the Moa-Baracoa massif have generally intermediate concentrations. Comparing these results with those published by Proenza et al. (1999b) on the Mayarí-Baracoa peridotites associated with chromite ore deposits, the samples of this study display significantly lower LREE and MREE and nearly identical HREE contents. The impregnated dunites from Moa-Baracoa massif exhibit higher REE contents than the other ultramafics and generally flat patterns occasionally associated with a positive anomaly in

Eu (Fig. 4.10c). These patterns are consistent with secondary precipitation of clinopyroxene and plagioclase in variable amounts.

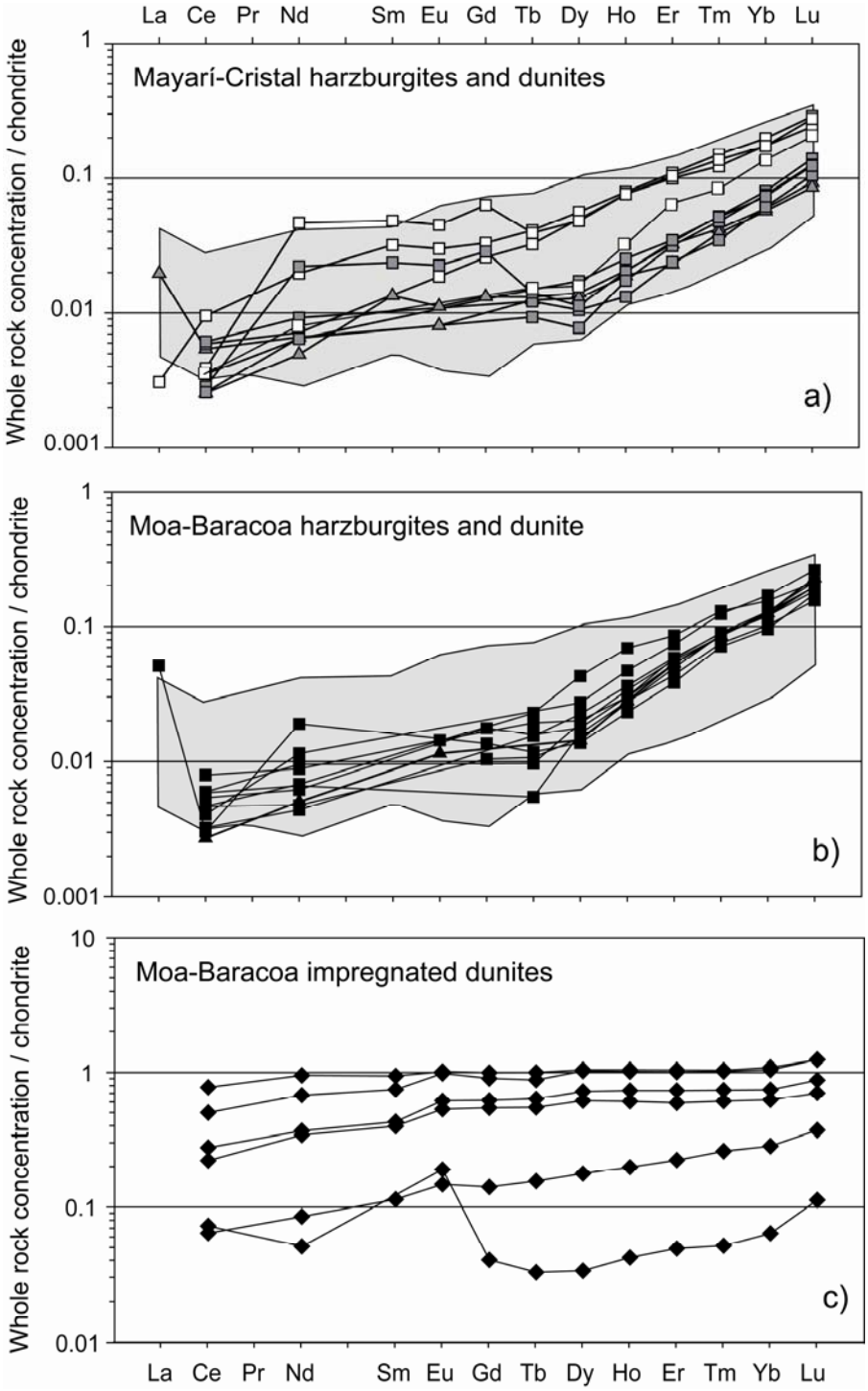

Figure 4.10 Chondrite-normalized abundances of REE in Mayarí-Baracoa peridotites (whole rock analyses). Symbols as in Figure 4.2. Normalizing values from Sun and McDonough (1989). Light grey shaded area in (a) and (b) encloses composition range of supra-subduction zone peridotites from Izu-Bonin-Mariana forearc (Parkinson and Pearce 1998).

The distribution of incompatible trace elements (Cs, Rb, Th, U, Nb, Ta, REE, Sr, Zr and Hf) normalized to primitive mantle for MBOB ultramafics is shown in Figure 4.11.

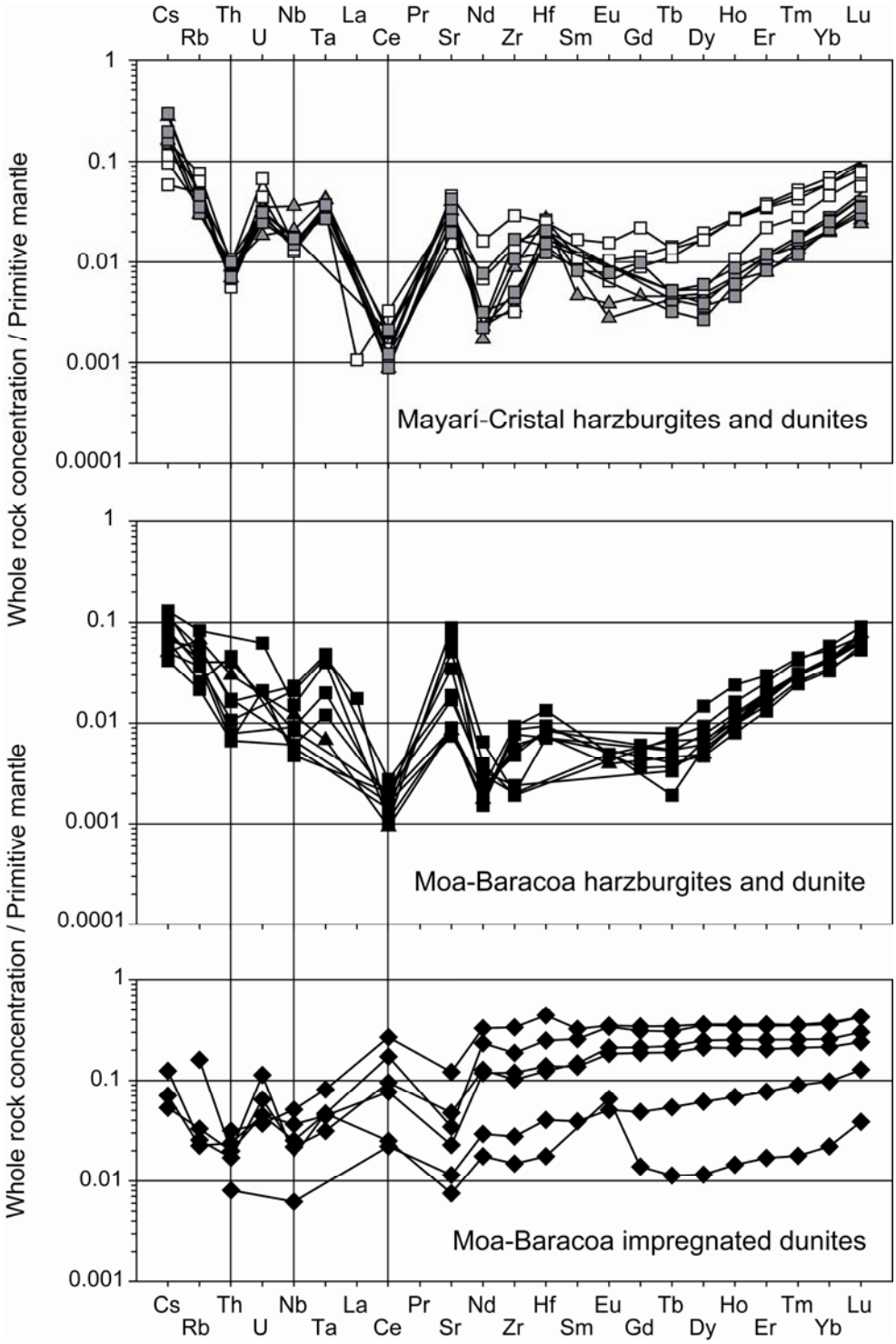

Figure 4.11 Primitive mantle-normalized trace element patterns of Mayarí-Baracoa peridotites (whole rock analyses). Symbols as in Figure 4.2. Normalizing values from Sun and McDonough (1989).

MBOB peridotites are highly depleted in terms of lithophile trace elements. Nevertheless, they exhibit variable relative enrichment in the most incompatible trace elements (Cs to Ta) and low LREE/HREE fractionation. Sr shows a positive spike particularly prominent for Moa-Baracoa peridotites. Zr and Hf are commonly enriched relative to LREE. Mayarí-Cristal tectonites are more depleted in Th and richer in Zr and Hf than Moa-Baracoa ones. Impregnated dunites exhibit higher average content in lithophile elements (except for Cs, Rb, Th and Sr) and flatter normalized patterns than the other ultramafics. Cs, Rb, U and Sr are commonly considered highly mobile during alteration of mantle rocks (Niu 2004) and their budgets are generally believed to be affected by late circulation of aqueous solutions; for this reason these elements will not be treated in the following discussion. Nevertheless it should be noted that all MBOB peridotites lack the high U/Th ratios indicative of low-temperature oxidative alteration (Pearce et al. 2000).

4.4.2. Gabbros

The degree of alteration of the Mayarí-Baracoa sills, dykes and layered gabbros is rather variable as suggested by LOI values and generally higher in sills and dykes than in crustal layered gabbros. Among the samples from Moa-Baracoa massif, sills and dykes are richer in MgO and poorer in SiO_2, Al_2O_3 and CaO than layered gabbros (Fig. 4.12). One studied dyke from the Mayarí-Cristal massif has a whole rock composition similar to those of Moa-Baracoa samples, whereas the other shows higher CaO related to the abundance of primary calcic-amphibole; this dyke is also enriched in TiO_2 (1.2 anhydrous wt%) because of the abundance of Ti oxide and amphibole.

The chondrite-normalized REE patterns of Moa-Baracoa layered gabbros display LREE-depleted to relatively flat REE patterns with homogenous LREE contents, sharp positive Eu anomalies, and variable HREE contents (Fig. 4.13a). These patterns suggest that gabbros are cumulates from variably fractionated melts (Kelemen et al. 1997a). MBOB sills and dykes are characterized by depleted or flat LREE concentrations, variable positive Eu anomalies, and generally flat HREE segments (Fig. 4.13b, c). One exception to this general trend is represented by the slight negative anomaly in Eu exhibited by the amphibole-rich dyke from the Mayarí-Cristal massif (Fig. 4.13d).

Figure 4.14 shows the distribution of lithophile trace elements normalized to primitive mantle for the MBOB sills, dykes and layered gabbros. All samples, except of the amphibole-bearing dyke from Mayarí-Cristal massif, exhibit a positive Sr spike. Moa-Baracoa crustal layered gabbros display quite homogeneous patterns. They are characterized by positive spikes for Rb and regular enrichment from Th to Sr; the gabbros

from the lower region of the crustal section differ from the others for lower contents in Rb. Moa-Baracoa sill patterns are relatively depleted in Th and Zr and show a steady enrichment towards the more compatible elements. MBOB dykes display flat patterns, characterized by positive anomalies in Cs and relative depletion in Th, U and Nb; only the amphibole-bearing dyke from the Mayarí-Cristal massif differs from this trend.

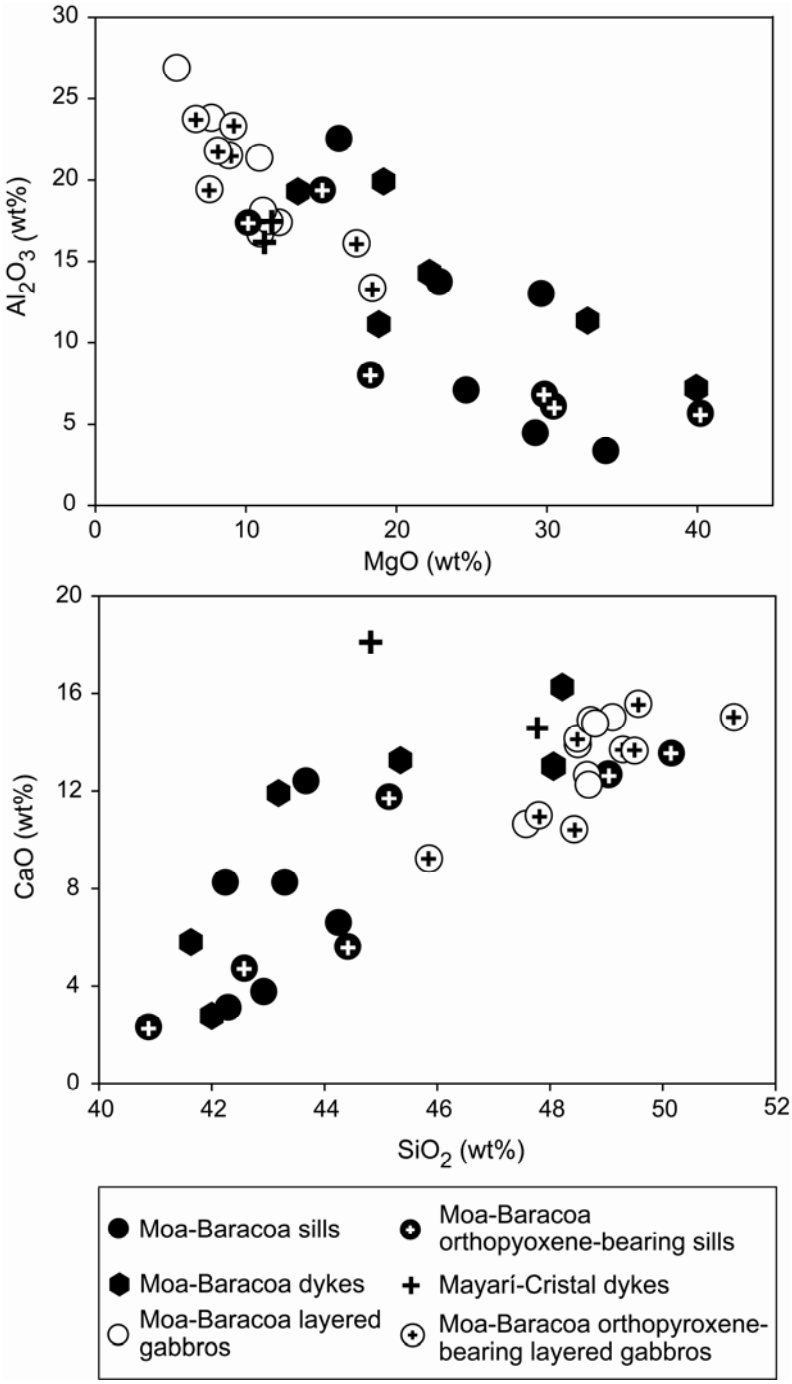

Figure 4.12 Whole rock major element compositions of Mayarí-Baracoa sills, dykes and layered gabbros illustrated by Al_2O_3 *vs* MgO and CaO *vs* SiO_2. All data on anhydrous basis in wt.%. Symbols as in Figure 4.4.

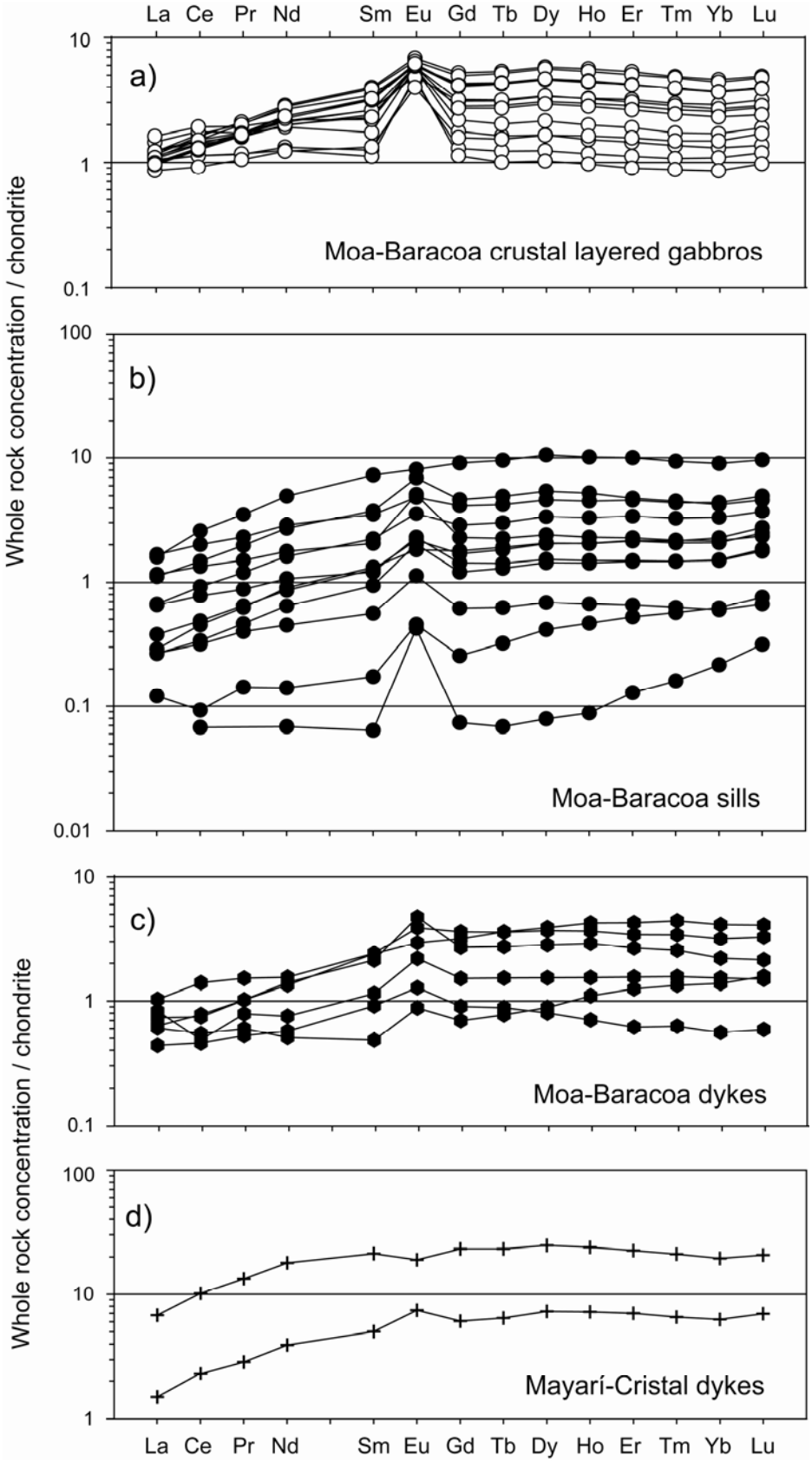

Figure 4.13 Chondrite-normalized REE patterns of Mayarí-Baracoa sills, dykes and layered gabbros (whole rock analyses). Symbols as in Figure 4.4. Normalizing values from Sun and McDonough (1989).

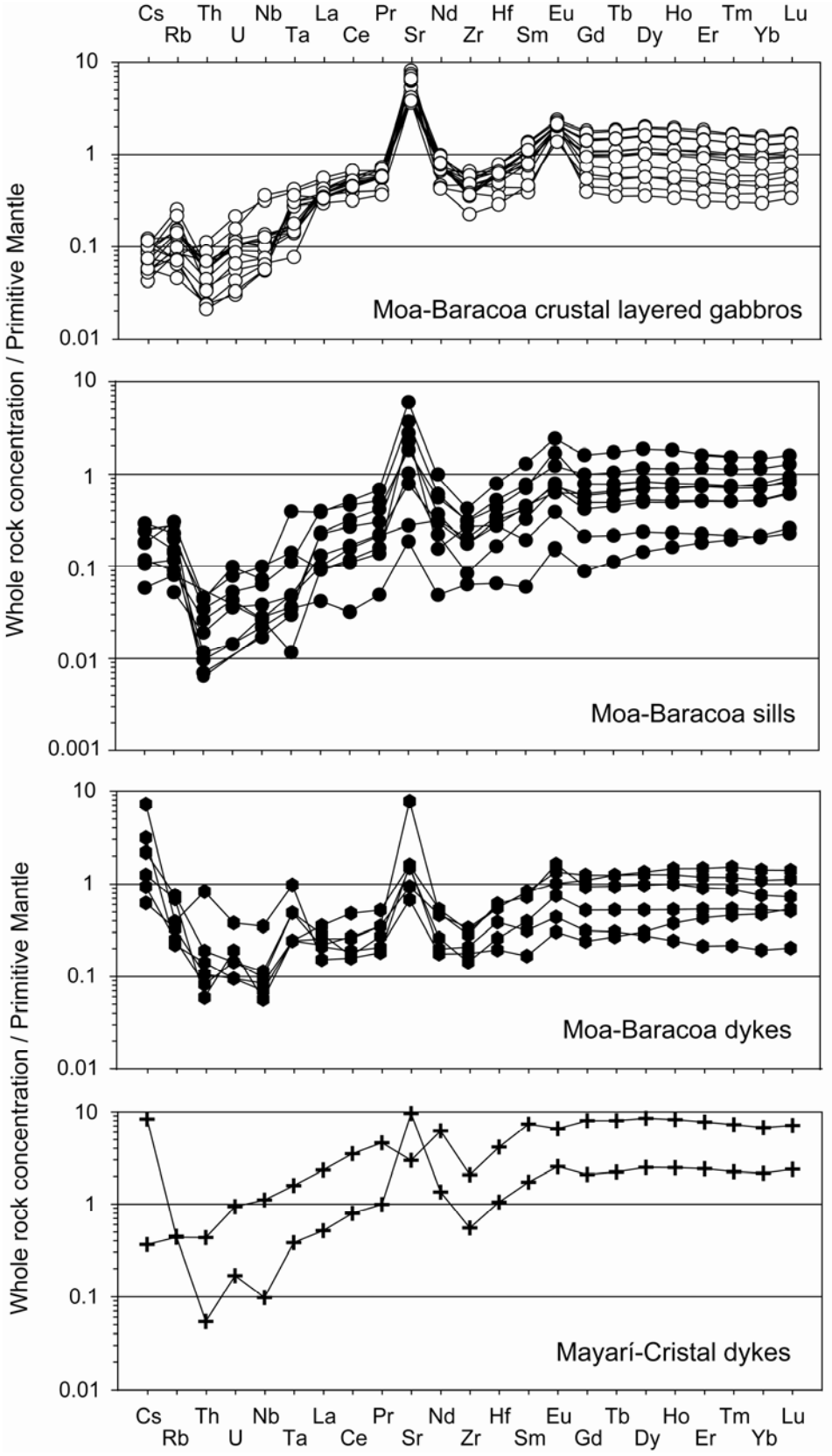

Figure 4.14 Primitive mantle-normalized trace element patterns of Mayarí-Baracoa sills, dykes and layered gabbros (whole rock analyses). Symbols as in Figure 4.4. Normalizing values from Sun and McDonough (1989).

4.5. DISCUSSION

4.5.1. Origin of the highly depleted signature and low bulk MgO/SiO_2 ratio in the Mayarí-Baracoa peridotites

MBOB harzburgites exhibit a highly depleted signature in terms of their modal compositions and whole rock contents in major and incompatible trace elements, suggesting that they are residues after high extents of partial melting. The highly residual character of MBOB harzburgites is attested by: (1) their lack of primary clinopyroxene or its alteration relics (Fig. 4.2); (2) their very low whole rock Al_2O_3 ($0.14 < Al_2O_3$ anhydrous wt% < 1.11) and HREE ($0.06 < Yb_{(N)} < 0.2$, normalized to chondrite composition) contents which are only comparable to those of supra-subduction and highly depleted ophiolitic and ocean ridge peridotites (Fig. 4.9); and (3) their very low abundances in lithophile trace elements which are well below primitive mantle values (Fig. 4.11). This refractory character has been also confirmed by Gervilla et al. (2005), who demonstrated that the Os isotopic signature of MBOB chromite ores indicates a highly depleted mantle source.

Figure 4.15 shows the V *vs* Yb diagram for the Mayarí-Baracoa peridotites. V and Yb are reputed immobile during alteration processes (Niu 2004) and they have been successfully used as proxies to infer the prevailing conditions of oxygen fugacity and the degree of partial melting in mantle peridotites (Pearce et al. 2000; Lee et al. 2003; Canil 2004 and references therein). When compared to the curves calculated for near-fractional melting of spinel peridotite at different conditions of oxygen fugacity (Pearce et al. 2000), the compositions of MBOB peridotites are consistent with 20-30% near-fractional melting at fO_2 varying between $-1 <$ QFM < 1 (Fig. 4.15). This not only confirms the highly residual nature of MBOB peridotites, but also suggests that fO_2 conditions prevailing during melting are similar to those of both ocean ridge and Izu-Bonin-Mariana forearc peridotites (cf. Fig. 1 of Lee et al. 2003). I remark that the composition of southern Mayarí-Cristal peridotites (dark-grey symbols in Fig. 4.15) is consistent with higher extents of melt extraction (> 25%) and slightly higher average fO_2 than other MBOB peridotites.

Except for impregnated dunites, most MBOB peridotites plot below the terrestrial mantle array (Jagoutz et al. 1979; Hart and Zindler 1986) in the MgO/SiO_2 *vs* Al_2O_3/SiO_2 diagram (Fig. 4.16a). This departure from the mantle array trend is specially marked for Mayarí-Cristal peridotites that display the lowest MgO/SiO_2 ratios. Thus, for most MBOB harzburgites different partial melting scenarios fail to explain their low MgO/SiO_2 ratio (Fig. 4.16a) and their unusually high SiO_2 and FeOt contents for a given Al_2O_3/SiO_2 ratio (Fig. 4.16b, c). Low MgO/SiO_2 ratios in such altered peridotites may be caused by MgO loss

during seafloor weathering (Snow and Dick 1995; Niu 2004). Assuming that the primary MgO/SiO_2 ratios laid on the mantle array and the Al_2O_3/SiO_2 ratios were not perturbed by alteration (cf. Snow and Dick 1995; Niu 2004), I can estimate the MgO loss underwent by MBOB peridotites. The difference between recalculated (open symbols in Fig. 4.16) and actual compositions (dark-grey symbols) implies relative MgO loss of about 6 wt% on average, which is consistent with previous Mg-loss estimates for highly altered abyssal peridotites (Niu 2004). Unlike actual values, the recalculated compositions of Mayarí-Baracoa peridotites have SiO_2 contents that are consistent with high extents of partial melting at low to moderate pressures (Fig. 4.16b). However, the recalculated compositions have unusually high FeOt contents to be residues of partial melting. Ocean ridge peridotites also display higher FeOt contents than those predicted by partial melting models (Niu 1997; Asimow 1999), and these variations are usually interpreted as due to olivine addition after melting (Niu 1997). Alternatively, Herzberg (2004) states that high FeOt and low MgO/SiO_2 ratios are characteristic of supra-subduction peridotites.

I hence conclude that, even if primary SiO_2 enrichment (e.g. Kelemen et al. 1992, 1998; Walter 2003) can not be fully ruled out for two southern Mayarí-Cristal harzburgites that show rather high abundances in modal orthopyroxene (Fig. 4.2), the good concordance between the recalculated compositions and the predictions of melting models supports that MBOB peridotites are highly depleted peridotites that lost MgO as a consequence of seafloor weathering.

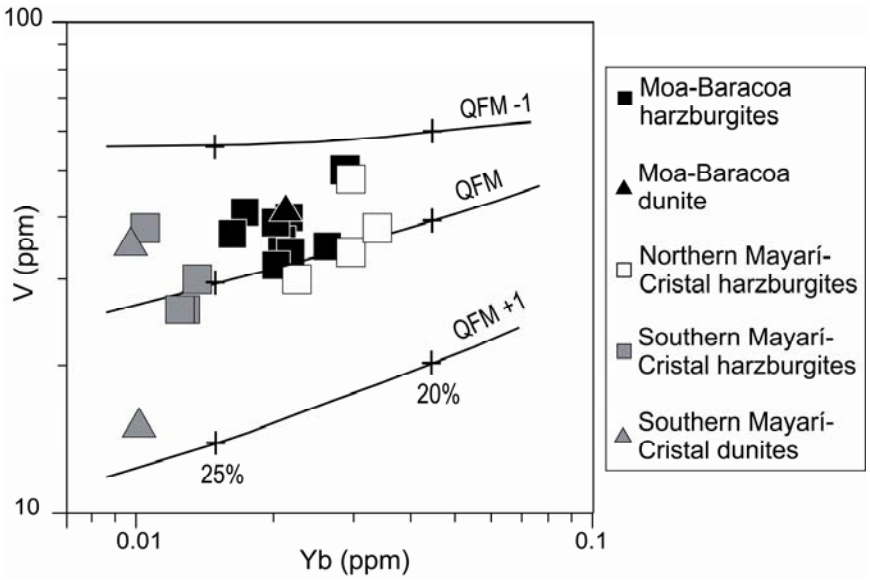

Figure 4.15 V-Yb (ppm) whole rock contents of Mayarí-Baracoa mantle peridotites. Modelling of melting extraction and oxygen fugacities from Pearce et al. (2000), and references therein. fO_2 expressed as log-unit deviations from QFM; QFM = quartz-fayalite-magnetite buffer. Symbols as in Figure 4.2.

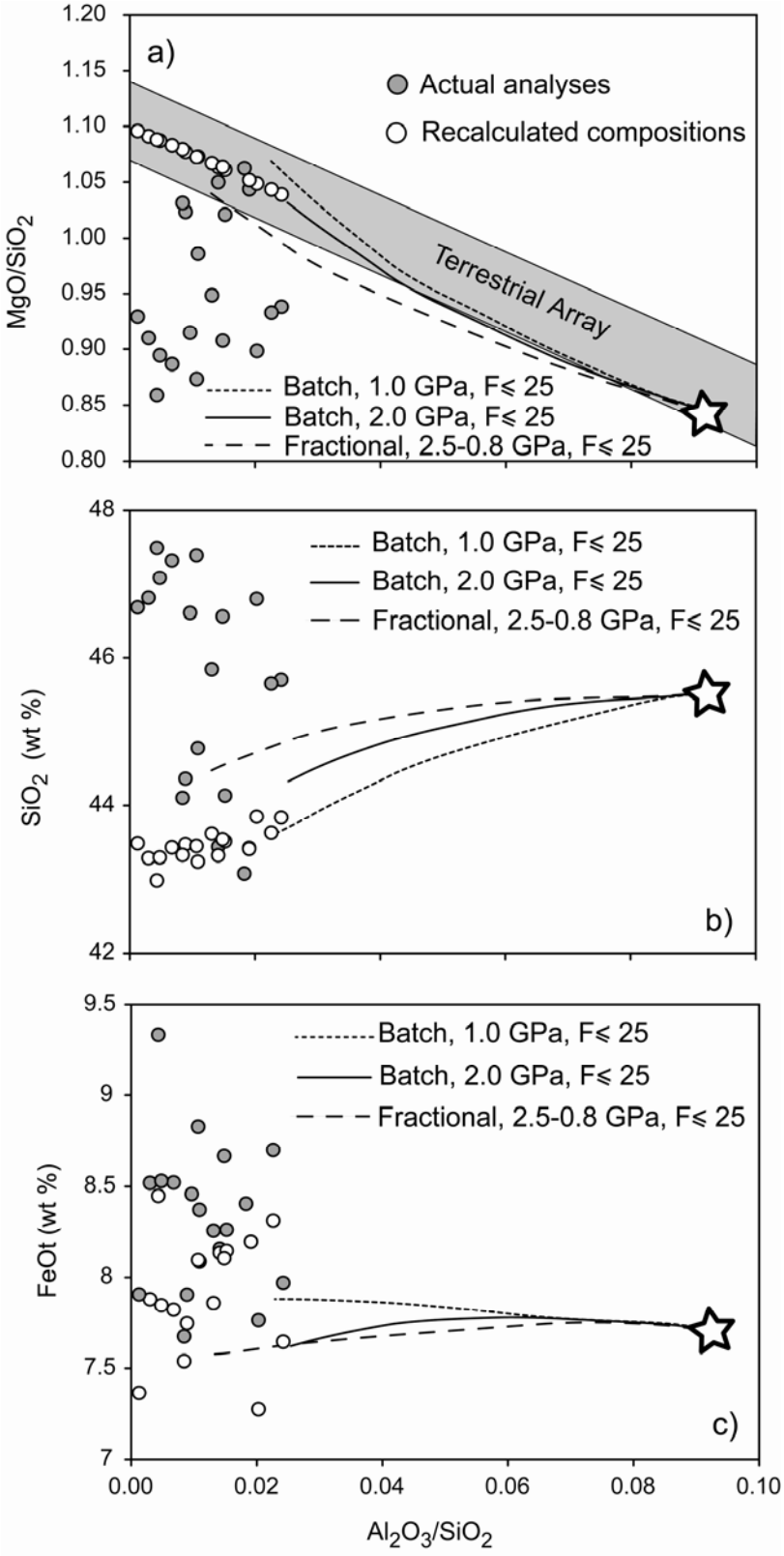

Figure 4.16 Comparison between actual bulk-rock analyses (dark-grey circles) and recalculated bulk rock compositions after MgO addition (open circles) for MBOB peridotites on Al_2O_3/SiO_2 *vs* MgO/SiO_2 (a), SiO_2 (b), FeOt (c). All data on anhydrous basis in wt%. Terrestrial array in (a) from Jagoutz et al. (1979) and Hart and Zindler (1986). Curves of polybaric near-fractional and isobaric batch melting of fertile mantle source (star) redrawn from Niu (1997).

4.5.2. Evidences of melt/ rock interaction in the Mayarí-Baracoa peridotites

As attested by modal compositions and major element contents, the overall low amount of lithophile trace elements is consistent with the highly residual character of the Mayarí-Baracoa peridotites. Nevertheless, their U-shaped Primitive Mantle normalized patterns (Fig. 4.11) display low LREE/HREE fractionation and variable enrichment in Nb and Ta relative to neighbouring elements indicating that these peridotites are not simply partial melting residues.

Enrichment in most incompatible trace elements is usually observed in oceanic and subcontinental peridotites (e.g. Bodinier and Godard 2003 and references therein) and may be due to alteration or primary mantle processes. However, it is unlikely that LREE are mobilized by fluids during serpentinization and seafloor weathering as they show positive correlation with immobile high field strength elements in strongly altered abyssal peridotites (Niu 2004). Moreover, highly incompatible trace elements commonly reputed immobile (Th, Nb and Ta) also exhibit relative enrichment in MBOB peridotites. This cannot be ascribed to secondary remobilization but is most likely due to mantle processes.

Mayarí-Baracoa peridotites display REE patterns similar to Oman (Godard et al. 2000) and Izu-Bonin-Mariana peridotites (Parkinson and Pearce 1998), both interpreted as portions of lithospheric mantle re-equilibrated with percolating melts during melt transport by reactive porous flow (e.g. Navon and Stolper 1987; Bodinier et al. 1990; Vernières et al. 1997). Additionally, in MBOB peridotites Nb and Ta are generally enriched relative to Th and LREE (average $(Nb/Th)_{PM}$ = 1.7; $(Nb/Ce)_{PM}$ = 10.5, normalized to primitive mantle composition) conversely to what is observed in oceanic abyssal peridotites (Niu 2004). This characteristic has already been remarked for MBOB peridotites as well as for Oman and Ronda peridotites (Bodinier and Godard 2003 and references therein). Selective enrichment in Nb and Ta may be related to chromatographic interaction between migrating melts and mantle peridotite (Kelemen et al. 1993) or to precipitation of Nb-rich rutile from volatile-rich magmas (Bodinier et al. 1996; Garrido et al. 2000) that may lead to corresponding depletion of Nb and Ta in ascending melts as peculiar to arc lavas.

4.5.3. Genesis of dunite in the Mayarí-Baracoa Ophiolitic Belt

There is an increasing consensus among mantle petrologists on the replacive origin of dunite. Dunites in the Moho transition zone are thought to be formed by pervasive melt/rock reaction of residual harzburgite tectonites with incoming olivine-saturated

basaltic melts at the thermal boundary layer represented by the MTZ (ca. 1280 ^{o}C) (Boudier and Nicolas 1995; Kelemen et al. 1997b and references therein; Kelemen and Aharonov 1998; Jousselin and Nicolas 2000; Godard et al. 2000; Bodinier and Godard 2003). Likewise, sub-concordant dunite lenses in the deep mantle section of ophiolites are interpreted as dissolution channels for focused melt flow under adiabatic asthenospheric conditions (Kelemen et al. 1995, 1997b).

The field, textural and compositional characteristics of Moa-Baracoa MTZ dunite point to a replacive origin as other MTZ dunites in ophiolites. The olivine Mg# of Moa-Baracoa MTZ dunite broadly overlaps that of harzburgite tectonite (Fig. 4.7a) as expected in dunite formed by melt/peridotite reactions at constant melt/rock ratios (Kelemen et al. 1997b; Bodinier and Godard 2003 and references therein). The TiO_2 content of spinel is a proxy for integrated melt/rock ratio during formation of dunite (Kelemen et al. 1995; Arai and Matsukage 1996; Matsumoto and Arai 2001). The coincident TiO_2 content of Moa-Baracoa dunite and harzburgite (Fig. 4.7e) supports a replacive origin of MTZ dunite at constant melt/rock ratios. On the other hand, impregnated dunites show very high TiO_2 content (up to 2 wt%) indicating formation of these dunites at decreasing melt/rock ratio. This led to precipitation of clinopyroxene and plagioclase locally forming werhlite and troctolite. Impregnated dunite hence records a refertilization of MTZ dunite resulting in an increase of TiO_2 and Al_2O_3 contents (Fig. 4.8c).

Sub-concordant dunite in southern Mayarí-Cristal massif shows unusually high olivine Mg# (Fig. 4.7a). This feature is indicative of dunites formed by melt extraction and/or melt-rock reaction at increasing melt mass. Kubo (2002) suggested that dunite with high olivine Mg# may be derived from harzburgite by the ingress of a hydrous basaltic melt leading to incongruent melting of orthopyroxene in a mantle wedge environment. The higher FeO and TiO_2 content of spinel in southern Mayarí-Cristal dunite relative to Moa-Baracoa dunite (Fig. 4.7d, e) may imply a different parental melt formed the Mayarí-Cristal dunite. However, more data on mineral chemistry of Mayarí-Cristal dunites are needed to better constrain their petrogenesis.

4.5.4. Genetical relationships between gabbroic cumulates and volcanic rocks

The Mg# of olivine (≤ 82) in MBOB gabbros and the strong positive Eu (and Sr) anomalies of their normalized patterns (Fig. 4.14) indicate that they are cumulitic rocks crystallized from mantle-derived basaltic melts. A similar origin has been proposed for the MTZ gabbro sills and lower crustal gabbros in the Oman ophiolite (Pallister and Knight 1981; Kelemen et al. 1997a; Korenaga and Kelemen 1997), as well as for gabbroic rocks in

Troodos and Bay of Islands ophiolites (Browning et al. 1989; Bédard 1993). The studied amphibole-rich Mayarí-Cristal dyke is an exception, as its pattern and high content of REE (Fig. 4.13d) are consistent with a composition closer to that of aggregated melt. Because of the lack of clear intrusive relationships owing to pervasive faulting, a critical issue for the regional geology of the Mayarí-Baracoa Ophiolitic Belt is the genetic relationship between gabbroic rocks and tectonically-related lavas. The Morel volcanics are in tectonic contact with the ophiolitic section of the Moa-Baracoa massif and they mainly consist of basalts interbedded with cherts, hyaloclastites, and minor tuffaceous rocks. Representative geochemical data of this volcanic formation have been published by Kerr et al. (1999) and Proenza et al. (2006) for two pillow lavas which have been interpreted as back-arc basalts. The Téneme formation is in tectonic contact with the Mayarí-Cristal ophiolitic rocks. These extrusives are mainly constituted by basalts and basaltic andesites and have been interpreted as arc-related volcanics (Proenza et al. 2006).

The calculated Mg# average value for liquids in equilibrium with the olivine of Moa-Baracoa cumulates is 0.51 (FeO/MgO olivine-liquid K_d from Roeder and Emslie 1970); such a low value implies that the parental magma experienced intense crystal fractionation after a primary mantle derived melt. The REE equilibrium concentrations in the melts coexisting with the cumulate gabbros have been calculated by whole rock and modal data following the method of Bédard (1994). The REE patterns of the melts in trace element exchange equilibrium with MBOB gabbroic rocks show N-MORB-like patterns (Fig. 4.17a, b) with $(La/Yb)_N$ and $(Ce/Sm)_N$ ratios ranging between 0.5-0.9 and 0.6-1.0, respectively. For two crustal gabbros from the Moa-Baracoa massif, I have performed additional in situ analyses of the trace element content of clinopyroxene by LA-ICP-MS (Fig. 4.17c) (Appendix 1). The melts in equilibrium with clinopyroxene have been calculated using the clinopyroxene/melt K_ds reported by Hart and Dunn (1993). The calculated melts using this alternative procedure are identical to those obtained by whole rock and modal data, confirming that gabbros from the Moa-Baracoa crustal section were in trace element equilibrium with N-MORB magmas (Fig. 4.17c).

In Figure 4.17(a, b) I compare the REE patterns of liquids in equilibrium with Mayarí-Cristal and Moa-Baracoa cumulates with the REE patterns of Téneme and Morel volcanics, respectively. Téneme volcanics exhibit patterns enriched in LREE and flat to slightly depleted for MREE and HREE which are very different from the liquid in equilibrium with the studied Mayarí-Cristal cumulate dyke. On the other hand, Morel volcanics display N-MORB type REE patterns comparable with calculated melts in equilibrium with Moa-Baracoa gabbros. Furthermore, the average Mg# of Morel lavas and

that of liquids in equilibrium with olivine of Moa-Baracoa cumulates coincide. These results indicate that Morel volcanics are melts derived after crystallization of the gabbro section of the Moa Baracoa massif. Conversely, the data indicate that Mayarí-Cristal dykes and Téneme volcanics are not cogenetic.

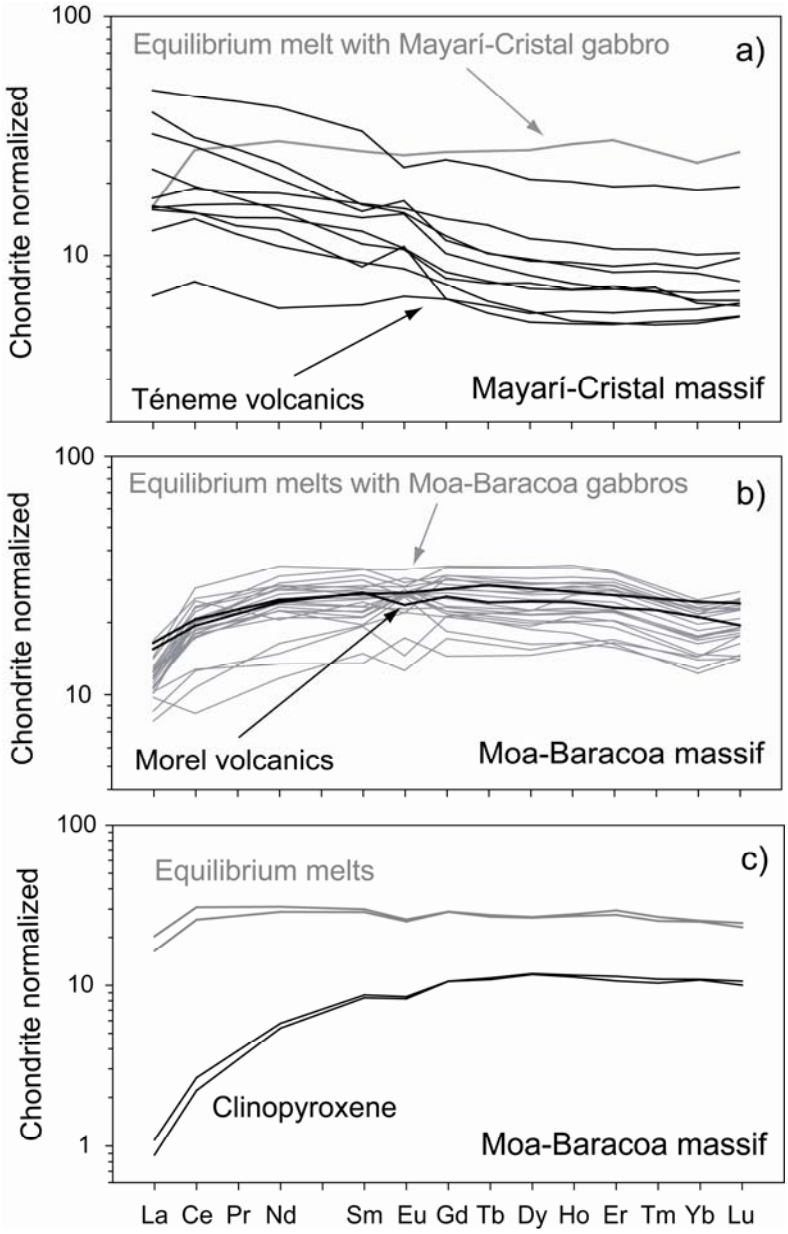

Figure 4.17 Calculated REE patterns of liquids in equilibrium with Mayarí-Baracoa cumulate gabbros compared to Téneme and Morel volcanics. a) Grey line represents the calculated REE pattern of the liquid coexisting with the studied Mayarí-Cristal cumulate dyke. This pattern is compared to REE contents of Téneme volcanics (black lines) (Proenza et al. in 2006). b) Grey lines are REE patterns of liquids in equilibrium with Moa-Baracoa sills, dykes and crustal layered cumulate gabbros. Patterns of representative data on volcanics from the Morel Formation (Kerr et al. 1999; Proenza et al. 2006) are shown for comparison (black lines). c) Black lines are average REE patterns of clinopyroxene for two layered gabbros from the Moa-Baracoa massif. Grey lines are calculated patterns for liquids in equilibrium with clinopyroxene.

5. PETROGENESIS OF THE CRETACEOUS MAGMATISM IN EASTERN CUBA

5. PETROGENESIS OF THE CRETACEOUS MAGMATISM IN EASTERN CUBA

5.1. SAMPLING AND PETROGRAPHY

For this study I selected 57 specimens from a larger sampling of igneous rocks from several localities in eastern Cuba (Fig. 5.1). As many samples showed clear evidence of intense hydrothermal alteration and tropical weathering, I chose only the least altered specimens on the basis of their petrography and the whole rock major element composition. I also excluded samples with petrographic and major element evidences of phenocryst accumulation.

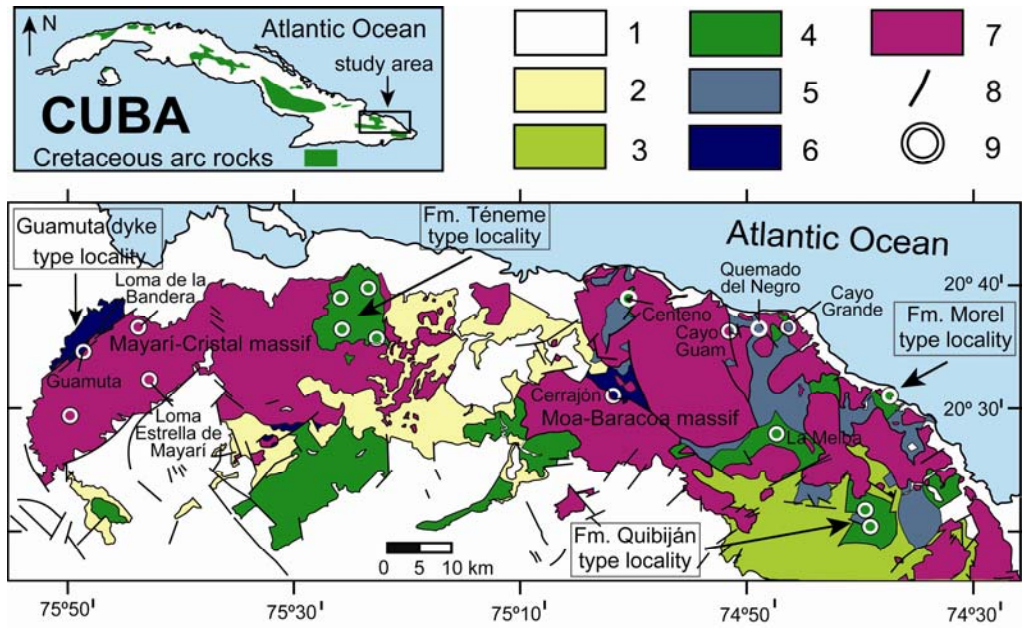

Figure 5.1 Geological map of eastern Cuba with the location of studied samples (white circles). 1 = Paleogene-Quaternary sedimentary and volcanic rocks; 2 = Ophiolitic and metamorphic melanges (La Picota and La Corea Fms.); 3 = Metamorphosed Cretaceous igneous and sedimentary rocks (Purial Complex); 4 = Cretaceous volcanic and minor plutonic rocks; 5 = Ophiolitic plutonic gabbroic rocks; 6 = Microgabbro dykes; 7 = Serpentinized peridotites locally intruded by mafic dykes; 8 = Faults; 9 = Sample locations. Inset: Geographic locations of Cretaceous arc rocks in Cuba (Iturralde-Vinent 1998); black box indicates the study area.

I selected 28 samples from the western part of the studied area, where igneous suites are spatially-associated with the Mayarí-Cristal peridotites (Fig. 5.1): 14 volcanic rocks of the Téneme Formation collected in their type locality (Fig. 2.11, 5.2a; most of

these samples (11) were previously studied by Proenza et al. (2006) and have been reanalysed here for determination of their trace element contents and radiogenic isotope ratios); 1 sample from the Téneme (Río Grande) intrusive; 11 subplutonic dykes collected in the NW region of the Mayarí-Cristal massif (Guamuta-Loma de la Bandera area) (Fig. 5.2b) and 2 dykes from the Loma Estrella de Mayarí area, all of them intrusive in mantle peridotite. In addition, I selected 29 samples from the eastern domain, where igneous suites are spatially associated with the Moa-Baracoa ophiolitic rocks (Fig. 5.1): 16 volcanic rocks collected along the Barbudo and Quibiján Rivers where the homonymous formation has been originally defined (Fig. 2.12) (Quintas 1988a); 6 pillow lavas from the localities of Morel and Centeno (Fig. 2.13, 5.2c); 2 volcanic rocks from La Melba area; and 1 mafic dyke intrusive in mantle peridotite from the Cerrajón area. Finally, I have also included in the database one pillow lava from Morel previously reported by Proenza et al. (2006), and three olivine gabbros from the crustal section (in Cayo Grande and Quemado del Negro) and Moho transition zone (in Cayo Guam) of the Moa-Baracoa ophiolite (Chapter 4), analysed for radiogenic isotope ratios.

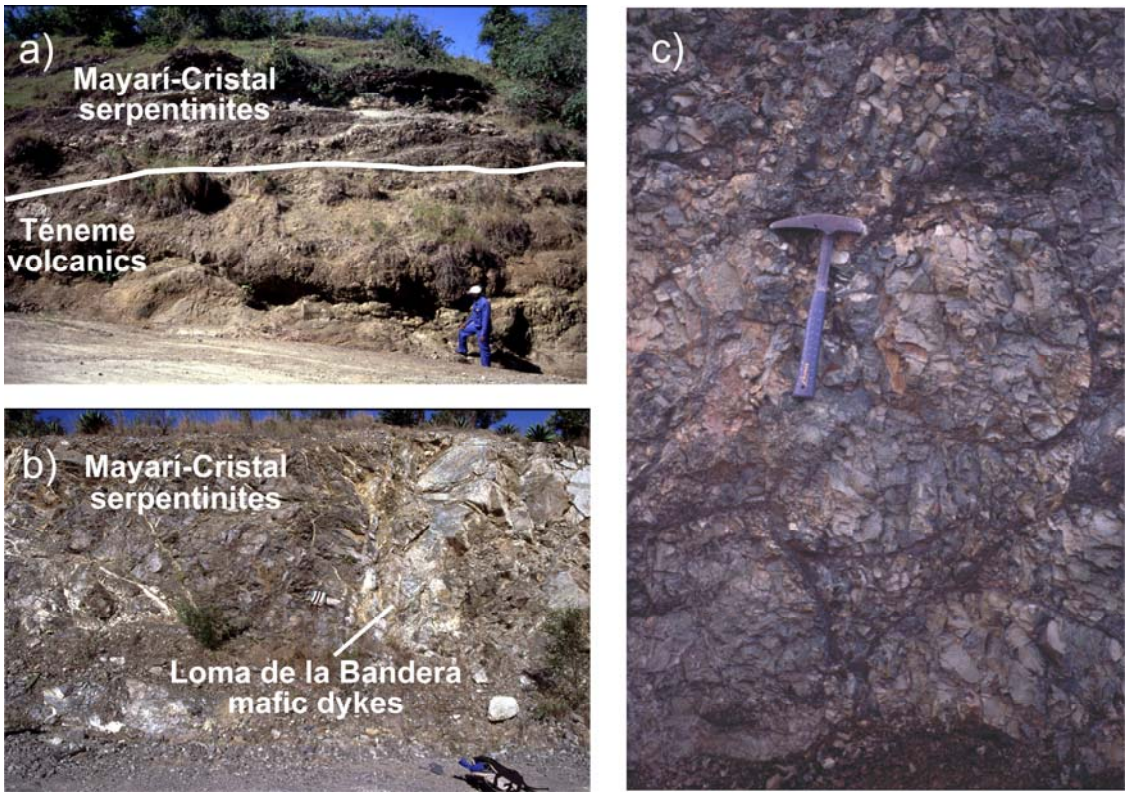

Figure 5.2 a) Outcrop picture of the Téneme Formation in its type locality where these volcanics are overlain by the serpentinized peridotites of the Mayarí-Cristal ophiolitic massif; b) mafic dyke in the Loma de la Bandera area that intrudes the serpentinized peridotites of the Mayarí-Cristal ophiolitic massif; c) pillow lavas of the Morel Formation.

Volcanic samples have micro/crypto-crystalline or porphyritic-aphanitic textures; in the latter, clinopyroxene, plagioclase and rare olivine (1-9 mm) phenocrysts are surrounded by a (< 100-500 μm) groundmass (Fig. 5.3a). Subplutonic dykes generally show fine phaneritic (< 1 mm) homogeneous texture (Fig. 5.3b). Major mineral phases in volcanic rocks and dykes are plagioclase, clinopyroxene, iron-titanium oxides, ± minor hornblende, quartz, orthopyroxene and rare olivine. Accessory minerals are epidote, apatite and sulphides. Primary minerals show an intense imprint of hydrothermal and weathering alterations and are often replaced by secondary pseudomorphic minerals. Albitized plagioclase grains are commonly altered to sericite, saussurite, chlorite or smectite, while green amphibole (uralite) and chlorite replace clinopyroxene (Fig. 5.3a, b). Several samples also display secondary alteration veins constituted by quartz-celadonite, sericite, serpentine, carbonate and Fe-oxyhydroxides. The Téneme intrusive is constituted by a fine grained (200-800 μm) groundmass of plagioclase, quartz and Fe-Ti oxides, and (2-5 mm) megacrysts of amphibole and quartz (Fig. 5.3c). Major and trace element compositions of minerals in the studied samples are listed in tables of Appendix 3.

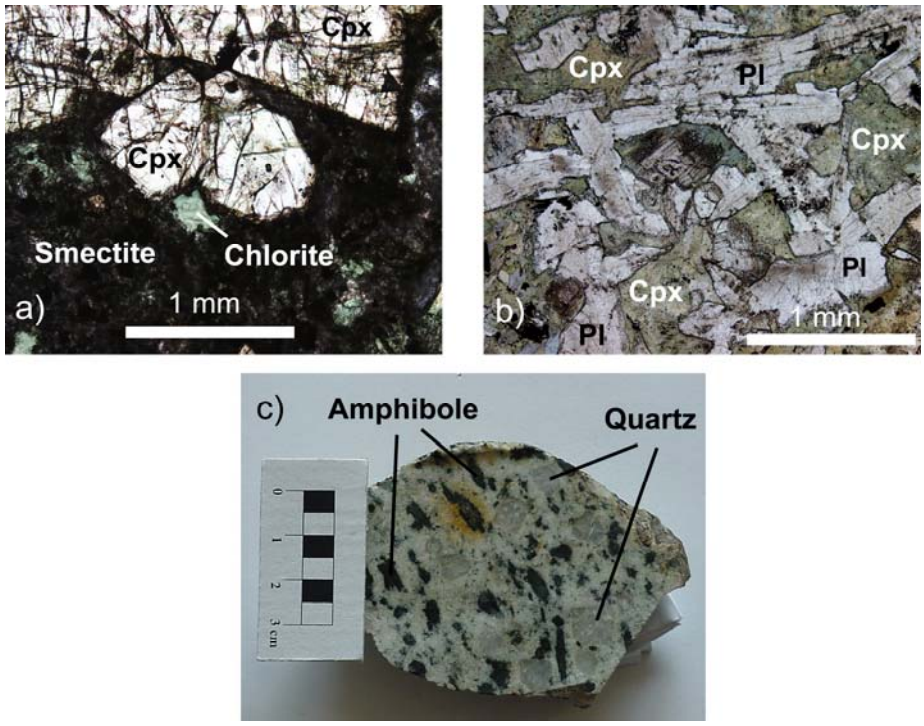

Figure 5.3 a) Porphyritic-aphanitic texture in volcanic rock from eastern Cuba constituted by millimetric-sized clinopyroxene (Cpx) porphyroclasts surrounded by a highly altered matrix of smectite and chlorite after plagioclase and clinopyroxene; b) fine phaneritic texture in mafic dyke from eastern Cuba constituted by < 1 mm slightly altered plagioclase (Pl) and uralitized clinopyroxene; c) representative sample of the Téneme (Río Grande) intrusive constituted by millimetric-sized megacrysts of amphibole and quartz surrounded by a fine grained groundmass of plagioclase, quartz and Fe-Ti oxides.

5.2. WHOLE ROCK GEOCHEMISTRY

Whole rock major and trace element compositions of the studied samples are given in the table of Appendix 4.

5.2.1. Major elements

Sampled volcanic rocks and dykes mainly consist of subalkaline basalts (25), basaltic andesites (12), andesites (8) and minor dacites (4) and basaltic trachy-andesites (3) (Fig. 5.4).

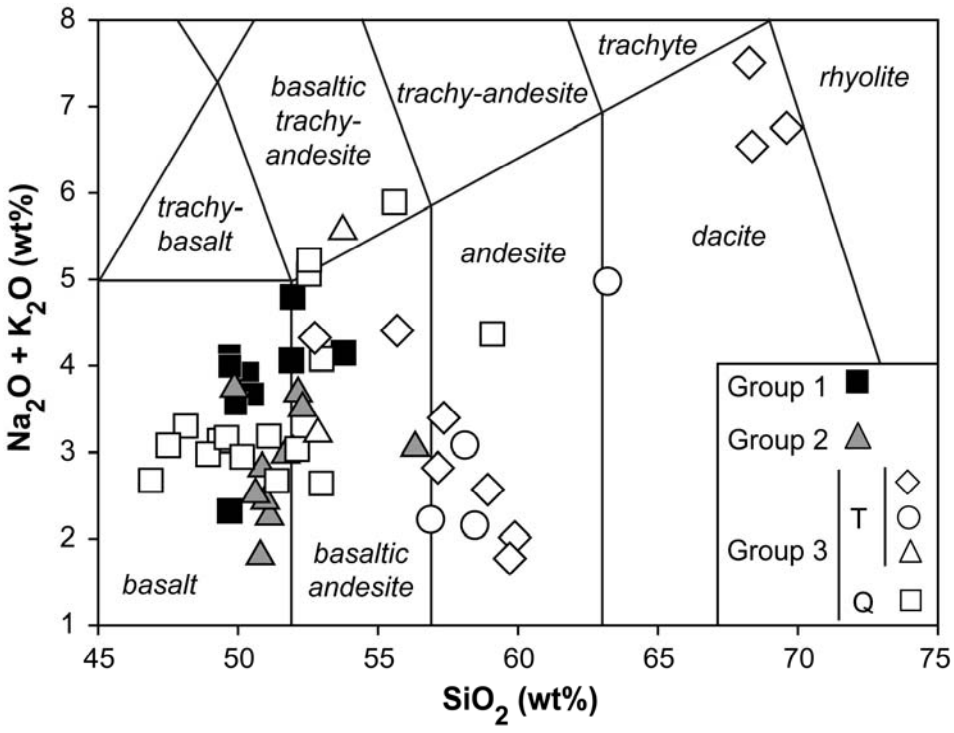

Figure 5.4 TAS (total alkali-silica) diagram (after Le Bas et al. 1986) for volcanic rocks and dykes from eastern Cuba. Data on anhydrous basis in wt%. Black squares: Group 1 volcanic rocks; grey triangles: Group 2 dykes; white diamonds: Téneme volcanic rocks (Group 3T); white circles: Téneme boninites (Group 3T); white triangles: Loma Estrella de Mayarí dykes (Group 3T); white squares: Quibiján volcanic rocks (Group 3Q). One dyke from Loma de la Bandera (LB 204) is not represented because its whole rock composition is affected by significant amphibole accumulation.

The alteration experienced by the samples may have affected their whole rock major element composition. In particular Si, Fe, Mg, Ca, Na and K may have been remobilized during secondary hydrothermal alteration and low grade metamorphism in mafic volcanic rocks (e.g. Staudigel et al. 1996; Alt and Teagle 2003). Spilitization processes may account for the scatter variation of K_2O *vs* Mg# [100 x molar

MgO/(MgO+FeOt); where FeOt is total Fe] exhibited by the samples and for the slightly high SiO_2-Na_2O and low CaO contents in several volcanic rocks. On the other hand, the trends of FeOt, TiO_2 and Al_2O_3 *vs* Mg# are well consistent with the magmatic differentiation of the suites (Fig. 5.5), and I can confidently assume that their contents have not been significantly affected by alteration.

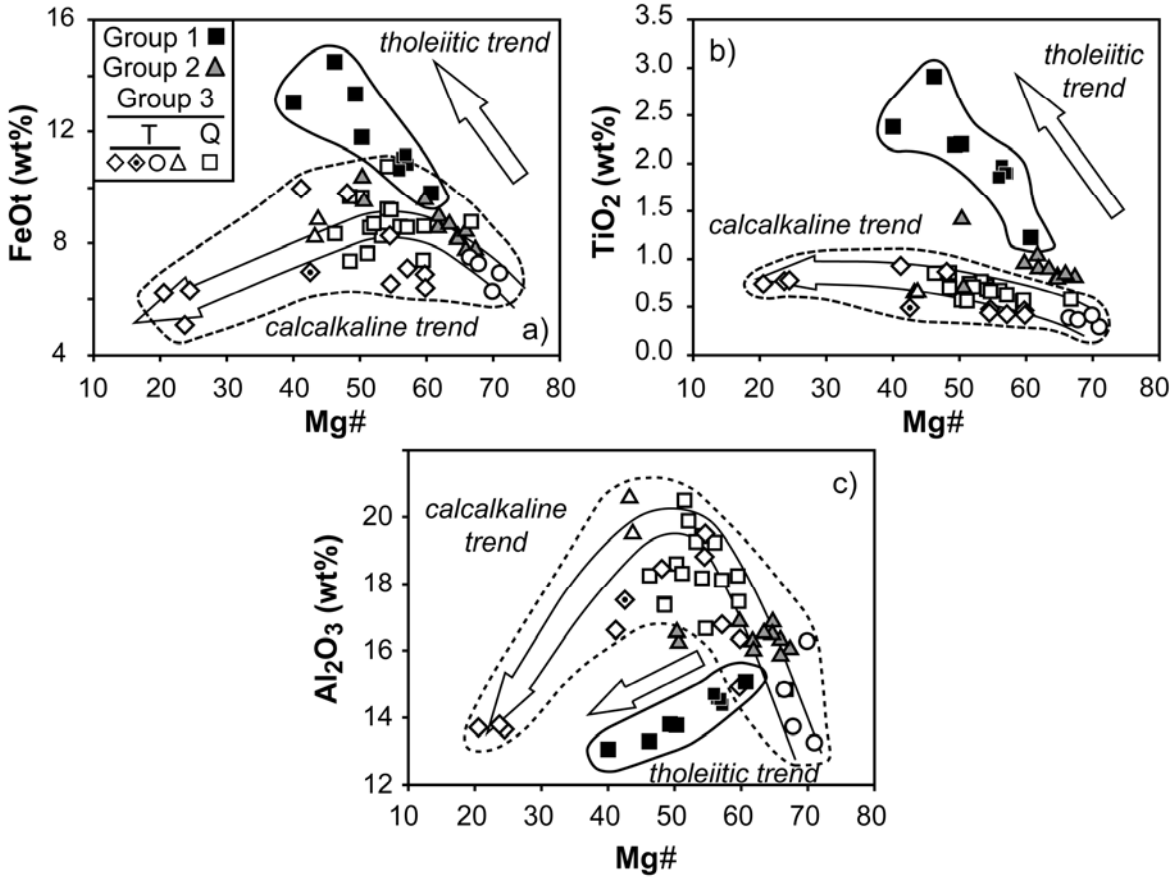

Figure 5.5 Bulk major element compositions of igneous rocks from eastern Cuba illustrated by Mg# *vs* FeOt (a), TiO_2 (b) and Al_2O_3(c). Data on anhydrous basis in wt%. Symbols as in Figure 5.4. Samples of Téneme volcanic rocks with bulk SiO_2 > 53 wt%, TiO_2 < 0.5 wt% and MgO > 8 wt% have been classified as boninites (white circles). The Téneme intrusive sample, not plotted in Figure 5.4, has been included here (white dotted diamond). Tholeiitic and calcalkaline differentiation trends marked by solid and dashed lines, respectively.

In terms of whole rock major element composition, the igneous rocks from eastern Cuba can be classified into three main magmatic groups that are discriminated by their trends in the FeOt *vs* Mg# diagram (Fig. 5.5a):

a) Group 1 comprises basalts and rare basaltic andesites from Morel, La Melba and Centeno that show a steady FeOt enrichment with increasing differentiation marked by decreasing Mg#. Despite the uncertainties of using this terminology (Arculus 2003),

FeO enrichment during differentiation is commonly ascribed to tholeiitic line of descent in arc settings.

b) Group 2 is constituted by dykes from the Guamuta-Loma de la Bandera and Cerrajón areas. They have a basaltic to basaltic andesitic composition. In terms of FeOt *vs* Mg# variations, these samples display a trend similar to Group 1 but show lower FeOt for a given Mg#.

c) Group 3 includes samples from the Téneme and Quibiján type localities and the Loma Estrella de Mayarí region. These rocks show a calcalkaline evolutionary trend that is characterized for Mg# > 50 by increasing FeOt content due to olivine and pyroxene fractionation (e.g. Kelemen et al. 2003a), whereas for Mg# < 50 FeOt decreases with Mg# evidencing the role of Fe-Ti-oxide fractionation. Within this group, I further distinguish two subgroups: the Group 3T that comprises the samples of the Téneme igneous rocks (some of them exhibiting a boninitic affinity: SiO_2 > 53 wt%, TiO_2 < 0.5 wt% and MgO > 8 wt%) and the Loma Estrella de Mayarí dykes; and the Group 3Q that includes the volcanic rocks of the Quibiján Formation. Group 3 encloses basaltic to dacitic compositions in the most evolved magmas of the Group 3T (Fig. 5.4).

Similar evolutionary trends are also observed in the TiO_2 *vs* Mg# diagram (Fig. 5.5b). In Group 1 and 2, the TiO_2 content increases during fractionation, whereas it shows a weak tent-shaped evolutionary trend in Group 3 evidencing the role of Fe-Ti oxide fractionation. The relatively high TiO_2 contents of Group 1 volcanic rocks are characteristic of the abyssal tholeiitic series from mid-ocean ridges and back arc basins, whereas the lower TiO_2 abundances of Group 2 and 3 are distinctive of island arc lavas (e.g. Jakeš and Gill 1970). In Group 1, plagioclase fractionation led to Al_2O_3 decrease from primitive to evolved lavas, whereas Group 2 shows nearly homogeneous Al_2O_3 contents (Fig. 5.5c). The delay of the plagioclase fractionation in Group 3 –likely evidencing the increasing role of H_2O– led to Al_2O_3 enrichment in the most primitive samples due to fractionation of mafic minerals; plagioclase fractionation is patent in the most evolved lavas (Mg# < 50) leading to decreasing Al_2O_3 content at lower Mg#. These different evolutionary trends are ascribed to variable role of higher pressure crystal fractionation and higher H_2O content of the parental melts of the calcalkaline relative to those of the tholeiitic series (e.g. Grove and Kinzler 1986 and references therein).

5.2.2. Rare Earth Elements (REE)

Figure 5.6 displays the chondrite-normalized (after Sun and McDonough 1989) REE patterns of the samples. Group 1 and 2 rocks show LREE-depleted to flat patterns

($La/Yb_{(N)}$ = 0.6-0.9) coincident with those commonly reported for mid-ocean ridge basalts (MORB) and island arc tholeiitic (IAT) lavas. Group 1 exhibits higher REE concentrations than Group 2 and variable negative Eu anomalies indicative of plagioclase fractionation. The REE contents of Group 2 are similar to those of the Early Cretaceous IAT series from the Caribbean realm (dashed line in Fig. 5.6).

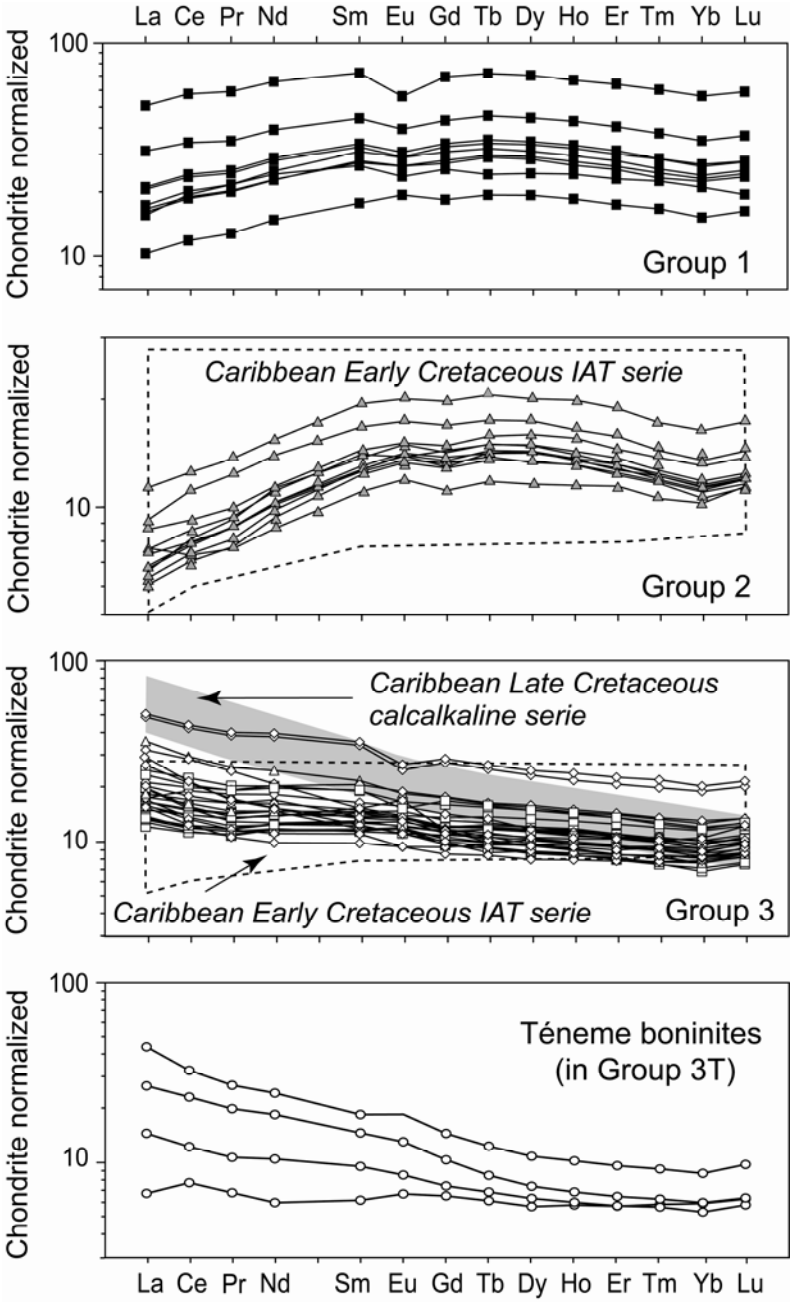

Figure 5.6 Chondrite-normalized REE patterns of igneous rocks from eastern Cuba (whole rock analyses). Symbols as in Figure 5.4. Normalizing values from Sun and McDonough (1989). Fields of the Caribbean Early Cretaceous IAT (dashed line) and Late Cretaceous calcalkaline series (grey area) from Blein et al. (2003) and references therein.

The REE patterns of Group 3 samples significantly differ from those of Group 1 and 2. Group 3 rocks display REE patterns characterized by LREE-enriched ($La/Sm_{(N)}$ = 1.0-2.1) and HREE-depleted ($Sm/Yb_{(N)}$ = 1.1-1.8) segments that are common in arc lavas (e.g. McCulloch and Gamble 1991; Hawkesworth et al. 1993; Kelemen et al. 2003a). Consistently with major elements, plagioclase fractionation generated negative Eu anomalies only in the most evolved lavas that are also characterized by the highest REE contents. No appreciable difference exists between the REE composition of Group 3T and 3Q. The 3T samples with a boninitic affinity display REE patterns ($La/Sm_{(N)}$ = 1.1-2.4; $Sm/Yb_{(N)}$ = 1-2.4) similar to those of the other Téneme volcanic rocks but show a wider range of LREE concentrations. Compared to the magmatic series of the Caribbean realm, the REE abundances of the Group 3 calcalkaline suite largely overlap the so-called IAT series and differ from the calcalkaline series reported in the literature (respectively dashed and grey areas in Fig. 5.6). As I will discuss in Chapter 6 (Section 6.2), this apparent discrepancy is a semantic issue as the calcalkaline volcanic series in the Caribbean realm are customarily classified on the basis of their trace element ratios (e.g. Kerr et al. 2003), whereas here I classify them on the basis of their major element evolutionary trends.

5.2.3. Other incompatible trace elements

All the samples of Group 1 and 2 have lower contents of several highly incompatible trace elements (Cs, Rb, Ba, Th, U, Pb and Sr) than rocks of Group 3 for similar Mg#. This signature can not be due to alteration but most likely reflects primary petrogenetic features (i.e. different mantle sources and/or degrees of melting).

Figure 5.7a shows that the three groups identified above for their distinct major element and REE signatures also differ significantly in terms of Th/Nb and La/Nb values. Group 1 samples clearly display MORB-like compositions whereas dykes of Group 2 have higher La/Nb and Th/Nb ratios that suggest an arc-related affinity. The samples of Group 3 show even higher ratios and plot in the field of common arc magmas. Figure 5.7a also displays isopleths of constant Th/La which is generally greater in arc setting compared to abyssal lavas and is mainly influenced by the composition of subducted sediments (Plank 2005). The majority of Group 3 samples has Th/La < 0.15 resembling that of Marianas arc lavas, whereas three 3Q and one 3T volcanic rocks are characterized by significant high Th/La (≥ 0.23) characteristic of Lesser Antilles and Aleutians arc volcanics.

The Ce/Pb *vs* Nb/U diagram (Fig. 5.7b) confirms the variable imprint of a subduction component in igneous rocks from eastern Cuba. These ratios strikingly vary among oceanic abyssal tholeiites, arc lavas and continental crust (Hofmann et al. 1986),

thus constituting useful tracers for subduction-related processes and recycled continental material. However, hot hydrothermal fluids may remobilize U and Pb at ocean floor (Michard and Albarède 1985) but this drawback can be partly overcome by interpolating the uranium concentrations between the normalized values of Th and La (U*) (Hofmann 2003). 6 volcanic rocks of Group 1 plot at the low Nb/U* edge of the MORB field, whereas three other samples show similar Nb/U* ratios but higher Ce/Pb that I relate to secondary Pb extraction by hydrothermal circulation. Group 2 samples display MORB-like Ce/Pb but clearly lower Nb/U* than MORB supporting a stronger subduction signature than for Group 1. Group 3 samples have low Nb/U* and Ce/Pb ratios typical of arc magmas, sediments and continental crust.

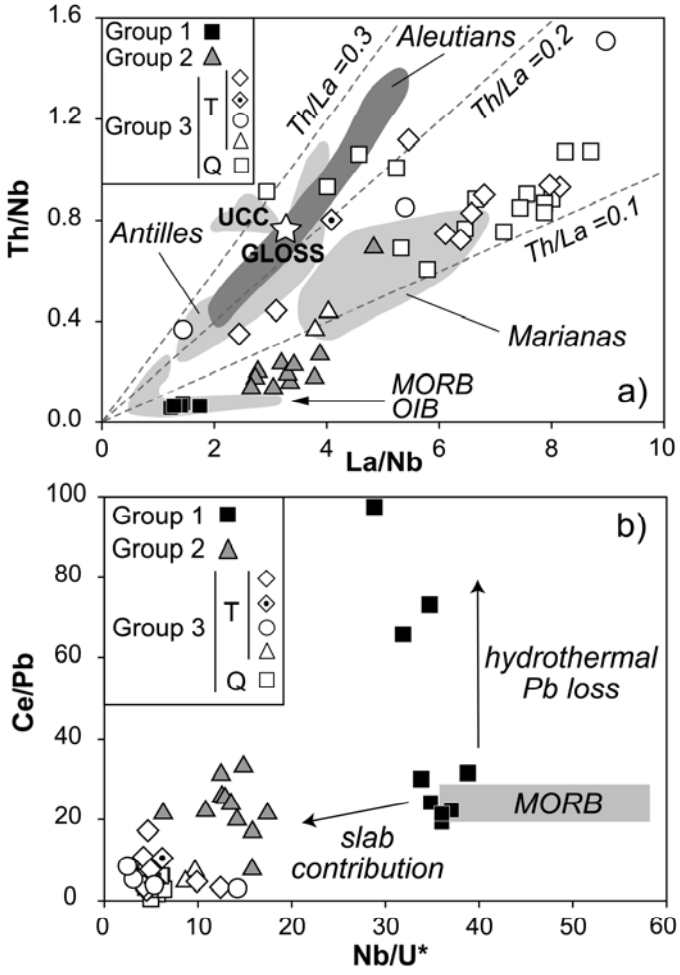

Figure 5.7 a) Th/Nb *vs* La/Nb and b) Ce/Pb *vs* Nb/U* (U* = interpolated value between normalized Th and La concentrations) plots for igneous rocks from eastern Cuba (whole rock analyses). Symbols as in Figure 5.5. Fields of MORB-OIB, Marianas, Aleutians, Antilles arcs, upper continental crust (UCC) and global subducting sediment (GLOSS, star) in (a) from Plank (2005) and references therein. MORB grey shaded area in (b) from Hofmann et al. (1986). One boninitic sample with high La/Nb ratio is not shown for clarity.

5.3. RADIOGENIC ISOTOPIC COMPOSITIONS

Figure 5.8 displays the Nd, Sr and Pb radiogenic isotopic compositions of mineral separates and whole rocks listed in Appendix 5. For the isotopic study, I selected fifteen volcanic samples (ten from the Téneme and Quibiján Formations., three from Centeno and two from Morel), six subplutonic dykes from the Guamuta-Loma de la Bandera and one from the Loma Estrella de Mayarí areas, one sample of the Téneme intrusive quartz-diorite and three cumulate gabbros from the Moa-Baracoa ophiolitic massif; in samples with a micro-crystalline aphanitic texture I only performed whole rock analyses. The measured isotopic ratios have been corrected for the in situ radioactive decay since 90 Ma according to the ages of crystallization assigned by Iturralde-Vinent et al. (2006). For samples with Rb, Sm, Th and U contents below the analytical detection limits I present the present-day age-uncorrected isotopic values (in italic in Appendix 5); this is the case for the great majority of the Pb isotopic ratios in mineral separates.

The samples of Group 1 and 2 exhibit high initial ε_{Nd} values (9.1-11.1) indicative of a depleted mantle source (DMM) (Workman and Hart 2005); in particular, Group 2 samples commonly have a slightly more depleted signature than Group 1. Three olivine gabbros from the Moa-Baracoa ophiolitic massif show Nd radiogenic isotopic ratios broadly similar to Group 1; this observation is in agreement with the conclusion that these gabbros are in REE exchange equilibrium with Group 1 (Morel) volcanic rocks (Chapter 4, Section 4.5.4). Group 3 samples display Nd isotope compositions significantly less radiogenic than Group 1 and 2, which are consistent with a stronger imprint of a subduction component in these samples; ε_{Nd} varies from 2.7 to 9.3 in Group 3T and from 3.4 to 9.4 in Group 3Q.

Seawater alteration clearly overprinted the Sr isotopic composition of those samples that show relatively high radiogenic $^{87}Sr/^{86}Sr$ ratios decoupled from ε_{Nd} decrease. The impossibility of obtaining highly pure clinopyroxene separates, along with the pervasive alteration of plagioclase, make it likely that neither mineral nor whole rock data reflect the primary Sr isotopic composition of these samples. Seawater contamination is particularly evident for Group 1 ($0.70351 < {}^{87}Sr/^{86}Sr < 0.70415$) and Group 2 ($0.70292 < {}^{87}Sr/^{86}Sr < 0.70432$) that depart from the Atlantic and Pacific MORB fields conversely to the Moa-Baracoa ophiolitic gabbros. Group 3 samples have quite variable $^{87}Sr/^{86}Sr$ ratios that increase from Group 3T ($0.70339 < {}^{87}Sr/^{86}Sr < 0.70478$) to Group 3Q ($0.70381 < {}^{87}Sr/^{86}Sr < 0.70531$).

Group 1 volcanic rocks exhibit rather variable $^{206}Pb/^{204}Pb$ (18.19-18.41) and more constant $^{207}Pb/^{204}Pb$ (15.49-15.51) and $^{208}Pb/^{204}Pb$ (37.65-37.74) ratios. Only one sample

(CEN 202) is similar to DMM and Moa-Baracoa gabbros in terms of Pb isotopic composition, whereas the remainders have somewhat more radiogenic ratios.

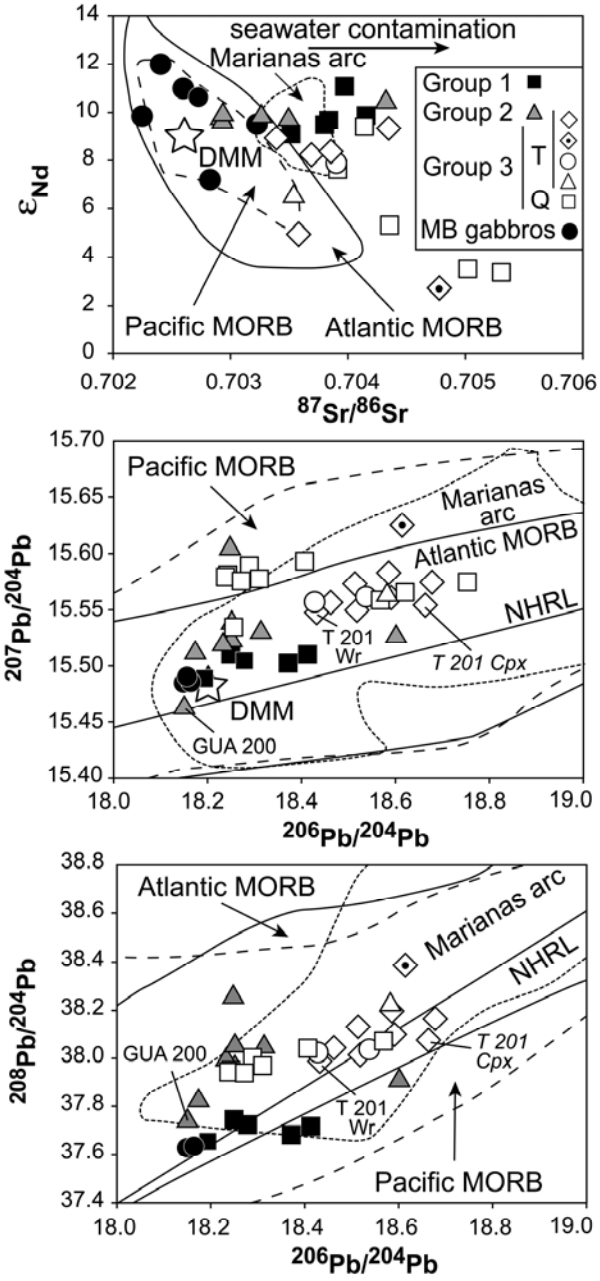

Figure 5.8 Nd, Sr and Pb radiogenic isotope ratios of whole rock and mineral separates for igneous rocks from eastern Cuba. For samples with available Rb, Sm, Th and U contents the values have been corrected for the time-integrated radioactive decay since 90 Ma, according to the crystallization ages assigned by Iturralde-Vinent et al. (2006); otherwise, maximum present-day age-uncorrected values have been plotted (in italic in Appendix 5). Symbols as in Figure 5.5. Black circles: cumulate gabbros from the Moa-Baracoa (MB) ophiolitic massif. Age-corrected (90 Ma) Depleted MORB Mantle (DMM, star) from Workman and Hart (2005); actual Atlantic (solid line) and Pacific (long dashed line) MORB fields from Hofmann (2003) and references therein; actual Marianas arc volcanic rocks field (short dashed line) from GEOROC database (http://georoc.mpch-mainz.gwdg.de/georoc/Entry.html); NHRL (Northern Hemisphere reference line) from Hart (1984); Wr = whole rock; Cpx = clinopyroxene.

Group 2 shows $^{206}Pb/^{204}Pb$ generally coincident with Group 1 but higher $^{207}Pb/^{204}Pb$ (15.51-15.60) and $^{208}Pb/^{204}Pb$ (37.82-38.25) ratios, with the exception of the sample GUA 200 ($^{206}Pb/^{204}Pb$ = 18.15; $^{207}Pb/^{204}Pb$ = 15.46; $^{208}Pb/^{204}Pb$ = 37.74). As the U/Pb of the specimens determines the age correction of their present-day $^{206}Pb/^{204}Pb$ and $^{207}Pb/^{204}Pb$ ratios for the in situ radioactive decay of U, I note that the high whole rock U/Pb ratio of one of Group 2 dykes (LB 204) (Appendix 4) leads to overestimate the time integrated U decay since its crystallization. This is reflected by the relatively low age-corrected Pb isotopic ratios displayed by this specimen (especially its $^{206}Pb/^{204}Pb$ ratio) compared to the other rocks of the suite. I interpret the high U/Pb ratio of sample LB 204 as a consequence of late U uptake and/or Pb leaching by hot hydrothermal fluids (Michard and Albarède 1985), and I have thus corrected its Pb isotopic whole rock ratios with the value of U* instead of U. Group 3 samples have more radiogenic Pb isotopic compositions than Group 1 and 2 ($^{206}Pb/^{204}Pb$ = 18.24-18.62; $^{207}Pb/^{204}Pb$ = 15.53-15.62; $^{208}Pb/^{204}Pb$ = 37.94-38.39), coherently with a stronger imprint of a subduction component in this group. Group 3Q samples with high Th/La ratios (Fig. 5.7a) cluster at lower $^{206}Pb/^{204}Pb$-$^{208}Pb/^{204}Pb$ and have higher $^{207}Pb/^{204}Pb$ ratios than the rest of Group 3 samples. The dispersion of mineral and whole rock data observed for some samples (e.g. T 201, Fig. 5.8, Appendix 5) is due to the fact that the great majority of mineral Pb isotopic data in this study consists of present-day ratios and has therefore to be considered as maximum values. The ratios of whole rock analyses, on the other hand, are age-corrected. For this reason in the following discussion I will consider only the age-corrected data for whole rock analyses, and I will focus particularly on their Pb and Nd isotopic variations that are little affected by seawater alteration (e.g. Schaule and Patterson 1981; McCulloch et al. 1981; Staudigel et al. 1995).

5.4. Ar-Ar GEOCHRONOLOGY

In order to constrain the intrusion age of Group 2 dykes, I have performed Ar-Ar geochronology on amphibole separates from one of these samples (LB 204) (Fig.5.9a). Step-heating laser probe analysis of single grain gives a plateau age of 88.6 ± 3.5 Ma for 81.9% of the argon released (Fig. 5.9b). The first heating steps contained a large amount of atmospheric argon probably lost from the surface and structural defects of the grain at the beginning of degassing. The Ca/K ratio and Cl/K corresponding to the plateau age are ~ 69 and ~ 0.5, respectively (calculated according to the relations in Onstott et al. 1991). These results coincide with the Late Cretaceous (Cenomanian-Coniacian) age of the eastern Cuba igneous rocks inferred by Iturralde-Vinent et al. (2006) on the basis of paleontologic dating of sedimentary rocks intercalated with volcanics. However, as noted

above, this sample displays a high whole rock U/Pb ratio that may be due to secondary hydrothermal alteration. This event may have also disturbed the Ar isotopic system, so I caution that the age inferred above may not record the primary crystallization of Group 2 dykes but a later alteration event, and hence should be considered as minimum age.

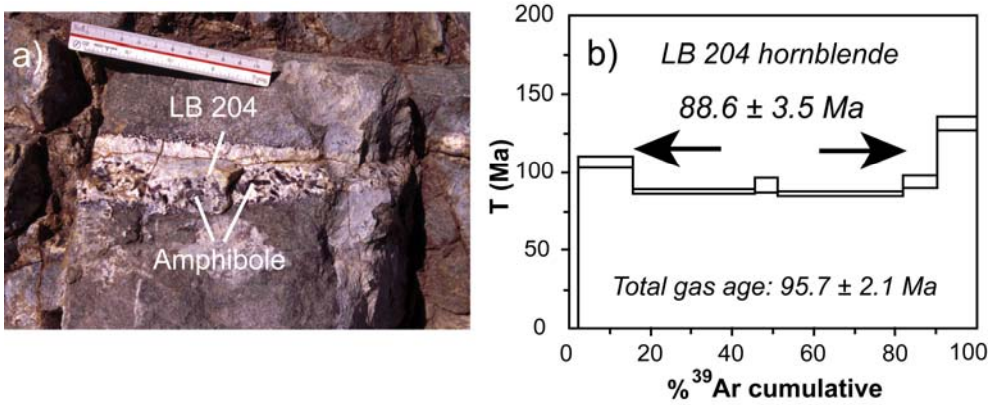

Figure 5.9 a) Field picture of one amphibole-rich dyke (sample LB 204) from Loma de la Bandera area (Group 2); b) ^{40}Ar-^{39}Ar step heating analysis of one hornblende grain from sample LB 204.

5.5. DISCUSSION

The trace element and isotopic compositions of the Cretaceous magmatism in eastern Cuba show a variable imprint of a subduction component related to the formation and evolution of the Cuban paleo-island arc within the realm of the Cretaceous Greater Antilles subduction system. The data indicate that the Cretaceous magmatism in eastern Cuba is characterized by the presence of three main magmatic groups. Group 1 is composed of rocks of basaltic to rare basaltic andesitic composition showing a MORB-like geochemical affinity that may have formed either in a mid-ocean or back-arc spreading centre. Group 2 comprises basaltic and minor basaltic andesitic dykes with a transitional composition between Group 1 and 3, and that show an island arc tholeiitic signature that may be related to the onset of the arc growth (Jakeš and Gill 1970), arc rifting (Gribble et al. 1998), or back-arc volcanism proximal to the arc front (Taylor and Martinez 2003). Group 3 consists of volcanic and minor (sub)plutonic rocks that exhibit an unambiguous subduction-related imprint and that formed in an island arc.

Discriminating between these tectonic scenarios and establishing potential genetic links among magmatic groups entails deciphering which geochemical signatures come from the mantle wedge and/or back-arc mantle and which are derived from the subducted slab (e.g. McCulloch and Gamble 1991; Hawkesworth et al. 1991, 1993; Pearce and

Parkinson 1993; Pearce and Peate 1995). Although the arc crust contributes certainly to the signature of some arc magmatic activity, it is conceivable that it has played a minor role in the genesis of this magmatism as the Cretaceous eastern Cuban island arc was characterized by a thin, volcanic-dominated crust and limited pre-existing oceanic crust and sediments (Iturralde-Vinent et al. 1996c, d, 2006). Furthermore, as Group 2 and in part Group 3T samples are intrusive subplutonic dykes in residual mantle peridotite, the imprint of their sources by a subduction component must have a deep origin. Below I use major and trace elements and radiogenic isotope ratios to examine the melting extents of the mantle source, asses the relative contributions of the mantle and the slab in the source, and identify the nature of the slab component for each magmatic group distinguished above.

5.5.1. Extent and depth of melting of the mantle source

Diverse major, minor and trace element contents and ratios are commonly employed as proxies of mantle source heterogeneity and its integrated melting extent. For instance, Plank and Langmuir (1988) and Niu et al. (1996) used the Na abundance corrected for fractionation and the Ca/Al ratio respectively to constrain the melting extent of the mantle source in subduction and mid-oceanic ridge settings. However, the possible Al and Na inputs from the slab component, coupled with the alteration displayed by the samples, make questionable the application of these parameters to subduction-related magmatism in general (e.g. Kelemen et al. 2003a; Sinton et al. 2003), and in this study particularly.

The abundances, corrected for fractionation, and the ratios involving the high-field strength elements (HFSE: Ti, Nb, Ta, Zr, Hf) and the HREE are generally preferred in arc volcanism to monitor the mantle heterogeneity and melting degree, as it is believed that the contents of these trace elements are essentially unaffected by the slab component (Pearce 1983; McCulloch and Gamble 1991; Woodhead et al. 1993; Pearce and Peate 1995). Under the above assumption, the ratios in volcanic rocks of HFSE and HREE with similar compatibility mimic those of the mantle source (e.g. Pearce and Parkinson 1993). Owing to the rather limited number of samples available for each magmatic group distinguished here, it is however impractical to correct the data for fractionation without inducing large errors. To infer the extent of melting of the mantle source I will exploit instead the abundances and ratios of HFSE and HREE in the most primitive lavas of each group, selected as samples having Mg# > 50 and SiO_2 < 53 wt%. Applying this compositional threshold, I exclude from this discussion the Group 3T. However, inferences on its mantle source will be deduced later on the basis of its isotopic composition.

A first approach to assess the extent of depletion and to constrain the depth of melting of the mantle source is to carry out conventional melting models and regard the fractionation of the MREE relative to the HREE. Figure 5.10 shows the Dy *vs* Lu plot of eastern Cuba primitive igneous rocks together with the results of non-modal batch melting models of spinel lherzolite with different degrees of depletion and garnet lherzolite mantle sources. Because Lu is fractionated from Dy during garnet-present melting, melting trends in the presence of spinel and garnet display different slopes in Figure 5.10.

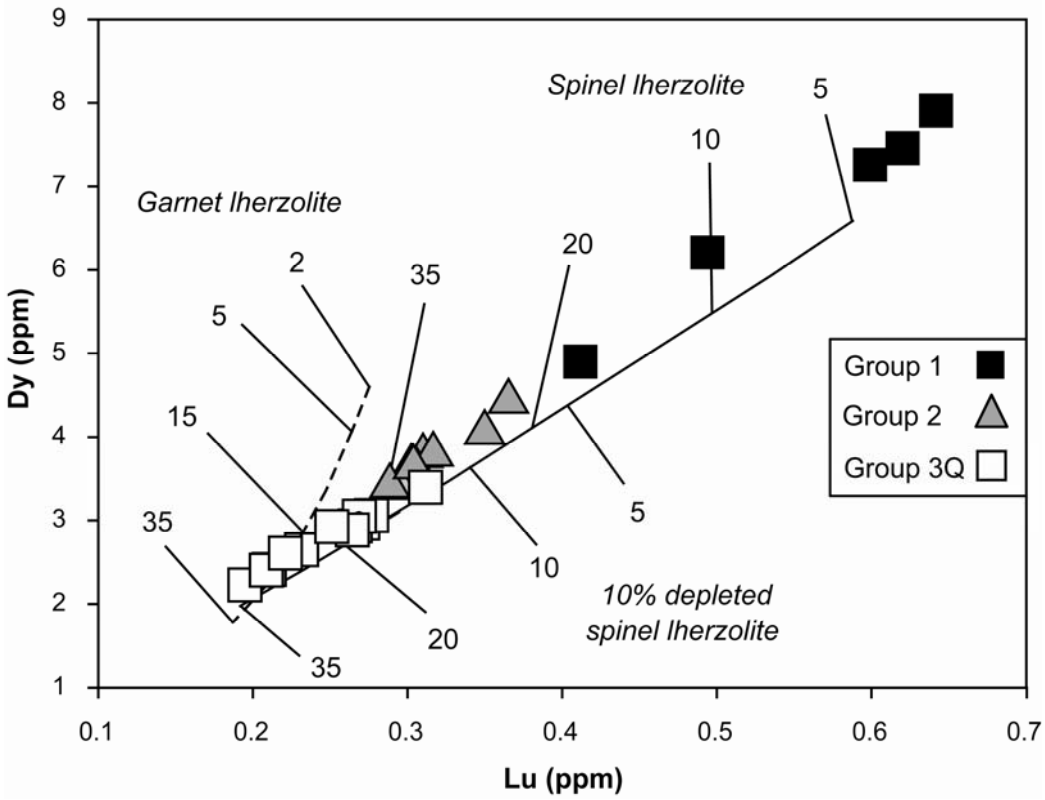

Figure 5.10 Dy *vs* Lu (in ppm concentrations) diagram for primitive volcanic rocks (Mg# > 50; SiO_2 < 53 wt%) from eastern Cuba (whole rock analyses). Symbols as in Figure 5.4. Non-modal batch melting curves are labelled with melting degrees of spinel lherzolite (solid line) [source and melting olivine:orthopyroxene:clinopyroxene proportions 0.57:0.28:0.15 and -0.13:-0.27:1.4, respectively (Walter et al. 1995)] and garnet lherzolite (dashed line) [source and melting olivine:orthopyroxene: clinopyroxene:garnet proportions 0.52:0.29:0.16:0.03 and 0:0.45:0.45:0.1, respectively (Gribble et al. 1998)] with variably depleted MORB mantle compositions (Donnelly et al. 2004). Partition coefficients from Bedini and Bodinier (1999), Su and Langmuir (2003) and Donnelly et al. (2004).

The Dy-Lu variations of Group 1 samples are consistent with melting degrees ranging from < 5 to 20% of a spinel lherzolite source with a relatively enriched DMM composition (Donnelly et al. 2004). The lower HREE contents of Group 2 samples may be

related to higher degrees of melting (20-35%) of the same source, or to lesser degrees of melting of a more depleted mantle. The lowest HREE abundances in Group 3Q samples indicate they derive from a depleted spinel lherzolite mantle source that underwent degree of melting ranging from 10 to 35%. Because Dy and Lu abundances are not corrected for fractionation, the inferred melting degrees should be taken as lower bound estimates. These results indicate that melting occurred mainly at spinel lherzolite facies depths, which constrains the maximum pressure of melting to ca. 2.5 GPa (Walter 2003) corresponding to depths of about 85 km. These estimates of maximum melting depths are similar to those inferred for coeval volcanism in the Puerto Rico paleo-island arc (Jolly et al. 2001) and likely imply a rather constant slab dip for the Cretaceous Greater Antilles subduction system.

If the HFSE contents of the mantle component are unmodified by slab additions and melting occurs at moderate to high degrees in the absence of residual garnet –as it is the case of these igneous suites (Fig. 5.10)– Ta/Yb variations in arc volcanic rocks highlight the relative depletion of their mantle source (Pearce 1983; Pearce et al. 2005). On the other hand, slab additions increase the Th/Yb ratio in arc volcanic rocks relative to the trend defined by the variably depleted MORB mantle sources (Pearce and Peate 1995). Figure 5.11 shows the Th/Yb *vs* Ta/Yb systematic of the most primitive samples of each magmatic group distinguished here. Group 1 and 2 show a limited within-group Ta/Yb variation, whereas this ratio is manifestly bimodal for Group 3Q. The mantle source of Group 1 has Ta/Yb ratio close to the Enriched-DMM (E-DMM; Fig. 5.11) (Workman and Hart 2005) and it is markedly less depleted than Group 2, which is characterized by Ta/Yb ratios between the Depleted-DMM (D-DDM; Fig. 5.11) and the average DMM (DMM; Fig. 5.11) end-members. The relative depletion of Group 2 is accompanied by a departure from the MORB-mantle trend due to its higher Th/Yb for a given Ta/Yb ratio. In active subduction settings, a similar relative depletion of the mantle source is commonly observed between back-arc (less-depleted source) and arc basalts (more depleted source) (Ryerson and Watson 1987; McCulloch and Gamble 1991; Woodhead et al. 1993). This systematic is interpreted as arc basalts recording re-melting of the back-arc mantle due to mantle corner flow coupled with the increasing influence of the slab component below the magmatic arc (Davidson 1987; Ewart and Hawkesworth 1987; Pearce and Parkinson 1993; Arculus 1994). In terms of Ta/Yb, most primitive Group 3Q rocks have a highly depleted source composition similar to Group 2 (Fig. 5.11), whereas three samples show higher Ta/Yb ratios suggestive of a relatively more enriched mantle source. These Group 3Q subgroups will be referred hereafter to as Group 3Q1 and 3Q2, respectively (Fig. 5.11). As Group 3Q samples come from the same volcanic sequence,

their Ta/Yb bimodality would likely reflect spatial and not temporal variation in the depletion of their mantle source.

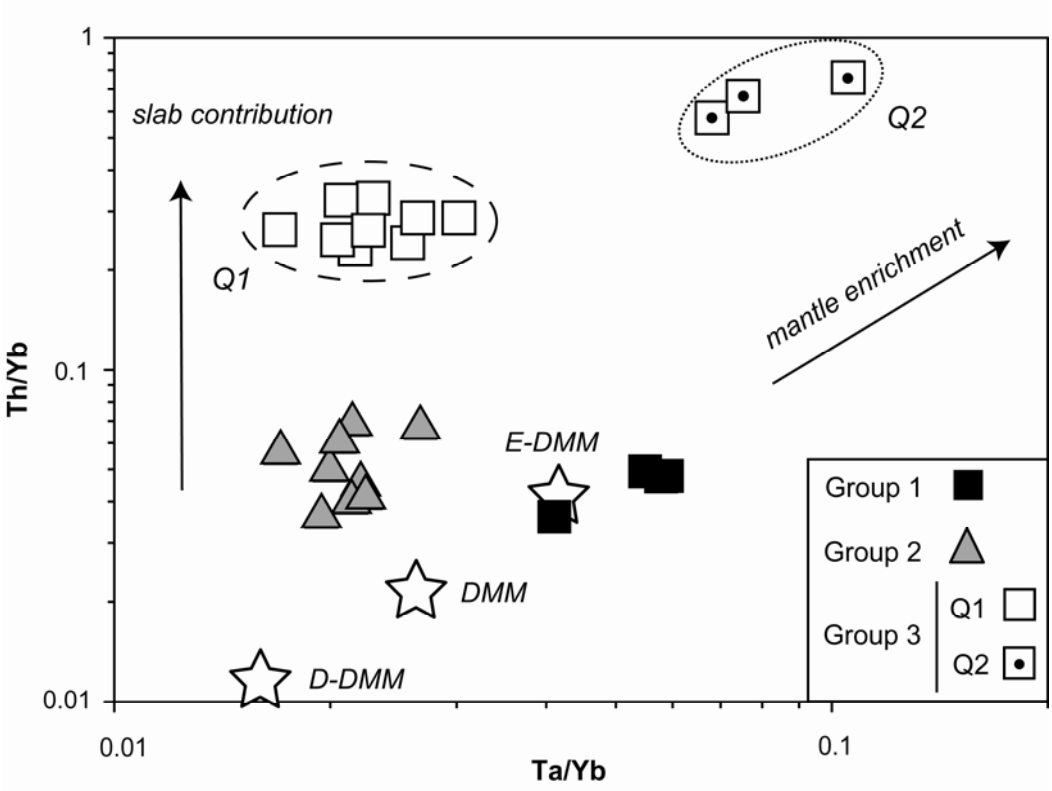

Figure 5.11 Th/Yb *vs* Ta/Yb plot for primitive volcanic rocks from eastern Cuba (whole rock analyses). Symbols as in Figure 5.4. Dotted squares: Quibiján 2 (Q2) volcanic rocks. DMM (Depleted MORB mantle), D (depleted)-DMM and E (enriched)-DMM (stars) from Workman and Hart (2005).

5.5.2. Fractionation of HFSE: deconvolving mantle wedge and slab contributions

If the HFSE budget is dominated by the mantle wedge component and unmodified by slab contributions, the ratios of HFSE with similar partition coefficients, such as Nb/Ta and Zr/Hf, of primitive basalts are further proxies to explore the relative depletion and the extent of melting of the subarc mantle (Plank and White 1995; Eggins et al. 1997; Elliott et al. 1997). The Nb/Ta and Zr/Hf of mantle-derived basalts are slightly fractionated during partial melting of mantle peridotite because of the more incompatible character of the numerators in clinopyroxene (Green et al. 1989; Forsythe et al. 1994).

Figure 5.12 shows the Nb/Ta *vs* Zr/Hf variations in the primitive samples from this study. Group 1 and 2 samples show subchondritic Nb/Ta ratios that on average decrease with decreasing Zr/Hf. As inferred from their Th/Yb *vs* Ta/Yb variations (Fig. 5.11), this trend is consistent with Group 2 samples being derived from a more depleted mantle than

Group 1. As for Ta/Yb, the distribution of the Nb/Ta ratio of Group 3Q is bimodal (Fig. 5.12). Group 3Q1 primitive volcanic rocks depart from the melting trend defined by Group 1 and 2 samples by showing relatively higher and rather variable Nb/Ta (13.5-17.3) and lower and restricted range of Zr/Hf (30.6-32.5). Group 3Q2 primitive samples show even lower Zr/Hf (28.2-30.1) and depart from the MORB field and the melting trend by showing low highly-subchondritic Nb/Ta (7.7-8.9) ratios that are negatively correlated with Zr/Hf (Fig. 5.12). The variations of Nb/Ta and Zr/Hf of Group 3Q samples are inconsistent with anhydrous melting of a peridotite source (Fig. 5.12). Nb and Ta may be fractionated by low degrees of melting, but, as I have shown above (Fig. 5.10), this is not the case of Group 3Q samples. Hydrous mantle melting in the presence of high-Mg# amphibole can neither explain the HFSE fractionations of Group 3Q samples because it does not fractionate Nb from Ta (Tiepolo et al. 2000; Foley et al. 2002).

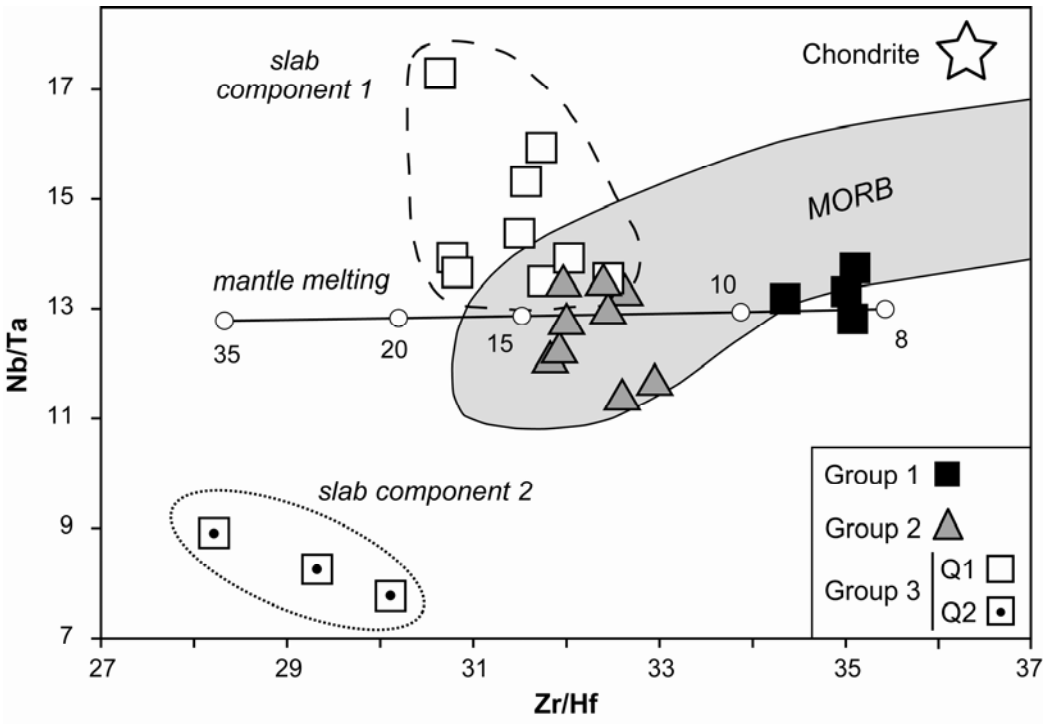

Figure 5.12 Nb/Ta *vs* Zr/Hf plot for primitive volcanic rocks from eastern Cuba (whole rock analyses). Symbols as in Figure 5.11. MORB grey shaded area from Münker et al. (2004) and references therein. Non-modal batch melting line is labelled with melting degrees of spinel lherzolite (melting parameters as in Figure 5.10) with DMM composition (Workman and Hart 2005). Nb/Ta initial ratio of the source chosen according to the best fitting with Nb/Ta in Group 1 and 2. Chondrite composition form Sun and McDonough (1989).

There is growing evidence that the presumably immobile behaviour of the HFSE –particularly Nb and Ta– in subduction zones is not universal and, in some instances, slab

additions in the form of metasomatic melts/fluids overprint the initial HFSE of the subarc mantle source (e.g. Münker 1998; Prouteau et al. 2000; Foley et al. 2002; Münker et al. 2004). The above observations on Group 3Q samples are inconsistent with a mantle wedge origin of the observed HFSE fractionations and likely indicate that they were imposed by the slab component. If so, the bimodal distribution of the Ta/Yb in Group 3Q (Fig. 5.11) cannot be interpreted in terms of a variably depleted subarc mantle source. Most likely, Group 3Q arc volcanic rocks shared a highly depleted mantle source as attested by their Lu-Dy variations (Fig. 5.10), and the systematic variations of their Ta/Yb, Nb/Ta, and to a much lesser extent, Zr/Hf ratios are most readily explained by slab additions of two distinct subduction components as will be discussed below.

5.5.3. Deciphering the contribution and nature of the slab components

5.5.3.1. Assessment of trace element slab additions

As I have shown before, the high Th/La and Th/Yb ratios of Group 3Q (Fig. 5.7a, 5.11) indicate a strong overprint of a slab component, as Th is mainly fractionated in metasomatic agents derived from dehydration and/or melting of subducted sediments (e.g. Turner et al. 1996; Elliott et al. 1997; Elliott 2003; Plank 2005). On the other hand, the trace element budgets of Group 2 and 1 show small and negligible slab-derived contributions, respectively (Fig. 5.7, 5.11). Interestingly, Group 3Q1 and 3Q2, that I have discriminated previously in terms of their bimodal Th/Yb-Ta/Yb (Fig. 5.11) and Nb/Ta-Zr/Hf (Fig. 5.12) systematics, also show distinct Th/La *vs* $^{206}Pb/^{204}Pb$ (Fig. 5.13a) and ε_{Nd} (Fig. 5.13b) variations. These signatures support the imprint of two discrete sediment-derived slab components, as proxied by their high Th/La, but with a component in Group 3Q1 showing higher $^{206}Pb/^{204}Pb$ and ε_{Nd} compared to Group 3Q2 (Fig. 5.13a, b).

The fact that Group 3Q1 and 3Q2 show two distinct subducted sediment contributions coupled with contrasting Ta/Yb, Nb/Ta (Fig. 5.13c) and Zr/Hf ratios is unlikely coincidental and most readily indicates that HFSE fractionation also fingerprints the contribution of the subduction component. Group 3Q2 samples show low Zr/Hf and highly subchondritic Nb/Ta ratios that cannot be easily explained by fractionation related to slab dehydration/melting as this signature is not consistent with the HFSE partition coefficients of the common slab mineral assemblages (Münker et al. 2004 and references therein). This suggests that the Nb/Ta ratios of Group 3Q2 samples were inherited from their slab sediment source. Furthermore, the highly subchondritic Nb/Ta ratios of Group 3Q2 are negatively correlated with Nb, Ta, and La/Yb thus supporting that Group 3Q2 samples have been likely contaminated by the continental crust (Münker 1998). As the

Cuban arc was an island arc characterized by limited pre-existing sediments in the crust (Iturralde-Vinent et al. 1996c, d, 2006), these geochemical signatures are unlikely to be due to intra-crustal assimilation. Therefore, the low Nb/Ta and high Th/La of Group 3Q2 were imposed by a slab agent derived from continental sediments. This slab agent may also influence the low Zr/Hf and Zr/Yb of this subgroup, which may be due to Zr retention during melting/dehydration of metasediments or eclogitic metabasalts relatively rich in garnet (garnet:clinopyroxene modal ratio > 1) (van Westrenen et al. 2001; Klemme et al. 2002). On the other hand, the higher Nb/Ta and the little fractionation of Zr/Hf ratios in Group 3Q1 (Fig. 5.12) may be both generated by subduction processes as this signature is coherent with the dehydration/melting of a rutile-bearing assemblage of clinopyroxene (alternatively amphibole) and garnet (garnet:clinopyroxene modal ratio ~ 1) in metasediments or eclogitic metabasalts (Klemme et al. 2002, 2005; Münker et al. 2004).

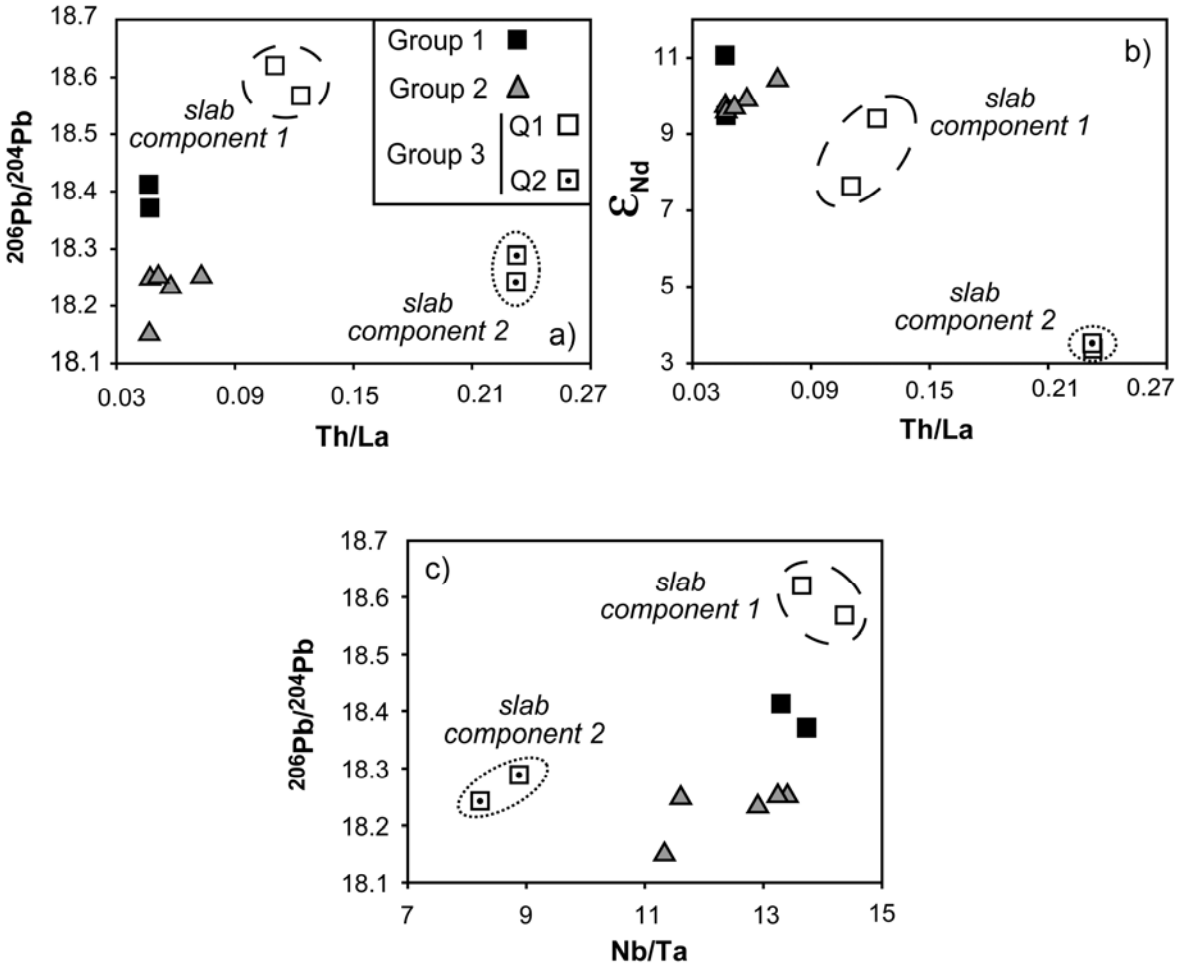

Figure 5.13 a) initial $^{206}Pb/^{204}Pb$ and b) ε_{Nd} *vs* Th/La and c) initial $^{206}Pb/^{204}Pb$ *vs* Nb/Ta for primitive volcanic rocks from eastern Cuba (whole rock analyses). Symbols as in Figure 5.11.

In the Nb/Ta *vs* Th/La diagram (Fig. 5.14) Group 3Q2 samples show a decrease of Nb/Ta with increasing Th/La which is generally distinctive of the continental crust and Andean-type continental arcs (Kalfoun 2002 and references therein). On the other hand, Group 3Q1 samples exhibit sub-constant Th/La at increasing Nb/Ta ratios and plot in the field of lavas from the Marianas and Vanuatu island arcs that are slightly influenced by recycling of continental sediments (Plank 2005). In summary, I infer that the mantle source of Group 3Q2 rocks received a larger contribution from continental sediments than Group 3Q1, as also supported by their higher La/Sm ratios (Appendix 4) (Elliott 2003).

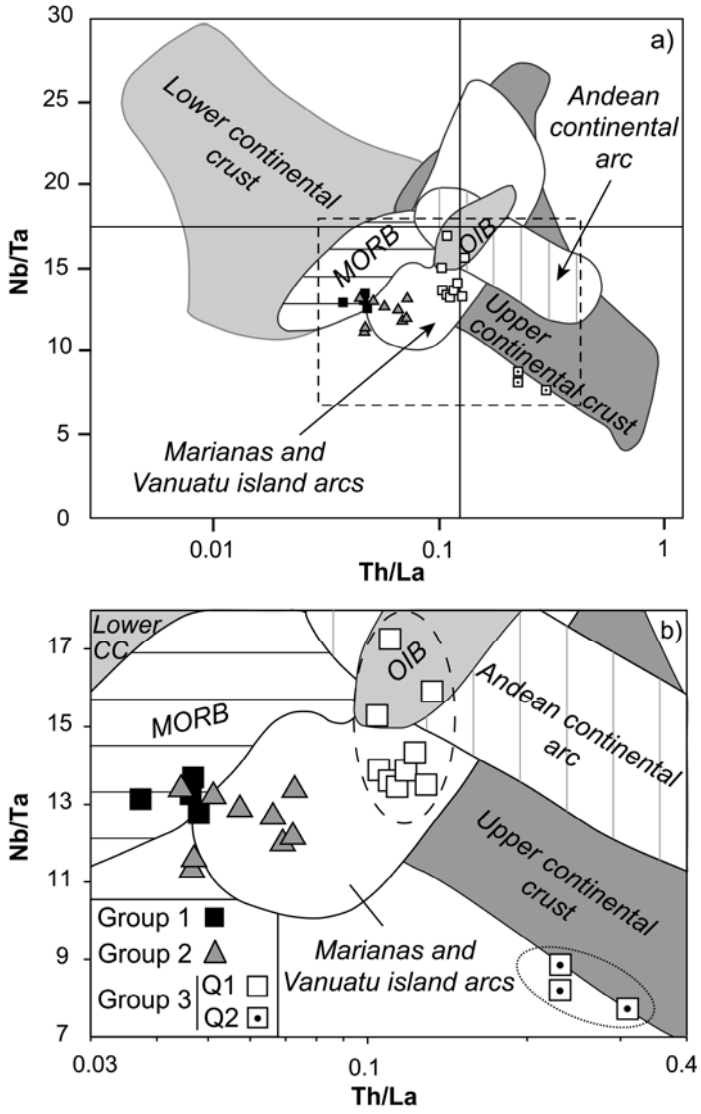

Figure 5.14 Nb/Ta *vs* Th/La plot for primitive volcanic rocks from eastern Cuba (whole rock analyses). Symbols as in Figure 5.11. Fields of lower and upper continental crust (CC), MORB, OIB, Marianas, Vanuatu, and Andean arcs from Kalfoun (2002) and references therein. The intersection of solid lines in (a) marks the chondritic composition (Sun and McDonough 1989); the dashed line defines the enlarged area in (b).

A contribution from continental sediments may also account for the more enriched composition of the Group 3Q2 subduction component in several highly incompatible trace elements (Th-U-Nb-Ta-Pb) as highlighted by their higher Yb-normalized ratios in Group 3Q2 relative to 3Q1. An alternative explanation may be that the higher content of these trace elements in Group 3Q2 does not reflect differences on initial composition of the sediment source but on nature of the subduction agent (i.e. fluids or melts). If so, as highly incompatible elements and HFSE are more easily transported by hydrous melts than aqueous fluids (e.g. Tatsumi et al. 1986; Brenan et al. 1995; Keppler 1996; Kogiso et al. 1997; Kessel et al. 2005), the subduction component of Group 3Q2 would have more melt-like character than that of Group 3Q1.

Interestingly, Group 2 samples also exhibit a general negative correlation of Nb/Ta with Th/La and plot off the mixing trend defined by the Group 3Q2 samples (Figure 5.14b). As further supported by their Pb isotope compositions (see below), this covariation suggests that Group 2 samples have been slightly overprinted by a continental-like sediment component similarly to Group 3Q2. On the other hand, Group 1 volcanic rocks plot among the highest Th/La end-member of MORB indicating a faint signature of the slab component supporting their back-arc affinity.

5.5.3.2. Tracking the nature and provenance of the slab components

Information on the nature and provenance of the slab component can be obtained from variations of the Pb, Sr and, to a lesser extent, Nd radiogenic isotopes that are sensitive tracers of slab additions (e.g. Hawkesworth 1982; White and Patchett 1984; Weaver et al. 1986; Hawkesworth et al. 1993; Santos et al. 2002; Elliott 2003). To assess relative slab contributions, the isotopic composition of the mantle wedge prior to subduction should be known. One sample of Group 2 (GUA 200) is the best candidate of being representative of the mantle wedge isotopic composition prior to slab addition as it plots along the NHRL in the $^{207}Pb/^{204}Pb$ *vs* $^{206}Pb/^{204}Pb$ diagram (Fig. 5.8), and shows high ε_{Nd} and the least radiogenic Pb and Sr isotopic ratios among the samples of Group 2 and 3.

In the $^{207}Pb/^{204}Pb$ *vs* $^{206}Pb/^{204}Pb$ diagram (Fig. 5.15a), Group 2 and 3 samples define two distinct trends diverging from the pristine composition of the mantle wedge represented by the sample GUA 200: Group 2 and 3Q2 define a steep trend characterized by relatively low $^{206}Pb/^{204}Pb$ (18.17-18.29) and quite variable $^{207}Pb/^{204}Pb$ (15.51-15.60), whereas the rest of samples (including Group 3Q1 and 3T) cluster at higher $^{206}Pb/^{204}Pb$ (18.43-18.62) values. The isotopic composition of Group 3Q1 and 3T is consistent with mixing of the pre-subduction mantle with marine sediments (Fig. 5.15a), particularly with

small percentages (0.05-0.2%) of Cretaceous Atlantic pelagic sediments (Jolly et al. 2006 and references therein). The Téneme intrusive has the most radiogenic Pb isotopic ratios, indicative of a relative higher contribution of marine sediments in its source.

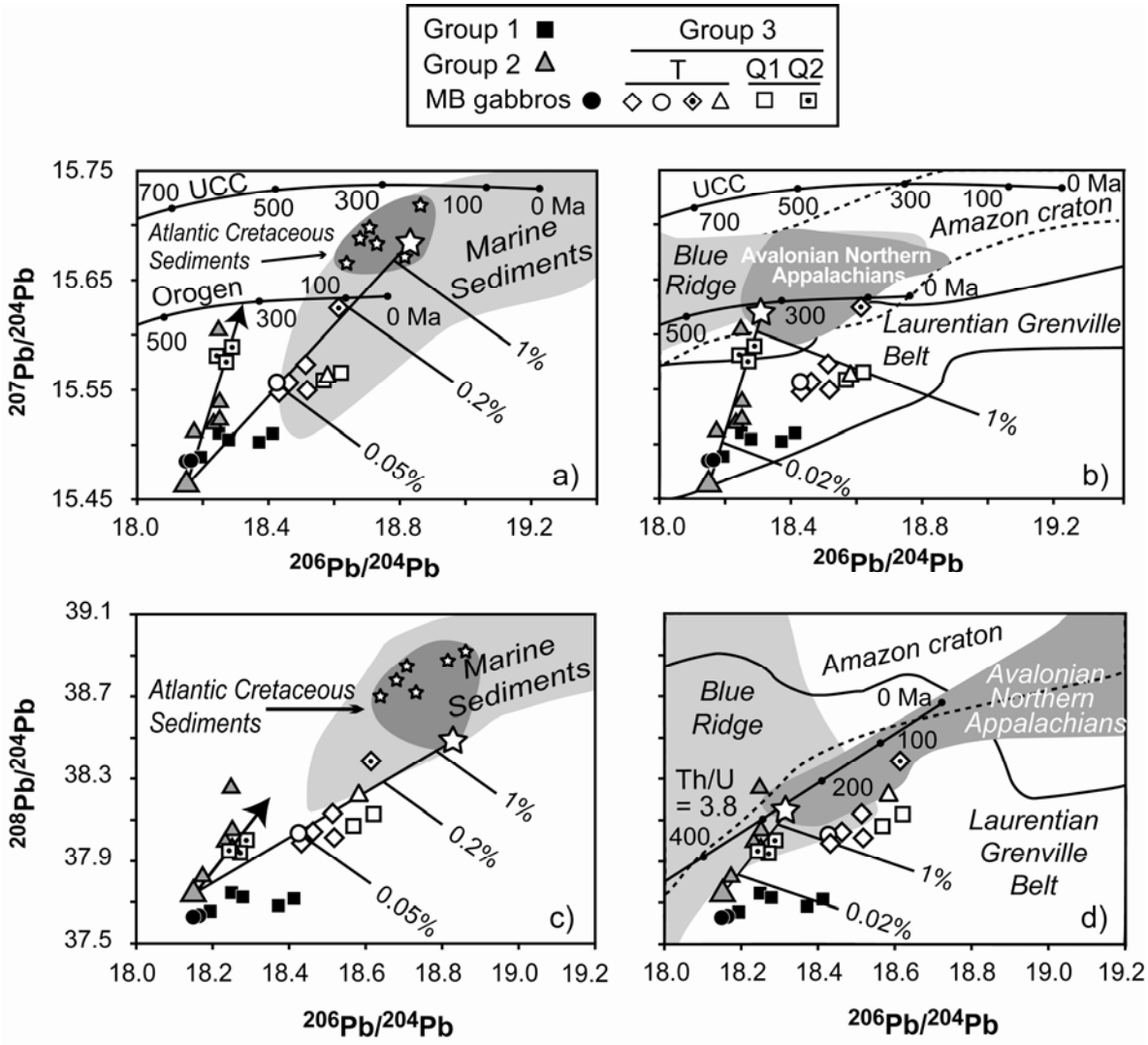

Figure 5.15 Whole rock Pb isotopic ratios of igneous rocks from eastern Cuba corrected for the radiogenic growth since 90 Ma. Symbols as in Figures 5.8 and 5.11. Light grey field of modern marine sediments in (a) and (c) from Ben Othman et al. (1989), Elliott et al. (1997) and Plank and Langmuir (1998); age-corrected ratios for Atlantic Cretaceous pelagic sediments (stars in dark grey fields) in (a) and (c) from Jolly et al. (2006) and references therein; orogenic and upper continental crust (UCC) curves from Doe and Zartman (1979). Fields of present-day ratios for Laurentian Grenville Belt (solid line), Blue Ridge Terrane and Amazon Craton (dashed line) in (b) and (d) from Tohver et al. (2004) and references therein; shaded area of the Avalonian Northern Appalachians continental crust from Ayuso and Bevier (1991). Pb isotopic growth line for average Th/U = 3.8 in (d) from Stacey and Kramers (1975). Mixing lines between the compositions of the assumed mantle wedge (largest grey triangle) and those of one Atlantic Cretaceous sediment and the Appalachians continental crust best fitting with the data (big stars) are shown.

On the other hand, Group 2 and 3Q2 volcanic rocks scatter toward lesser radiogenic $^{206}Pb/^{204}Pb$ compositions than marine sediments. In particular they point toward a crustal end-member characterized by lower $^{206}Pb/^{204}Pb$ ratios than the orogenic and upper continental crust at 100 Ma (the approximate age of eastern Cuba magmatism) (Doe and Zartman 1979). This feature indicates that the continental component involved in the genesis of these magmatic groups had a lower time-integrated μ ($^{238}U/^{204}Pb$) than the common upper continental crust. Taking into account the paleogeography of the Caribbean realm in the Late Cretaceous (e.g. Meschede and Frisch 1998; Pindell et al. 2006), North and South America are the two most likely sources of continental material entering the western Greater Antilles subduction zone. Despite the large number of potential candidates for the provenance of these continental sediments, only the Avalonian continental crust and the Blue Ridge terrane of the Appalachians range present the necessary Pb isotopic signature inferred for the continental mixing end-member involved in the genesis of Group 2 and 3Q2 (Fig. 5.15b). These domains exhibit $^{207}Pb/^{204}Pb$ ratios intermediate between the Laurentian Grenville Belt and the Amazon craton (Ayuso and Bevier 1991; Tohver et al. 2004) and are interpreted as exotic peri-Gondwanan continental terranes derived from South American Proterozoic crust subsequently incorporated to North America (Nance and Murphy 1994). The same tectonic evolution has been inferred for Northern Florida, Yucatán and Chortis blocks (Murphy et al. 2004 and references therein) that were located relatively close to the Cuban arc in the Late Cretaceous (e.g. Pindell et al. 2006). The Pb isotopic systematic of Group 2 and 3Q2 is in particular consistent with contamination of the mantle wedge with small percentages (< 1%) of a slab agent derived from detritic sediments of the North American exotic continental crust in the Appalachians (Fig. 5.15b).

The above inferences are further supported by the $^{208}Pb/^{204}Pb$ *vs* $^{206}Pb/^{204}Pb$ variations of the samples (Fig. 5.15c, d) that confirm the need of two different mixing trends involving Cretaceous Atlantic pelagic and Appalachian-derived continental sediments to account for the Pb isotopic systematics of Group 2 and 3. Group 2 and 3Q2 variations can be explained by mixing with an end-member characterized by a time-integrated Th/U ratio lower than 3.8 (average value of the Earth in the two-stage model of Stacey and Kramers 1975) as indicated by their relatively low $^{208}Pb/^{204}Pb$ ratios (Fig. 5.15d). This observation is much in keeping with the previous conclusion that the continental material involved in the Cuban paleo-arc derived from a relatively depleted continental crust with rather low time-integrated U/Pb and Th/U ratios. These compositions are characteristic of North American terranes and are significantly different from the signature of the Amazon craton (Tohver et al. 2004). The conclusions inferred on

the basis of the Pb isotopic systematics are further corroborated by the Nd-Sr isotopic ratios as Group 3Q2 generally exhibits lower ε_{Nd} (Fig. 5.16) and higher $^{87}Sr/^{86}Sr$ (Appendix 5) compared to Group 3Q1 and 3T volcanic rocks.

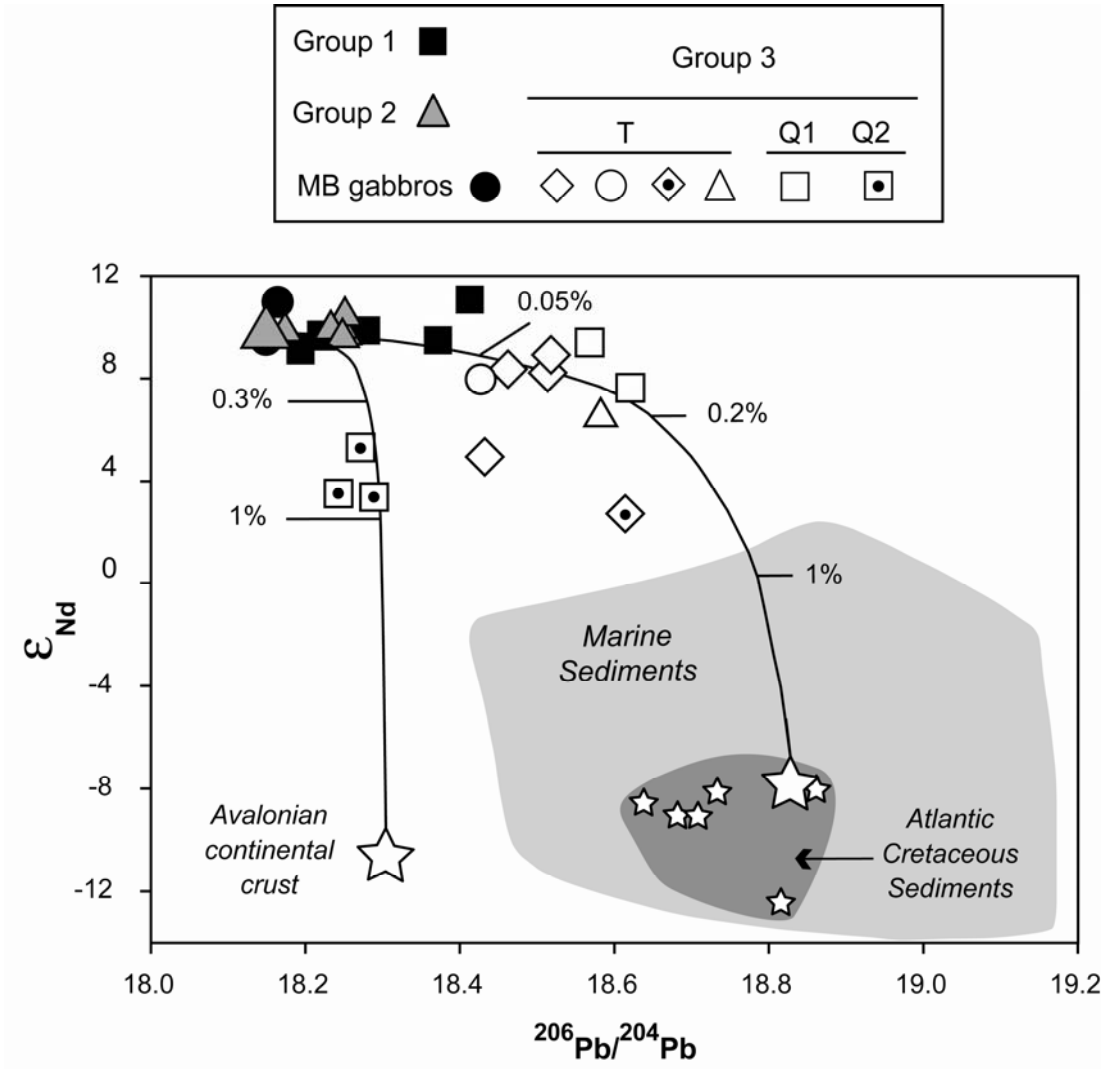

Figure 5.16 Whole rock ε_{Nd} *vs* $^{206}Pb/^{204}Pb$ systematics of igneous rocks from eastern Cuba corrected for the radiogenic growth since crystallization. Symbols and references of the fields as in Figure 5.15. Mixing lines between the compositions of the assumed mantle wedge (largest grey triangle) with one Atlantic Cretaceous sediment and the Avalonian continental crust (ε_{Nd}, corrected for the radiogenic growth since 90 Ma, from Samson et al. 2000) best fitting with the samples are shown.

Group 1 samples plot close to the average DMM Pb isotopic composition and the NHRL (Fig. 5.8); this is consistent with the absence of a conspicuous subduction component in this group (Fig. 5.7, 5.11). However, four samples of this suite show rather elevated $^{206}Pb/^{204}Pb$ ratios (Fig. 5.15) that are not observed in the plutonic rocks of the Moa-Baracoa ophiolitic massif thought to be cogenetic with Group 1 volcanics (Chapter 4,

Section 4.5.4). Only one volcanic sample (CEN 202) has relatively low radiogenic Pb isotopic ratios similar to the Moa-Baracoa plutonics (Fig. 5.15). This is also the only sample that has both MORB-like Nb/U and Ce/Pb ratios and shows no signs of U and Pb remobilization by hydrothermal fluids. The higher $^{206}Pb/^{204}Pb$ of some Group 1 volcanic rocks may be interpreted at first sight as the slight imprint of a subduction component. Yet their $^{208}Pb/^{204}Pb$ ratios are anomalously low and cannot be accounted by the contribution of Atlantic mafic oceanic crust or sediments (Fig. 5.8, 5.15c). Similar apparent discrepancies in the Pb isotopic composition have been reported between the Troodos sheeted dykes and related sulphide deposits (Booij et al. 2000), where it has been inferred to be due to late alteration processes (postdating the hydrothermal event) that assimilated Pb with a sedimentary-like isotopic signal but low $^{208}Pb/^{204}Pb$ ratio. If such model is also applicable to Group 1 samples, corrections for radiogenic growth since their extrusion would be insufficient to obtain the initial Pb isotopic composition preceding the disturbance of the U-Pb system by hydrothermal fluids. This indicates that the primary signature of the Group 1 volcanic rocks would be only preserved in the sample with the least radiogenic Pb isotopic ratios that are similar to those of the Moa-Baracoa gabbros (Fig. 5.15), supporting the genetic link between Group 1 volcanics and Moa-Baracoa plutonic rocks (Chapter 4, Section 4.5.4).

6. GEODYNAMIC SETTING OF THE MAGMATIC ACTIVITY RECORDED IN THE MAYARÍ-BARACOA OPHIOLITIC BELT AND THE SPATIALLY-RELATED CRETACEOUS IGNEOUS SUITES

6. GEODYNAMIC SETTING OF THE MAGMATIC ACTIVITY RECORDED IN THE MAYARÍ-BARACOA OPHIOLITIC BELT AND THE SPATIALLY-RELATED CRETACEOUS IGNEOUS SUITES

6.1. TECTONIC SETTING OF THE MOA-BARACOA AND MAYARÍ-CRISTAL OPHIOLITIC MASSIFS

The Moa-Baracoa and Mayarí-Cristal peridotites have mineral and whole-rock compositions characteristic of mantle sections from both ocean basins and supra-subduction settings (Fig. 4.7, 4.9, 4.10). In this way they are similar to Conical Seamount peridotites from the Izu-Bonin-Mariana forearc and to the South Sandwich forearc peridotites interpreted as residual mid-ocean ridge or back-arc mantle accreted on the forearc mantle lithosphere (Parkinson and Pearce 1998; Pearce et al. 2000).

I note that the oxygen fugacities displayed by the Mayarí-Baracoa melting residues (Fig. 4.15) are toward the upper end of the ocean ridge range (-3 < QFM < 0 according to Lee et al. 2003) which may support a back-arc setting with a slight supra-subduction zone signature for the Mayarí-Baracoa lithosphere. For the Mayarí-Cristal massif an ancient supra-subduction setting is corroborated by the mineral chemistry of spinel in dunites that indicates they formed when subduction-related (island arc tholeiitic) magmas interacted with mantle tectonites (Fig. 4.7d).

The mafic rocks of the Mayarí-Baracoa Ophiolitic Belt (gabbroic sills and dykes intruded in the mantle section and layered gabbros of the lower oceanic crust) display MORB-like or transitional MORB-IAT geochemical signatures (Fig. 4.13, 4.14) consistent with an origin at a mid-ocean ridge or back-arc spreading centre. This last interpretation is supported by the genetical link between the Moa-Baracoa cumulates and tectonically-related Morel volcanics (Fig. 4.17b) interpreted in this study as back-arc tholeiites as already proposed by Kerr et al. (1999).

I stress that Moa-Baracoa and Mayarí-Cristal massifs significantly differ in terms of field occurrence, mineral chemistry and geochemical characteristics. (1) The Moa-Baracoa massif shows a continuous plutonic section with a well-defined Moho transition zone, whereas both are absent in the Mayarí-Cristal massif (Fig. 4.1b). Moreover, (2) the

Mayarí-Cristal massif shows higher olivine Mg# and spinel Cr# in peridotites (Fig. 4.7a, b), (3) higher anorthite content in plagioclase from mafic rocks (Fig. 4.7c) and (4) a more depleted nature and slightly higher values of oxygen fugacity in melting residues (Fig. 4.15). I interpret these differences as evidence that the two massifs were not part of a single lithospheric section, but that the Mayarí-Cristal massif was a portion of lithosphere located closer to the paleo-arc than the Moa-Baracoa massif, as attested by a more important role of H_2O in its petrogenesis.

The inferred conclusions are consistent with the model of Iturralde-Vinent (1994) who provided evidences that the Mayarí-Baracoa Ophiolitic Belt is a portion of an original back-arc lithosphere. In this context, I propose a relatively close arc position for the original setting of the Mayarí-Cristal massif based on the stronger imprint of a subduction-related geochemical signature indicating the increasing influence of slab melts or fluids. This interpretation fits with the model of Gervilla et al. (2005) who related the Cr-rich chromitites hosted in the Mayarí-Cristal peridotites to island arc magmas generated from a highly depleted mantle source, and the Al-rich chromitites from the Moa-Baracoa massif to back-arc basin tholeiites produced by lower degrees of mantle melting or by melting of a less depleted source.

6.2. GEOCHEMICAL CLASSIFICATION OF THE CRETACEOUS IGNEOUS ROCKS FROM EASTERN CUBA IN THE FRAME OF THE CARIBBEAN MAGMATIC SUITES

Previous studies have classified the Cretaceous subduction-related magmatism in the Caribbean as belonging either to an island arc tholeiitic (La/Yb < 4; Th/Hf < 0.7) or calcalkaline suite (La/Yb > 4; Th/Hf > 0.7) mainly according to ratios involving the rare earth elements and/or the high-field strength elements (e.g. Jolly et al. 2001; Kerr et al. 2003 and references therein). Following this classification, the Cretaceous igneous suites from eastern Cuba belong to the island arc tholeiitic series (Fig. 5.6) generally associated with the Caribbean early island arc developed in Lower Cretaceous (Donnelly and Rogers 1980). However, this temporal classification is at odds with the paleontologic ages of the sediments intercalated with volcanic deposits that place the magmatic activity of eastern Cuba in Late Cretaceous (Cenomanian-Coniacian) (Iturralde-Vinent et al. 2006). This result is in keeping with the ~ 90 Ma Ar-Ar age derived in Chapter 5 (Fig. 5.9b) and indicates that igneous rocks with the geochemical signature characteristic of the Caribbean early island arc were also formed in Late Cretaceous (see also Proenza et al. 2006). Furthermore, as I have shown in Figures 5.5 and 5.6, some igneous suites from

eastern Cuba, i.e. the Téneme and Quibiján Formations (Group 3 in Chapter 5), classified as tholeiitic in terms of their La/Yb-Th/Hf ratios do not follow a tholeiitic evolutionary trend in terms of major elements. This incongruity is expected when the terms “tholeiitic” and “calcalkaline” are defined by different discriminants (Arculus 2003). So, in eastern Cuba arc rocks with moderate La/Yb-Th/Hf ratios record tholeiitic and calcalkaline evolutionary trends that reflect more intricate temporal and/or spatial variations of subduction magmatism than previously believed.

6.3. TECTONIC SETTING OF THE CRETACEOUS IGNEOUS SUITES FROM EASTERN CUBA AND GEODYNAMIC IMPLICATIONS FOR THE PALEO-CARIBBEAN REALM

Although the Late Cretaceous age of the eastern Cuba magmatism is adequately constrained, the relative ages of eruption and the time span of the different magmatic groups identified in Chapter 5 are presently unknown. These groups seem to overlap in time (Iturralde-Vinent et al. 2006) but given the uncertainties in their eruption age it is not possible to infer if this overlapping reflects temporal or spatial variations of the magmatism within the paleo-island arc. Many active subduction zones show systematic chemical variations of their magmatism along and across strike the volcanic front reflecting variable imprints of the slab component and extents of depletion of their mantle source (e.g. McCulloch and Gamble 1991; Woodhead et al. 1993; Arculus 1994; Kelemen et al. 2003b; Pearce et al. 2005). These chemical variations may be used to discriminate among different potential spatial/temporal scenarios for the genesis of the eastern Cuba magmatism. Thus, focusing the discussion on possible spatial variations of the magmatic activity, the increasing imprint of a slab component from the Group 1 to the Group 2 and 3 (Fig. 5.7) may reflect an increasing proximity to the arc volcanic front. In active subduction settings, these variations are observed both across strike (e.g. Hochstaedter et al. 2001; Sinton et al. 2003) or along strike in a back-arc basin formed by rifting of the pre-existing volcanic arc as is the case of the southern Marianas subduction zone (Pearce et al. 2005). In the first scenario the stronger contribution from the slab is generally coupled with relatively greater depletion of the mantle source of the arc volcanism, whereas in the second much more subtle or no variations in the depletion of the source are associated with the distance from the volcanic front (Pearce et al. 2005). As the mantle sources of Group 2 and 3 show not only a progressive stronger imprint of slab component(s) but are also significantly more depleted than Group 1 (Fig. 5.10, 5.11, 5.12), I conclude that the geochemical variability of the igneous suites from eastern Cuba likely reflects the across arc variation as that portrayed in Figure 6.1. This tectonic configuration fits with the

genetic relationships between the Mayarí-Baracoa ophiolitic gabbros and the volcanic rocks from eastern Cuba (Chapter 4, Section 4.5.4), and supports that Group 1 volcanics and the Moa-Baracoa ophiolite were originated at the same back-arc spreading centre.

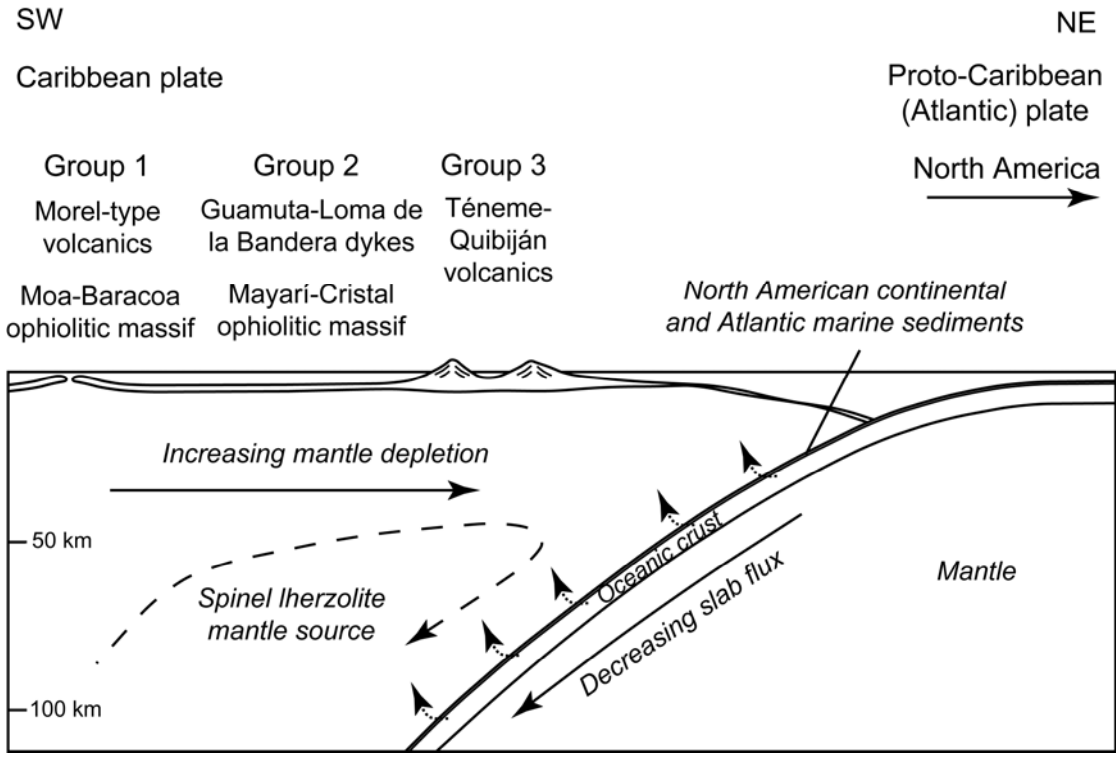

Figure 6.1 Proposed tectonic configuration of eastern Cuba in Late Cretaceous (pre-Campanian) with the inferred settings of the Moa-Baracoa and Mayarí-Cristal ophiolitic massifs and the Cretaceous igneous suites identified in Chapter 5. The dashed arrow symbolizes the hypothetical flow trajectory of the mantle in the subduction zone. Short dotted arrows represent the flux of fluid/melt from the subducting slab to the mantle wedge.

One point of recurring controversy in the models of the Caribbean tectonic evolution is the polarity of subduction of the Cretaceous Greater Antilles Arc (Kerr et al. 1999; Jolly et al. 2001 and references therein) and the age (Aptian *vs* Campanian) of subduction reversal from NE to SW dipping slab (Kerr et al. 2003; Pindell et al. 2006). The two main alternatives proposed in the literature are the south-westerly dipping subduction of the Proto-Caribbean (North American-Proto Atlantic) oceanic lithosphere beneath the Caribbean plate and the opposite north-easterly dipping geometry of the Caribbean plate (Pindell 1994; Pindell et al. 2006). The geochemical evidences provided in Chapter 5 (Section 5.5.3.2) of the involvement of North American continental sediments in the genesis of eastern Cuba magmatism (Fig. 5.15, 5.16) imply a SW subduction of the Proto-Caribbean ocean beneath the Caribbean plate during the Late Cretaceous (Fig. 6.1). Moreover, the pre-Campanian age of the eastern Cuba igneous suites supports models

that establish the onset of south-westward dipping subduction beneath the Great Caribbean Arc in the Aptian (Pindell et al. 2006; García-Casco et al. 2006). The involvement of continental sediments in the Cretaceous Greater Antilles subduction zone has been previously suggested by several authors (Lebron and Perfit 1994; Kerr et al. 1999) but so far has not been proved in the eastern domain of the Greater Antilles paleo-arc (Hispaniola, Puerto Rico, Virgin Islands) that generally shows a major contribution of marine sediments (e.g. Lebron and Perfit 1994; Jolly et al. 2001, 2006). These results then confirm that the Late Cretaceous Cuban arc was located in a setting relatively close to North America (Pindell 1994; Meschede and Frisch 1998) where inputs of detritic sediments from the paleo-north American continental margin into the Greater Antilles subduction zone were present but likely sporadic.

7. CONCLUSIONS - CONCLUSIONES

7. CONCLUSIONS

The Moa-Baracoa and Mayarí-Cristal massifs are two strongly faulted ophiolitic complexes occurring in eastern Cuba. These massifs are mainly constituted by a mantle section made up of harzburgite tectonites and minor sub-concordant dunites cut by mafic and ultramafic dykes. In terms of field occurrence the two massifs strikingly differ. Moa-Baracoa displays a well developed Moho transition zone constituted by dunites, harzburgites and minor gabbroic sills intruded by relatively abundant mafic dykes; dunites in the Moho transition zone are locally impregnated by basaltic melts testifying pervasive interaction of the mantle with percolating magmas. Upward in the reconstructed section, the Moa-Baracoa massif shows a plutonic crustal unit mainly composed of layered olivine (orthopyroxene) gabbros. On the other hand, the Moho transition zone and the plutonic crustal unit are absent in the Mayarí-Cristal lithospheric section. Both the ophiolitic massifs lack exposures of isotropic gabbros and diabase sheeted-dyke complexes, and are in tectonic contact with Upper Cretaceous volcanic suites: the Morel and Quibiján Formations with the Moa-Baracoa massif and the Téneme Formation with the Mayarí-Cristal massif.

Modal abundances, major and trace element whole rock compositions of Moa-Baracoa and Mayarí-Cristal harzburgites indicate that they are residues of high extents (20-30%) of partial melting under intermediate fO_2 conditions (-1 < QFM < 1); in particular the harzburgites from the southern region of Mayarí-Cristal record the highest melting degrees. Peridotites extensively interacted by reactive porous flow with percolating melts leading to selective enrichment of Th, Nb, Ta and light rare earth elements in refractory melting residues. Dunites originated by interaction of harzburgite tectonites with orthopyroxene-undersaturated melts in two different settings. In Moa-Baracoa massif, dunites formed by melt/rock reaction close to the paleo-Moho; dunites acted as channels for melt arriving to the Moho transition zone where they generated impregnated dunites due to clinopyroxene + plagioclase crystallization/segregation upon cooling. Dunites in the Mayarí-Cristal massif are likely related to mantle-melt reaction during melt extraction into dunite channels deeper in the mantle. Low MgO/SiO_2 whole rock ratios in peridotites are caused by relative MgO loss of 6 wt% on average due to intense seafloor weathering.

The calculated rare earth element patterns and Mg-numbers of melts in trace-element exchange equilibrium with Moa-Baracoa cumulate gabbros (sills and dikes in the

Moho transition zone and crustal layered gabbros) show that they are cogenetic with Morel back-arc volcanics. Conversely, the studied cumulate dyke intruding the Mayarí-Cristal peridotites is not in trace element equilibrium with the spatially-related arc volcanics of the Téneme Formation.

Several Upper Cretaceous igneous suites are spatially-related with the Moa-Baracoa and Mayarí-Cristal ophiolitic massifs. The Moa-Baracoa massif is in tectonic contact with the volcanic rocks of the Morel and Quibiján Formations, whereas the Mayarí-Cristal peridotites are cut by mafic dykes especially abundant in the Guamuta-Loma de la Bandera area and tectonically overlie the igneous rocks of the Téneme Formation. These igneous suites show three main geochemical signatures that mostly reflect the different extent of depletion and the variable imprint of a subduction component in their mantle sources. Group 1 (Morel-type volcanics) consists of basaltic tholeiites formed by variable melting degrees (< 5-20%) of a moderately depleted mantle (E-DMM). They exhibit MORB-like compositions with a slight affinity to back-arc basin basalts. Group 2 (Guamuta-Loma de la Bandera dykes) derived by similar melting degrees of a more depleted mantle that was significantly overprinted by a subduction component. The sources of Group 3T (Téneme igneous rocks) and 3Q (Quibiján volcanics) show a depleted signature coupled with high degrees of melting (20-35%) and an evident subduction-related imprint. Melting mainly occurred at depths (< 85 km) characteristic of the spinel-lherzolite stability field.

The Nb/Ta ratios in the primitive arc lavas of Group 3Q do not reflect the highly depleted composition of their mantle source but fingerprint the contributions of two distinct slab-derived components with different trace element and isotopic signatures in Group 3Q1 and 3Q2, respectively. The highly subchondritic Nb/Ta ratio of one of these agents was not created by the dehydration/melting of the slab but was inherited from the composition of the subducted upper continental material. These sediments derived from the paleo-north American continental margin and were intercalated with marine deposits from the Atlantic Ocean; both these sedimentary materials entered the Cuban paleo-subduction zone and mixed in small percentages (< 1%) with the depleted mantle sources of Group 2 and 3Q2, and Group 3T and 3Q1, respectively.

I propose that the Moa-Baracoa and Mayarí-Cristal massifs represent two portions of back-arc lithosphere. Moa-Baracoa massif displays mid ocean ridge-like signature and melting oxygen fugacities consistent with an original position located close to the back-arc spreading centre. Mayarí-Cristal lithosphere exhibits an increasing role of H_2O in its petrogenesis and evidences of interaction with subduction-related (island arc tholeiitic)

magmas, attesting for an original setting located closer to the paleo-volcanic arc than Moa-Baracoa. The variable depletion and influence of a subduction component in the mantle sources of the Cretaceous igneous rocks spatially-related with the ophiolites implicate temporal and/or spatial compositional variations more complex than previously considered for the eastern Cuba magmatism. The different geochemical signatures displayed by these suites may reflect across arc different settings of the igneous activity. In this context Morel-type volcanics were probably extruded at a back-arc ocean ridge and were part of the Moa-Baracoa lithospheric section. On the other hand, the Guamuta-Loma de la Bandera island arc tholeiitic dykes were generated closer to the paleo-volcanic arc than the Morel volcanics in a setting probably coincident with the Mayarí-Cristal lithospheric section. Finally the Quibiján-Téneme calcalkaline rocks likely record the magmatic activity produced at the paleo-island arc.

The involvement of North American and Atlantic sediments in the sources of eastern Cuba igneous rocks indicates that the Proto-Caribbean (Proto-Atlantic) lithosphere was subducting beneath the Greater Antilles Arc in Late Cretaceous (pre-Campanian). Morel and Quibiján extrusives record two distinct volcanic activities and should be separated into different formations, conversely to previously believed. On the other hand, the volcanic suites so far distinguished in the Téneme and Quibiján Formations should be coupled on the basis of their coincident whole rock compositions.

CONCLUSIONES

El Cinturón Ofiolítico Mayarí-Baracoa (Cuba oriental) se compone de dos complejos ofiolíticos intensamente fallados: el macizo de Moa-Baracoa, situado en la región oriental del área de estudio, y el macizo de Mayarí-Cristal, que se encuentra en la región occidental. Estos dos complejos están formados principalmente por una secuencia mantélica constituida por harzburgitas con textura de tectonitas y menores cantidades de niveles duniticos, sub-concordantes con la foliación en las harzburgitas. Ambas litologías están intruidas por diques máficos y ultramáficos. En términos litoestratigráficos los dos macizos difieren considerablemente. El macizo de Moa-Baracoa presenta una zona de transición manto/corteza (Moho transition zone) bien desarrollada constituida por dunitas, harzburgitas y, en menor medida, sills gabróicos, intruida por diques máficos relativamente abundantes. Las dunitas en la zona de transición manto/corteza están localmente impregnadas por fundidos basálticos lo que evidencia una interacción

pervasiva entre el manto y fundidos percolantes. Hacia arriba en la secuencia litoestratigráfica reconstruida, el macizo de Moa-Baracoa presenta una unidad plutónica cortical compuesta principalmente por gabros olivinicos bandeados con escaso ortopiroxeno. Por otro lado, tanto la zona de transición manto/corteza como la unidad plutónica cortical están ausentes en la secuencia litosférica del macizo de Mayarí-Cristal. Ambos macizos ofiolíticos carecen de afloramientos de la unidad de gabros isotrópicos y del complejo de diques paralelos, y están en contacto tectónico con rocas volcánicas de edad Cretácico Superior: las rocas de las Formaciones Morel y Quibiján con el macizo de Moa-Baracoa y las rocas de la Formación Téneme con el macizo de Mayarí-Cristal.

Las abundancias modales y las composiciones de la roca total, tanto en elementos mayores como traza, de las harzburgitas del Cinturón Ofiolítico Mayarí-Baracoa indican que estas rocas son residuos generados mediante altas tasas (20-30%) de fusión parcial, la cual tuvo lugar, principalmente, en condiciones de fugacidad de oxigeno intermedias (fO_2: -1 < QFM < 1); en particular, las harzburgitas de la región meridional del macizo de Mayarí-Cristal registran las tasas de fusión más elevadas. Las peridotitas interactuaron intensamente con fundidos que circulaban intersticialmente mediante flujo poroso en el manto, causando un enriquecimiento relativo en Th, Nb, Ta y en elementos de las tierras raras ligeras en los residuos de fusión. Las dunitas se generaron por interacción de las harzburgitas con fundidos subsaturados en ortopiroxeno en dos escenarios diferentes. En el macizo de Moa-Baracoa, las dunitas se formaron por reacción entre el manto y los fundidos percolantes en proximidad de la paleo-Moho; las dunitas actuaron como canales preferenciales para los fundidos que fluían en la zona de transición manto/corteza donde localmente se generaron dunitas impregnadas por cristalización/segregación de clinopiroxeno y plagioclasa. Las dunitas del macizo de Mayarí-Cristal están probablemente relacionadas con reacciones manto/fundido asociadas a la extracción de los fundidos en canales duniticos más profundos en el manto. Las bajas razones MgO/SiO_2 observadas en las peridotitas fueron causadas por la pérdida promedio del 6% en peso de MgO, producida por la intensa alteración sufrida por estas rocas en el fondo del mar.

Los espectros de tierras raras y los números de Mg calculados para los fundidos en equilibrio con los gabros cumulíticos del macizo de Moa-Baracoa (sills y diques de la zona de transición manto/corteza y gabros bandeados de la corteza) indican que estas rocas y las volcánicas de la Formación Morel derivaron de un mismo magma parental. Por otro lado, la muestra estudiada de los diques cumuliticos intruidos en las peridotitas

del macizo de Mayarí-Cristal no está en equilibrio geoquímico con las rocas volcánicas de la Formación Téneme.

Varios conjuntos de rocas ígneas de edad Cretácico Superior están relacionadas espacialmente con los macizos ofiolíticos de Moa-Baracoa y de Mayarí-Cristal. El macizo de Moa-Baracoa está en contacto tectónico con las rocas volcánicas de las Formaciones Morel y Quibiján, mientras que las peridotitas de Mayarí-Cristal están cortadas por diques máficos, especialmente abundantes en el área de Guamuta-Loma de la Bandera, y generalmente yacen encima de las rocas ígneas de la Formación Téneme por contacto tectónico. Estas rocas ígneas muestran tres signaturas geoquímicas principales que reflejan el diferente grado de empobrecimiento y la diferente influencia de un componente de subducción en sus fuentes mantélicas. El Grupo 1 (rocas afines a la Formación Morel) está constituido por toleitas basálticas generadas por tasas de fusión variables (< 5-20%) de un manto moderadamente empobrecido (E-DMM). Estas rocas tienen composiciones tipo MORB con una ligera afinidad con los basaltos formados en una cuenca de trasera de arco. Las rocas del Grupo 2 (diques de la región de Guamuta-Loma de la Bandera) se formaron por tasas de fusión similares, a partir de un manto más empobrecido cuya composición fue afectada considerablemente por el flujo de un componente de subducción. Las fuentes del Grupo 3T (rocas ígneas de la Formación Téneme) y 3Q (rocas volcánicas de la Formación Quibiján) muestran una composición fuertemente empobrecida asociada a altas tasas de fusión (20-35%) y a una evidente influencia de un componente de subducción. La fusión ocurrió principalmente a profundidades inferiores a 85 km, características del campo de estabilidad de las lherzolitas con espinela.

La razón Nb/Ta en las lavas primitivas del Grupo 3Q no refleja la composición altamente empobrecida de su fuente mantélica sino que registra las contribuciones de dos componentes de subducción distintos, con diferentes signaturas en elementos traza e isótopos radiogénicos de Pb y Nd. La razón Nb/Ta altamente sub-condrítica de uno de estos componentes no fue creada por deshidratación/fusión de la placa que subducía sino que fue heredada de la composición de los sedimentos continentales reciclados. Este material derivó del paleo-margen continental Norteamericano y estaba intercalado con depósitos marinos procedentes del Océano Atlántico; ambos tipos de sedimentos entraron en la zona de subducción del paleo-arco cubano y se mezclaron en pequeñas proporciones (< 1%), respectivamente, con las fuentes mantélicas del Grupo 2 y 3Q2, y del Grupo 3T y 3Q1.

Los macizos ofiolíticos de Moa-Baracoa y Mayarí-Cristal representan dos porciones litosféricas probablemente generadas en una cuenca de trasera de arco. El

macizo de Moa-Baracoa muestra una signatura geoquímica similar a la que caracteriza un ambiente de dorsal medio-oceánica y presenta condiciones de fugacidad de oxigeno compatibles con una posición original próxima a un centro de expansión de trasera de arco. La litosfera del macizo de Mayarí-Cristal muestra una mayor influencia de H_2O en su petrogénesis e indicios de interacción con magmas toleíticos de arco de isla, sustentando la conclusión que su posición tectónica original estuviera más próxima al frente del paleo-arco volcánico que la litosfera representada por el macizo de Moa-Baracoa. La variabilidad en el grado de empobrecimiento y en la influencia de un componente de subducción registrada por las fuentes de las rocas ígneas Cretácicas de Cuba oriental implica unas variaciones temporales y/o espaciales más complejas de lo que hasta ahora se consideraba para el magmatismo Cretácico de esta región. Las diferentes signaturas geoquímicas presentadas por estas series magmáticas pueden reflejar diferentes ambientes geodinámicos de la actividad ígnea, alineados en dirección perpendicular al frente volcánico. En esta visión, las rocas volcánicas afines a la Formación Morel (Grupo 1) pudieron haber extruido en una dorsal oceánica de trasera de arco y pasaron a formar parte de la secuencia litosférica del macizo de Moa-Baracoa. Por otro lado, los diques intrusivos con afinidad de toleitas de arco, que afloran especialmente en el área de Guamuta-Loma de la Bandera (Grupo 2), fueron generados más cerca del paleo-arco volcánico que las rocas de la Formación Morel, en un ambiente geodinámico probablemente coincidente con la secuencia litosferica del macizo de Mayarí-Cristal. Finalmente, las rocas calcoalcalinas pertenecientes a las Formaciones Téneme y Quibiján registran la actividad magmática producida en el frente volcánico del antiguo paleo-arco cubano.

La implicación de sedimentos procedentes del Océano Atlántico y del continente Norteamericano en las fuentes de las rocas ígneas Cretácicas de Cuba oriental indica que la litosfera Proto-Caribeña (Proto-Atlántica) fue subduciendo debajo del arco de las Antillas Mayores en el Cretácico Superior (Pre-Campaniense). Las rocas volcánicas de tipo Morel y Quibiján registran dos actividades magmáticas diferentes y tienen que ser separadas en distintas formaciones, contrariamente a lo considerado previamente. Por otro lado, las suites volcánicas hasta ahora diferenciadas en las Formaciones Téneme y Quibiján tendrían que ser asociadas, basándose en sus signaturas geoquímicas coincidentes.

REFERENCES

REFERENCES

Alt JC, Teagle DAH (2003) Hydrothermal alteration of upper oceanic crust formed at a fast-spreading ridge: mineral, chemical, and isotopic evidence from ODP Site 801. Chemical Geology 201:191-211

Anderson TH, Schmidt VA (1983) The evolution of Middle America and the Gulf of Mexico-Caribbean Sea region during Mesozoic time. Geological Society of America Bulletin 94:941-966

Andó J, Harangi S, Szkmány B, Dosztály L (1996) Petrología de la Asociación Ofiolítica de Holguín. In: Iturralde-Vinent MA (ed) Ofiolitas y Arcos Volcanicos de Cuba. IUGS-UNESCO Project 364, Caribbean Ophiolites and Volcanic Arcs, Special Contribution, vol 1, pp 154-178, Miami

Arai S, Matsukage K (1996) Petrology of the gabbro-troctolite-peridotite complex from Hess Deep, Equatorial Pacific: implications for mantle-melt interaction within the oceanic lithosphere. In: Mevel C, Gillis KM, Allan JF, Meyer PS (eds) Proceedings of the Ocean Drilling Program, Scientific Results, vol 147, pp 135-155

Arculus RJ (1994) Aspects of magma genesis in arcs. Lithos 33:189-208

Arculus RJ (2003) Use and Abuse of the Terms Calcalkaline and Calcalkalic. Journal of Petrology 44(5):929-935

Armstrong RL (1968) A model for Sr and Pb isotope evolution in a dynamic earth. Review of Geophysics 6:175-199

Armstrong RL (1981) Radiogenic isotopes: the case for crustal recycling on a near steady-state no-continental growth Earth. Philosophical Transactions of the Royal Society of London, Series A, 301:443-472

Asimow PD (1999) A model that reconciles major- and trace-element data from abyssal peridotites. Earth and Planetary Science Letters 169:303-319

Aubouin J, Baltuck M, Arnott RJ, Bourgois J, Filewiez M, Helm R, Kvenvolden KA, Lienert B, Mc Donald T, Mc Dougall K, Ogawa Y, Taylor E, Winsborough B (1982) Leg 84 of the Deep Sea Drilling Project, subduction without accretion, Middle America Trench off Guatemala. Nature 297:458-460

Auzende A, Devouard B, Guillot S, Daniel I, Baronnet A, Lardeaux JM (2002) Serpentinites from Central Cuba: petrology and HRTEM study. European Journal of Mineralogy 14:905-914

Ayuso RA, Bevier M (1991) Regional differences in Pb isotopic compositions of feldspars in plutonic rocks of the Northern Appalachian Mountains, U.S.A. and Canada: a geochemical method of terrane correlation. Tectonics 10(1):191-312

Baker MB, Beckett JR (1998) The origin of abyssal peridotites: a reinterpretation of constraints based on primary bulk compositions. Earth and Planetary Science Letters 171:49-61

Baker MB, Stolper EM (1994) Determining the composition of high-pressure melts using diamond aggregates. Geochimica et Cosmochimica Acta 58:2811-2827

Ball MM, Harrison CGA, Supko PR (1969) Atlantic opening and the origin of the Caribbean. Nature 223:167-168

Barrell J (1914) The strength of the Earth's crust (I). Geologic tests of the limits of strength. Journal of Geology 22:28-48

Beard JS (1986) Characteristic Mineralogy of Arc-Related Cumulate Gabbros-Implications for the Tectonic Setting of Gabbroic Plutons and for Andesite Genesis. Geology 14(10):848-851

Beccaluva L, Coltorti M, Giunta G, Siena F (2004) Tethyan vs. Cordilleran ophiolites: a reappraisal of distinctive tectono-magmatic features of supra-subduction complexes in relation to the subduction mode. Tectonophysics 393:163-174

Bédard JH (1993) Oceanic crust as a reactive filter: Synkinematic intrusion, hybridization, and assimilation in an ophiolitic magma chamber, western Newfoundland. Geology 21:77-80

Bédard JH (1994) A procedure for calculating the equilibrium distribution of trace elements among the minerals of cumulate rocks, and the concentration of trace elements in the coexisting liquids. Chemical Geology 118:143-153

Bedini RM, Bodinier JL (1999) Distribution of incompatible trace elements between the constituents of spinel peridotite xenoliths: ICP-MS data from the East African Rift. Geochimica et Cosmochimica Acta 63(22):3883-3900

Bellizzia A, Dengo G (1990) The Caribbean mountain system, northern South America; A summary. In: Dengo G, Case J (eds) The Geology of North America, vol H, The Caribbean Region, pp 167-175. Geological Society of America

Ben Othman D, White WM, Patchett J (1989) The geochemistry of marine sediments, island arc magma genesis, and crust-mantle recycling. Earth and Planetary Science Letters 94:1-21

Blein O, Guillot S, Lapierre H, Mercier de Lépinay B, Lardeaux JM, Millan Trujillo G, Campos M, Garcia A (2003) Geochemistry of the Mabujina Complex, Central Cuba: Implications on the Cuban Cretaceous Arc Rocks. The Journal of Geology 111:89-101

Bodinier JL, Godard M (2003) Orogenic, Ophiolitic, and Abyssal Peridotites. In: Carlson RW (ed) The Mantle and Core, Treatise on Geochemistry, vol 2, pp 103-170. Elsevier

Bodinier JL, Vasseur G, Vernières J, Dupuy C, Fabries J (1990) Mechanisms of mantle metasomatism-geochemical evidence from the Lherz orogenic peridotite. Journal of Petrology 31(3):597-628

Bodinier JL, Merlet C, Bedini RM, Simien F, Remaidi M, Garrido CJ (1996) Distribution of niobium, tantalum, and other highly incompatible trace elements in the lithospheric mantle: The spinel paradox. Geochimica et Cosmochimica Acta 60(3):545-550

Boiteau A, Michard A, Saliot P (1972) Métamorphisme de haute pression dans le complexe ophiolitique du Purial (Oriente, Cuba). Comptes Rendus de l'Academie des Sciences 274:2137-2140

Bonatti E, Michael JP (1989) Mantle peridotites from continental rifts to ocean basins to subduction zones. Earth and Planetary Science Letters 91:297-311

Bonatti E, Honnorez J, Ferrara G (1971) Peridotite-gabbro-basalt complex from the equatorial mid-Atlantic ridge. Philosophical Transactions of the Royal Society of London, Series A, 268:385-402

Booij E, Bettison-Varga L, Farthing D, Staudigel H (2000) Pb-isotope systematics of a fossil hydrothermal system from the Troodos ophiolite, Cyprus: Evidence for a polyphased alteration history. Geochimica et Cosmochimica Acta 64:3559-3569

Boudier F, Nicolas A (1985) Harzburgite and lherzolite subtypes in ophiolitic and oceanic environments. Earth and Planetary Science Letters 76:84-92

Boudier F, Nicolas A (1988) The ophiolite of Oman. Tectonophysics, Special issue, vol 151, pp 1-410

Boudier F, Nicolas A (1995) Nature of the Moho Transition Zone in the Oman Ophiolite. Journal of Petrology 36(3):777-796

Boyd FR (1989) Compositional distinction between oceanic and cratonic lithosphere. Earth and Planetary Science Letters 96:15-26

Brandon AD, Draper DS (1996) Constraints on the origin of the oxidation state of mantle overlying subduction zones: An example from Simcoe, Washington, USA. Geochimica et Cosmochimica Acta 60:1739-1749

Brenan J, Shaw HF, Ryerson FJ, Phinney DL (1995) Mineral-aqueous fluid partitioning of trace elements at 900 ºC and 2.0 GPa: Constraints on the trace element chemistry of mantle and deep crustal fluids. Geochimica et Cosmochimica Acta 59:3331-3350

Browning P, Roberts S, Alabaster T (1989) Fine-scale modal layering and cyclic units in ultramafic cumulates from the CY-4 borehole, Troodos ophiolite: evidence for an open system magma chamber. In: Gibson IL, Malpas J, Robinson PT, Xenophontos C (eds) Drillhole CY-4, the Troodos Ophiolite, Cyprus (Cyprus Crustal Study Project: Initial Report, Hole CY-4), pp 193-220. Geological Survey of Canada

Burke K (1988) Tectonic evolution of the Caribbean. Annual Reviews of Earth and Planetary Sciences 16:201-230

Calais E, Béthoux N, Mercier de Lépinay B (1992) From transcurrent faulting to frontal subduction: a seismotectonic study of the northern Caribbean Plate boundary from Cuba to Puerto Rico. Tectonics 11:114-123

Canil D (2004) Mildly incompatible elements in peridotites and the origins of mantle lithosphere. Lithos 77:375-393

Cannat M, Lagabrielle Y, Bougault H, Casey J, de Coutures N, Dmitriev L, Fouquet Y (1997) Ultramafic and gabbroic exposures at the Mid-Atlantic Ridge: geological mapping in the 15 degrees N region. Tectonophysics 279:193-213

Case JE, MacDonald WD, Fox PJ (1990) Caribbean crustal provinces; Seismic and gravity evidence. In: Dengo G, Case J (eds) The Geology of North America, vol H, The Caribbean Region, pp 15-36. Geological Society of America

Casey JF (1997) Comparison of major and trace element geochemistry of abyssal peridotites and mafic plutonic rocks with basalt from the MARK region of the mid-Atlantic ridge. In: Karson JA, Cannat M, Miller DJ, Elthon D (eds) Mid-Atlantic Ridge: Leg 153, Sites 920-924, ODP Proceeding Scientific Results, vol 153, pp 181-241. College Station

Cazañas X, Proenza JA, Kysar-Mattietti G, Lewis J, Melgarejo JC (1998) Rocas volcánicas de la series Inferior y Media del Grupo El Cobre en la Sierra Maestra (Cuba Oriental): volcanismo generado en un arco de islas tholeiítico. Acta Geologica Hispanica 33:57-74

Ceuleneer G, Rabinowicz M (1992) Mantle Flow and Melt Migration beneath Oceanic Ridges: Models derived from Observations in Ophiolites. In: Phipps Morgan J, Blackman DK, Sinton JM (eds) Mantle Flow and Melt Generation at Mid-Ocean Ridges. Geophysical Monograph Series, vol 71, pp 123-154. American Geophysical Union

Chase CG (1981) Oceanic island Pb: two-stage histories and mantle evolution. Earth and Planetary Science Letters 52:277-284

Cobiella J (1978) Una melange en Cuba oriental. La Minería en Cuba 4:46-51

Cobiella J (1988) El vulcanismo paleogénico cubano. Apuntes para un nuevo enfoque. Tecnológica 18(4):25-32

Cobiella J, Campos M, Boiteau A, Quintas F (1977) Geología del flanco sur de la Sierra del Purial. La Minería en Cuba 3(1):54-62

Cobiella-Reguera JL (2002) Remains of oceanic lithosphere in Cuba. types, origins and emplacement ages. In: Jackson T (ed) Caribbean Geology into the Third Millennium, Transactions of the Fifteenth Caribbean Geological Conference, pp 35-46. University of the West Indies

Cobiella-Reguera JL (2005) Emplacement of Cuban Ophiolites. Geologica Acta 3:273-294

Coleman RG (1977) Ophiolites: Ancient Oceanic Lithosphere? Springer-Verlag, p 229

Condie KC (1997) Plate Tectonics and Crustal Evolution. Butterworth Heienemann, p 282

Constantin M (1995) Petrologie des gabbros et peridotites de la dorsale Est-Pacifique: la transition croute-manteau aux dorsale rapides. PhD thesis, Universitè de Bretagne occidentale, Brest, p 286

Cox KC (1991) A superplume event in the mantle. Nature 352:564-565

Crock JG, Lichte FE (1982) Determination of rare earth elements in geologic materials by inductively couple argon plasma/atomic emission spectrometry. Analytical Chemistry 54:1329-1332

Davidson JP (1987) Crustal contamination *versus* subduction zone enrichment: Examples from the Lesser Antilles and implications for mantle source compositions of island arc volcanic rocks. Geochimica et Cosmochimica Acta 51:2185-2198

Díaz de Villalvilla L, Dilla M (1985) Proposición para una división de la llamada Formación Tobas (Provincia de Cienfuegos, Villa Clara y Sancti Spiritus). Serie Geológica del Centro de Investigaciones Geológicas (Cuba) 1:133-149

Dick HJB (1989) Abyssal peridotites, very slow spreading ridges and ocean ridge magmatism. In: Magmatism in the Ocean Basins. Geological Society of London Special Publications, vol. 42, pp 71-105

Dick HJB, Bullen T (1984) Chromian Spinel as a Petrogenetic Indicator in Abyssal and Alpine-Type Peridotites and Spatially Associated Lavas. Contributions to Mineralogy and Petrology 86(1):54-76

Dick HJB, Fisher RL, Bryan WB (1984) Mineralogic Variability of the Uppermost Mantle Along Mid-Ocean Ridges. Earth and Planetary Science Letters 69(1):88-106

Dilek Y, Moores EM, Elthon D, Nicolas A (2000) Ophiolites and Oceanic Crust; New insights from Field Studies and the Ocean Drilling Program, Geological Society of America Special Papers, vol 349, p 466

Doe BR, Zartman RE (1979) Plumbotectonics, the Phanerozoic. In: Barnes H (ed) Geochemistry of Hydrothermal Ore Deposits, pp 22-70. Wiley-Interscience, New York

Doherty W (1989) An internal standardization procedure for the determination of yttrium and the rare earth elements in geological materials by inductively coupled plasma mass spectrometry. Spectrochemica Acta 44:263-280

Donnelly KE, Goldstein SL, Langmuir CH, Spiegelman M (2004) Origin of enriched ocean ridge basalts and implications for mantle dynamics. Earth and Planetary Science Letters 226:347-366

Donnelly TW (1989) Geologic history of the Caribbean and Central America. In: Bally AW, Palmer AR (eds) The Geology of North America-An overview, vol A, pp 299-321. Geological Society of America

Donnelly TW (1994) The Caribbean Sea Floor. In: Donovan SK, Jackson TA (eds) Caribbean Geology: An Introduction, pp 41-64. University of West Indies Publishers' Association, Kingston

Donnelly TW, Rogers JJW (1980) Igneous Series in Island Arcs: The Northeastern Caribbean Compared With Worldwide Island-Arc Assemblages. Bulletin of Volcanology 43(2):347-382

Donnelly TW, Beets D, Carr MJ, Jackson T, Klaver G, Lewis J, Maury RC, H. S, Smith AL, Wadge G, Westercamp D (1990) History and tectonic setting of Caribbean magmatism. In: Dengo G, Case J (eds) The Geology of North America, vol H, The Caribbean Region, pp 339-374. Geological Society of America

Draper G, Barros JA (1994) Cuba. In: Donovan SK, Jackson TA (eds) Caribbean Geology: An Introduction, pp 65-86. University of West Indies Publishers' Association, Kingston

Draper G, Dengo G (1990) History of the geological investigation in the Caribbean region. In: Dengo G, Case J (eds) The Geology of North America, vol H, The Caribbean Region, pp 1-14. Geological Society of America

Draper G, Jackson TA, Donovan SK (1994) Geologic Provinces of the Caribbean Region. In: Donovan SK, Jackson TA (eds) Caribbean Geology: An Introduction, pp 3-12. University of West Indies Publishers' Association, Kingston

Draper G, Gutiérrez G, Lewis J (1996) Thrust emplacement of the Hispaniola peridotite belt: Orogenic expression of the mid-Cretaceous Caribbean arc polarity reversal? Geology 24(12):1143-1146

Duncan RA, Hargraves RB (1984) Plate tectonic evolution of the Caribbean region in the mantle reference frame. In: Bonini WE, Hargraves RB, Shagam R (eds) The Caribbean-South American Plate boundary and regional tectonics. Geological Society of America Memoir, vol 162, pp 81-84

Eggins SM, Woodhead JD, Kinsley LPJ, Mortimer GE, Sylvester P, McCulloch MT, Hergt JM, Handler MR (1997) A simple method for the precise determination of > 40 trace

elements in geological samples by ICPMS using enriched isotope internal standardization. Chemical Geology 134:311-326

Eldholm O, Coffin MF (2000) Large igneous provinces and plate tectonics. In: Richards MA, Gordon RG, van der Hilst RD (eds) The History and Dynamics of Global Plate Motions. Geophysical Monograph Series, vol 121, pp 309-326. American Geophysical Union

Elliott T (2003) Tracers of the slab. In: Eiler J (ed) Inside the Subduction Factory. Geophysical Monograph Series, vol 138, pp 23-45. American Geophysical Union

Elliott T, Plank T, Zindler A, White W, Bourdon B (1997) Element transport from slab to volcanic front at the Mariana arc. Journal of Geophysical Research 102:14991-15019

Escartin J, Cannat M (1999) Ultramafic exposures and the gravity signature of the lithosphere near the Fifteen-Twenty Fracture Zone (Mid-Atlantic Ridge, 14 degrees-16.5 degrees N). Earth and Planetary Science Letters 171:411-424

Ewart AW, Hawkesworth CJ (1987) Pleistocene to recent Tonga-Kermadec arc lavas: interpretation of new isotope and rare earth data in terms of a depleted mantle source model. Journal of Petrology 28:495-530

Foley S, Tiepolo M, Vannucci R (2002) Growth of early continental crust controlled by melting of amphibolite in subduction zones. Nature 417:837-840

Fonseca E, Zelepugin VN, Heredia M (1985) Structure of the ophiolite association of Cuba. Geotectonics 19:321-329

Fonseca E, Sladkevich V, Santa Cruz M, Morales A, Rodríguez R, Capote C, Navarrete M, García I (1992) Geología de los yacimientos cromíticos con evaluación pronóstico. Informe final tema 401-12, Unidad Minera Punta Gorda, Moa, Cuba

Forsythe LM, Nielsen RL, Fisk MR (1994) High-field strength element partitioning between pyroxene and basaltic to dacitic magmas. Chemical Geology 117:107-125

García-Casco A (2005) Partial melting and counter-clockwise P-T path of subducted oceanic crust: a case study of hot subduction in the northern Caribbean (E Cuba). In: Metamorphic Studies Group Research in Progress and Annual General Meeting. Geological Society of London, March 2005

García-Casco A, Torres-Roldán RL, Millán G, Monié P, Haissen F (2001) High-grade metamorphism and hydrous melting of metapelites in the Pinos terrane (W Cuba): Evidence for crustal thickening and extension in the northern Caribbean collisional belt. Journal of metamorphic Geology 19:699-715

García-Casco A, Torres-Roldán RL, Millán G, Monié P, Schneider J (2002) Oscillatory zoning in eclogitic garnet and amphibole, Northern Serpentinite Melange, Cuba: a record of tectonic instability during subduction? Journal of metamorphic Geology 20:581-598

García-Casco A, Torres-Roldán RL, Iturralde-Vinent MA, Millán G, Núñez-Cambra K, Lázaro C, Rodríguez-Vega A (2006) High pressure metamorphism of ophiolites in Cuba. Geologica Acta 4:63-88

Garrido CJ, Bodinier JL, Alard O (2000) Incompatible trace element partitioning and residence in anhydrous spinel peridotites and websterites from the Ronda orogenic peridotite. Earth and Planetary Science Letters 181(3):341-358

Garrido CJ, Sánchez-Vizcaíno VL, Gómez-Pugnaire MT, Trommsdorff V, Alard O, Bodinier JL, Godard M (2005) Enrichment of HFSE in chlorite-harzburgite produced by high-pressure dehydration of antigorite-serpentinite: Implications for subduction magmatism. Geochemistry Geophysics Geosystems 6:Art. No. Q01J15

Gass IG, Lippard SJ, Shelton AW (1984) Ophiolites and Oceanic Lithosphere. Geological Society of London Special Publications, vol 13, p 413

Gervilla F, Proenza JA, Frei R, González-Jiménez JM, Garrido CJ, Melgarejo JC, Meibom A, Díaz-Martínez R, Lavaut W (2005) Distribution of platinum-group elements and Os isotopes in chromite ores from Mayarí-Baracoa Ophiolitic Belt (eastern Cuba). Contributions to Mineralogy and Petrology 150:589-607

Gill JB (1981) Orogenic Andesites and Plate Tectonics. Springer-Verlag, New York, p 330

Giunta G, Beccaluva L, Siena F (2006) Caribbean Plate margin evolution: constraints and current problems. Geologica Acta 4:265-277

Gladczenko TP, Coffin MF, Eldholm O (1997) Crustal structure of the Ontong Java Plateau: Modeling of new gravity and existing seismic data. Journal of Geophysical Research 102:22711-22729

Godard M, Jousselin D, Bodinier JL (2000) Relationships between geochemistry and structure beneath a palaeo-spreading centre: a study of the mantle section in the Oman ophiolite. Earth and Planetary Science Letters 180:133-148

Govindaraju K (1994) Compilation of working values and sample description for 383 geostandards. Geostandards Newsletter, Special Issue, 18:1-158

Green DH (1972) Magmatic activity as the major process in the chemical evolution of the earth's crust and mantle. Tectonophysics 13:47-71

Green TH (1995) Significance of Nb/Ta as an indicator of geochemical processes in the crust-mantle system. Chemical Geology 120:347-359

Green TH, Sie SH, Ryan CG, Cousens DR (1989) Proton microprobe-determined partitioning of Nb, Ta, Zr, Sr and Y between garnet, clinopyroxene and basaltic magma at high pressure and temperature. Chemical Geology 74:201-216

Gribble RF, Stern RJ, Newman S, Bloomer SH, O'Hearn T (1998) Chemical and Isotopic Composition of Lavas from the Northern Mariana Trough: Implications for Magmagenesis in Back-arc Basins. Journal of Petrology 39(1):125-154

Grove TL, Kinzler R (1986) Petrogenesis of andesites. Annual Review of Earth and Planetary Sciences 14:417-454

Gunther D, Heinrich CA (1999) Enhanced sensitivity in LA-ICP-MS using helium-argon mixtures as aerosol carrier. Journal of Analytical Atomic Spectrometry 14:1369-1374

Gyarmati P, Méndez I, Lay M (1998) Caracterización de las rocas del arco de islas Cretácico en la Zona Estructuro-Facial Nipe-Cristal-Baracoa. In: Furrazola GF, Nuñez-Cambra KE (eds) Estudios sobre Geología de Cuba, pp 357-364. Instituto de Geología y Paleontología, Ciudad de La Habana, Cuba

Hall CM, Kesler SE, Russell N, Piñero E, Sánchez R, Pérez M, Moreira J, Borges M (2004) Age and Tectonic Setting of the Camagüey Volcanic-Intrusive Arc, Cuba: Late Cretaceous Extension and Uplift in the Western Greater Antilles. The Journal of Geology 112:521-542

Hart SR (1984) A large-scale isotope anomaly in the Southern Hemisphere mantle. Nature 309:753-757

Hart SR, Dunn T (1993) Experimental cpx/melt partitioning of 24 trace elements. Contributions to Mineralogy and Petrology 113:1-8

Hart SR, Zindler A (1986) In search of a bulk-Earth composition. Chemical Geology 57:247-267

Hauff F, Hoernle K, Tilton G, Graham DW, Kerr AC (2000) Large volume recycling of oceanic lithosphere over short time scales: Geochemical constraints from the Caribbean Large Igneous Province. Earth and Planetary Science Letters 174:247-263

Hawkesworth CJ (1982) Isotope characteristics of magmas erupted along destructive plate margins. In: Thorpe RS (ed) Andesites: Orogenic andesites and related rocks, pp 549-571. Wiley, London

Hawkesworth CJ, Norry MJ, Roddick JC, Vollmer R (1979) $^{143}Nd/^{144}Nd$ and $^{87}Sr/^{86}Sr$ ratios from the Azores and their significance in LIL-element enriched mantle. Nature 280:28-31

Hawkesworth CJ, Hergt JM, Ellam RM, McDermott F (1991) Element fluxes associated with subduction related magmatism. Philosophical Transactions of the Royal Society of London, Series A, 335:393-405

Hawkesworth CJ, Gallagher K, Hergt JM, McDermott F (1993) Mantle and slab contributions in arc magmas. Annual Review of Earth and Planetary Sciences 21:175-204

Hellebrand E, Snow JE, Hoppe P, Hofmann AW (2002) Garnet-field melting and late-stage refertilization in 'residual' abyssal peridotites from the Central Indian Ridge. Journal of Petrology 43(12):2305-2338

Herzberg C (2004) Geodynamic Information in Peridotite Petrology. Journal of Petrology 45:2507-2530

Hochstaedter A, Gill J, Peters R, Broughton P, Holden P (2001) Across-arc geochemical trends in the Izu-Bonin arc: Contributions from the subducting slab. Geochemistry Geophysics Geosystems 2: doi:10.1029/2000GC000105

Hofmann AW (2003) Sampling Mantle Heterogeneity through Oceanic Basalts: Isotopes and Trace Elements. In: Carlson RW (ed) The Mantle and Core, Treatise on Geochemistry, vol 2, pp 61-101. Elsevier

Hofmann AW, Jochum KP, Seufert M, White WM (1986) Nb and Pb in Oceanic Basalts-New Constraints on Mantle Evolution. Earth and Planetary Science Letters 79:33-45

Holcombe TL, Ladd JW, Westbrook GK, Edgar NT, Bowland CL (1990) Caribbean marine geology: Ridges and basins of the plate interior. In: Dengo G, Case J (eds) The Geology of North America, vol H, The Caribbean Region, pp 231-260. Geological Society of America

Ionov DA, Savoyant L, Dupuy C (1992) Application of the ICP-MS Technique to Trace-Element Analysis of Peridotites and Their Minerals. Geostandards Newsletter 16(2):311-315

Isacks B, Oliver J, Sykes LR (1968) Seismology and the new global tectonics. Journal of Geophysical Research 73:5855-5900

Ishiwatari A (1985) Igneous petrogenesis of the Yakuno ophiolite (Japan) in the context of the diversity of ophiolites. Contributions to Mineralogy and Petrology 89:155-167

Ishiwatari A, Malpas J, Ishizuka H (1994) Circum Pacific Ophiolites, Proceedings of the 29th International Geological Congress, vol D. VSP Publishers, p 286

Iturralde-Vinent MA (1976) Estratigrafía de la zona Calabazas-Achotal, Mayarí Arriba, Oriente, Parte I. La Minería en Cuba 5:9-23

Iturralde-Vinent MA (1977) Estratigrafía de la zona Calabazas-Achotal, Mayarí Arriba, Oriente, Parte II. La Minería en Cuba 6:32-40

Iturralde-Vinent MA (1989) Role of ophiolites in the geological constitution of Cuba. Geotectonics 4:63-74

Iturralde-Vinent MA (1990) Reconstrucción paleogeológica del archipiélago volcánico paleogénico temprano en Cuba, Transactions of the 12th Caribbean Geological Conference, Miami, p 547

Iturralde-Vinent MA (1991) Deslizamientos y descensos del terreno en el flanco meridional de la Sierra Maestra, Cuba sudoriental. In: Morfotectónica de Cuba Oriental, pp 24-27. Instituto de Geografía, Academia de Ciencias de Cuba

Iturralde-Vinent MA (1994) Cuban Geology: a new plate tectonic synthesis. Journal of Petroleum Geology 17:39-69

Iturralde-Vinent MA (1996a) Introduction to Cuban Geology and Geophysics. In: Iturralde-Vinent MA (ed) Ofiolitas y Arcos Volcánicos de Cuba. IUGS-UNESCO Project 364, Caribbean Ophiolites and Volcanic Arcs, Special Contribution, vol 1, pp 3-35, Miami

Iturralde-Vinent MA (1996b) Geología de las Ofiolitas de Cuba. In: Iturralde-Vinent MA (ed) Ofiolitas y Arcos Volcánicos de Cuba. IUGS-UNESCO Project 364, Caribbean Ophiolites and Volcanic Arcs, Special Contribution, vol 1, pp 83-120, Miami

Iturralde-Vinent MA (1996c) Cuba: el arco de islas volcánicas del Cretácico. In: Iturralde-Vinent MA (ed) Ofiolitas y Arcos Volcánicos de Cuba. IUGS-UNESCO Project 364, Caribbean Ophiolites and Volcanic Arcs, Special Contribution, vol 1, pp 179-189, Miami

Iturralde-Vinent MA (1996d) Estratigrafía del arco volcánico Cretácico en Cuba. In: Iturralde-Vinent MA (ed) Ofiolitas y Arcos Volcánicos de Cuba. IUGS-UNESCO Project 364, Caribbean Ophiolites and Volcanic Arcs, Special Contribution, vol 1, pp 190-230, Miami

Iturralde-Vinent MA (1996e) El Archipiélago Volcánico Paleoceno-Eoceno. In: Iturralde-Vinent MA (ed) Ofiolitas y Arcos Volcánicos de Cuba. IUGS-UNESCO Project 364, Caribbean Ophiolites and Volcanic Arcs, Special Contribution, vol 1, pp 231-246, Miami

Iturralde-Vinent MA (1998) Sinopsis de la Constitución Geológica de Cuba. In: Melgarejo JC, Proenza JA (eds) Geología y Metalogenia de Cuba: una introducción. Acta Geologica Hispanica 33(1-4) pp 9-56

Iturralde-Vinent MA (2003) The relationships between the ophiolites, the metamorphic terrains, the Cretaceous volcanic arcs and the Paleocene-Eocene volcanic arc. Field guide to a geological excursion to Eastern Cuba. In: V Cuban Geological and Mining Congress. IGCP Project 433, Cuban Geological Society, p 16

Iturralde-Vinent MA, Lidiak EG (2006) Caribbean Tectonic, Magmatic, Metamorphic and Stratigraphic Events. Implications for Plate Tectonics (UNESCO/IUGS IGCP Project 433 "Caribbean Plate Tectonics"). Geologica Acta 4:1-5

Iturralde-Vinent MA, Wolf D, Thieke HU (1989) Edades radiométricas del territorio camagüeyano. Resúmenes del Primer Congreso Cubano de Geología, La Habana, p 117

Iturralde-Vinent MA, Díaz-Otero C, Rodríguez-Vega A, Díaz-Martínez R (2006) Tectonic implications of paleontologic dating of Cretaceous-Danian sections of Eastern Cuba. Geologica Acta 4:89-102

Jagoutz E, Palme H, Blum H, Cendales M, Dreibus G, Spettel B, Lorenz V, Wanke H (1979) The abundances of major, minor and trace elements in the Earth's mantle as derived from primitive ultramafic nodules. Proceeding of the 10th Lunar Planetary Science Conference. Geochimica et Cosmochimica Acta Supplement 10:2031–2051

Jakeš P, Gill J (1970) Rare earth elements and the island arc tholeiitic series. Earth and Planetary Science Letters 9:17-28

Jakus P (1983) Formaciones vulcanógeno-sedimentarias y sedimentarias de Cuba oriental. In: Nagy E (ed) Contribución a la geología de Cuba oriental, pp 17-85. Instituto de Geología y Paleontología, Academia de Ciencias de Cuba

James KH (2006) Arguments for and against the Pacific origin of the Caribbean Plate: discussion, finding for an inter-American origin. Geologica Acta 4:279-302

Jansa LF, Weidmann J (1982) Mesozoic-Cenozoic development of the eastern North American and northwest African continental margins: a comparison. In: von Rad U, Hinz K, Sarnthein M, Siebold E (eds) Geology of Northwest African Margin, pp 215-269. Springer-Verlag, New York

Jochum KP, Seufert HM, Thirwall MF (1990) High-sensitivity Nb analysis by spark-source mass spectrometry (SSMS) and calibration of XRF Nb and Zr. Chemical Geology 81:1-16

Johnson DM, Hooper PR, Conrey RM (1999) XRF Analysis of Rocks and Minerals for Major and Trace Elements on a Single Low Dilution Li-tetraborate Fused Bead. Advances in X-ray Analysis 41:843-867

Johnson KTM, Dick HJB, Shimizu N (1990) Melting in the oceanic upper mantle: An ion microprobe study of diopsides in abyssal peridotites. Journal of Geophysical Research 95:2661-2678

Jolly WT, Lidiak EG, Dickin AP, Wu TW (2001) Secular Geochemistry of Central Puerto Rican Island Arc Lavas: Constraints on Mesozoic Tectonism in the Eastern Greater Antilles. Journal of Petrology 42(12):2197-2214

Jolly WT, Lidiak EG, Dickin AP (2006) Cretaceous to Mid-Eocene pelagic sediment budget in Puerto Rico and the Virgin Islands (northeast Antilles Island arc). Geologica Acta 4:35-62

Jordan TH (1975) The continental tectosphere. Reviews of Geophysics and Space Physics 13:1-12

Jousselin D, Nicolas A (2000) The Moho transition zone in the Oman ophiolite - relation with wehrlites in the crust and dunites in the mantle. Marine Geophysical Researches 21:229-241

Kalfoun F (2002) Géochimie du Niobium et du Tantale: distribution et fractionnement de ces deux éléments dans les différents réservoirs terrestres. Mémoires des Géosciences de Montpellier, vol 27. Institut des Sciences de la Terre de l'Eau et de l'Espace de Montpellier, p 275

Karson JA, Klein EM, Hurst SD, Lee CE, Rivizzigno PA, Curewitz D, Morris AK, Hess Deep '99 Scientific Party (2002) Structure of uppermost fast-spread oceanic crust exposed at the Hess Deep Rift: Implications for subaxial processes at the East Pacific Rise. Geochemistry Geophysics Geosystems 3: doi:10.1029/2001GC000155

Kay RW (1980) Volcanic arc magmas: implications of a melting-mixing model for element recycling in the crust upper mantle system. Journal of Geology 88:497-522

Kelemen PB, Aharonov E (1998) Periodic formation of magma fractures and generation of layered gabbros in the lower crust beneath oceanic spreading ridges. In: Buck WR, Delaney PT, Karson JA, Lagabrielle Y (eds) Faulting and Magmatism at Mid-Ocean Ridges. Geophysical Monograph Series, vol 106, pp 267-289. American Geophysical Union, Washington

Kelemen PB, Dick HJB, Quick JE (1992) Formation of Harzburgite by Pervasive Melt Rock Reaction in the Upper Mantle. Nature 358:635-641

Kelemen PB, Shimizu N, Dunn T (1993) Relative depletion of niobium in some arc magmas and the continental crust: partitioning of K, Nb, La and Ce during melt/rock reaction in the upper mantle. Earth and Planetary Science Letters 120:111-134

Kelemen PB, Shimizu N, Salters VJM (1995) Extraction of Mid-Ocean-Ridge Basalt from the Upwelling Mantle by Focused Flow of Melt in Dunite Channels. Nature 375:747-753

Kelemen PB, Koga K, Shimizu N (1997a) Geochemistry of gabbro sills in the crust-mantle transition zone of the Oman ophiolite: Implications for the origin of the oceanic lower crust. Earth and Planetary Science Letters 146:475-488

Kelemen PB, Hirth G, Shimizu N, Spiegelman M, Dick H (1997b) A review of melt migration processes in the adiabatically upwelling mantle beneath oceanic spreading ridges. Philosophical Transactions of the Royal Society of London, Series A, 355(1723):283-318

Kelemen PB, Hart SR, Bernstein S (1998) Silica enrichment in the continental upper mantle via melt/rock reaction. Earth and Planetary Science Letters 164:387-406

Kelemen PB, Hanghøj K, Greene AR (2003a) One view of the Geochemistry of Subduction-related Magmatic Arcs, with an Emphasis on Primitive Andesite and Lower Crust. In: Rudnick R (ed) The Crust, Treatise on Geochemistry, vol 3, pp 593-659. Elsevier

Kelemen PB, Yogodzinski GM, Scholl DW (2003b) Along-strike variation in lavas of the Aleutian island arc: Implications for the genesis of high Mg# andesite and the continental crust. In: Eiler J (ed) Inside the Subduction Factory. Geophysical Monograph Series, vol.138, pp 223-246. American Geophysical Union

Keppler H (1996) Constraints from partitioning experiments on the composition of subduction-zone fluids. Nature 380:237–240

Kerr AC, Tarney J, Marriner GF, Nivia A, Saunders AD (1997a) The Caribbean-Colombian Cretaceous igneous province: the internal anatomy of an oceanic plateau. In:

Mahoney JJ, Coffin M (eds) Large igneous provinces; continental, oceanic and planetary flood volcanism. Geophysical Monograph Series, vol 100, pp 123-144. American Geophysical Union

Kerr AC, Marriner GF, Tarney J, Nivia A, Saunders AD, Thirlwall MF, Sinton CW (1997b) Cretaceous Basaltic Terranes in Western Colombia: Elemental, Chronological and Sr-Nd Isotopic Constraints on Petrogenesis. Journal of Petrology 38:677-702

Kerr AC, Tarney J, Nivia A, Marriner GF, Saunders AD (1998) The internal structure of oceanic plateaus: Inferences from obducted Cretaceous terranes in western Colombia and the Caribbean. Tectonophysics 292:173-188

Kerr AC, Iturralde-Vinent MA, Saunders AD, Babbs TL, Tarney J (1999) A new plate tectonic model of the Caribbean: Implications from a geochemical reconnaissance of Cuban Mesozoic volcanic rocks. Geological Society of America Bulletin 111(11):1581-1599

Kerr AC, Aspden JA, Tarney J, Pilatasig LF (2002) The nature and provenance of accreted oceanic terranes in western Ecuador: geochemical and tectonic constraints. Journal of the Geological Society of London 159:577-594

Kerr AC, White RV, Thompson PME, Tarney J, Saunders AD (2003) No oceanic plateau - no Caribbean plate? The seminal role of an oceanic plateau in Caribbean plate evolution. In: Bartolini C, Buffler RT, Blickwede J (eds) The Circum-Gulf of Mexico and the Caribbean: Hydrocarbon habitats, basin formation, and plate tectonics. American Association of Petroleum Geologists Memoir, vol 79, pp 126-168

Kesler SE, Levy E, Martín CF (1990) Metallogenic evolution of the Caribbean region. In: Dengo G, Case J (eds) The Geology of North America, vol H, The Caribbean Region, pp 459-482. Geological Society of America

Kesler SE, Campbell IH, Allen CM (2005) Age of the Los Ranchos Formation, Dominican Republic: Timing and tectonic setting of primitive island arc volcanism in the Caribbean region. Geological Society of America Bulletin 117:987-995

Kessel R, Schmidt MW, Ulmer P, Pettke T (2005) Trace element signature of subduction zone fluids, melts and supercritical liquids at 120-180 km depth. Nature 437:724-727

Khudoley K, Meyerhoff AA (1971) Paleogeography and geological history of Greater Antilles. Geological Society of America Memoirs, vol 129, pp 1-199

Kinzler RJ, Grove TL (1992) Primary Magmas of Midocean Ridge Basalts. 1. Experiments and Methods. Journal of Geophysical Research 97(B5):6885-6906

Klein EM (2003) Geochemistry of the Igneous Oceanic Crust. In: Rudnick RL (ed) The Crust, Treatise on Geochemistry, vol 3, pp 433-463. Elsevier

Klemme S, Blundy JD, Wood BJ (2002) Experimental constraints on major and trace element partitioning during partial melting of eclogite. Geochimica et Cosmochimica Acta 66(17):3109-3123

Klemme S, Prowatke S, Hametner K, Günther D (2005) Partitioning of trace elements between rutile and silicate melts: Implications for subduction zones. Geochimica et Cosmochimica Acta 69:2361-2371

Koga KT, Kelemen PB, Shimizu N (2001) Petrogenesis of the crust-mantle transition zone and the origin of lower crustal wehrlite in the Oman ophiolite. Geochemistry Geophysics Geosystems 2:Art. No. 2000GC000132

Kogiso T, Tatsumi Y, Nakano S (1997) Trace element transport during dehydration processes in the subducted oceanic crust. 1. Experiments and implications for the origin of ocean island basalts. Earth and Planetary Science Letters 148:193-205

Korenaga J, Kelemen PB (1997) Origin of gabbro sills in the Moho transition zone of the Oman ophiolite: Implications for magma transport in the oceanic lower crust. Journal of Geophysical Research 102(B12):27729-27749

Kubo K (2002) Dunite Formation Process in Highly Depleted Peridotite: Case Study of the Iwanaidake Peridotite, Hokkaido, Japan. Journal of Petrology 43(3):423-448

Kysar-Mattietti G (2001) The role of Paleogene Magmatism in the evolution of the northern Caribbean margin. The Sierra Maestra (southern Cuba). Unpublished Ph.D. thesis. George Washington University, p 187

Ladd JW, Holcombe TL, Westbrook GK, Edgar NT (1990) Caribbean marine geology: Active margins of the plate boundary. In: Dengo G, Case J (eds) The Geology of North America, vol H, The Caribbean Region, pp 261-290. Geological Society of America

Lapierre H, Dupuis V, Mercier de Lépinay B, Bosch D, Monié P, Tardy M, Maury RC, Hernandez J, Polvé M, Yeghicheyan D, Cotten J (1999) Late Jurassic Oceanic Crust and Upper Cretaceous Caribbean Plateau Picritic Basalts Exposed in the Duarte Igneous Complex, Hispaniola. The Journal of Geology 107:193-207

Lapierre H, Bosch D, Dupuis V, Polvé M, Maury RC, Hernandez J, Monié P, Yeghicheyan D, Jaillard E, Tardy M, Mercier de Lépinay B, Mamberti M, Desmet A, Keller F, Sénebier F (2000) Multiple plume events in the genesis of the peri-Caribbean Cretaceous oceanic plateau province. Journal of Geophysical Research 105:8403-8421

Larson RL (1991) Latest pulse of earth: evidence for mid-Cretaceous superplume. Geology 19:547-550

Lázaro C (2004) Caracterización litológica y geoquímica de la mélange de la Sierra del Convento, E Cuba. Programa de Tercer Ciclo "Ciencias de la Tierra", Trabajo de Investigación (DEA), Universidad de Granada, p 86

Le Bas MJ, Le Maitre RW, Streckseisen A, Zanetti B (1986) A chemical classification of volcanic rocks based on total alkali-silica diagram. Journal of Petrology 27:745-754

Le Pichon X, Francheteau J, Bonnin J (1973) Plate tectonics. Elsevier Scientific, Amsterdam, p 300

Lebron MC, Perfit MR (1993) Stratigraphic and Petrochemical Data Support Subduction Polarity Reversal of the Cretaceous Caribbean Island Arc. The Journal of Geology 101:389-396

Lebron MC, Perfit MR (1994) Petrochemistry and tectonic significance of Cretaceous island-arc rocks, Cordillera Oriental, Dominican Republic. Tectonophysics 229:69-100

Lee C-TA, Brandon AD, Norman M (2003) Vanadium in peridotites as a proxy of paleo-fO_2 during partial melting: Prospects, limitations and implications. Geochimica et Cosmochimica Acta 67(16):3045-3064

Lewis JF, Draper G (1990) Geology and tectonic evolution of the northern Caribbean margin. In: Dengo G, Case J (eds) The Geology of North America, vol H, The Caribbean Region, pp 77-140. Geological Society of America

Lewis JF, Escuder Viruete J, Hernaiz Huerta PP, Gutierrez G, Draper G, Pérez-Estaún A (2002) Subdivisión geoquímica del Arco de Isla Circum-Caribeño, Cordillera Central Dominicana: Implicaciones para la formación, acrecio y crecimiento cortical en un ambiente intraoceánico. Acta Geologica Hispanica 37:81-122

Lewis JF, Draper G, Proenza JA, Espaillat J, Jiménez J (2006) Ophiolite-Related Ultramafic Rocks (Serpentinites) in the Caribbean Region: A Review of their Occurrence, Composition, Origin, Emplacement and Ni-Laterite Soil Formation. Geologica Acta 4:237-263

Lippard SJ, Shelton AW, Gass IG (1986) The Ophiolite of Northern Oman. The Geological Society Memoirs, vol 11. Blackwell Scientific Publications, p 178

Luais B, Télouk P, Albarède F (1997) High-precision Nd isotopic measurements using plasma-source mass spectrometry. Geochimica et Cosmochimica Acta 61:4847-4854

Macdonald R, Hawkesworth CJ, Heath E (2000) The Lesser Antilles volcanic chain: a study in arc magmatism. Earth-Science Reviews 49:1-76

Mahoney JJ, Storey M, Duncan RA, Spencer KJ, Pringle M (1993) Geochemistry and age of the Ontong Java Plateau. In: Pringle MS (ed) The Mesozoic Pacific: Geology, tectonics and volcanism. Geophysical Monograph Series, vol 77, pp 233-261. American Geophysical Union

Malfait BT, Dinkelman MG (1972) Circum-Caribbean tectonic and igneous activity and the evolution of the Caribbean plate. Geological Society of America Bulletin 83:251-272

Mamberti M, Lapierre H, Bosch D, Jaillard E, Ethien R, Hernandez J, Polvé M (2003) Accreted fragments of the Late Cretaceous Caribbean-Colombian Plateau in Ecuador. Lithos 66:173-199

Mann P (1999) Caribbean sedimentary basins: Classification and tectonic setting. In: Mann P (ed) Caribbean Basins, Sedimentary Basins of the World, vol 4, pp 3-31. Elsevier Science B.V.

Mann P, Schubert C, Burke K (1990) Review of Caribbean neotectonics. In: Dengo G, Case J (eds) The Geology of North America, vol H, The Caribbean Region, pp 307-338. Geological Society of America

Matsumoto I, Arai S (2001) Morphological and chemical variations of chromian spinel in dunite-harzburgite complexes from the Sangun zone (SW Japan): implications for mantle/melt reaction and chromitite formation processes. Mineralogy and Petrology 73:305-323

Mattson PH (1979) Subduction, buoyant breaking, flipping and strike-slip faulting in the northern Caribbean. Journal of Geology 87:293-304

Maury RC, Westbrook GK, Baker PE, Bouysse P, Westercamp D (1990) Geology of the Lesser Antilles. In: Dengo G, Case J (eds) The Geology of North America, vol H, The Caribbean Region, pp 141-166. Geological Society of America

McCann WR, Pennington WD (1990) Seismicity, large earthquakes, and the margin of the Caribbean Plate. In: Dengo G, Case J (eds) The Geology of North America, vol H, The Caribbean Region, pp 291-306. Geological Society of America

McCulloch MT, Gamble AJ (1991) Geochemical and geodynamical constraints on subduction zone magmatism. Earth and Planetary Science Letters 102:358-374

McCulloch MT, Gregory RT, Wasserburg GJ, Taylor HT (1981) Sm–Nd, Rb–Sr, and $^{18}O/^{16}O$ isotope systematics in an oceanic crustal section: evidence from the Samail ophiolite. Journal of Geophysical Research 86:2721–2735

McDonough WF (1990) Constraints on the composition of the continental lithospheric mantle. Earth and Planetary Science Letters 101:1-18

McDougall I, Harrison TM (1988) Geochronology and Thermochronology by the $^{40}Ar/^{39}Ar$ Method. Monographs on Geology and Geophysics, vol 9. Oxford University Press, p 212

McKenzie DP (1969) Speculations on the consequences and causes of plate motions. Geophysical Journal of the Royal Astronomical Society 18:1-32

Mercier JCC, Nicolas A (1975) Textures and Fabrics of Upper-Mantle Peridotites as Illustrated by Xenoliths from Basalts. Journal of Petrology 16(2):454-487

Meschede M, Frisch W (1998) A plate tectonic model for the Mesozoic and Early Cenozoic history of the Caribbean plate. Tectonophysics 296:269-291

Metzger EP, Miller RB, Harper GD (2002) Geochemistry and tectonic setting of the ophiolitic Ingalls complex, North Cascades, Washington: implications for correlations of Jurassic cordilleran ophiolites. Journal of Geology 110:543-560

Meyerhoff AA, Hatten CW (1968) Diapiric structures in central Cuba. American Association of Petroleum Geologists Memoirs, vol 8, pp 315-357

Michard A, Albarède F (1985) Hydrothermal uranium uptake at ridge crests. Nature 317:244-246

Millán G (1996) Metamorfitas de la Asociación Ofiolítica de Cuba. In: Iturralde-Vinent MA (ed) Ofiolitas y Arcos Volcánicos de Cuba. IUGS-UNESCO Project 364, Caribbean Ophiolites and Volcanic Arcs, Special Contribution, vol 1, pp 131-153, Miami

Millán G, Somin M (1985) Contribución al conocimiento geológico de las metamorfitas del Escambray y Purial, Reportes de Investigación, vol 2, pp 1-74. Academia de Ciencias de Cuba

Miyashiro A (1973) The Troodos complex was probably formed as an island arc. Earth and Planetary Science Letters 25:217-222

Molnar P, Sykes LR (1969) Tectonics of the Caribbean and middle America regions from focal mechanism and seismicity. Geological Society of America Bulletin 80:1639-1684

Moores E, Kellogg LH, Dilek Y (2000) Tethyan ophiolites, mantle convection, and tectonic "historical contingency": a resolution of the "ophiolite conundrum". In: Dilek Y, Moores EM, Elthon D, Nicolas A (eds) Ophiolites and Oceanic Crust; New insights from Field Studies and the Ocean Drilling Program, Geological Society of America Special Paper, vol 349, pp 3-12

Morris AEL, Taner I, Meyerhoff HA, Meyerhoff AA (1990) Tectonic evolution of the Caribbean region; Alternative hypothesis. In: Dengo G, Case J (eds) The Geology of North America, vol H, The Caribbean Region, pp 433-457. Geological Society of America

Münker C (1998) Nb/Ta fractionation in a Cambrian arc/back arc system, New Zealand: source constraints and application of refined ICPMS techniques. Chemical Geology 144:23-45

Münker C, Wörner G, Yogodzinski G, Churikova T (2004) Behaviour of high field strength elements in subduction zones: constraints from Kamchatka–Aleutian arc lavas. Earth and Planetary Science Letters 224:275-293

Murashko VI, Lavandero RM (1989) Chromite in the hyperbasite belt of Cuba. International Geology Review 31:90-99

Murphy JB, Pisarevsky SA, Nance RD, Keppie JD (2004) Neoproterozoic-Early Paleozoic evolution of peri-Gondwanan terranes: implications for Laurentia-Gondwana connections. International Journal of Earth Sciences 93:659-682

Mutter CZ, Mutter JC (1993) Variation in thickness of Layer 3 dominated oceanic crustal structure. Earth and Planetary Science Letters 117:295-317

Nance RD, Murphy JB (1994) Contrasting basement isotopic signatures and the palinspastic restoration of peripheral orogens: Example from the Neoproterozoic Avalonian-Cadomian belt. Geology 22:617-620

Navon O, Stolper E (1987) Geochemical consequence of melt percolation: the upper mantle as a chromatographic column. Journal of Geology 95:285-307

Nicolas A (1989) Structures of Ophiolites and Dynamics of Oceanic Lithosphere. Kluwer Academic Publishers, p 367

Nicolas A, Jackson ED (1972) Répartition en deux provinces des péridotites des chaînes alpines longeant la Méditerranée: implications géotectoniques. Bulletin Suisse de Mineralogie et Petrologie 53:385-401

Nicolas A, Prinzhofer A (1983) Cumulative or Residual Origin for the Transition Zone in Ophiolites: Structural Evidence. Journal of Petrology 24:188-206

Niu Y (1997) Mantle melting and melt extraction processes beneath ocean ridges: evidence from abyssal peridotites. Journal of Petrology 38:1047-1074

Niu Y (2004) Bulk-rock major and trace element compositions of abyssal peridotites: implications for mantle melting, melt extraction and post-melting processes beneath mid-ocean ridges. Journal of Petrology 45:2423-2458

Niu Y, Hékinian R (1997) Basaltic liquids and harzburgitic residues in the Garrett Transform: a case study at fast-spreading ridges. Earth and Planetary Science Letters 146:243-258

Niu Y, Waggoner DG, Sinton JM, Mahoney JJ (1996) Mantle source heterogeneity and melting processes beneath seafloor spreading centers: the East Pacific Rise, 18º-19ºS. Journal of Geophysical Research 101:27711-27733

Niu YL, Langmuir CH, Kinzler RJ (1997) The origin of abyssal peridotites: a new perspective. Earth and Planetary Science Letters 152:251-265

Ohara Y, Stern RJ, Ishii T, Yurimoto H, Yamazaki T (2002) Peridotites from the Mariana Trough: first look at the mantle beneath an active back-arc basin. Contributions to Mineralogy and Petrology 143:1-18

Onstott TC, Phillips D, Pringle-Goodell L (1991) Laser microprobe measurement of chlorine and argon zonation in biotite. Chemical Geology 90:145-168

Pallister JS, Hopson CA (1981) Samail Ophiolite plutonic suite: Field relations, phase variation, cryptic variation and layering, and a model of a spreading ridge magma chamber. Journal of Geophysical Research 86:2593-2644

Pallister JS, Knight RJ (1981) Rare-earth element geochemistry of the Samail ophiolite near Ibra, Oman. Journal of Geophysical Research 86:2673-2697

Pardo G (1975) Geology of Cuba. In: Nairn AE, Stehli FG (eds) The Ocean Basins and Margins: The Gulf of Mexico and the Caribbean, pp 553-615. Plenum Press, New York

Parkinson IJ, Pearce JA (1998) Peridotites from the Izu-Bonin-Mariana Forearc (ODP Leg 125): Evidence for mantle melting and melt-mantle interaction in a supra-subduction zone setting. Journal of Petrology 39:1577-1618

Parson LM, Murton BJ, Browning P (1992) Ophiolites and their Modern Analogues. Geological Society of London Special Publications, vol 60, p 330

Peacock SM, Rushmer T, Thompson AB (1994) Partial melting of subducting oceanic crust. Earth and Planetary Science Letters 121:227-244

Pearce JA (1983) The role of sub-continental lithosphere in magma genesis at destructive plate margins. In: Hawkesworth CJ, Norris MJ (eds) Continental Basalts and Mantle Xenoliths, pp 230-249. Shiva, Nantwich

Pearce JA, Parkinson IJ (1993) Trace element models for mantle melting: application to volcanic arc petrogenesis. In: Prichard HM, Alabaster T, Harris NB, Neary CR (eds) Magmatic Processes and Plate Tectonics. Geological Society of London Special Publications, vol 76, pp 373-403

Pearce JA, Peate DW (1995) Tectonic Implications of the Composition of Volcanic Arc Magmas. Annual Review of Earth and Planetary Sciences 23:251-285

Pearce JA, Alabaster T, Shelton AW, Searle MP (1981) The Oman Ophiolite as a Cretaceous Arc-Basin Complex - Evidence and Implications. Philosophical Transactions of the Royal Society of London, Series A, vol 300(1454):299-317

Pearce JA, Lippard SJ, Roberts S (1984) Characteristics and tectonic significance of supra-subduction zone ophiolites. In: Kokelaar BP, Howells MF (eds) Marginal Basin Geology: Volcanic and Associated Sedimentary and Tectonic Processes in Modern and Ancient Marginal Basins. Geological Society of London Special Publications, vol 16, pp 77-94

Pearce JA, Barker PF, Edwards SJ, Parkinson IJ, Leat PT (2000) Geochemistry and tectonic significance of peridotites from the South Sandwich arc-basin system, South Atlantic. Contributions to Mineralogy and Petrology 139:36-53

Pearce JA, Stern RJ, Bloomer SH, Fryer P (2005) Geochemical mapping of the Mariana arc-basin system: Implications for the nature and distribution of subduction components. Geochemistry Geophysics Geosystems 6(7): doi:10.1029/2004 GC000895

Penrose Conference Participants (1972) Penrose field conference on ophiolites. Geotimes 17:24-25

Pérez M, Rodríguez J, Castillo O (1983) Petrología de las rocas del Macizo Daiquirí. Revista Minería y Geología 2:99-130

Pérez M, Soto T, Sukar K (1986) Particularidades petrológicas de los granitoides de las provincias villaclareñas. Serie Geológica del Centro de Investigaciones Geológicas (Cuba) 3:3-14

Pin C, Briot D, Bassin C, Poitrasson F (1994) Concomitant extraction of Sr and Sm-Nd for isotopic analysis in silicate samples based on specific extraction chromatography. Analytica Chimica Acta 298:209-217

Pindell JL (1985) Alleghenian reconstruction and the subsequent evolution of the Gulf of Mexico, Bahamas and Proto-Caribbean Sea. Tectonics 4:1-39

Pindell JL (1994) Evolution of the Gulf of Mexico and the Caribbean. In: Donovan SK, Jackson TA (eds) Caribbean Geology: An Introduction, pp 13-40. University of West Indies Publishers' Association, Kingston

Pindell JL, Barrett SF (1990) Geological evolution of the Caribbean Region; A plate-tectonic perspective. In: Dengo G, Case J (eds) The Geology of North America, vol H, The Caribbean Region, pp 405-432. Geological Society of America

Pindell JL, Dewey JF (1982) Permo-Triassic reconstruction of western Pangea and the evolution of the Gulf of Mexico-Caribbean region. Tectonics 1:179-212

Pindell JL, Kennan L (2001) Kinematic Evolution of the Gulf of Mexico and Caribbean. In: Fillon R, Rosen N, Weimer P, Lowrie A, Pettingill H, Phair R, Roberts H, van Hoorn B (eds) Transactions of the Gulf Coast Section Society of Economic Paleontologists and Mineralogists (GCSSEPM) pp 193-220. 21st Annual Bob F. Perkins Research Conference, Petroleum Systems of Deep-Water Basins, Houston, Texas, USA

Pindell JL, Kennan L, Stanek KP, Maresch WV, Draper G (2006) Foundations of Gulf of Mexico and Caribbean evolution: eight controversies resolved. Geologica Acta 4:303-341

Plank T (2005) Constraints from Thorium/Lanthanum on Sediment Recycling at Subduction Zones and the Evolution of the Continents. Journal of Petrology 46:921-944

Plank T, Langmuir CH (1988) An evaluation of the global variations in the major element chemistry of arc basalts. Earth and Planetary Science Letters 90:349-370

Plank T, Langmuir CH (1998) The chemical composition of subducting sediment and its consequences for the crust and mantle. Chemical Geology 145:325-394

Plank T, White WM (1995) Nb and Ta in arc and mid-ocean basalts. American Geophysical Union Fall Meeting Abstracts. EOS 76(46). Supplement 655

Presnall DC, Gudfinnsson GH, Walter MJ (2002) Generation of mid-ocean ridge basalts at pressures from 1 to 7 GPa. Geochimica et Cosmochimica Acta 50:2073-2090

Proenza JA, Carralero NM (1994) Un nuevo enfoque sobre la geología de la parte sur de la cuenca de Sagua de Tánamo. Revista Minería y Geología 11:3-10

Proenza J, Gervilla F, Melgarejo JC (1999a) La Moho Transition Zone en el Macizo Ofiolítico Moa-Baracoa: un ejemplo de interacción magma/peridotita. Revista de la Sociedad Geológica de España 12:309-327

Proenza J, Gervilla F, Melgarejo JC, Bodinier JL (1999b) Al- and Cr-rich chromitites from the Mayarí-Baracoa Ophiolitic Belt (Eastern Cuba): consequence of interaction

between volatile-rich melts and peridotite in suprasubduction mantle. Economic Geology 94:547-566

Proenza JA, Gervilla F, Melgarejo JC, Vera O, Alfonso P, Fallick A (2001) Genesis of sulfide-rich chromite ores by interaction between chromitite and pegmatitic olivine-norite dikes in the Potosí Mine (Moa-Baracoa ophiolitic massif, eastern Cuba). Mineralium Deposita 36:658-669

Proenza J, Alfonso J, Melgarejo JC, Gervilla F, Tritlla J, Fallick AE (2003) D, O and C isotopes in podiform chromitites as fluid tracers for hydrothermal alteration processes of the Mayarí-Baracoa Ophiolitic Belt, eastern Cuba. Journal of Geochemical Exploration 78-79:117-122

Proenza JA, Díaz-Martínez R, Iriondo A, Marchesi C, Melgarejo JC, Gervilla F, Garrido CJ, Rodríguez-Vega A, Lozano-Santacruz R, Blanco-Moreno J (2006) Primitive Cretaceous island-arc volcanic rocks in eastern Cuba: the Téneme Formation. Geologica Acta 4:103-121

Prouteau G, Maury RC, Sajona FG, Cotten J, Joron JL (2000) Behaviour of Nb, Ta and other HFSE in adakites and related lavas from The Philippines. Island Arc 9:487-498

Pushcharovsky Y (1988) Mapa geológico de la República de Cuba escala 1: 250 000 (42 sheets). Academy of Science of Cuba and USSR

Pushcharovsky Y, Mossakovsky A, Nekrasov G, Sokolov S, Iturralde-Vinent MA (1989) Tectonics of the Republic of Cuba. Explanatory note to the tectonic map of Cuba scale 1:500.000. Nauka, Moscow, p 77

Quick JE (1981) Petrology and petrogenesis of the Trinity peridotite, an upper mantle diapir in the eastern Klamath mountains, northern California. Journal of Geophysical Research 86:11837-11863

Quintas F (1987) Formación Mícara en Yumurí Arriba, Baracoa, Clave Para la Interpretación de la Geología Histórica Pre-Paleocénica de Cuba Oriental. Revista Minería y Geología 5:3-20

Quintas F (1988a) Características Estratigráficas y Estructurales del Complejo Ofiolítico y Eugeosinclinal de la Cuenca del Río Quibiján, Baracoa. Revista Minería y Geología 6(2):11-22

Quintas F (1988b) Formación Mícara en Yumurí Arriba, Baracoa, Clave Para la Interpretación de la Geología Histórica Pre-Paleocenica de Cuba Oriental, 2ª Parte. Revista Minería y Geología 6(1):3-16

Quintas F (1989) Estratigrafía y paleogeografía del Cretácico superior y Paleógeno de la provincia Guantánamo y zonas cercanas. Unpublished Thesis. Instituto Superior Minero-Metalúrgico de Moa, Cuba

Quintas F, Blanco-Moreno J (1993) Paleogeografía de la cuenca San Luis y su importancia para la interpretación de la evolución geológica de Cuba Oriental. Revista Minería y Geología 10:3-14

Quintas F, Hernández M, Campos M (1994) Origen y evolución del arco de islas volcánicas de Sierra Maestra. Revista Minería y Geología 11:3-12

Rampone E, Hofmann AW, Piccardo GB, Vannucci R, Bottazzi P, Ottolini L (1996) Trace element and isotope geochemistry of depleted peridotites from an N-MORB type

ophiolite (Internal Liguride N Italy). Contributions to Mineralogy and Petrology 123:61-76

Révillon S, Hallot E, Arndt NT, Chauvel C, Duncan RA (2000) A Complex History for the Caribbean Plateau: Petrology, Geochemistry, and Geochronology of the Beata Ridge, South Hispaniola. The Journal of Geology 108:641-661

Ribe NM (1985) The generation and composition of partial melts in the earth's mantle. Earth and Planetary Science Letters 73:361–376

Ríos YI, Cobiella JL (1984) Estudio preliminar del Macizo de gabroides Quesigua de las ofiolitas del este de la provincia de Holguín. Revista Minería y Geología 2:109-132

Robertson AHF (2002) Overview of the genesis and emplacement of Mesozoic ophiolites in the Eastern Mediterrean Tethyan region. Lithos 65:1-67

Robertson AHF (2004) Development of concepts concerning the genesis and emplacement of Tethyan ophiolites in the Eastern Mediterranean and Oman regions. Earth-Science Reviews 66:331-387

Rodgers DA (1984) Mexia and Talco fault zones, east Texas: comparison of origins predicted by two tectonic models. In: Presley MW (ed) The Jurassic of East Texas. Transactions of the East Texas Jurassic Exploration Conference, pp 23-31. East Texas Geological Society

Roeder PL, Emslie RF (1970) Olivine-Liquid Equilibrium. Contributions to Mineralogy and Petrology 29:275-289

Rojas-Agramonte Y, Neubauer F, Bojar AV, Hejl E, Handler R, García-Delgado DE (2006) Geology, age and tectonic evolution of the Sierra Maestra Mountains, southeastern Cuba. Geologica Acta 4:123-150

Roque Marrero F, Iturralde-Vinent MA (1987) Redifinición de la zona de Cayo Coco en la provincia de Camagüey. Tecnológica 17:18-21

Ross M, Scotese CR (1988) A hierarchical tectonic model of the Gulf of Mexico and Caribbean region. Tectonophysics 155:139-168

Ryerson FJ, Watson EB (1987) Rutile saturation in magmas: implications for Ti-Nb-Ta depletion in island arc basalts. Earth and Planetary Science Letters 86:225-239

Samson SC, Alexander EC (1987) Calibration of the interlaboratory $^{40}Ar/^{39}Ar$ dating standard MMHb-1. Chemical Geology 66:27-34

Samson SD, Barr SM, White CE (2000) Nd isotopic characteristics of terranes within the Avalon Zone, southern New Brunswick. Canadian Journal of Earth Sciences 37:1039-1052

Santos JF, Schärer U, Gil Ibarguchi JI, Girardeau J (2002) Genesis of Pyroxenite-rich Peridotite at Cabo Ortegal (NW Spain): Geochemical and Pb-Sr-Nd Isotope Data. Journal of Petrology 43:17-43

Sawyer DS, Buffler RT, Pilger RH (1991) The crust under the Gulf of Mexico basin in Salvador. In: Salvador A (ed) The Gulf of Mexico basin, The Geology of North America, vol J, pp 53-72. Geological Society of America

Schaule BK, Patterson CC (1981) Lead concentrations in the northeast Pacific: evidence for global anthropogenic perturbations. Earth and Planetary Science Letters 54:97-116

Schmidt MW, Poli S (1998) Experimentally based water budgets for dehydrating slabs and consequences for arc magma generation. Earth and Planetary Science Letters 163:361-379

Schmidt MW, Poli S (2003) Generation of Mobile Components during Subduction of Oceanic Crust. In: Rudnick R (ed) The Crust, Treatise on Geochemistry, vol 3, pp 567-591. Elsevier

Schmidt MW, Dardonb A, Chazotb G, Vannucci R (2004) The dependence of Nb and Ta rutile–melt partitioning on melt composition and Nb/Ta fractionation during subduction processes. Earth and Planetary Science Letters 226:415-432

Schneider J, Bosch D, Monié P, Guillot S, García-Casco A, Lardeaux JM, Torres-Roldán RL, Millan Trujillo G (2004) Origin and evolution of the Escambray Massif (Central Cuba): an example of HP/LT rocks exhumed during intraoceanic subduction. Journal of metamorphic Geology 22:227-247

Shervais JW (2001) Birth, death, and resurrection: the life cycle of suprasubduction zone ophiolites. Geochemistry Geophysics Geosystems 2:Art. No 2000GC000080

Shibata T, Thompson G (1986) Peridotites from the mid-Atlantic ridge at 43ºN and their petrogenetic relation to abyssal tholeiites. Contributions to Mineralogy and Petrology 93:144-159

Sinton CW, Duncan RA, Storey M, Lewis J, Estrada JJ (1998) An oceanic flood basalt province within the Caribbean plate. Earth and Planetary Science Letters 155:221-235

Sinton JM, Ford LL, Chappell B, McCulloch MT (2003) Magma Genesis and Mantle Heterogeneity in the Manus Back-arc Basin, Papua New Guinea. Journal of Petrology 44(1):159-195

Snow JE, Dick HJB (1995) Pervasive Magnesium Loss by Marine Weathering of Peridotite. Geochimica et Cosmochimica Acta 59(20):4219-4235

Somin M, Millán G (1981) Geología de los complejos metamórficos de Cuba. Nauka, Moscow, p 219

Somin ML, Arakelyants MM, Kolesnikow EM (1992) Age and tectonic significance of high-pressure metamorphic rocks in Cuba. International Geology Review 34:105-118

Stacey JS, Kramers JD (1975) Approximation of terrestrial lead isotopic evolution by a two-stage model. Earth and Planetary Science Letters 26:207-221

Stanek KP, Maresh WV, Grafe F, Grevel C, Baumann A (2006) Structure, tectonics and metamorphic development of the Sancti Spiritus Dome (eastern Escambray massif, Central Cuba). Geologica Acta 4:151-170

Staudigel H, Davies GR, Hart SR, Marchant KM, Smith BM (1995) Large scale isotopic Sr, Nd and O isotopic anatomy of altered oceanic crust: DSDP/ODP sites 417/418. Earth and Planetary Science Letters 130:169-185

Staudigel H, Plank T, White W, Schmincke HU (1996) Geochemical fluxes during seafloor alteration of the basaltic upper oceanic crust: DSDP sites 417 and 418. In: Bebout GE, Scholl DW, Kirby SH, Platt JP (eds) Subduction Top to Bottom. Geophysical Monograph Series, vol 96, pp 19-38. American Geophysical Union

Stern RJ (2004) Subduction initiation: spontaneous and induced. Earth and Planetary Science Letters 226:275-292

Su Y, Langmuir CH (2003) Global MORB chemistry compilation at the segment scale. Department of Earth and Environmental Sciences, Columbia University, Palisades, USA. http://petdb.ldeo.columbia.edu/documentation/morbcompilation/

Suhr G (1992) Upper mantle peridotites in the Bay of Islands Ophiolite, Newfoundland: formation during the final stages of a spreading centre. Tectonophysics 206:31-53

Sun S-S, McDonough WF (1989) Chemical and isotopic systematics of oceanic basalts: implications for mantle composition and processes. In: Saunders AD, Norry MJ (eds) Magmatism in the Ocean Basins. Geological Society of London Special Publications, vol 42, pp 313-345

Tatsumi Y, Hamilton DL, Nesbitt RW (1986) Chemical characteristics of fluid phase released from a subducted lithosphere and origin of arc magmas-Evidence from high-pressure experiments and natural rocks. Journal of Volcanology and Geothermal Research 29:293-309

Taylor B, Martinez F (2003) Back-arc basin basalt systematics. Earth and Planetary Science Letters 210:481-497

Taylor SR, McLennan SM (1985) The Continental Crust: its Composition and Evolution. Blackwell Scientific Publications, p 307

Tiepolo M, Vannucci R, Oberti R, Foley S, Bottazzi P, Zanetti A (2000) Nb and Ta incorporation and fractionation in titanian pargasite and kaersutite: crystal-chemical constraints and implications for natural systems. Earth and Planetary Science Letters 176:185-201

Tiepolo M, Bottazzi P, Foley SF, Oberti R, Vannucci R, Zanetti A (2001) Fractionation of Nb and Ta from Zr and Hf at Mantle Depths: the Role of Titanian Pargasite and Kaersutite. Journal of Petrology 42:221-232

Todt W, Cliff RA, Hanser A, Hofmann AW (1996) Evaluation of a ^{202}Pb-^{205}Pb double spike for high-precision lead isotope analysis. In: Basu A, Hart S (eds) Earth Processes: reading the Isotopic Code. Geophysical Monograph Series, vol 95, pp 429-437. American Geophysical Union

Tohver E, Bettencourt JS, Tosdal R, Mezger K, Leite WB, Payolla BL (2004) Terrane transfer during the Grenville orogeny: tracing the Amazonian ancestry of southern Appalachian basement through Pb and Nd isotopes. Earth and Planetary Science Letters 228:161-176

Turner S, Hawkesworth C, vanCalsteren P, Heath E, Macdonald R, Black S (1996) U-series isotopes and destructive plate margin magma genesis in the Lesser Antilles. Earth and Planetary Science Letters 142:191-207

van Westrenen W, Blundy JD, Wood BJ (2001) High field strength element/rare earth element fractionation during partial melting in the presence of garnet: Implications for identification of mantle heterogeneities. Geochemistry Geophysics Geosystems 2:Art. No 2000GC000133

Vernières J, Godard M, Bodinier JL (1997) A plate model for the simulation of trace element fractionation during partial melting and magma transport in the Earth's upper mantle. Journal of Geophysical Research 102:24771-24784

Vissers RLM, Nicolas A (1995) Mantle and Lower Crust Exposed in Oceanic Ridges and Ophiolites: Contributions to a Specialized Symposium of the VII EUG Meeting, Strasbourg, Spring 1993 (Petrology and Structural Geology). Springer-Verlag, p 224

Wadge G, Draper G, Lewis JF (1984) Ophiolites of the northern Caribbean: A reappraisal of their roles in the evolution of the Caribbean plate boundary. In: Gass IG, Lippard SJ, Shelton AW (eds) Ophiolites and oceanic lithosphere. Geological Society of London Special Publications, vol 13, pp 367-380. Blackwell Scientific Publications

Walter MJ (1998) Melting of garnet peridotite and the origin of komatiite and depleted lithosphere. Journal of Petrology 39:29-60

Walter MJ (2003) Melt Extraction and Compositional Variability in Mantle Lithosphere. In: Carlson RW (ed) The Mantle and Core, Treatise on Geochemistry, vol 2, pp 363-394. Elsevier

Walter MJ, Sisson TW, Presnall DC (1995) A mass proportion method for calculating melting reactions and application to melting of model upper mantle lherzolite. Earth and Planetary Science Letters 135:77-90

Weaver BL, Wood DA, Tarney JA, Joron JL (1986) Role of subducted sediment in the genesis of ocean-island basalts: geochemical evidence from South Atlantic Islands. Geology 14:275-278

Weis D, Ingle S, Damasceno D, Frey FA, Nicolaysen K, Barling J (2001) Origin of continental components in Indian Ocean basalts: Evidence from Elan Bank (Kerguelen Plateau, ODP Leg 183, Site 1137). Geology 29:147-150

White MW, Albarède F, Télouk P (2000) High precision analysis of Pb isotopic ratios by multi-collector ICP-MS. Chemical Geology 167:257-270

White WM, Dupré BJ (1986) Sediment subduction and magma genesis in the Lesser Antilles: isotopic and trace element constraints. Journal of Geophysical Research 91:5927-5941

White WM, Patchett J (1984) Hf-Nd-Sr isotopes and incompatible element abundances in island arcs: implications for magma origins and crust-mantle evolution. Earth and Planetary Science Letters 67:167-185

Wilson JT (1966) Are the structures of the Caribbean and Scotia arcs analogous to ice rafting? Earth and Planetary Science Letters 1:335-338

Woodhead J, Eggins S, Gamble J (1993) High field strength and transition element systematics in island arc and back-arc basin basalts: evidence for multi-phase melt extraction and a depleted mantle wedge. Earth and Planetary Science Letters 114:491-504

Workman RK, Hart SR (2005) Major and trace element composition of the depleted MORB mantle (DMM). Earth and Planetary Science Letters 231:53-72

York D (1969) Least squares fitting of a straight line with correlated errors. Earth and Planetary Science Letters 5:320-324

APPENDIX 1

MINERAL CHEMISTRY OF THE ULTRAMAFIC AND MAFIC ROCKS FROM THE MAYARÍ-BARACOA OPHIOLITIC BELT

Table A1.1 EPM analyses of olivine in ultramafic and mafic rocks from the Mayarí-Baracoa Ophiolitic Belt

Massif	***Moa-Baracoa***																							
Rocktype	*Harzburgite*													*Dunite*									*Impregnated dunite*		
Sample	CG 3	YM 14								YM 16				CG 16									CG 4	CG 18	
SiO_2 (wt%)	40.54	40.40	40.63	40.55	40.18	40.46	40.07	40.43	40.85	41.15	41.45	40.79	40.59	40.39	40.42	40.30	40.44	40.30	40.28	40.10	40.62	40.22	40.59	40.97	40.99
TiO_2	0.02	0.03	0.00	0.01	0.01	0.00	0.02	0.01	0.00	0.00	0.02	0.02	0.00	0.03	0.00	0.00	0.01	0.01	0.02	0.04	0.01	0.03	0.03	0.00	0.00
Al_2O_3	0.00	0.00	0.02	0.02	0.01	0.02	0.01	0.05	0.03	0.00	0.00	0.00	0.00	0.00	0.00	0.00	0.00	0.00	0.00	0.00	0.00	0.00	0.00	0.00	0.00
FeO	9.07	9.06	9.15	9.03	9.08	8.90	9.20	9.12	9.35	9.48	9.12	9.36	9.16	8.76	8.45	8.62	8.84	9.10	8.70	8.61	8.40	8.52	9.94	11.02	10.57
MnO	0.17	0.14	0.16	0.12	0.13	0.11	0.14	0.16	0.18	0.14	0.15	0.11	0.18	0.15	0.13	0.12	0.11	0.14	0.10	0.14	0.13	0.16	0.16	0.15	0.10
MgO	50.65	50.21	49.61	50.27	50.61	49.98	49.78	49.71	49.61	49.21	49.64	49.92	49.80	50.81	50.96	50.90	51.00	51.44	50.98	51.30	51.07	51.06	50.34	48.65	48.75
CaO	0.01	0.00	0.03	0.02	0.00	0.03	0.04	0.02	0.04	0.03	0.04	0.05	0.05	0.05	0.05	0.05	0.03	0.03	0.04	0.04	0.00	0.02	0.02	0.04	0.04
NiO	0.40	0.39	0.43	0.42	0.42	0.45	0.40	0.43	0.40	0.40	0.40	0.42	0.44	0.40	0.37	0.39	0.38	0.38	0.38	0.41	0.46	0.38	0.23	0.28	0.26
Total	100.86	100.23	100.03	100.44	100.44	99.94	99.67	99.93	100.45	100.40	100.82	100.67	100.22	100.59	100.38	100.38	100.81	101.40	100.50	100.64	100.69	100.39	101.31	101.11	100.70
Structural formula																									
Si	0.99	0.99	1.00	0.99	0.98	0.99	0.99	0.99	1.00	1.00	1.01	0.99	0.99	0.99	0.99	0.98	0.98	0.98	0.98	0.98	0.99	0.98	0.99	1.00	1.00
Ti	0.00	0.00	0.00	0.00	0.00	0.00	0.00	0.00	0.00	0.00	0.00	0.00	0.00	0.00	0.00	0.00	0.00	0.00	0.00	0.00	0.00	0.00	0.00	0.00	0.00
Al	0.00	0.00	0.00	0.00	0.00	0.00	0.00	0.00	0.00	0.00	0.00	0.00	0.00	0.00	0.00	0.00	0.00	0.00	0.00	0.00	0.00	0.00	0.00	0.00	0.00
Fe^{2+}	0.18	0.19	0.19	0.18	0.19	0.18	0.19	0.19	0.19	0.19	0.19	0.19	0.19	0.18	0.17	0.18	0.18	0.19	0.18	0.18	0.17	0.18	0.20	0.23	0.22
Mn	0.00	0.00	0.00	0.00	0.00	0.00	0.00	0.00	0.00	0.00	0.00	0.00	0.00	0.00	0.00	0.00	0.00	0.00	0.00	0.00	0.00	0.00	0.00	0.00	0.00
Mg	1.83	1.83	1.81	1.83	1.84	1.82	1.83	1.82	1.80	1.79	1.79	1.81	1.81	1.83	1.84	1.84	1.84	1.85	1.84	1.85	1.84	1.84	1.81	1.77	1.77
Ca	0.00	0.00	0.00	0.00	0.00	0.00	0.00	0.00	0.00	0.00	0.00	0.00	0.00	0.00	0.00	0.00	0.00	0.00	0.00	0.00	0.00	0.00	0.00	0.00	0.00
Ni	0.00	0.00	0.00	0.00	0.00	0.00	0.00	0.00	0.00	0.00	0.00	0.00	0.00	0.00	0.00	0.00	0.00	0.00	0.00	0.00	0.00	0.00	0.00	0.00	0.00
Mg #	90.9	90.8	90.6	90.8	90.9	90.9	90.6	90.7	90.4	90.3	90.6	90.5	90.7	91.0	91.5	91.1	91.1	90.7	91.1	91.1	91.5	91.1	90.0	88.7	89.1

CG = Cayo Guam section; YM = Yamaniguey section; ZCS = Casimba section; QN = Quemado del Negro section; J = Mercedita section. MTZ = Moho transition zone

Table A1.1 (continued)

Massif	***Moa-Baracoa***									***Southern Mayarí-Cristal***																		
Rocktype	*Impregnated dunite*									*Dunite*																		
Sample	CG 18									ZCS 203																		
SiO_2 (wt%)	40.45	40.66	40.80	40.08	40.81	40.46	40.87	40.44	40.40	40.57	40.18	40.49	39.63	39.52	39.60	39.72	40.08	40.13	40.01	39.44	39.32	39.76	39.96	39.90	39.57	39.30	39.36	39.29
TiO_2	0.00	0.02	0.04	0.01	0.01	0.01	0.02	0.07	0.01	0.00	0.01	0.00	0.00	0.01	0.00	0.00	0.00	0.00	0.00	0.00	0.00	0.00	0.00	0.01	0.00	0.00	0.00	0.00
Al_2O_3	0.00	0.00	0.03	0.00	0.00	0.01	0.00	0.00	0.01	0.00	0.00	0.00	0.00	0.00	0.00	0.00	0.00	0.00	0.00	0.01	0.00	0.00	0.00	0.00	0.00	0.00	0.00	0.00
FeO	10.68	10.61	10.74	10.44	10.79	10.64	10.62	10.67	10.49	8.00	7.98	8.04	7.96	7.79	7.82	8.01	8.04	7.95	7.91	7.97	7.79	7.64	7.74	7.75	7.56	7.97	7.96	7.79
MnO	0.14	0.20	0.13	0.17	0.20	0.19	0.19	0.17	0.12	0.08	0.11	0.14	0.11	0.13	0.11	0.13	0.10	0.11	0.13	0.11	0.10	0.14	0.11	0.11	0.07	0.12	0.11	0.14
MgO	48.71	48.67	48.51	48.99	48.86	48.67	48.66	48.79	48.42	51.76	51.11	51.22	51.70	51.68	51.55	51.88	51.76	51.64	51.41	51.77	51.68	51.48	51.75	51.59	51.57	51.33	51.71	51.49
CaO	0.05	0.02	0.04	0.04	0.04	0.06	0.06	0.05	0.04	0.03	0.04	0.03	0.02	0.02	0.02	0.03	0.01	0.02	0.03	0.04	0.05	0.05	0.05	0.06	0.05	0.05	0.04	0.03
NiO	0.30	0.28	0.29	0.27	0.28	0.28	0.27	0.29	0.23	0.47	0.51	0.48	0.48	0.53	0.48	0.52	0.48	0.48	0.46	0.46	0.44	0.49	0.44	0.47	0.47	0.55	0.50	0.45
Total	100.33	100.44	100.57	100.00	100.99	100.31	100.67	100.48	99.72	100.90	99.93	100.40	99.90	99.66	99.57	100.29	100.48	100.34	99.95	99.79	99.39	99.56	100.06	99.90	99.30	99.32	99.68	99.20
Structural formula																												
Si	0.99	1.00	1.00	0.99	1.00	0.99	1.00	0.99	1.00	0.98	0.98	0.98	0.97	0.97	0.97	0.97	0.97	0.98	0.98	0.97	0.97	0.97	0.97	0.97	0.97	0.97	0.97	0.97
Ti	0.00	0.00	0.00	0.00	0.00	0.00	0.00	0.00	0.00	0.00	0.00	0.00	0.00	0.00	0.00	0.00	0.00	0.00	0.00	0.00	0.00	0.00	0.00	0.00	0.00	0.00	0.00	0.00
Al	0.00	0.00	0.00	0.00	0.00	0.00	0.00	0.00	0.00	0.00	0.00	0.00	0.00	0.00	0.00	0.00	0.00	0.00	0.00	0.00	0.00	0.00	0.00	0.00	0.00	0.00	0.00	0.00
Fe^{2+}	0.22	0.22	0.22	0.22	0.22	0.22	0.22	0.22	0.22	0.16	0.16	0.16	0.16	0.16	0.16	0.16	0.16	0.16	0.16	0.16	0.16	0.16	0.16	0.16	0.16	0.16	0.16	0.16
Mn	0.00	0.00	0.00	0.00	0.00	0.00	0.00	0.00	0.00	0.00	0.00	0.00	0.00	0.00	0.00	0.00	0.00	0.00	0.00	0.00	0.00	0.00	0.00	0.00	0.00	0.00	0.00	0.00
Mg	1.78	1.78	1.77	1.80	1.78	1.78	1.77	1.78	1.78	1.86	1.86	1.86	1.89	1.89	1.88	1.89	1.88	1.87	1.87	1.89	1.89	1.88	1.88	1.88	1.89	1.88	1.89	1.89
Ca	0.00	0.00	0.00	0.00	0.00	0.00	0.00	0.00	0.00	0.00	0.00	0.00	0.00	0.00	0.00	0.00	0.00	0.00	0.00	0.00	0.00	0.00	0.00	0.00	0.00	0.00	0.00	0.00
Ni	0.00	0.00	0.00	0.00	0.00	0.00	0.00	0.00	0.00	0.00	0.00	0.00	0.00	0.00	0.00	0.00	0.00	0.00	0.00	0.00	0.00	0.00	0.00	0.00	0.00	0.00	0.00	0.00
Mg #	89.1	89.1	88.9	89.3	89.0	89.1	89.1	89.1	89.2	92.0	91.9	91.9	92.1	92.2	92.2	92.0	92.0	92.0	92.0	92.0	92.2	92.3	92.3	92.2	92.4	92.0	92.0	92.2

Table A1.1 (continued)

Massif	***Southern Mayarí-Cristal***													***Moa-Baracoa***												
Rocktype	*Dunite*													*Crustal gabbro*												
Sample	ZCS 203													QN 18				QN 16								
SiO_2 (wt%)	39.82	39.47	39.49	39.78	39.73	39.79	39.71	39.63	40.58	40.52	40.40	40.12	39.87	38.13	38.25	38.99	38.53	38.75	38.40	38.37	38.20	38.38	38.35	38.97	38.31	38.58	38.30
TiO_2	0.00	0.00	0.00	0.01	0.00	0.00	0.00	0.00	0.01	0.00	0.00	0.00	0.00	0.03	0.03	0.01	0.00	0.03	0.01	0.02	0.03	0.02	0.00	0.01	0.04	0.05	0.03
Al_2O_3	0.00	0.00	0.00	0.00	0.00	0.00	0.00	0.00	0.00	0.00	0.00	0.00	0.00	0.00	0.00	0.00	0.00	0.00	0.00	0.01	0.03	0.00	0.03	0.00	0.04	0.00	0.00
FeO	7.82	7.80	7.73	7.83	7.86	7.92	7.82	7.73	7.90	8.04	7.81	7.87	8.04	20.78	20.57	20.89	20.86	21.12	21.25	20.97	20.68	20.84	21.28	21.02	21.00	20.86	20.80
MnO	0.11	0.10	0.13	0.16	0.11	0.11	0.11	0.11	0.11	0.09	0.15	0.13	0.13	0.32	0.32	0.32	0.40	0.31	0.30	0.30	0.32	0.32	0.28	0.32	0.31	0.30	0.25
MgO	51.43	51.48	51.88	51.57	51.84	51.48	51.42	51.62	51.38	51.29	51.18	51.42	51.70	40.93	41.30	40.72	40.96	40.23	40.49	40.19	40.10	40.79	40.76	40.28	40.71	40.72	40.65
CaO	0.04	0.04	0.03	0.04	0.04	0.05	0.03	0.03	0.02	0.03	0.02	0.04	0.05	0.04	0.03	0.03	0.03	0.05	0.03	0.05	0.04	0.01	0.05	0.04	0.02	0.03	0.05
NiO	0.52	0.51	0.44	0.47	0.49	0.46	0.51	0.47	0.48	0.46	0.51	0.49	0.54	0.15	0.12	0.12	0.10	0.16	0.13	0.17	0.14	0.08	0.14	0.12	0.12	0.13	0.12
Total	99.75	99.40	99.70	99.86	100.08	99.81	99.60	99.59	100.48	100.44	100.07	100.07	100.32	100.38	100.62	101.08	100.88	100.65	100.61	100.08	99.54	100.44	100.89	100.76	100.55	100.67	100.20
Structural formula																											
Si	0.97	0.97	0.97	0.97	0.97	0.97	0.97	0.97	0.98	0.98	0.98	0.98	0.97	0.98	0.98	1.00	0.99	1.00	0.99	0.99	0.99	0.99	0.99	1.00	0.99	0.99	0.99
Ti	0.00	0.00	0.00	0.00	0.00	0.00	0.00	0.00	0.00	0.00	0.00	0.00	0.00	0.00	0.00	0.00	0.00	0.00	0.00	0.00	0.00	0.00	0.00	0.00	0.00	0.00	0.00
Al	0.00	0.00	0.00	0.00	0.00	0.00	0.00	0.00	0.00	0.00	0.00	0.00	0.00	0.00	0.00	0.00	0.00	0.00	0.00	0.00	0.00	0.00	0.00	0.00	0.00	0.00	0.00
Fe^{2+}	0.16	0.16	0.16	0.16	0.16	0.16	0.16	0.16	0.16	0.16	0.16	0.16	0.16	0.45	0.44	0.45	0.45	0.45	0.46	0.45	0.45	0.45	0.46	0.45	0.45	0.45	0.45
Mn	0.00	0.00	0.00	0.00	0.00	0.00	0.00	0.00	0.00	0.00	0.00	0.00	0.00	0.01	0.01	0.01	0.01	0.01	0.01	0.01	0.01	0.01	0.01	0.01	0.01	0.01	0.01
Mg	1.88	1.89	1.89	1.88	1.89	1.88	1.88	1.89	1.86	1.86	1.86	1.87	1.88	1.57	1.58	1.55	1.56	1.54	1.55	1.55	1.55	1.56	1.56	1.54	1.56	1.56	1.56
Ca	0.00	0.00	0.00	0.00	0.00	0.00	0.00	0.00	0.00	0.00	0.00	0.00	0.00	0.00	0.00	0.00	0.00	0.00	0.00	0.00	0.00	0.00	0.00	0.00	0.00	0.00	0.00
Ni	0.00	0.00	0.00	0.00	0.00	0.00	0.00	0.00	0.00	0.00	0.00	0.00	0.00	0.00	0.00	0.00	0.00	0.00	0.00	0.00	0.00	0.00	0.00	0.00	0.00	0.00	0.00
Mg #	92.1	92.2	92.3	92.2	92.2	92.1	92.1	92.2	92.1	91.9	92.1	92.1	92.0	77.7	78.2	77.5	77.6	77.4	77.1	77.5	77.5	77.6	77.2	77.4	77.6	77.6	77.6

Table A1.1 (continued)

Massif	***Moa-Baracoa***																	
Rocktype	*Crustal gabbro*						*Moho transition zone (MTZ) gabbroic sill*										*MTZ Gabbro dyke*	
Sample	QN 8			QN 2			YM 4					CG 17					J3b	
SiO_2 (wt%)	38.50	38.54	38.77	38.41	38.73	38.69	38.22	38.20	38.07	38.15	38.31	38.87	39.24	39.51	39.70	39.95	39.62	39.61
TiO_2	0.01	0.05	0.02	0.02	0.00	0.03	0.00	0.02	0.00	0.01	0.00	0.00	0.00	0.01	0.05	0.04	0.00	0.03
Al_2O_3	0.00	0.01	0.00	0.00	0.00	0.02	0.00	0.00	0.00	0.01	0.00	0.00	0.01	0.00	0.02	0.02	0.00	0.01
FeO	22.04	22.13	21.93	21.46	21.10	21.07	23.85	23.55	23.53	23.69	24.06	17.78	17.58	17.26	17.31	17.51	16.62	16.53
MnO	0.34	0.37	0.37	0.38	0.36	0.27	0.34	0.38	0.31	0.36	0.38	0.26	0.24	0.31	0.23	0.22	0.26	0.25
MgO	40.02	39.92	39.89	40.56	40.47	40.58	38.38	38.69	38.19	38.36	38.26	43.05	42.69	42.90	43.04	43.02	44.54	44.50
CaO	0.05	0.02	0.03	0.05	0.03	0.03	0.04	0.05	0.02	0.02	0.05	0.02	0.02	0.02	0.02	0.01	0.00	0.01
NiO	0.15	0.17	0.12	0.17	0.14	0.17	0.11	0.16	0.22	0.20	0.16	0.29	0.29	0.31	0.25	0.26	0.28	0.29
Total	101.11	101.21	101.13	101.05	100.83	100.86	100.94	101.05	100.34	100.80	101.22	100.27	100.06	100.31	100.63	101.03	101.32	101.23
Structural formula																		
Si	0.99	0.99	1.00	0.99	0.99	0.99	0.99	0.99	0.99	0.99	0.99	0.99	1.00	1.00	1.00	1.00	0.99	0.99
Ti	0.00	0.00	0.00	0.00	0.00	0.00	0.00	0.00	0.00	0.00	0.00	0.00	0.00	0.00	0.00	0.00	0.00	0.00
Al	0.00	0.00	0.00	0.00	0.00	0.00	0.00	0.00	0.00	0.00	0.00	0.00	0.00	0.00	0.00	0.00	0.00	0.00
Fe^{2+}	0.47	0.48	0.47	0.46	0.45	0.45	0.52	0.51	0.51	0.51	0.52	0.38	0.37	0.37	0.37	0.37	0.35	0.35
Mn	0.01	0.01	0.01	0.01	0.01	0.01	0.01	0.01	0.01	0.01	0.01	0.01	0.01	0.01	0.01	0.01	0.01	0.00
Mg	1.53	1.53	1.52	1.55	1.55	1.55	1.49	1.49	1.49	1.49	1.48	1.63	1.62	1.62	1.62	1.61	1.66	1.66
Ca	0.00	0.00	0.00	0.00	0.00	0.00	0.00	0.00	0.00	0.00	0.00	0.00	0.00	0.00	0.00	0.00	0.00	0.00
Ni	0.00	0.00	0.00	0.00	0.00	0.00	0.00	0.00	0.00	0.00	0.00	0.00	0.00	0.00	0.00	0.00	0.00	0.00
Mg #	76.5	76.1	76.4	77.1	77.5	77.5	74.2	74.5	74.5	74.5	74.0	81.2	81.2	81.6	81.6	81.4	82.6	82.6

Table A1.2 EPM analyses of orthopyroxene in Moa-Baracoa ultramafic and mafic rocks

Rocktype	*Harzburgite*																								
Sample	CG 5						CG 6													CG 10						
SiO_2 (wt%)	56.63	56.75	57.00	56.97	57.08	57.18	57.23	57.12	56.99	57.25	57.11	56.11	56.26	56.30	55.75	56.49	56.45	56.40	56.45	56.15	56.09	57.53	57.46	57.61	57.13	55.98
TiO_2	0.04	0.02	0.01	0.01	0.01	0.05	0.02	0.03	0.03	0.03	0.00	0.05	0.09	0.07	0.04	0.08	0.08	0.12	0.10	0.02	0.00	0.00	0.00	0.01	0.00	0.00
Al_2O_3	2.30	2.27	2.14	2.28	2.40	2.27	2.62	2.56	2.43	2.45	2.52	3.47	3.07	2.96	3.11	3.04	3.18	3.19	3.02	2.15	2.03	2.06	1.99	1.90	2.08	2.01
FeO	5.62	5.58	5.80	5.80	5.68	5.63	5.79	5.77	5.68	5.55	5.69	5.93	5.20	5.23	5.27	6.22	6.17	5.78	6.10	6.00	5.96	5.76	5.91	5.94	6.00	5.91
MnO	0.11	0.15	0.17	0.17	0.16	0.13	0.14	0.14	0.16	0.19	0.12	0.12	0.17	0.12	0.19	0.07	0.17	0.16	0.08	0.13	0.16	0.13	0.09	0.13	0.18	0.10
MgO	33.85	34.11	34.30	34.14	33.81	33.69	33.48	33.62	33.88	33.61	33.85	33.46	33.67	33.62	33.41	33.66	33.48	33.60	33.57	33.53	33.14	33.05	33.52	33.93	33.89	33.78
CaO	1.54	1.70	1.66	1.47	1.67	1.73	1.73	1.93	1.90	1.90	1.86	1.13	1.54	1.65	1.33	0.98	1.22	1.34	1.23	1.72	1.90	1.96	2.16	1.22	1.64	1.54
Total	100.10	100.58	101.08	100.82	100.80	100.67	101.01	101.17	101.06	100.98	101.14	100.27	99.99	99.95	99.10	100.54	100.77	100.59	100.54	99.69	99.28	100.49	101.14	100.74	100.91	99.33
Structural formula																										
Si	1.95	1.95	1.95	1.95	1.95	1.96	1.95	1.95	1.95	1.95	1.94	1.91	1.91	1.92	1.92	1.93	1.92	1.92	1.93	1.95	1.95	1.97	1.96	1.97	1.95	1.95
Ti	0.00	0.00	0.00	0.00	0.00	0.00	0.00	0.00	0.00	0.00	0.00	0.00	0.00	0.00	0.00	0.00	0.00	0.00	0.00	0.00	0.00	0.00	0.00	0.00	0.00	0.00
Al	0.09	0.09	0.09	0.09	0.10	0.09	0.11	0.10	0.10	0.10	0.10	0.14	0.12	0.12	0.13	0.12	0.13	0.13	0.12	0.09	0.08	0.08	0.08	0.08	0.08	0.08
Fe^{2+}	0.16	0.16	0.17	0.17	0.16	0.16	0.17	0.16	0.16	0.16	0.17	0.17	0.15	0.15	0.15	0.18	0.18	0.16	0.17	0.17	0.17	0.17	0.17	0.17	0.17	0.17
Mn	0.00	0.00	0.00	0.00	0.00	0.00	0.00	0.00	0.00	0.00	0.00	0.00	0.01	0.00	0.01	0.00	0.01	0.01	0.00	0.00	0.00	0.00	0.00	0.00	0.00	0.00
Mg	1.74	1.74	1.75	1.74	1.72	1.72	1.70	1.71	1.72	1.71	1.72	1.70	1.71	1.71	1.71	1.71	1.70	1.70	1.71	1.73	1.72	1.69	1.71	1.73	1.73	1.75
Ca	0.06	0.06	0.06	0.05	0.06	0.06	0.06	0.07	0.07	0.07	0.07	0.04	0.06	0.06	0.05	0.04	0.05	0.05	0.05	0.06	0.07	0.05	0.08	0.04	0.06	0.06
Mg #	91.5	91.6	91.3	91.3	91.4	91.4	91.2	91.2	91.4	91.5	91.1	91.0	92.0	92.0	91.9	90.6	90.6	91.2	90.8	90.9	90.8	91.1	91.0	91.1	91.0	91.1

CG = Cayo Guam section; YM = Yamaniguey section; QN = Quemado del Negro section. MTZ = Moho transition zone

Table A1.2 (continued)

Rocktype	*Harzburgite*																								
Sample	CG 13										YM 14														
SiO_2 (wt%)	55.04	55.60	56.11	56.26	56.30	55.75	56.49	56.45	56.40	56.45	56.91	55.93	56.58	56.29	56.74	55.94	56.08	57.09	56.56	56.69	57.94	57.51	56.15	57.75	56.91
TiO_2	0.07	0.09	0.05	0.09	0.07	0.04	0.08	0.08	0.12	0.10	0.03	0.01	0.00	0.04	0.00	0.01	0.03	0.00	0.04	0.00	0.04	0.00	0.01	0.02	0.00
Al_2O_3	3.34	3.16	3.47	3.07	2.96	3.11	3.04	3.18	3.19	3.02	1.94	2.01	2.08	2.06	2.00	2.04	2.02	2.00	2.07	1.96	2.08	2.10	2.24	2.00	1.86
FeO	6.34	6.38	5.93	5.20	5.23	5.27	6.22	6.17	5.78	6.10	5.67	6.06	5.85	5.84	5.77	6.13	6.33	6.07	5.85	5.98	6.05	5.92	5.95	6.29	6.01
MnO	0.19	0.12	0.12	0.17	0.12	0.19	0.07	0.17	0.16	0.08	0.16	0.16	0.18	0.13	0.14	0.17	0.16	0.14	0.07	0.16	0.16	0.15	0.10	0.15	0.19
MgO	33.44	33.84	33.46	33.67	33.62	33.41	33.66	33.48	33.60	33.57	33.04	33.55	33.31	33.39	33.96	33.43	33.71	33.45	33.16	33.51	33.15	33.30	32.90	33.50	33.64
CaO	1.34	1.22	1.13	1.54	1.65	1.33	0.98	1.22	1.34	1.23	2.02	1.53	1.86	1.77	1.39	1.51	1.26	1.45	1.73	1.50	1.55	1.72	1.84	1.26	1.31
Total	99.76	100.41	100.27	99.99	99.95	99.10	100.54	100.77	100.59	100.54	99.76	99.25	99.86	99.51	100.01	99.22	99.58	100.18	99.46	99.80	100.97	100.70	99.19	100.97	99.93
Structural formula																									
Si	1.91	1.92	1.91	1.91	1.92	1.92	1.93	1.92	1.92	1.93	1.97	1.97	1.96	1.95	1.96	1.95	1.95	1.96	1.96	1.96	1.98	1.97	1.95	1.97	1.96
Ti	0.00	0.00	0.00	0.00	0.00	0.00	0.00	0.00	0.00	0.00	0.00	0.00	0.00	0.00	0.00	0.00	0.00	0.00	0.00	0.00	0.00	0.00	0.00	0.00	0.00
Al	0.14	0.13	0.14	0.12	0.12	0.13	0.12	0.13	0.13	0.12	0.08	0.08	0.08	0.08	0.08	0.08	0.08	0.08	0.08	0.08	0.08	0.08	0.09	0.08	0.08
Fe^{2+}	0.18	0.18	0.17	0.15	0.15	0.15	0.18	0.18	0.16	0.17	0.16	0.16	0.17	0.17	0.17	0.18	0.18	0.17	0.17	0.17	0.17	0.17	0.17	0.18	0.17
Mn	0.00	0.00	0.00	0.01	0.00	0.01	0.00	0.01	0.01	0.00	0.00	0.00	0.00	0.00	0.00	0.00	0.00	0.00	0.00	0.00	0.00	0.00	0.00	0.00	0.00
Mg	1.73	1.74	1.70	1.71	1.71	1.71	1.71	1.70	1.70	1.71	1.70	1.70	1.72	1.73	1.75	1.74	1.74	1.72	1.71	1.73	1.69	1.70	1.71	1.71	1.73
Ca	0.05	0.05	0.04	0.06	0.06	0.05	0.04	0.05	0.05	0.05	0.05	0.04	0.05	0.07	0.05	0.06	0.05	0.05	0.06	0.06	0.06	0.06	0.07	0.05	0.05
Mg #	90.4	90.4	91.0	92.0	92.0	91.9	90.6	90.6	91.2	90.8	91.2	91.2	91.0	91.1	91.3	90.7	90.5	90.8	91.0	90.9	90.7	90.9	90.8	90.5	90.9

Table A1.2 (continued)

Rocktype	*Harzburgite*													*Crustal Gabbro*				*MTZ gabbroic sill*				
Sample	YM 16													QN 18			QN 8	CG 17				
SiO_2 (wt%)	56.91	56.75	56.14	57.01	57.83	57.95	57.84	56.91	57.50	57.20	56.97	57.74	57.00	55.08	55.35	55.10	54.98	56.34	55.88	54.64	56.08	55.54
TiO_2	0.02	0.01	0.00	0.01	0.01	0.02	0.03	0.02	0.04	0.02	0.04	0.03	0.03	0.45	0.47	0.48	0.43	0.38	0.35	0.38	0.30	0.41
Al_2O_3	2.04	2.06	1.98	2.10	1.99	2.05	1.90	2.13	2.11	2.12	2.13	2.01	2.24	1.35	1.36	1.42	1.19	1.70	1.94	1.97	1.53	1.61
FeO	5.66	6.18	5.66	6.07	6.14	6.31	5.98	6.13	6.20	6.11	6.23	6.03	6.02	12.33	12.18	12.66	14.48	11.54	11.56	11.37	11.29	11.17
MnO	0.10	0.15	0.19	0.06	0.18	0.17	0.13	0.15	0.18	0.12	0.21	0.13	0.10	0.32	0.35	0.34	0.38	0.25	0.20	0.29	0.29	0.30
MgO	32.73	33.65	32.93	33.25	33.35	33.42	33.68	33.43	33.18	33.37	33.03	32.89	33.20	29.06	29.35	29.01	27.84	30.00	29.18	29.38	30.03	29.98
CaO	2.63	1.25	2.50	1.51	1.68	1.16	0.97	1.54	1.53	1.30	1.89	1.69	1.70	1.30	1.18	1.23	1.18	0.92	1.34	1.29	0.99	1.06
Total	100.08	100.06	99.39	100.01	101.19	101.08	100.52	100.30	100.73	100.23	100.50	100.51	100.29	99.89	100.24	100.24	100.48	101.13	100.44	99.33	100.51	100.06
Structural formula																						
Si	1.96	1.96	1.95	1.96	1.96	1.97	1.97	1.95	1.96	1.96	1.95	1.97	1.95	1.95	1.94	1.94	1.94	1.96	1.96	1.94	1.97	1.96
Ti	0.00	0.00	0.00	0.00	0.00	0.00	0.00	0.00	0.00	0.00	0.00	0.00	0.00	0.01	0.01	0.01	0.01	0.01	0.01	0.01	0.01	0.01
Al	0.08	0.08	0.08	0.09	0.08	0.08	0.08	0.09	0.09	0.09	0.09	0.08	0.09	0.06	0.06	0.06	0.05	0.07	0.08	0.08	0.06	0.07
Fe^{2+}	0.16	0.18	0.16	0.17	0.17	0.18	0.17	0.18	0.18	0.18	0.18	0.17	0.17	0.37	0.36	0.37	0.43	0.34	0.34	0.34	0.33	0.33
Mn	0.00	0.00	0.00	0.00	0.01	0.01	0.00	0.00	0.01	0.00	0.01	0.00	0.00	0.01	0.01	0.01	0.01	0.01	0.01	0.01	0.01	0.01
Mg	1.68	1.73	1.71	1.70	1.69	1.69	1.71	1.71	1.69	1.70	1.69	1.67	1.69	1.53	1.53	1.53	1.47	1.56	1.53	1.55	1.57	1.57
Ca	0.10	0.05	0.09	0.06	0.06	0.04	0.04	0.06	0.06	0.05	0.07	0.06	0.06	0.05	0.05	0.05	0.05	0.03	0.05	0.05	0.04	0.04
Mg #	91.2	90.7	91.2	90.7	90.7	90.4	91.0	90.7	90.5	90.7	90.4	90.7	90.8	80.5	81.0	80.5	77.4	82.3	81.8	82.2	82.6	82.7

Table A1.3 EPM analyses of clinopyroxene in ultramafic and mafic rocks from the Mayarí-Baracoa Ophiolitic Belt

Massif	***Moa-Baracoa***																									
Rocktype	*Impregnated dunite*													*Crustal gabbro*												
Sample	CG 4						CG 18							QN 18					QN 16					QN 12	QN 8		
SiO_2 (wt%)	53.04	52.22	51.89	51.97	51.37	51.94	51.12	51.96	52.03	51.83	52.47	51.04	51.09	51.81	52.06	52.08	53.41	52.23	52.90	51.80	52.05	51.64	51.78	50.84	52.74	52.49	52.50
TiO_2	1.13	1.13	1.14	1.21	1.27	1.13	1.41	1.36	1.37	1.37	1.19	1.42	1.30	0.88	0.91	0.84	0.62	0.78	0.64	0.74	0.73	0.78	0.69	0.60	0.88	0.87	0.88
Al_2O_3	3.29	3.28	3.46	3.37	3.40	3.19	3.82	3.62	3.56	3.28	3.40	3.71	3.63	2.63	2.51	2.42	1.98	2.21	2.24	2.27	2.24	2.35	2.28	2.31	2.56	2.59	2.74
Cr_2O_3	1.21	1.19	1.24	1.05	1.21	1.26	0.97	1.17	0.94	0.93	1.02	1.29	1.05	0.21	0.18	0.19	0.16	0.23	0.30	0.35	0.34	0.33	0.32	0.35	0.35	0.42	0.39
FeO	2.92	3.20	3.05	3.02	2.75	3.10	3.86	3.44	2.86	3.43	3.60	3.37	3.15	6.13	5.73	5.93	9.49	6.29	9.23	6.40	5.98	6.14	6.32	10.40	7.23	6.63	6.77
MnO	0.13	0.11	0.04	0.13	0.07	0.09	0.16	0.10	0.13	0.16	0.07	0.14	0.10	0.26	0.19	0.12	0.23	0.25	0.21	0.20	0.20	0.19	0.17	0.27	0.25	0.22	0.27
MgO	16.85	17.38	17.26	16.79	16.71	17.38	16.86	16.91	15.63	16.62	17.41	16.10	16.35	16.93	16.27	16.23	21.00	16.98	20.42	16.94	16.25	15.92	16.00	21.91	16.60	15.82	15.79
CaO	21.98	21.40	22.01	22.00	22.23	21.64	21.01	20.80	23.13	21.70	20.94	22.19	22.36	21.18	21.64	21.77	13.71	20.78	14.63	20.68	21.72	22.04	21.85	12.80	20.14	22.07	21.57
Total	100.54	99.90	100.09	99.54	99.01	99.72	99.21	99.36	99.64	99.33	100.09	99.26	99.01	100.03	99.49	99.58	100.60	99.75	100.57	99.38	99.51	99.39	99.41	99.48	100.75	101.11	100.91
Structural formula																											
Si	1.91	1.90	1.89	1.90	1.89	1.90	1.87	1.90	1.90	1.90	1.90	1.88	1.88	1.89	1.91	1.91	1.93	1.91	1.91	1.90	1.91	1.90	1.88	1.85	1.92	1.90	1.91
Ti	0.03	0.03	0.03	0.03	0.04	0.03	0.04	0.04	0.04	0.04	0.03	0.04	0.04	0.02	0.03	0.02	0.02	0.02	0.02	0.02	0.02	0.02	0.02	0.02	0.02	0.02	0.02
Al	0.14	0.14	0.15	0.15	0.15	0.14	0.17	0.16	0.15	0.14	0.15	0.16	0.16	0.11	0.11	0.10	0.08	0.09	0.09	0.10	0.10	0.10	0.10	0.10	0.11	0.11	0.12
Cr	0.03	0.03	0.04	0.03	0.04	0.04	0.03	0.03	0.03	0.03	0.03	0.04	0.03	0.01	0.00	0.01	0.00	0.01	0.01	0.01	0.01	0.01	0.01	0.01	0.01	0.01	0.01
Fe^{2+}	0.09	0.10	0.09	0.09	0.08	0.09	0.12	0.11	0.09	0.11	0.11	0.10	0.10	0.11	0.14	0.13	0.25	0.12	0.22	0.12	0.12	0.11	0.08	0.13	0.20	0.16	0.17
Mn	0.00	0.00	0.00	0.00	0.00	0.00	0.01	0.00	0.00	0.01	0.00	0.00	0.00	0.01	0.01	0.00	0.01	0.01	0.01	0.01	0.01	0.01	0.00	0.01	0.01	0.01	0.01
Mg	0.91	0.94	0.94	0.91	0.92	0.95	0.94	0.92	0.85	0.91	0.94	0.88	0.90	0.92	0.89	0.89	1.13	0.92	1.10	0.93	0.89	0.87	0.88	1.18	0.90	0.86	0.86
Ca	0.85	0.83	0.86	0.86	0.88	0.85	0.84	0.81	0.91	0.85	0.81	0.88	0.88	0.83	0.85	0.86	0.53	0.81	0.56	0.81	0.85	0.87	0.87	0.50	0.78	0.86	0.84
Mg #	91.1	90.7	91.0	90.9	91.6	91.0	88.6	89.8	90.7	89.6	89.6	89.5	90.3	89.3	86.4	87.3	81.9	88.5	83.3	88.6	88.1	88.8	91.7	90.1	81.8	84.3	83.5

CG = Cayo Guam section; QN = Quemado del Negro section; YM = Yamaniguey section; ZCS = Casimba section; J = Mercedita section; LB = Loma de la Bandera section. MTZ = Moho transition zone

Table A1.3 (continued)

Massif	***Moa-Baracoa***																										
Rocktype	*Crustal gabbro*																				*Moho transition zone (MTZ) gabbroic sill*						
Sample	QN 8						QN 4									QN 2					YM 3			YM 4			
SiO_2 (wt%)	52.16	52.29	52.12	52.04	52.87	52.09	51.57	51.39	51.27	51.48	51.66	51.90	51.54	51.32	51.57	51.94	51.94	52.80	51.87	51.93	51.00	51.80	51.63	51.36	51.56	51.40	52.30
TiO_2	0.93	0.88	0.81	0.84	0.77	0.85	0.69	0.67	0.68	0.65	0.67	0.58	0.63	0.64	0.65	0.69	0.68	0.66	0.84	0.67	0.54	0.80	0.79	0.66	0.85	0.95	0.86
Al_2O_3	2.64	2.60	2.51	2.48	2.34	2.65	2.37	2.55	2.30	2.28	2.24	2.17	2.40	2.38	2.34	2.51	2.44	2.32	2.58	2.49	3.05	2.92	2.84	2.25	2.63	2.63	2.73
Cr_2O_3	0.45	0.40	0.44	0.39	0.33	0.37	0.35	0.33	0.34	0.32	0.28	0.29	0.28	0.31	0.29	0.38	0.37	0.32	0.44	0.34	0.57	0.43	0.49	0.16	0.12	0.18	0.17
FeO	6.81	6.54	7.36	6.50	7.62	6.73	6.21	5.92	6.07	7.16	5.87	6.66	5.94	5.90	5.82	5.97	5.98	7.33	5.67	6.36	8.36	7.46	6.99	11.46	10.23	7.96	7.43
MnO	0.19	0.20	0.33	0.19	0.19	0.27	0.18	0.16	0.15	0.24	0.17	0.21	0.21	0.18	0.19	0.22	0.14	0.26	0.23	0.18	0.20	0.21	0.18	0.29	0.29	0.20	0.24
MgO	16.00	15.89	16.40	15.69	17.70	16.26	15.89	15.21	15.27	17.19	15.44	16.49	15.46	15.50	16.14	15.97	16.33	18.32	15.84	16.46	16.44	15.13	15.38	18.01	17.35	15.50	16.67
CaO	21.15	21.70	20.85	21.79	19.11	21.51	22.19	23.06	22.97	20.36	23.16	21.17	22.82	22.86	22.42	22.12	21.81	18.97	23.00	21.22	19.99	22.03	22.21	16.48	17.61	21.37	19.43
Total	100.33	100.50	100.82	99.92	100.93	100.73	99.45	99.29	99.06	99.66	99.49	99.47	99.26	99.09	99.41	99.80	99.69	100.98	100.47	99.65	100.14	100.78	100.49	100.67	100.63	100.20	99.83
Structural formula																											
Si	1.90	1.90	1.89	1.91	1.91	1.89	1.91	1.91	1.91	1.90	1.91	1.92	1.91	1.91	1.91	1.90	1.90	1.90	1.89	1.90	1.88	1.91	1.90	1.89	1.89	1.90	1.91
Ti	0.03	0.02	0.02	0.02	0.02	0.02	0.02	0.02	0.02	0.02	0.02	0.02	0.02	0.02	0.02	0.02	0.02	0.02	0.02	0.02	0.02	0.02	0.02	0.02	0.02	0.03	0.02
Al	0.11	0.11	0.11	0.11	0.10	0.11	0.10	0.11	0.11	0.10	0.10	0.09	0.11	0.10	0.10	0.11	0.10	0.10	0.11	0.11	0.13	0.13	0.12	0.10	0.11	0.12	0.12
Cr	0.01	0.01	0.01	0.01	0.01	0.01	0.01	0.01	0.01	0.01	0.01	0.01	0.01	0.01	0.01	0.01	0.01	0.01	0.01	0.01	0.02	0.01	0.01	0.01	0.00	0.01	0.00
Fe^{2+}	0.16	0.15	0.15	0.16	0.19	0.13	0.17	0.16	0.16	0.16	0.16	0.18	0.16	0.15	0.14	0.11	0.11	0.15	0.09	0.12	0.20	0.22	0.20	0.26	0.27	0.22	0.20
Mn	0.01	0.01	0.01	0.01	0.01	0.01	0.01	0.01	0.01	0.01	0.01	0.01	0.01	0.01	0.01	0.01	0.00	0.01	0.01	0.01	0.01	0.01	0.01	0.01	0.01	0.01	0.01
Mg	0.87	0.86	0.89	0.86	0.95	0.88	0.88	0.84	0.84	0.94	0.85	0.91	0.86	0.86	0.89	0.87	0.89	0.99	0.86	0.90	0.90	0.83	0.84	0.99	0.95	0.85	0.91
Ca	0.83	0.85	0.81	0.86	0.74	0.84	0.88	0.92	0.92	0.80	0.92	0.84	0.91	0.91	0.89	0.87	0.86	0.73	0.90	0.83	0.79	0.87	0.88	0.65	0.69	0.85	0.76
Mg #	84.5	85.1	85.6	84.3	83.3	87.1	84.1	83.8	83.8	85.5	84.6	83.4	84.1	85.1	86.3	88.8	89.0	86.8	90.5	88.2	82.2	78.8	81.1	79.0	78.2	79.5	82.0

Table A1.3 (continued)

Massif	***Moa-Baracoa***																									
Rocktype	*Moho transition zone (MTZ) gabbroic sill*																		*MTZ Gabbro dyke*			***Northern Mayarí-Cristal*** *Gabbro dyke*					
Sample	YM 4					CG 17													J3b			LB 1					
SiO_2 (wt%)	51.56	52.16	51.69	51.36	52.18	52.21	51.25	51.89	53.68	51.82	54.00	52.20	51.84	52.05	51.80	52.23	51.79	51.76	52.63	52.06	52.13	53.39	54.28	54.20	53.16	53.28	53.66
TiO_2	0.98	0.97	0.87	0.89	0.87	1.00	0.95	1.02	0.58	1.01	0.67	0.85	0.87	0.90	0.92	0.97	0.97	0.96	0.56	0.70	0.65	0.34	0.12	0.10	0.24	0.25	0.29
Al_2O_3	2.65	2.75	2.48	2.61	2.61	3.40	3.24	3.34	2.32	3.32	2.56	3.25	3.11	3.29	3.19	3.22	3.00	3.38	3.31	3.46	3.52	1.46	0.63	0.72	1.07	1.32	1.24
Cr_2O_3	0.19	0.20	0.17	0.18	0.17	0.87	0.94	0.84	0.47	0.90	0.45	0.75	1.04	0.99	1.01	0.79	0.92	0.78	0.79	1.04	1.08	0.03	0.04	0.01	0.03	0.01	0.02
FeO	6.56	6.64	8.17	7.13	7.64	4.64	4.91	4.78	8.78	4.84	8.33	5.13	5.80	5.22	5.78	5.14	4.64	4.72	7.59	4.11	3.88	7.29	6.12	6.09	7.13	7.62	7.09
MnO	0.25	0.14	0.16	0.18	0.24	0.18	0.19	0.18	0.28	0.17	0.25	0.21	0.23	0.11	0.19	0.11	0.22	0.19	0.18	0.21	0.10	0.30	0.17	0.04	0.17	0.22	0.20
MgO	15.72	15.69	16.95	15.81	17.03	15.23	15.42	16.16	23.46	15.70	22.10	16.68	17.01	16.45	15.84	16.94	15.82	15.70	21.60	15.76	16.00	15.03	15.65	15.78	15.53	15.12	15.20
CaO	21.84	21.41	18.97	21.06	19.67	22.21	22.32	21.17	10.30	21.48	11.32	20.79	20.06	20.81	21.77	20.38	21.77	22.21	13.49	22.15	22.30	22.66	24.03	23.36	22.68	22.66	22.77
Total	99.75	99.96	99.46	99.22	100.41	99.75	99.21	99.38	99.88	99.22	99.68	99.87	99.96	99.82	100.51	99.77	99.11	99.71	100.15	99.49	99.66	100.50	101.04	100.30	100.01	100.48	100.47
Structural formula																											
Si	1.89	1.91	1.90	1.89	1.90	1.92	1.90	1.91	1.94	1.91	1.95	1.91	1.90	1.91	1.90	1.91	1.91	1.90	1.89	1.90	1.90	1.96	1.98	1.99	1.96	1.96	1.97
Ti	0.03	0.03	0.02	0.03	0.02	0.03	0.03	0.03	0.02	0.03	0.02	0.02	0.02	0.03	0.03	0.03	0.03	0.03	0.01	0.02	0.02	0.01	0.00	0.00	0.01	0.01	0.01
Al	0.12	0.12	0.11	0.11	0.11	0.15	0.14	0.15	0.10	0.14	0.11	0.14	0.13	0.14	0.14	0.14	0.13	0.15	0.14	0.15	0.15	0.06	0.03	0.03	0.05	0.06	0.05
Cr	0.00	0.01	0.00	0.00	0.00	0.03	0.03	0.02	0.01	0.03	0.01	0.02	0.03	0.03	0.03	0.02	0.03	0.02	0.02	0.03	0.03	0.00	0.00	0.00	0.00	0.00	0.00
Fe^{2+}	0.13	0.16	0.19	0.15	0.18	0.14	0.15	0.15	0.27	0.15	0.25	0.16	0.18	0.16	0.18	0.16	0.14	0.15	0.18	0.10	0.09	0.21	0.17	0.19	0.18	0.20	0.22
Mn	0.01	0.00	0.00	0.01	0.01	0.01	0.01	0.01	0.01	0.01	0.01	0.01	0.01	0.00	0.01	0.00	0.01	0.01	0.01	0.01	0.00	0.01	0.00	0.00	0.00	0.01	0.01
Mg	0.86	0.86	0.93	0.87	0.93	0.83	0.85	0.89	1.26	0.86	1.19	0.91	0.93	0.90	0.87	0.92	0.87	0.86	1.16	0.86	0.87	0.82	0.85	0.86	0.85	0.83	0.83
Ca	0.86	0.84	0.75	0.83	0.77	0.87	0.89	0.83	0.40	0.85	0.44	0.82	0.79	0.82	0.86	0.80	0.86	0.88	0.52	0.87	0.87	0.89	0.94	0.92	0.89	0.89	0.90
Mg #	86.9	84.3	83.0	85.3	83.8	85.4	84.8	85.8	82.6	85.3	82.6	85.3	83.9	84.9	83.0	85.5	85.8	85.6	86.6	89.6	90.6	79.6	83.3	81.9	82.5	80.6	79.0

Table A1.4 Average LA-ICP-MS analyses of clinopyroxene in Moa-Baracoa crustal gabbros

Sample	QN 2 (n=12)	RSD%	QN 4 (n=15)	RSD%
Sr (ppm)	4.6	7	4.4	21
Y	16	5	17	10
Zr	10	9	12	15
Nb	0.07	35	0.11	33
La	0.21	6	0.26	19
Ce	1.4	8	1.6	15
Nd	2.5	10	2.7	14
Sm	1.3	12	1.3	15
Eu	0.48	9	0.49	15
Gd	2.2	8	2.2	16
Tb	0.41	7	0.41	14
Dy	3.0	7	3.0	14
Ho	0.64	6	0.65	13
Er	1.8	7	1.9	13
Tm	0.26	7	0.28	12
Yb	1.8	7	1.8	9
Lu	0.25	6	0.27	12
Hf	0.43	18	0.48	23

RSD% = relative standard deviation (percentage);
QN = Quemado del Negro section

Table A1.5 EPM analyses of spinel in ultramafic rocks from the Mayarí-Baracoa Ophiolitic Belt

Massif	***Moa-Baracoa***																												
Rocktype	*Harzburgite*																												
Sample	CG 3						CG 5							CG 6															
TiO_2	0.05	0.04	0.06	0.06	0.03	0.05	0.02	0.00	0.06	0.07	0.02	0.05	0.02	0.05	0.06	0.04	0.03	0.05	0.04	0.06	0.02	0.03	0.02	0.02	0.04	0.04	0.05	0.05	
Al_2O_3	24.78	24.78	25.35	25.63	24.80	24.85	27.01	26.71	26.68	27.44	27.58	27.14	27.38	29.73	29.88	29.74	29.61	30.47	30.63	30.84	30.99	30.35	30.15	30.58	30.40	30.24	30.73	30.55	
V_2O_3	0.26	0.26	0.25	0.27	0.21	0.23	0.20	0.24	0.22	0.21	0.20	0.22	0.24	0.20	0.22	0.21	0.20	0.20	0.21	0.20	0.22	0.22	0.21	0.19	0.23	0.18	0.23	0.22	
Cr_2O_3	43.44	43.24	43.20	43.16	43.41	43.36	41.81	41.73	41.90	41.45	41.81	41.92	41.24	38.16	38.27	38.29	38.32	38.14	38.14	37.84	38.10	37.72	37.96	37.51	38.24	38.23	38.16	38.37	
FeOt	18.55	18.43	18.46	18.37	18.67	18.79	17.59	17.39	17.32	16.62	17.49	17.48	17.70	16.44	16.97	16.61	16.74	15.61	15.93	16.27	15.72	16.96	17.01	16.97	15.79	16.19	16.23	16.23	
MnO	0.22	0.31	0.26	0.32	0.24	0.24	0.21	0.26	0.27	0.25	0.19	0.25	0.25	0.19	0.27	0.26	0.24	0.29	0.17	0.21	0.23	0.23	0.24	0.21	0.25	0.30	0.19	0.20	
MgO	12.28	12.43	12.66	12.98	12.62	12.38	13.73	13.49	13.69	14.03	13.87	13.72	13.69	14.34	14.03	14.15	14.12	14.74	14.73	14.50	14.70	13.99	13.77	14.05	14.80	14.50	14.71	14.70	
Total	99.58	99.48	100.23	100.79	99.99	99.91	100.57	99.80	100.12	100.08	101.16	100.78	100.52	99.11	99.69	99.31	99.27	99.50	99.83	99.91	99.98	99.50	99.36	99.52	99.74	99.69	100.31	100.32	
Structural formula																													
Ti	0.01	0.01	0.01	0.01	0.01	0.01	0.00	0.00	0.01	0.01	0.00	0.01	0.00	0.01	0.01	0.01	0.01	0.01	0.01	0.01	0.00	0.01	0.00	0.00	0.01	0.01	0.01	0.01	
Al	7.14	7.15	7.24	7.25	7.11	7.14	7.59	7.58	7.54	7.72	7.69	7.61	7.69	8.33	8.35	8.34	8.31	8.47	8.48	8.55	8.57	8.48	8.45	8.53	8.44	8.41	8.48	8.44	
V	0.05	0.05	0.05	0.05	0.04	0.05	0.04	0.05	0.04	0.04	0.04	0.04	0.05	0.04	0.04	0.04	0.04	0.04	0.04	0.04	0.04	0.04	0.04	0.04	0.04	0.03	0.04	0.04	
Cr	8.40	8.36	8.27	8.19	8.35	8.36	7.88	7.94	7.94	7.82	7.82	7.89	7.77	7.18	7.17	7.20	7.22	7.11	7.09	7.04	7.06	7.07	7.14	7.02	7.12	7.13	7.07	7.11	
Fe^{3+}	0.35	0.40	0.39	0.44	0.46	0.41	0.46	0.42	0.44	0.38	0.42	0.42	0.47	0.41	0.40	0.40	0.42	0.34	0.35	0.34	0.30	0.38	0.34	0.38	0.38	0.38	0.38	0.38	
Mn	0.05	0.06	0.05	0.07	0.05	0.05	0.04	0.05	0.06	0.05	0.04	0.05	0.05	0.04	0.06	0.05	0.05	0.06	0.03	0.04	0.05	0.05	0.05	0.04	0.05	0.06	0.04	0.04	
Mg	4.48	4.53	4.57	4.64	4.58	4.50	4.88	4.84	4.89	4.99	4.89	4.87	4.86	5.08	4.96	5.02	5.01	5.18	5.16	5.08	5.14	4.95	4.88	4.95	5.19	5.10	5.14	5.13	
Fe^{2+}	3.44	3.37	3.35	3.25	3.35	3.42	3.05	3.08	3.03	2.94	3.04	3.06	3.06	2.86	2.97	2.91	2.92	2.74	2.78	2.86	2.79	2.99	3.04	2.98	2.73	2.82	2.81	2.80	
Cr #	0.54	0.54	0.53	0.53	0.54	0.54	0.51	0.51	0.51	0.50	0.50	0.51	0.50	0.46	0.46	0.46	0.46	0.46	0.46	0.45	0.45	0.45	0.46	0.45	0.46	0.46	0.45	0.46	
Mg #	56.5	57.3	57.7	58.8	57.8	56.8	61.6	61.1	61.7	62.9	61.7	61.4	61.4	64.0	62.6	63.3	63.2	65.4	65.0	64.0	64.8	62.4	61.6	62.5	65.5	64.4	64.7	64.7	

n.a. = not analyzed; CG = Cayo Guam section; YM = Yamaniguey section; LB = Loma de la Bandera section; LEM = Loma Estrella de Mayarí section; LAS = Loma Arroyo Seco section; LJ = Loma Juanita section; ZCS = Casimba section

Table A1.5 (continued)

Massif	***Moa-Baracoa***																											
Rocktype	*Harzburgite*																									*Dunite*				
Sample	CG 10					YM 14		YM 16																		CG 16				
TiO_2	0.01	0.05	0.03	0.04	0.05	0.03	0.06	0.05	0.03	0.05	0.03	0.05	0.02	0.04	0.06	0.04	0.04	0.03	0.06	0.07	0.06	0.04	0.03	0.01	0.06	0.05	0.06	0.04
Al_2O_3	25.13	24.80	24.25	24.29	24.48	25.33	25.11	24.88	24.30	24.34	24.49	24.53	24.84	25.13	25.08	24.45	24.38	24.56	24.93	24.89	24.36	24.42	24.47	26.62	26.60	26.99	26.10	26.25
V_2O_3	0.30	0.24	0.28	0.28	0.27	0.26	0.22	0.25	0.23	0.22	0.29	0.23	0.28	0.28	0.27	0.26	0.30	0.30	0.23	0.23	0.29	0.27	0.26	0.25	0.24	0.14	0.27	0.16
Cr_2O_3	43.29	43.40	44.17	43.77	44.17	41.75	41.65	43.30	42.32	43.57	43.73	43.41	43.66	43.04	43.38	43.37	43.71	43.50	42.99	42.93	43.21	43.79	43.93	41.75	41.70	41.38	41.87	42.00
FeOt	17.96	18.16	17.63	17.62	18.29	19.49	20.01	18.34	20.53	18.50	18.46	19.08	18.17	19.33	18.85	18.41	18.18	19.04	18.16	18.52	17.99	17.86	18.12	18.84	18.86	18.63	18.85	18.62
MnO	0.27	0.28	0.29	0.28	0.25	0.27	0.19	0.24	0.29	0.34	0.24	0.31	0.27	0.26	0.27	0.26	0.29	0.27	0.28	0.22	0.17	0.28	0.25	0.25	0.21	0.18	0.22	0.25
MgO	13.26	12.77	12.95	13.08	12.94	12.07	11.95	13.11	12.91	13.12	12.74	12.64	13.22	12.49	12.84	12.98	12.67	12.37	13.26	12.91	13.61	13.35	13.00	13.11	12.92	12.54	12.51	12.61
Total	100.22	99.68	99.59	99.38	100.46	99.20	99.19	100.16	100.62	100.13	99.98	100.24	100.46	100.57	100.75	99.75	99.57	100.07	99.90	99.78	99.68	100.01	100.06	100.83	100.59	99.91	99.88	99.93
Structural formula																												
Ti	0.00	0.01	0.01	0.01	0.01	0.01	0.01	0.01	0.01	0.01	0.01	0.01	0.00	0.01	0.01	0.01	0.01	0.01	0.01	0.01	0.01	0.01	0.01	0.00	0.01	0.01	0.01	0.01
Al	7.15	7.12	6.97	7.00	6.99	7.32	7.27	7.10	6.93	6.96	7.03	7.03	7.07	7.17	7.13	7.01	7.03	7.06	7.10	7.12	6.91	6.98	7.01	7.49	7.51	7.68	7.45	7.48
V	0.06	0.05	0.05	0.06	0.05	0.05	0.04	0.05	0.05	0.04	0.06	0.05	0.05	0.06	0.05	0.05	0.06	0.06	0.05	0.05	0.06	0.05	0.05	0.05	0.05	0.03	0.05	0.03
Cr	8.27	8.36	8.52	8.46	8.46	8.10	8.09	8.29	8.09	8.36	8.42	8.34	8.34	8.24	8.27	8.35	8.45	8.39	8.22	8.23	8.22	8.40	8.44	7.88	7.90	7.90	8.02	8.03
Fe^{3+}	0.50	0.43	0.41	0.46	0.46	0.50	0.55	0.52	0.90	0.60	0.47	0.55	0.52	0.50	0.50	0.54	0.43	0.47	0.55	0.51	0.63	0.54	0.47	0.52	0.47	0.34	0.42	0.40
Mn	0.06	0.06	0.06	0.06	0.05	0.06	0.04	0.05	0.06	0.07	0.05	0.06	0.05	0.05	0.06	0.05	0.06	0.06	0.06	0.04	0.04	0.06	0.05	0.05	0.04	0.04	0.05	0.05
Mg	4.77	4.64	4.71	4.77	4.67	4.41	4.38	4.73	4.65	4.74	4.62	4.58	4.76	4.51	4.61	4.71	4.62	4.50	4.78	4.67	4.88	4.83	4.71	4.66	4.62	4.51	4.52	4.54
Fe^{2+}	3.13	3.28	3.19	3.15	3.25	3.50	3.56	3.19	3.26	3.16	3.29	3.33	3.15	3.41	3.30	3.20	3.29	3.42	3.12	3.25	2.99	3.09	3.21	3.24	3.31	3.43	3.40	3.37
Cr #	0.54	0.54	0.55	0.55	0.55	0.53	0.53	0.54	0.54	0.55	0.54	0.54	0.54	0.53	0.54	0.54	0.55	0.54	0.54	0.54	0.54	0.55	0.55	0.51	0.51	0.51	0.52	0.52
Mg #	60.4	58.6	59.6	60.2	59.0	55.8	55.1	59.7	58.8	60.0	58.4	57.9	60.1	56.9	58.3	59.5	58.4	56.8	60.5	59.0	62.0	61.0	59.4	59.0	58.3	56.8	57.1	57.4

Table A1.5 (continued)

Massif	***Moa-Baracoa***																										
Rocktype	*Dunite*							*Impregnated dunite*																***Northern Mayarí-Cristal*** *Harzburgite*						
Sample	CG 16							CG 4							CG 18								LB 2						
TiO_2	0.02	0.04	0.05	0.01	0.02	0.05	0.06	1.87	1.98	1.83	2.02	1.49	1.72	1.73	1.41	1.50	1.63	1.83	1.63	1.35	1.48	0.06	0.03	0.05	0.09	0.07	0.06	0.10
Al_2O_3	26.32	26.45	26.51	26.74	26.25	26.43	26.48	20.07	19.37	18.50	19.54	20.16	20.34	19.62	19.39	18.48	18.30	17.91	18.02	19.12	19.25	21.76	21.61	21.87	21.95	22.20	21.70	21.88
V_2O_3	0.25	0.21	0.25	0.18	0.17	0.13	0.16	0.54	0.52	0.58	0.55	0.51	0.48	0.52	0.46	0.42	0.45	0.53	0.45	0.45	0.45	0.19	0.23	0.20	0.22	0.25	0.17	0.21
Cr_2O_3	41.92	41.53	41.83	41.54	41.89	42.01	41.68	39.53	39.19	39.22	39.38	40.43	39.47	39.61	38.05	37.82	37.64	37.51	37.79	37.55	37.50	46.58	46.45	46.48	46.34	46.45	46.47	46.40
FeOt	18.72	18.49	18.41	18.49	18.69	18.26	18.40	27.29	27.56	27.94	27.38	26.01	26.89	27.42	28.89	31.08	31.18	31.78	31.66	29.50	30.69	18.08	18.12	17.93	18.22	17.77	17.83	17.93
MnO	0.25	0.31	0.24	0.25	0.27	0.33	0.32	0.34	0.26	0.33	0.33	0.32	0.34	0.28	0.32	0.39	0.30	0.31	0.38	0.31	0.33	0.23	0.29	0.30	0.23	0.26	0.27	0.21
MgO	12.74	12.60	12.81	13.05	12.71	12.80	12.76	10.59	10.20	10.83	10.49	10.54	10.80	10.36	10.63	9.71	9.58	9.44	9.45	11.18	9.66	12.48	12.63	12.66	12.71	12.82	12.79	13.04
Total	100.22	99.63	100.10	100.26	100.00	100.01	99.86	100.23	99.09	99.22	99.68	99.45	100.05	99.55	99.15	99.41	99.09	99.32	99.38	99.44	99.37	99.37	99.37	99.50	99.76	99.81	99.28	99.78
Structural formula																												
Ti	0.00	0.01	0.01	0.00	0.00	0.01	0.01	0.35	0.38	0.36	0.38	0.28	0.32	0.33	0.27	0.29	0.31	0.35	0.31	0.26	0.28	0.01	0.01	0.01	0.02	0.01	0.01	0.02
Al	7.48	7.56	7.52	7.56	7.47	7.52	7.54	5.92	5.80	5.64	5.80	5.98	5.99	5.84	5.78	5.55	5.52	5.40	5.43	5.55	5.76	6.36	6.31	6.38	6.38	6.44	6.34	6.35
V	0.05	0.04	0.05	0.04	0.03	0.03	0.03	0.11	0.11	0.12	0.11	0.10	0.10	0.11	0.09	0.09	0.09	0.11	0.09	0.09	0.09	0.04	0.05	0.04	0.04	0.05	0.03	0.04
Cr	7.99	7.96	7.96	7.88	8.00	8.02	7.97	7.82	7.87	8.02	7.85	8.05	7.80	7.91	7.61	7.61	7.61	7.58	7.63	7.22	7.53	9.13	9.10	9.09	9.04	9.04	9.11	9.03
Fe^{3+}	0.44	0.40	0.40	0.47	0.44	0.38	0.40	1.44	1.46	1.49	1.46	1.28	1.45	1.48	1.97	2.16	2.13	2.18	2.20	2.20	2.03	0.43	0.51	0.46	0.49	0.43	0.49	0.53
Mn	0.05	0.06	0.05	0.05	0.06	0.07	0.06	0.07	0.06	0.07	0.07	0.07	0.07	0.06	0.07	0.08	0.07	0.07	0.08	0.07	0.07	0.05	0.06	0.06	0.05	0.05	0.06	0.04
Mg	4.58	4.55	4.60	4.67	4.58	4.61	4.60	3.95	3.86	3.79	3.94	3.95	4.02	3.90	4.01	3.69	3.65	3.60	3.60	3.98	3.66	4.61	4.67	4.67	4.67	4.70	4.72	4.79
Fe^{2+}	3.33	3.35	3.31	3.24	3.33	3.30	3.32	4.27	4.40	4.42	4.31	4.20	4.17	4.31	4.14	4.46	4.54	4.62	4.57	3.95	4.49	3.32	3.25	3.25	3.27	3.22	3.21	3.17
Cr #	0.52	0.51	0.51	0.51	0.52	0.52	0.51	0.57	0.58	0.59	0.57	0.57	0.57	0.58	0.57	0.58	0.58	0.58	0.58	0.57	0.57	0.59	0.59	0.59	0.59	0.58	0.59	0.59
Mg #	57.9	57.6	58.2	59.0	57.9	58.3	58.1	48.0	46.7	46.1	47.7	48.5	49.1	47.5	49.2	45.2	44.6	43.8	44.1	50.2	44.9	58.2	58.9	59.0	58.9	59.3	59.5	60.2

Table A1.5 (continued)

Massif	***Northern Mayarí-Cristal***																				***Southern Mayarí-Cristal***							
Rocktype	*Harzburgite*																				*Harzburgite*							
Sample	LB 2												LB 5								LEM 2							
TiO_2	0.06	0.05	0.07	0.06	0.06	0.08	0.06	0.04	0.05	0.04	0.06	0.08	0.03	0.05	0.06	0.05	0.05	0.04	0.05	0.02	0.03	0.06	0.02	0.04	0.03	0.04	0.06	0.05
Al_2O_3	22.99	23.04	22.84	23.02	23.68	24.08	22.72	23.01	23.03	23.06	22.83	22.64	22.75	22.81	22.83	24.09	23.33	22.94	24.75	23.50	16.92	17.56	17.97	17.83	18.69	17.45	19.81	17.60
V_2O_3	0.27	0.23	0.24	0.16	0.24	0.19	0.20	0.21	0.29	0.23	0.26	0.22	0.26	0.24	0.25	0.31	0.27	0.27	0.22	0.17	0.29	0.38	0.25	0.30	0.29	0.27	0.30	0.27
Cr_2O_3	44.63	44.70	44.98	44.84	44.43	43.97	45.13	45.07	44.96	44.94	45.14	45.12	45.08	45.33	45.33	43.76	44.93	44.73	42.26	44.72	50.72	49.50	49.05	49.15	49.02	49.51	48.10	50.22
FeOt	18.88	18.65	18.83	19.06	19.02	19.35	18.90	18.80	19.23	18.67	18.37	18.09	18.86	18.85	18.26	18.56	18.71	19.34	19.92	18.99	21.21	22.05	22.39	21.76	22.40	22.61	20.58	21.58
MnO	0.26	0.31	0.23	0.22	0.26	0.23	0.24	0.25	0.23	0.25	0.15	0.22	0.23	0.28	0.34	0.20	0.16	0.16	0.22	0.21	0.38	0.35	0.31	0.31	0.33	0.35	0.32	0.34
MgO	12.52	12.41	12.30	12.34	12.61	12.76	12.25	12.60	12.27	12.50	12.92	13.00	12.79	12.98	12.99	13.37	13.19	12.68	12.11	13.06	9.99	9.96	10.10	10.10	10.19	9.69	11.52	10.28
Total	99.61	99.39	99.48	99.71	100.30	100.65	99.51	99.96	100.05	99.69	99.74	99.37	100.00	100.54	100.06	100.34	100.64	100.16	99.53	100.67	99.54	99.86	100.09	99.49	100.95	99.92	100.69	100.34
Structural formula																												
Ti	0.01	0.01	0.01	0.01	0.01	0.01	0.01	0.01	0.01	0.01	0.01	0.01	0.01	0.01	0.01	0.01	0.01	0.01	0.01	0.00	0.01	0.01	0.00	0.01	0.00	0.01	0.01	0.01
Al	6.66	6.70	6.64	6.68	6.81	6.88	6.61	6.65	6.67	6.68	6.60	6.53	6.56	6.55	6.57	6.88	6.67	6.62	7.14	6.72	5.11	5.28	5.38	5.37	5.53	5.26	5.75	5.26
V	0.05	0.05	0.05	0.03	0.05	0.04	0.04	0.04	0.06	0.05	0.05	0.04	0.05	0.05	0.05	0.06	0.05	0.05	0.04	0.03	0.06	0.08	0.05	0.06	0.06	0.06	0.06	0.05
Cr	8.67	8.72	8.78	8.72	8.57	8.42	8.81	8.74	8.74	8.74	8.75	8.73	8.73	8.73	8.75	8.38	8.61	8.66	8.18	8.58	10.28	9.98	9.85	9.93	9.74	10.00	9.37	10.07
Fe^{3+}	0.55	0.50	0.48	0.52	0.54	0.60	0.48	0.53	0.52	0.50	0.55	0.56	0.61	0.64	0.56	0.65	0.63	0.64	0.58	0.64	0.49	0.61	0.68	0.60	0.63	0.63	0.64	0.57
Mn	0.05	0.07	0.05	0.05	0.06	0.05	0.05	0.05	0.05	0.05	0.03	0.05	0.05	0.06	0.07	0.04	0.03	0.03	0.05	0.04	0.08	0.08	0.07	0.07	0.07	0.08	0.07	0.07
Mg	4.59	4.56	4.53	4.53	4.58	4.61	4.51	4.60	4.50	4.58	4.72	4.74	4.67	4.71	4.73	4.83	4.77	4.63	4.42	4.73	3.82	3.79	3.82	3.84	3.82	3.69	4.23	3.88
Fe^{2+}	3.33	3.35	3.41	3.41	3.34	3.32	3.42	3.32	3.44	3.34	3.22	3.15	3.25	3.20	3.17	3.11	3.17	3.32	3.50	3.21	4.06	4.09	4.07	4.05	4.07	4.20	3.60	4.01
Cr #	0.57	0.57	0.57	0.57	0.56	0.55	0.57	0.57	0.57	0.57	0.57	0.57	0.57	0.57	0.57	0.55	0.56	0.57	0.53	0.56	0.67	0.65	0.65	0.65	0.64	0.66	0.62	0.66
Mg #	58.0	57.7	57.1	57.0	57.8	58.1	56.9	58.1	56.7	57.8	59.5	60.1	59.0	59.5	59.9	60.8	60.1	58.2	55.8	59.6	48.5	48.1	48.4	48.7	48.4	46.8	54.0	49.2

Table A1.5 (continued)

Massif	***Southern Mayarí-Cristal***																													
Rocktype	*Dunite*																													
Sample	LAS 1									LJ 1																				
TiO_2	0.16	0.13	0.15	0.12	0.11	0.14	0.13	0.14	0.13	0.08	0.12	0.09	0.11	0.10	0.07	0.10	0.10	0.12	0.10	0.12	0.09	0.08	0.10	0.09	0.13	0.09	0.08	0.11	0.13	0.08
Al_2O_3	18.18	17.93	17.67	17.58	17.16	16.68	17.17	17.82	16.81	21.90	21.40	21.10	20.72	20.23	19.99	20.16	21.02	20.46	20.71	21.08	21.21	19.98	19.58	20.53	20.32	19.89	20.00	20.22	21.41	20.10
V_2O_3	0.19	0.25	0.23	0.21	0.08	0.22	0.19	0.17	0.23	0.19	0.17	0.13	0.12	0.22	0.16	0.14	0.18	0.24	0.26	0.16	0.23	0.11	0.25	0.23	0.25	0.28	0.19	0.18	0.28	0.16
Cr_2O_3	50.16	49.78	49.93	49.80	49.40	49.83	49.96	49.65	50.24	46.42	46.69	47.04	47.44	47.36	47.95	47.26	47.03	48.05	47.78	47.12	46.56	47.75	47.82	47.93	48.44	48.72	48.37	48.40	46.35	47.52
FeOt	19.94	19.05	19.48	20.08	21.75	22.02	20.01	20.26	20.82	18.86	19.63	18.71	19.11	19.20	19.52	19.57	19.90	19.08	19.28	19.62	20.10	19.55	19.73	17.72	17.28	18.07	18.17	17.55	21.29	20.75
MnO	0.30	0.30	0.31	0.27	0.34	0.36	0.36	0.26	0.36	0.34	0.36	0.33	0.29	0.27	0.33	0.28	0.24	0.35	0.20	0.22	0.27	0.29	0.29	0.30	0.20	0.28	0.29	0.23	0.28	0.30
MgO	11.83	12.02	11.87	11.80	10.82	10.73	11.51	11.53	11.17	11.54	12.28	12.29	12.09	12.05	11.80	11.87	12.04	12.04	11.96	12.11	11.78	11.54	11.59	12.83	12.63	12.30	12.59	12.83	9.98	10.79
Total	100.76	99.46	99.63	99.86	99.67	99.99	99.31	99.83	99.76	99.32	100.64	99.68	99.88	99.43	99.82	99.38	100.51	100.34	100.27	100.43	100.24	99.30	99.35	99.62	99.26	99.62	99.69	99.53	99.71	99.68
Structural formula																														
Ti	0.03	0.02	0.03	0.02	0.02	0.03	0.03	0.03	0.02	0.02	0.02	0.02	0.02	0.02	0.01	0.02	0.02	0.02	0.02	0.02	0.02	0.02	0.02	0.02	0.02	0.02	0.02	0.02	0.02	0.01
Al	5.35	5.33	5.26	5.22	5.15	5.00	5.14	5.31	5.04	6.44	6.20	6.18	6.07	5.96	5.89	5.95	6.12	5.98	6.05	6.13	6.19	5.92	5.78	6.00	5.97	5.85	5.87	5.93	6.35	5.96
V	0.04	0.05	0.05	0.04	0.02	0.05	0.04	0.03	0.05	0.04	0.03	0.03	0.02	0.05	0.03	0.03	0.04	0.05	0.05	0.03	0.05	0.02	0.05	0.05	0.05	0.06	0.04	0.04	0.06	0.03
Cr	9.91	9.93	9.97	9.93	9.95	10.02	10.04	9.92	10.10	9.16	9.08	9.24	9.32	9.36	9.48	9.37	9.18	9.43	9.37	9.19	9.12	9.50	9.47	9.40	9.55	9.61	9.52	9.52	9.22	9.45
Fe^{3+}	0.63	0.62	0.65	0.74	0.81	0.84	0.70	0.67	0.75	0.31	0.62	0.51	0.52	0.58	0.56	0.60	0.60	0.49	0.48	0.56	0.59	0.51	0.57	0.50	0.35	0.43	0.53	0.46	0.30	0.49
Mn	0.06	0.07	0.07	0.06	0.07	0.08	0.08	0.06	0.08	0.07	0.07	0.07	0.06	0.06	0.07	0.06	0.05	0.07	0.04	0.05	0.06	0.06	0.06	0.06	0.04	0.06	0.06	0.05	0.06	0.06
Mg	4.41	4.52	4.47	4.44	4.11	4.07	4.36	4.34	4.24	4.29	4.50	4.55	4.48	4.49	4.40	4.43	4.43	4.45	4.42	4.45	4.35	4.33	4.33	4.75	4.69	4.58	4.67	4.75	3.74	4.04
Fe^{2+}	3.54	3.40	3.46	3.50	3.82	3.84	3.55	3.61	3.68	3.62	3.42	3.38	3.46	3.44	3.52	3.50	3.51	3.47	3.52	3.49	3.58	3.60	3.56	3.18	3.25	3.34	3.25	3.19	4.18	3.87
Cr #	0.65	0.65	0.65	0.66	0.66	0.67	0.66	0.65	0.67	0.59	0.59	0.60	0.61	0.61	0.62	0.61	0.60	0.61	0.61	0.60	0.60	0.62	0.62	0.61	0.62	0.62	0.62	0.62	0.59	0.61
Mg #	55.5	57.0	56.3	55.9	51.8	51.4	55.1	54.6	53.5	54.2	56.8	57.4	56.4	56.6	55.5	55.9	55.8	56.2	55.7	56.1	54.9	54.6	54.8	59.9	59.1	57.8	59.0	59.8	47.2	51.1

Table A1.5 (continued)

Massif	***Southern Mayarí-Cristal***																	
Rocktype	*Dunite*																	
Sample	ZCS 203																	
TiO_2	0.10	0.10	0.11	0.14	0.13	0.13	0.12	0.13	0.13	0.12	0.11	0.11	0.11	0.11	0.10	0.10	0.10	0.10
Al_2O_3	14.63	14.57	15.02	15.22	15.33	13.41	14.18	14.82	15.57	14.81	14.83	14.74	12.48	12.30	13.00	12.35	12.33	12.34
V_2O_3	*n.a*	*n.a*	*n.a*	*n.a*	*n.a*	*n.a*	*n.a*	*n.a*	*n.a*	*n.a*	*n.a*	*n.a*	*n.a*	*n.a*	*n.a*	*n.a*	*n.a*	*n.a*
Cr_2O_3	52.48	52.90	51.74	51.56	51.47	53.69	53.04	52.45	51.00	51.92	52.04	52.56	54.39	54.65	53.91	54.87	54.41	54.90
FeOt	22.34	21.91	21.69	22.06	21.74	21.47	22.04	23.09	22.36	21.73	21.68	21.14	22.29	21.93	23.07	22.07	22.01	21.92
MnO	0.37	0.38	0.36	0.35	0.37	0.37	0.36	0.41	0.41	0.38	0.29	0.36	0.37	0.37	0.35	0.35	0.40	0.35
MgO	10.05	10.06	10.24	10.30	10.49	10.30	10.03	9.84	10.40	10.35	10.38	10.41	9.68	9.86	9.75	10.06	10.02	10.05
Total	99.98	99.92	99.16	99.62	99.53	99.37	99.76	100.73	99.87	99.31	99.34	99.31	99.32	99.21	100.18	99.80	99.27	99.66
Structural formula																		
Ti	0.02	0.02	0.02	0.03	0.02	0.03	0.02	0.02	0.03	0.02	0.02	0.02	0.02	0.02	0.02	0.02	0.02	0.02
Al	4.46	4.44	4.59	4.63	4.66	4.12	4.34	4.49	4.72	4.53	4.53	4.51	3.87	3.82	3.99	3.80	3.81	3.81
V	-	-	-	-	-	-	-	-	-	-	-	-	-	-	-	-	-	-
Cr	10.72	10.82	10.61	10.52	10.49	11.07	10.88	10.65	10.36	10.64	10.66	10.77	11.31	11.37	11.09	11.33	11.28	11.36
Fe^{3+}	0.78	0.70	0.74	0.78	0.78	0.75	0.74	0.80	0.86	0.78	0.77	0.67	0.78	0.76	0.88	0.81	0.83	0.79
Mn	0.08	0.08	0.08	0.08	0.08	0.08	0.08	0.09	0.09	0.08	0.06	0.08	0.08	0.08	0.08	0.08	0.09	0.08
Mg	3.87	3.88	3.96	3.96	4.03	4.00	3.88	3.77	3.98	4.00	4.01	4.02	3.80	3.87	3.78	3.92	3.92	3.92
Fe^{2+}	4.05	4.04	3.97	3.98	3.90	3.93	4.05	4.16	3.94	3.93	3.93	3.91	4.13	4.06	4.14	4.01	4.00	4.01
Cr #	0.71	0.71	0.70	0.69	0.69	0.73	0.71	0.70	0.69	0.70	0.70	0.71	0.75	0.75	0.74	0.75	0.75	0.75
Mg #	48.8	49.0	50.0	49.9	50.8	50.5	48.9	47.5	50.3	50.4	50.5	50.7	47.9	48.8	47.7	49.4	49.5	49.4

Table A1.6 EPM analyses of plagioclase in mafic rocks from the Mayarí-Baracoa Ophiolitic Belt

Massif	***Moa-Baracoa***																											
Rocktype	*Crustal gabbro*																											
Sample	QN 18										QN 8							QN 4										
SiO_2 (wt%)	49.72	49.90	50.18	49.64	50.29	49.62	50.51	50.02	50.15	49.02	51.14	51.12	50.96	50.85	50.28	50.82	51.34	49.60	50.03	49.59	48.91	49.56	49.50	48.41	48.65	48.92	49.70	49.90
Al_2O_3	31.07	31.08	31.61	31.42	31.75	31.77	31.36	31.93	31.33	32.40	30.88	31.24	30.64	31.00	31.53	30.96	31.00	31.80	31.54	31.72	32.44	31.57	31.98	32.09	32.55	32.52	31.66	31.88
FeO	0.55	0.44	0.38	0.37	0.48	0.38	0.53	0.50	0.39	0.51	0.34	0.40	0.41	0.42	0.38	0.38	0.46	0.34	0.36	0.36	0.48	0.38	0.36	0.47	0.39	0.33	0.51	0.35
CaO	14.65	14.48	14.64	14.51	14.74	15.22	14.64	14.83	14.45	15.82	14.12	14.20	14.19	14.18	14.73	14.24	14.05	14.67	14.51	14.59	15.51	14.65	14.88	15.55	15.56	15.29	14.35	14.73
Na_2O	3.52	3.39	3.31	3.25	3.27	3.08	3.47	3.34	3.44	2.90	3.68	3.51	3.46	3.65	3.22	3.51	3.74	3.25	3.40	3.25	2.78	3.42	3.31	2.76	2.85	2.93	3.26	3.20
Total	99.51	99.29	100.12	99.19	100.53	100.07	100.51	100.62	99.76	100.65	100.16	100.47	99.66	100.10	100.14	99.91	100.59	99.67	99.84	99.51	100.13	99.58	100.02	99.28	100.00	99.98	99.48	100.05
Structural formula																												
Si	2.29	2.29	2.29	2.28	2.28	2.27	2.29	2.27	2.29	2.23	2.32	2.32	2.33	2.31	2.29	2.32	2.32	2.27	2.29	2.27	2.24	2.27	2.26	2.23	2.23	2.24	2.28	2.28
Al	1.68	1.68	1.70	1.70	1.70	1.71	1.68	1.71	1.69	1.74	1.65	1.67	1.65	1.66	1.69	1.66	1.65	1.72	1.70	1.72	1.75	1.71	1.72	1.75	1.76	1.75	1.71	1.71
Fe^{2+}	0.02	0.02	0.01	0.01	0.02	0.01	0.02	0.02	0.01	0.02	0.01	0.01	0.02	0.02	0.01	0.01	0.02	0.01	0.01	0.01	0.02	0.01	0.01	0.02	0.02	0.01	0.02	0.01
Ca	0.72	0.71	0.71	0.71	0.72	0.75	0.71	0.72	0.71	0.77	0.69	0.69	0.69	0.69	0.72	0.69	0.68	0.72	0.71	0.72	0.76	0.72	0.73	0.77	0.76	0.75	0.71	0.72
Na	0.31	0.30	0.29	0.29	0.29	0.27	0.31	0.29	0.31	0.26	0.32	0.31	0.31	0.32	0.28	0.31	0.33	0.29	0.30	0.29	0.25	0.30	0.29	0.25	0.25	0.26	0.29	0.28
An (wt%)	70	70	71	71	71	74	70	71	70	75	68	69	69	68	72	69	67	71	70	71	75	70	71	76	75	74	71	72

QN = Quemado del Negro section; YM = Yamaniguey section; CG = Cayo Guam section; J = Mercedita section; LB = Loma de la Bandera section. MTZ = Moho transition zone

Table A1.6 (continued)

Massif	***Moa-Baracoa***																						
Rocktype	*Crustal gabbro*							*Moho transtion zone (MTZ) gabbroic sill*													*MTZ Gabbro dyke*			
Sample	QN 2							YM 4									CG 17				J3b			
SiO_2 (wt%)	48.67	48.54	49.28	48.55	48.42	48.93	48.99	51.35	51.93	51.78	52.13	51.88	52.13	52.20	51.99	51.88	51.33	52.22	52.70	52.79	50.31	49.87	49.72	49.81
Al_2O_3	32.82	32.90	31.91	32.07	32.72	32.49	32.67	30.71	28.25	30.40	30.50	30.32	30.46	30.35	30.16	30.09	30.90	30.42	30.68	30.59	31.76	31.91	31.62	31.60
FeO	0.46	0.31	0.36	0.69	0.32	0.33	0.34	0.34	0.32	0.28	0.20	0.27	0.17	0.26	0.19	0.24	0.19	0.14	0.16	0.19	0.06	0.09	0.05	0.10
CaO	15.35	15.74	14.81	15.00	15.55	15.15	15.61	13.26	15.57	13.41	13.22	13.21	13.19	13.13	12.96	13.06	13.67	13.28	13.33	13.42	14.56	14.71	14.57	14.52
Na_2O	3.02	2.80	3.37	2.85	2.96	3.14	2.99	3.74	3.42	4.00	4.22	4.04	4.09	4.11	4.11	4.26	3.82	4.18	3.97	4.14	3.50	3.45	3.47	3.68
Total	100.32	100.29	99.73	99.16	99.97	100.04	100.60	99.40	99.49	99.87	100.27	99.72	100.04	100.05	99.41	99.53	99.91	100.23	100.83	101.12	100.19	100.03	99.43	99.71
Structural formula																								
Si	2.22	2.22	2.26	2.23	2.22	2.24	2.23	2.34	2.37	2.35	2.36	2.36	2.36	2.37	2.37	2.36	2.34	2.36	2.37	2.37	2.29	2.27	2.28	2.28
Al	1.76	1.77	1.72	1.74	1.77	1.75	1.75	1.65	1.54	1.63	1.63	1.62	1.63	1.62	1.62	1.63	1.66	1.62	1.62	1.62	1.70	1.71	1.71	1.70
Fe^{2+}	0.02	0.01	0.01	0.03	0.01	0.01	0.01	0.01	0.01	0.01	0.01	0.01	0.01	0.01	0.01	0.01	0.01	0.01	0.01	0.01	0.00	0.00	0.00	0.00
Ca	0.75	0.77	0.73	0.74	0.76	0.74	0.76	0.65	0.77	0.65	0.64	0.64	0.64	0.64	0.63	0.64	0.67	0.64	0.64	0.65	0.71	0.72	0.71	0.71
Na	0.27	0.25	0.30	0.26	0.26	0.28	0.26	0.33	0.31	0.35	0.37	0.36	0.36	0.36	0.36	0.38	0.34	0.37	0.35	0.36	0.31	0.31	0.31	0.33
An (wt%)	74	76	71	74	74	73	74	66	71	65	63	64	64	64	64	63	66	64	65	64	70	70	70	68

Table A1.6 (continued)

Massif	***Northern Mayarí-Cristal***								
Rocktype	*Gabbro dyke*								
Sample	LB 1								
SiO_2 (wt%)	46.41	46.84	46.48	46.90	45.89	47.54	47.84	46.15	46.37
Al_2O_3	33.68	33.93	33.93	34.12	34.44	33.42	32.94	33.99	33.99
FeO	0.31	0.28	0.39	0.44	0.28	0.19	0.29	0.37	0.39
CaO	17.61	17.39	17.28	17.77	17.74	16.06	16.26	17.44	17.65
Na_2O	1.71	1.71	1.61	1.61	1.44	2.21	2.16	1.67	1.53
Total	99.72	100.15	99.69	100.84	99.79	99.42	99.49	99.62	99.93
Structural formula									
Si	2.14	2.15	2.14	2.14	2.12	2.18	2.20	2.13	2.14
Al	1.83	1.84	1.84	1.84	1.87	1.82	1.79	1.85	1.85
Fe^{2+}	0.01	0.01	0.01	0.02	0.01	0.01	0.01	0.01	0.01
Ca	0.87	0.86	0.85	0.87	0.88	0.80	0.80	0.86	0.87
Na	0.15	0.15	0.14	0.14	0.13	0.20	0.19	0.15	0.14
An (wt%)	85	85	86	86	87	80	81	85	86

APPENDIX 2

WHOLE ROCK COMPOSITION OF THE ULTRAMAFIC AND MAFIC ROCKS FROM THE MAYARÍ-BARACOA OPHIOLITIC BELT

Table A2.1 Whole rock major and trace element data of studied peridotites from the Mayarí-Baracoa Ophiolitic Belt

Massif	***Moa-Baracoa***																***MayaríCristal***									
																	North				***South***					
Rocktype	*Harzburgite*									*Dunite*	*Impregnated Dunite*						*Harzburgite*				*Harzburgite*				*Dunite*	
Sample	CG 3	CG 5	CG 6	CG 7	CG 10	CG 13	CG 14	YM 14	YM 16	CG 16	CG 1	CG 2	CG 4	CG 18	YM 12	YM 13	LB 2	LB 3	LB 5	LB 6	LEM 1	LEM 2	LEM 3	LAS 2	LAS 1	LEM 4
SiO_2 (wt%)	38.55	39.23	41.89	36.66	38.02	38.23	37.45	38.19	39.11	36.81	38.66	38.29	37.01	36.79	34.57	35.86	39.67	39.07	44.63	41.16	39.93	39.39	39.24	39.71	39.33	39.62
TiO_2	0.006	0.008	0.007	0.005	0.005	0.016	0.006	0.004	0.002	0.005	0.05	0.06	0.08	0.08	0.02	0.01	0.008	0.006	0.008	0.006	0.004	0.003	0.003	0.004	0.004	0.005
Al_2O_3	0.42	0.95	0.85	0.70	0.86	0.70	0.57	0.34	0.33	0.52	3.09	2.38	1.94	2.57	0.89	0.54	0.52	0.58	0.43	0.44	0.27	0.19	0.17	0.12	0.05	*bdl*
Fe_2O_3	8.01	7.60	7.72	7.69	8.05	8.29	7.79	7.56	7.56	7.68	9.50	9.85	8.91	9.34	8.76	8.25	7.94	8.08	9.00	8.52	7.99	7.93	8.57	8.03	7.40	9.24
MnO	0.11	0.12	0.13	0.11	0.11	0.11	0.11	0.11	0.11	0.11	0.13	0.14	0.12	0.13	0.12	0.08	0.08	0.08	0.11	0.09	0.10	0.11	0.11	0.11	0.09	0.11
MgO	38.01	36.81	37.63	38.26	35.47	40.62	38.24	39.09	40.34	38.65	35.69	36.31	39.41	39.10	39.64	38.42	37.63	35.46	40.82	35.95	35.40	35.23	33.71	36.13	36.55	33.84
CaO	0.35	0.32	0.48	0.32	0.05	*0.28*	*bdl*	0.17	0.57	0.34	0.80	0.67	1.13	1.86	0.15	0.02	0.03	n.d.	0.04	0.07	0.02	0.17	0.04	0.06	0.01	0.02
Na_2O	*bdl*	*bdl*	*bdl*	*bdl*	*bdl*	*bdl*	*bdl*	*bdl*	*bdl*	*bdl*	*bdl*	*bdl*	*bdl*	*bdl*	*bdl*	*bdl*	*bdl*	*bdl*	*bdl*	*bdl*	*bdl*	*bdl*	*bdl*	*bdl*	*bdl*	*bdl*
K_2O	*bdl*	*bdl*	*bdl*	*bdl*	*bdl*	*bdl*	*bdl*	*bdl*	*bdl*	*bdl*	*bdl*	*bdl*	*bdl*	*bdl*	*bdl*	*bdl*	*bdl*	*bdl*	*bdl*	*bdl*	*bdl*	*bdl*	*bdl*	*bdl*	*bdl*	*bdl*
Total	85.46	85.03	88.70	83.74	82.57	88.24	84.16	85.46	88.02	84.12	87.92	87.69	88.60	89.86	84.15	83.19	85.87	83.28	95.04	86.24	83.71	83.02	81.85	84.16	83.44	82.84
LOI*	14.54	14.97	11.30	16.26	17.44	11.76	15.84	14.54	11.98	15.89	12.08	12.31	11.40	10.14	15.85	16.82	14.13	16.72	4.96	13.76	16.29	16.98	18.15	15.84	16.56	17.16
V (ppm)	40	41	50	39	37	35	36	34	32	41	58	50	42	49	40	25	48	38	30	34	30	26	26	38	15	35
Cr	2394	3467	3633	2824	2605	1520	2769	2327	2484	2437	3217	3572	1547	2251	3462	4457	2618	2437	2730	2052	2623	2449	3069	2605	3173	5003
Ni	2223	2293	2142	2186	2610	2205	2244	2209	2277	2154	2064	2205	1473	1743	2505	2428	2163	2109	2484	2418	2238	2212	2533	2234	2724	2659
Li	0.45	0.36	0.7	0.31	0.28	0.66	0.26	0.23	0.40	0.29	1.2	0.7	1.4	1.9	0.26	0.038	0.26	0.31	0.24	0.39	0.27	0.24	0.32	0.26	0.13	0.19
Co	99	82	91	97	105	98	102	97	97	101	100	86	116	108	109	110	92	95	100	103	96	97	108	97	112	119
Rb	0.026	0.023	0.016	0.053	0.024	0.036	0.036	0.014	0.027	0.043	0.016	0.021	0.014	*bdl*	*bdl*	0.10	0.031	0.048	0.022	0.040	0.019	0.022	0.029	0.030	0.019	0.030
Sr	0.36	0.7	1.1	0.19	1	0.16	0.40	0.18	1.9	0.18	1.0	0.48	0.7	2.6	0.24	0.16	0.48	0.7	0.33	1.0	0.41	0.55	0.9	0.7	0.7	0.8
Zr	0.027	0.10	0.021	0.09	0.022	0.053	0.022	0.060	0.10	0.0683	1.1	1.3	2.1	3.8	0.31	0.17	0.18	0.16	0.036	0.32	0.19	0.12	0.056	0.049	0.10	0.040
Nb	0.0060	0.0034	0.0041	0.011	0.015	*bdl*	0.017	0.0043	0.0065	0.009	0.016	0.026	0.018	0.036	0.0044	0.013	0.013	0.011	0.009	0.010	0.011	0.011	0.012	0.011	0.015	0.026
Cs	0.0039	0.0016	0.0021	0.0041	0.0027	0.0021	0.0036	0.0013	0.0024	0.0016	0.0040	0.0017	0.0023	*bdl*	*bdl*	*bdl*	0.0019	0.0050	0.0031	0.0037	0.0052	0.0062	0.009	0.0058	0.0052	0.009
La	*bdl*	*bdl*	*bdl*	*bdl*	*bdl*	*bdl*	*bdl*	*bdl*	*bdl*	*bdl*	*bdl*	*bdl*	*bdl*	*bdl*	*bdl*	*bdl*	*bdl*	0.0007	*bdl*	*bdl*	*bdl*	*bdl*	*bdl*	*bdl*	*bdl*	*bdl*
Ce	0.0037	0.0036	0.0025	0.0020	0.0019	0.0029	0.0049	0.0033	0.0029	0.0017	0.17	0.14	0.31	0.47	0.039	0.044	0.0036	0.0058	0.0021	0.0024	0.0017	0.0016	0.0021	0.0038	0.0016	0.0033
Nd	0.0044	0.0031	0.0053	0.0021	0.009	0.0032	0.0041	0.0029	0.0022	0.0024	0.17	0.16	0.32	0.44	0.040	0.024	0.0033	0.009	0.0037	0.022	0.010	0.0031	0.0030	0.0043	0.0023	0.0031
Sm	*bdl*	*bdl*	*bdl*	*bdl*	*bdl*	*bdl*	*bdl*	*bdl*	*bdl*	*bdl*	0.065	0.061	0.11	0.14	0.017	*bdl*	*bdl*	0.0049	*bdl*	0.007	0.0036	*bdl*	*bdl*	*bdl*	0.0021	*bdl*
Eu	*bdl*	*bdl*	*bdl*	*bdl*	*bdl*	*bdl*	0.0008	*bdl*	*bdl*	0.0007	0.036	0.031	0.057	0.059	0.009	0.011	0.0011	0.0017	*bdl*	0.0026	0.0013	*bdl*	*bdl*	*bdl*	0.0006	0.0005
Gd	*bdl*	*bdl*	*bdl*	*bdl*	0.0028	*bdl*	*bdl*	0.0036	0.0021	*bdl*	0.13	0.11	0.19	0.20	0.029	0.008	0.0053	0.007	*bdl*	0.013	0.0059	*bdl*	*bdl*	*bdl*	0.0027	*bdl*
Tb	0.0004	0.0002	*bdl*	0.0006	0.0004	0.0009	0.0007	0.0006	0.0004	*bdl*	0.024	0.020	0.033	0.037	0.0058	0.0012	0.0012	0.0015	0.0006	0.0015	0.0005	0.0003	0.0006	0.0005	0.0005	0.0005
Dy	0.0048	0.0041	0.007	0.0057	0.0035	0.011	0.0051	0.0045	0.0037	0.0036	0.18	0.16	0.26	0.26	0.045	0.008	0.013	0.014	0.0040	0.012	0.0029	0.0020	0.0044	0.0027	0.0036	0.0033
Ho	0.0019	0.0016	0.0026	0.0020	0.0013	0.0039	0.0017	0.0017	0.0015	0.0016	0.042	0.034	0.057	0.059	0.011	0.0024	0.0043	0.0045	0.0018	0.0043	0.0012	0.0010	0.0014	0.0007	0.0012	0.0011
Er	0.009	0.007	0.012	0.010	0.0063	0.014	0.009	0.010	0.008	0.009	0.12	0.10	0.17	0.17	0.037	0.008	0.017	0.018	0.011	0.017	0.0056	0.0052	0.0057	0.0039	0.0054	0.0038
Tm	0.0022	0.0019	0.0031	0.0023	0.0018	0.0033	0.0022	0.0023	0.0022	0.0022	0.019	0.016	0.026	0.026	0.0066	0.0013	0.0031	0.0038	0.0021	0.0035	0.0013	0.0012	0.0013	0.0009	0.0011	0.0010
Yb	0.022	0.017	0.029	0.020	0.016	0.026	0.021	0.022	0.020	0.021	0.13	0.11	0.18	0.18	0.048	0.011	0.030	0.034	0.023	0.030	0.014	0.013	0.012	0.010	0.010	0.010
Lu	0.0050	0.0039	0.007	0.0046	0.0044	0.0054	0.0050	0.0054	0.0050	0.0058	0.022	0.018	0.032	0.031	0.009	0.0029	0.0062	0.007	0.0051	0.007	0.0035	0.0032	0.0031	0.0027	0.0024	0.0022
Hf	*bdl*	0.0041	*bdl*	0.0022	0.0022	0.0026	*bdl*	0.0026	0.0029	0.0023	0.038	0.043	0.08	0.14	0.012	0.0054	0.0062	0.008	0.0052	0.008	0.0045	0.0038	0.0047	0.0063	0.008	0.007
Ta	*bdl*	*bdl*	*bdl*	0.0016	0.0018	*bdl*	0.0020	0.0005	0.0008	0.0003	0.0013	0.0018	0.0019	0.0033	*bdl*	0.0019	*bdl*	0.0013	0.0013	0.0015	0.0014	0.0015	0.0011	0.0013	0.0017	0.0017
Th	0.0034	0.0006	0.0039	*bdl*	0.0009	0.0015	0.0014	0.0006	0.0007	0.0026	0.0014	0.0017	0.0020	0.0027	0.0007	0.0017	0.0009	0.0008	0.0006	0.0005	0.0008	0.0006	0.0006	0.0006	0.0008	0.0006
U	*bdl*	0.0004	*bdl*	0.0013	*bdl*	*bdl*	*bdl*	*bdl*	*bdl*	*bdl*	0.0014	0.0009	0.0009	0.0008	*bdl*	0.0024	0.0007	0.0014	0.0009	0.0006	0.0005	0.0005	0.0007	0.0006	0.0004	0.0007

**Reported Loss on ignition is not the measured LOI but an estimate assuming that primary major oxide totals are equal to 100; bdl = below detection limit. CG = Cayo Guam section; YM = Yamaniguey section; LB = Loma de la Bandera section; LEM = Loma Estrella Mayarí section; LAS = Loma Arroyo Seco section*

Table A2.2 Whole rock major and trace element data of mafic rocks from the Mayarí-Baracoa Ophiolitic Belt

Massif	***Moa-Baracoa***																								
	Crustal Layered Gabbros															*Sills in the Moho Transition Zone (MTZ)*									
Rocktype	*Olivine Gabbro*											*Ol-opx-Gabbro*			*Gabbro*	*Olivine Gabbro*					*Ol-opx-Gabbro*				
Sample	QN 21	QN 18	QN 16	QN 12	QN 11b	QN 10a	QN 10b	QN 8	QN 5	QN 2	QN 1	QN 9	QN 7	QN 4	QN 14	YM 3	YM 4	YM 5	YM 7	YM10b	YM10c	YM10d	YM10e	AM 14	CG 17
SiO_2 (wt%)	46.40	45.99	47.02	48.16	46.45	47.26	45.82	47.71	49.56	48.32	47.49	45.53	42.81	50.00	49.85	39.00	40.28	37.23	39.53	39.35	46.74	41.88	38.77	48.83	41.06
TiO_2	0.20	0.19	0.26	0.20	0.16	0.21	0.11	0.19	0.24	0.24	0.23	0.09	0.11	0.29	0.31	0.12	0.26	0.03	0.04	0.10	0.45	0.16	0.09	0.26	0.21
Al_2O_3	17.96	20.41	16.86	21.31	25.66	23.13	20.58	22.89	17.59	17.31	17.62	22.20	15.02	16.85	18.89	4.06	6.45	11.49	20.42	12.50	7.63	17.99	5.56	16.91	6.30
Fe_2O_3	7.87	5.18	6.44	5.05	3.88	5.31	7.85	4.17	6.20	6.26	5.94	6.73	10.22	6.10	4.39	19.16	16.51	6.56	4.50	11.02	11.15	7.21	15.84	6.83	12.73
MnO	0.11	0.08	0.10	0.08	0.05	0.07	0.10	0.07	0.11	0.11	0.10	0.08	0.14	0.11	0.09	0.26	0.23	0.10	0.06	0.16	0.22	0.10	0.21	0.12	0.19
MgO	11.39	8.43	11.81	7.95	5.15	7.48	10.49	6.44	11.23	11.47	10.84	8.72	16.20	11.05	7.36	26.55	22.43	26.10	14.65	20.77	17.43	13.99	27.71	9.89	27.59
CaO	12.43	13.19	13.73	13.39	12.08	11.90	10.24	13.16	15.17	14.79	14.38	10.47	8.62	15.71	14.61	3.43	6.01	7.28	11.24	7.51	12.09	10.91	4.30	13.20	5.19
Na_2O	1.36	1.85	1.38	2.04	2.40	2.22	1.90	2.15	1.43	1.30	1.29	2.08	1.25	1.37	2.17	0.18	0.50	*bdl*	0.49	0.57	0.72	1.23	0.16	1.98	0.45
K_2O	*bdl*	*bdl*	*bdl*	0.01	0.01	0.01	*bdl*	0.01	*bdl*	*bdl*	*bdl*	0.01	*bdl*	*bdl*	0.01	*bdl*	*bdl*	*bdl*	0.03	*bdl*	*bdl*	0.01	*bdl*	0.02	*bdl*
Total	97.72	95.33	97.60	98.20	95.84	97.59	97.09	96.79	101.53	99.80	97.90	95.91	94.36	101.48	97.68	92.77	92.67	88.79	90.96	91.99	96.42	93.48	92.64	98.03	93.72
LOI*	2.28	4.67	2.40	1.80	4.16	2.41	2.92	3.21		0.20	2.10	4.09	5.64		2.32	7.23	7.33	11.21	9.04	8.01	3.58	6.52	7.36	1.97	6.29
V (ppm)	88	95	116	77	22	46	26	88	138	140	121	41	42	157	148	63	97	33	35	44	231	55	46	130	108
Cr	393	346	655	639	32	155	88	487	797	869	712	56	268	855	1083	220	450	1488	771	229	1535	166	398	409	2275
Ni	278	169	220	217	159	254	408	154	234	279	258	322	472	243	124	907	761	1034	544	664	435	373	933	184	1400
Li	1.5	2.2	1.7	1.8	2.0	2.2	2.2	1.9	1.1	1.7	1.7	2.4	2.2	1.4	2.1	1.8	2.8	1.0	2.4	3.7	1.6	1.4	2.0	1.7	2.1
Co	53	33	43	29	24	32	52	24	41	42	41	42	79	40	19	126	108	73	51	84	68	53	114	49	88
Rb	0.10	0.16	0.09	0.08	0.05	0.06	0.08	0.05	0.03	0.04	0.04	0.09	0.06	0.05	0.14	0.057	0.09	0.07	0.19	0.10	0.09	0.15	0.051	0.13	0.09
Sr	80	99	113	141	171	157	135	139	87	76	80	149	81	78	132	17	47	3.9	58	45	37	77	21	125	38
Zr	5.9	5.1	6	5	7	7	5	5	4	4	4	4	3	5	6	2.0	9	0.7	3.0	2.0	13	3.5	0.9	4.7	3.5
Nb	0.08	0.10	0.09	0.09	0.23	0.26	0.06	0.09	0.04	0.05	0.04	0.07	0.05	0.05	0.05	0.019	0.22	0.016	0.07	0.020	0.08	0.045	0.019	0.051	0.012
Cs	0.0028	0.0033	0.0031	0.0039	0.0017	0.0017	0.0019	0.0013	0.0018	0.0024	0.0037	0.0023	0.0017	0.0032	0.0027	0.0037	0.0059	0.003	0.0057	0.008	0.0060	0.009	0.0019	*bdl*	0.007
La	0.26	0.25	0.29	0.29	0.34	0.38	0.24	0.29	0.23	0.24	0.23	0.25	0.20	0.26	0.27	0.09	0.40	0.029	0.063	0.15	0.38	0.27	0.063	0.26	0.16
Ce	0.9	0.8	1.0	0.9	1.1	1.2	0.7	0.9	0.8	0.8	0.8	0.7	0.6	0.9	1.0	0.30	1.2	0.057	0.19	0.48	1.6	0.8	0.21	0.9	0.56
Nd	1.0	0.9	1.2	1.0	0.9	1.0	0.6	0.9	1.0	1.1	1.1	0.6	0.6	1.3	1.3	0.40	1.3	0.066	0.21	0.50	2.3	0.8	0.30	1.3	0.8
Sm	0.40	0.37	0.53	0.40	0.26	0.34	0.19	0.35	0.48	0.49	0.49	0.17	0.20	0.59	0.61	0.19	0.54	0.026	0.09	0.18	1.1	0.31	0.14	0.57	0.34
Eu	0.28	0.30	0.35	0.34	0.33	0.34	0.26	0.34	0.35	0.35	0.36	0.28	0.23	0.38	0.40	0.13	0.28	0.026	0.065	0.13	0.47	0.30	0.12	0.40	0.21
Gd	0.63	0.58	0.88	0.65	0.36	0.45	0.27	0.55	0.83	0.85	0.85	0.23	0.32	1.02	1.07	0.35	0.9	0.053	0.13	0.29	1.9	0.47	0.25	1.0	0.59
Tb	0.12	0.11	0.16	0.12	0.06	0.08	0.05	0.10	0.16	0.16	0.16	0.04	0.06	0.19	0.20	0.07	0.16	0.012	0.023	0.053	0.36	0.08	0.048	0.18	0.11
Dy	0.9	0.8	1.2	0.9	0.4	0.5	0.3	0.7	1.2	1.2	1.2	0.3	0.4	1.4	1.5	0.52	1.2	0.11	0.17	0.39	2.7	0.61	0.36	1.4	0.9
Ho	0.18	0.17	0.25	0.18	0.09	0.11	0.07	0.16	0.25	0.25	0.25	0.05	0.09	0.30	0.32	0.12	0.26	0.026	0.038	0.08	0.57	0.13	0.08	0.30	0.19
Er	0.52	0.47	0.70	0.50	0.24	0.31	0.18	0.43	0.70	0.70	0.69	0.15	0.26	0.83	0.88	0.36	0.8	0.09	0.11	0.25	1.7	0.37	0.24	0.79	0.56
Tm	0.08	0.07	0.10	0.07	0.03	0.04	0.03	0.06	0.10	0.10	0.10	0.02	0.04	0.12	0.12	0.054	0.11	0.014	0.016	0.038	0.24	0.055	0.037	0.12	0.08
Yb	0.49	0.43	0.63	0.45	0.22	0.29	0.19	0.39	0.62	0.63	0.62	0.14	0.25	0.75	0.78	0.38	0.7	0.11	0.10	0.25	1.53	0.37	0.26	0.7	0.56
Lu	0.08	0.07	0.10	0.07	0.03	0.05	0.03	0.06	0.10	0.10	0.10	0.02	0.04	0.12	0.12	0.07	0.13	0.019	0.017	0.045	0.24	0.060	0.047	0.12	0.09
Hf	0.20	0.17	0.24	0.18	0.20	0.19	0.14	0.15	0.18	0.20	0.19	0.11	0.09	0.24	0.23	0.09	0.32	0.020	0.09	0.10	0.52	0.13	0.051	0.24	0.16
Ta	0.007	0.007	0.007	0.006	0.016	0.017	0.006	0.007	0.011	0.012	0.015	0.006	0.011	0.013	0.003	0.0020	0.016	0.0014	0.0058	0.0015	0.0063	0.0046	0.0005	0.016	0.0012
Th	0.005	0.005	0.006	0.005	0.009	0.007	0.006	0.006	0.002	0.002	0.002	0.005	0.004	0.003	0.003	0.0022	0.014	0.0008	0.0039	0.0010	0.007	0.0029	*bdl*	0.0037	0.0006
U	0.0022	0.0025	0.0022	0.0021	0.0045	0.0033	0.0019	0.0021	0.0006	0.0009	0.0007	0.0023	0.0018	0.0014	0.0012	0.0009	0.0054	*bdl*	0.0016	0.00001	0.0028	0.0011	*bdl*	0.0021	*bdl*

**Loss on ignition (LOI) was not measured except for Moa-Baracoa dykes; LOI values reported for the other samples are estimations assuming that primary major oxide totals were equal to 100. Ol = olivine; opx = orthopyroxene; hbl = hornblende; bdl = below detection limit; n.a. = not analysed. QN = Quemado del Negro section; YM = Yamaniguey section; AM = Amores section; CG = Cayo Guam section; MER & J = Mercedita section; LB = Loma de la Bandera section. MTZ = Moho transition zone*

Table A2.2 (continued)

Massif	***Moa-Baracoa***								***Northern Mayarí-Cristal***	
	Sills in the MTZ		*Intrusive Dykes in the Moho Transition Zone*						*Dykes*	
Rocktype	*Troctolite*	*Werhlite*	*Olivine-gabbro*				*Troctolite*	*Werhlite*	*Gabbro*	*Px-Hbl-Gabbro*
Sample	MER 1	YM 10a	CG 4b	CG 5b	CG 7b	J 3b	CG 9b	J 2b	LB 1	LB 4
SiO_2 (wt%)	37.27	38.39	39.75	45.50	42.20	46.46	39.33	38.13	45.18	41.76
TiO_2	0.01	0.11	0.09	0.17	0.16	0.16	0.07	0.06	0.45	1.14
Al_2O_3	5.36	3.05	18.33	10.52	13.29	18.66	10.74	6.53	15.23	15.85
Fe_2O_3	9.71	17.03	5.76	5.47	4.76	4.66	8.67	7.87	8.56	7.19
MnO	0.13	0.22	0.09	0.12	0.10	0.08	0.13	0.12	0.15	0.12
MgO	36.71	30.78	17.63	17.78	20.66	13.01	30.90	36.25	10.77	10.64
CaO	2.21	2.84	10.96	15.34	12.35	12.58	5.48	2.53	13.78	16.82
Na_2O	0.03	0.06	*bdl*	*bdl*	*bdl*	1.51	*bdl*	0.07	1.26	0.31
K_2O	*bdl*	*bdl*	*bdl*	*bdl*	*bdl*	*bdl*	*bdl*	*bdl*	0.02	*bdl*
Total	91.44	92.47	92.61	94.90	93.52	97.12	95.32	91.56	95.40	93.85
LOI*	8.56	7.53	6.94	4.24	6.18	2.67	5.95	8.69	4.60	6.15
V	30	66	*n.a.*	*n.a.*	*n.a.*	*n.a.*	*n.a.*	*n.a.*	278	265
Cr	3414	505	*n.a.*	*n.a.*	*n.a.*	*n.a.*	*n.a.*	*n.a.*	247	285
Ni (ppm)	1857	1005	*n.a.*	*n.a.*	*n.a.*	*n.a.*	*n.a.*	*n.a.*	120	195
Li	2.4	1.0	17	12	15	3	10	2	15	21
Co	111	125	54	40	43	41	90	100	45	38
Rb	0.18	0.033	0.48	0.14	0.21	0.44	0.16	0.25	0.28	0.28
Sr	18	5.9	32	20	34	163	14	34	202	62
Zr	0.10	2.3	1.6	3.7	3.5	3.2	2.0	2.3	6.2	23
Nb	0.013	0.027	0.08	0.060	0.050	0.040	0.07	0.25	0.07	0.8
Cs	0.008	*bdl*	0.07	0.10	0.020	0.040	0.030	0.23	0.27	0.012
La	*bdl*	0.07	0.20	0.15	0.24	0.18	0.14	0.10	0.35	1.6
Ce	0.041	0.28	0.30	0.48	0.9	0.46	0.34	0.28	1.4	6.2
Nd	0.032	0.42	0.35	0.63	0.7	0.66	0.24	0.27	1.8	8
Sm	0.010	0.20	0.18	0.36	0.37	0.32	0.07	0.14	0.8	3.2
Eu	0.025	0.11	0.13	0.17	0.23	0.28	0.051	0.07	0.43	1.1
Gd	0.015	0.37	0.31	0.65	0.7	0.55	0.14	0.19	1.2	4.8
Tb	0.003	0.07	0.057	0.14	0.13	0.10	0.029	0.033	0.24	0.9
Dy	0.020	0.52	0.39	1.0	0.9	0.7	0.23	0.20	1.8	6.3
Ho	0.0050	0.12	0.09	0.24	0.21	0.16	0.062	0.040	0.41	1.4
Er	0.021	0.35	0.26	0.7	0.57	0.44	0.21	0.10	1.2	3.7
Tm	0.0041	0.053	0.040	0.11	0.09	0.065	0.034	0.016	0.17	0.54
Yb	0.037	0.35	0.26	0.7	0.54	0.37	0.24	0.10	1.1	3.3
Lu	0.008	0.063	0.038	0.10	0.08	0.054	0.040	0.015	0.18	0.53
Hf	0.0039	0.11	0.08	0.17	0.17	0.19	0.060	0.12	0.32	1.3
Ta	0.0015	0.0019	0.020	0.010	0.010	0.010	0.020	0.040	0.0157	0.065
Th	0.0005	0.0016	0.016	0.012	0.009	0.0050	0.007	0.07	0.0046	0.037
U	*bdl*	0.0008	0.0030	0.002	0.0020	0.0040	0.0030	0.008	0.0035	0.020

APPENDIX 3

MINERAL CHEMISTRY OF THE CRETACEOUS IGNEOUS ROCKS SPATIALLY-RELATED WITH THE MAYARÍ-BARACOA OPHIOLITIC BELT

Table A3.1 EPM analyses of clinopyroxene in igneous rocks spatially-related with the Mayarí-Baracoa Ophiolitic Belt

Rocktype	*Guamuta dyke*					*Téneme volcanics*																								
Sample	GUA 205					T 201															T 202									
SiO_2 (wt%)	50.22	50.52	49.63	54.23	50.11	51.70	51.25	52.77	52.50	53.09	53.00	51.26	51.18	50.98	51.54	51.55	50.80	51.24	50.54	51.32	51.29	50.89	52.37	52.06	51.11	51.35	51.46	52.16	51.58	
TiO_2	0.39	0.34	1.23	0.23	0.37	0.39	0.44	0.36	0.27	0.26	0.28	0.58	0.52	0.50	0.38	0.38	0.41	0.31	0.59	0.38	0.33	0.44	0.27	0.34	0.45	0.38	0.37	0.35	0.32	
Al_2O_3	4.94	4.42	5.08	1.57	4.85	2.14	1.52	2.01	2.40	2.40	2.41	2.06	1.74	2.06	1.61	1.97	2.94	1.80	2.38	1.43	1.59	2.63	1.68	1.49	2.49	1.69	2.45	1.49	1.61	
FeO	13.38	12.67	14.44	10.70	13.37	12.83	13.48	9.62	5.41	5.76	5.63	13.90	14.38	12.63	12.11	10.12	11.96	10.75	13.29	13.75	10.82	11.90	9.14	10.73	8.97	10.79	9.61	9.61	9.71	
MnO	0.22	0.20	0.28	0.25	0.23	0.25	0.30	0.22	0.16	0.18	0.19	0.37	0.47	0.39	0.34	0.25	0.38	0.28	0.40	0.48	0.41	0.43	0.25	0.27	0.25	0.27	0.34	0.29	0.30	
MgO	14.75	15.23	14.40	17.44	15.01	14.81	14.54	15.92	16.92	17.26	17.03	13.69	13.39	14.79	15.22	15.89	15.57	16.01	14.49	14.26	13.89	14.05	15.81	14.73	14.60	14.11	14.28	14.65	14.73	
CaO	16.30	16.40	14.71	15.57	16.29	17.82	17.96	19.40	21.52	21.56	21.11	18.35	17.61	18.25	18.27	18.94	17.70	18.54	17.66	17.84	20.76	19.38	20.27	19.88	21.23	20.54	21.15	20.95	20.92	
Na_2O	0.57	0.47	0.64	0.17	0.61	0.26	0.26	0.26	0.17	0.16	0.15	0.22	0.19	0.28	0.21	0.29	0.26	0.22	0.25	0.24	0.22	0.23	0.15	0.19	0.25	0.27	0.24	0.22	0.33	
Total	100.78	100.25	100.40	100.16	100.83	100.20	99.75	100.56	99.35	100.67	99.80	100.43	99.48	99.88	99.68	99.39	100.02	99.15	99.60	99.70	99.31	99.95	99.94	99.69	99.35	99.40	99.90	99.72	99.50	
Structural formula																														
Si	1.86	1.87	1.85	2.00	1.85	1.93	1.93	1.94	1.93	1.93	1.94	1.92	1.95	1.91	1.93	1.92	1.89	1.92	1.90	1.94	1.93	1.91	1.94	1.95	1.91	1.93	1.92	1.95	1.93	
Ti	0.01	0.01	0.03	0.01	0.01	0.01	0.01	0.01	0.01	0.01	0.01	0.02	0.01	0.01	0.01	0.01	0.01	0.01	0.02	0.01	0.01	0.01	0.01	0.01	0.01	0.01	0.01	0.01	0.01	
Al	0.22	0.19	0.22	0.07	0.21	0.09	0.07	0.09	0.10	0.10	0.10	0.09	0.08	0.09	0.07	0.09	0.13	0.08	0.11	0.06	0.07	0.12	0.07	0.07	0.11	0.07	0.11	0.07	0.07	
Fe^{2+}	0.41	0.39	0.45	0.33	0.41	0.40	0.42	0.30	0.17	0.17	0.17	0.44	0.46	0.40	0.38	0.32	0.37	0.34	0.42	0.43	0.34	0.37	0.28	0.34	0.28	0.34	0.30	0.30	0.30	
Mn	0.01	0.01	0.01	0.01	0.01	0.01	0.01	0.01	0.00	0.01	0.01	0.01	0.02	0.01	0.01	0.01	0.01	0.01	0.01	0.02	0.01	0.01	0.01	0.01	0.01	0.01	0.01	0.01	0.01	
Mg	0.81	0.84	0.80	0.96	0.82	0.82	0.82	0.87	0.93	0.93	0.93	0.77	0.76	0.83	0.85	0.88	0.86	0.89	0.81	0.80	0.78	0.78	0.87	0.82	0.81	0.79	0.79	0.81	0.82	
Ca	0.65	0.65	0.59	0.62	0.64	0.71	0.72	0.77	0.85	0.84	0.83	0.74	0.72	0.73	0.73	0.76	0.71	0.74	0.71	0.72	0.84	0.78	0.80	0.80	0.85	0.83	0.84	0.84	0.84	
Na	0.04	0.03	0.05	0.01	0.04	0.02	0.02	0.02	0.01	0.01	0.01	0.02	0.01	0.02	0.02	0.02	0.02	0.02	0.02	0.02	0.02	0.02	0.01	0.01	0.02	0.02	0.02	0.02	0.02	
Mg #	0.66	0.68	0.64	0.74	0.67	0.67	0.66	0.75	0.85	0.84	0.84	0.64	0.62	0.68	0.69	0.74	0.70	0.73	0.66	0.65	0.70	0.68	0.75	0.71	0.74	0.70	0.73	0.73	0.73	

Table A3.1 (continued)

Rocktype	*Téneme volcanics*																		*Téneme boninite*				*Loma Estrella de Mayarí dyke*		
Sample	T 202												TEN 1		TM 21				TM 1				CAR 4		
SiO_2 (wt%)	52.28	52.15	54.28	53.66	54.31	55.38	52.01	52.68	51.91	52.14	50.97	51.72	51.58	51.83	50.95	51.08	51.28	50.64	52.27	52.12	52.79	52.52	51.57	51.39	51.27
TiO_2	0.34	0.17	0.08	0.18	0.03	0.07	0.30	0.29	0.33	0.33	0.47	0.38	0.28	0.25	0.44	0.26	0.27	0.25	0.24	0.27	0.20	0.23	0.69	0.67	0.68
Al_2O_3	1.68	2.95	0.93	1.61	0.79	0.77	1.51	1.31	1.84	1.98	2.94	1.94	1.39	1.35	3.25	3.43	3.33	4.20	2.64	2.79	1.60	1.52	2.37	2.55	2.30
FeO	10.42	5.62	3.17	6.79	3.46	3.45	9.09	9.28	10.17	8.50	10.66	10.42	10.49	9.79	5.96	5.62	5.84	4.97	5.45	5.76	5.73	7.28	6.21	5.92	6.07
MnO	0.30	0.03	0.17	0.18	0.06	0.17	0.25	0.26	0.22	0.24	0.29	0.28	0.35	0.34	0.33	0.36	0.36	0.34	0.16	0.18	0.29	0.22	0.18	0.16	0.15
MgO	14.25	17.23	18.92	18.12	19.02	19.03	15.27	15.35	14.48	16.16	13.68	14.21	14.59	14.80	15.90	15.88	16.01	15.53	17.35	17.14	18.24	16.87	15.89	15.21	15.27
CaO	20.74	20.98	21.73	19.41	21.59	21.52	20.65	21.13	20.45	20.25	20.55	20.62	20.34	20.61	21.90	22.30	22.39	22.98	20.79	20.66	19.95	20.59	22.19	23.06	22.97
Na_2O	0.28	0.15	0.17	0.11	0.12	0.18	0.18	0.14	0.27	0.16	0.24	0.23	0.17	0.18	0.36	0.18	0.23	0.13	0.30	0.27	0.25	0.18	0.37	0.42	0.33
Total	100.29	99.28	99.45	100.06	99.38	100.57	99.26	100.44	99.67	99.76	99.80	99.80	99.17	99.14	99.10	99.11	99.70	99.03	99.18	99.19	99.05	99.41	99.47	99.38	99.05
Structural formula																									
Si	1.95	1.91	1.97	1.96	1.98	1.99	1.94	1.95	1.94	1.93	1.91	1.93	1.94	1.95	1.88	1.89	1.88	1.87	1.92	1.92	1.94	1.94	1.90	1.90	1.90
Ti	0.01	0.00	0.00	0.00	0.00	0.00	0.01	0.01	0.01	0.01	0.01	0.01	0.01	0.01	0.01	0.01	0.01	0.01	0.01	0.01	0.01	0.01	0.02	0.02	0.02
Al	0.07	0.13	0.04	0.07	0.03	0.03	0.07	0.06	0.08	0.09	0.13	0.09	0.06	0.06	0.14	0.15	0.14	0.18	0.11	0.12	0.07	0.07	0.10	0.11	0.10
Fe^{2+}	0.32	0.17	0.10	0.21	0.11	0.10	0.28	0.29	0.32	0.26	0.33	0.33	0.33	0.31	0.18	0.17	0.18	0.15	0.17	0.18	0.18	0.22	0.19	0.18	0.19
Mn	0.01	0.00	0.01	0.01	0.00	0.01	0.01	0.01	0.01	0.01	0.01	0.01	0.01	0.01	0.01	0.01	0.01	0.01	0.01	0.01	0.01	0.01	0.01	0.01	0.00
Mg	0.79	0.94	1.02	0.99	1.03	1.02	0.85	0.85	0.81	0.89	0.76	0.79	0.82	0.83	0.88	0.87	0.88	0.86	0.95	0.94	1.00	0.93	0.87	0.84	0.85
Ca	0.83	0.83	0.85	0.76	0.84	0.83	0.83	0.84	0.82	0.80	0.82	0.83	0.82	0.83	0.87	0.88	0.88	0.91	0.82	0.81	0.79	0.81	0.88	0.91	0.91
Na	0.02	0.01	0.01	0.01	0.01	0.01	0.01	0.01	0.02	0.01	0.02	0.02	0.01	0.01	0.03	0.01	0.02	0.01	0.02	0.02	0.02	0.01	0.03	0.03	0.02
Mg #	0.71	0.85	0.91	0.83	0.91	0.91	0.75	0.75	0.72	0.77	0.70	0.71	0.71	0.73	0.83	0.83	0.83	0.85	0.85	0.84	0.85	0.81	0.82	0.82	0.82

Table A3.1 (continued)

Rocktype	*Quibiján volcanics (Q1)*					*Quibiján volcanics (Q2)*																		
Sample	Q 206			Q 208		Q 202									Q 209									
SiO_2 (wt%)	52.48	52.60	52.23	52.30	52.44	52.05	52.73	51.23	52.29	51.77	52.82	51.73	50.49	49.97	52.67	52.20	51.55	52.44	51.47	48.79	49.60	49.53	50.59	50.30	50.62
TiO_2	0.35	0.34	0.34	0.31	0.54	0.33	0.29	0.49	0.33	0.39	0.22	0.42	0.70	0.68	0.37	0.39	0.36	0.35	0.55	1.02	0.87	0.85	0.75	0.71	0.65
Al_2O_3	2.09	2.06	2.66	1.93	1.49	2.10	2.43	1.40	2.15	2.11	2.01	2.64	3.71	3.13	1.89	1.88	2.17	2.06	1.98	4.58	4.13	4.17	3.41	3.63	3.70
FeO	4.18	4.31	3.88	6.68	7.38	6.52	7.04	12.11	7.14	8.00	6.15	7.73	9.30	11.70	8.94	9.30	7.50	8.65	8.95	11.38	9.89	10.05	12.12	10.05	10.54
MnO	0.32	0.29	0.18	0.30	0.39	0.13	0.28	0.43	0.18	0.27	0.25	0.23	0.21	0.36	0.28	0.35	0.21	0.25	0.20	0.32	0.29	0.31	0.31	0.25	0.23
MgO	16.82	16.85	16.70	16.64	16.77	16.51	15.61	15.58	16.29	15.91	16.94	16.03	14.87	13.80	16.64	16.74	16.69	16.77	16.34	14.29	14.83	14.95	13.46	14.58	14.28
CaO	22.46	22.45	23.09	20.66	19.86	21.16	21.49	17.67	21.03	20.62	21.19	20.28	20.35	19.50	19.07	18.79	20.69	19.50	19.53	18.64	19.44	19.49	19.61	20.11	19.20
Na_2O	0.33	0.23	0.21	0.25	0.23	0.24	0.20	0.21	0.24	0.27	0.13	0.20	0.29	0.24	0.25	0.18	0.22	0.18	0.28	0.29	0.22	0.25	0.31	0.25	0.21
Total	99.03	99.12	99.29	99.07	99.11	99.04	100.06	99.11	99.65	99.34	99.71	99.26	99.91	99.39	100.12	99.83	99.38	100.20	99.31	99.30	99.28	99.59	100.56	99.88	99.43
Structural formula																									
Si	1.93	1.93	1.92	1.94	1.95	1.93	1.94	1.93	1.93	1.92	1.94	1.92	1.87	1.88	1.94	1.93	1.90	1.93	1.91	1.83	1.85	1.84	1.89	1.87	1.90
Ti	0.01	0.01	0.01	0.01	0.02	0.01	0.01	0.01	0.01	0.01	0.01	0.01	0.02	0.02	0.01	0.01	0.01	0.01	0.02	0.03	0.02	0.02	0.02	0.02	0.02
Al	0.09	0.09	0.12	0.08	0.07	0.09	0.11	0.06	0.09	0.09	0.09	0.12	0.16	0.14	0.08	0.08	0.09	0.09	0.09	0.20	0.18	0.18	0.15	0.16	0.16
Fe^{2+}	0.13	0.13	0.12	0.21	0.23	0.20	0.22	0.38	0.22	0.25	0.19	0.24	0.29	0.37	0.28	0.29	0.23	0.27	0.28	0.36	0.31	0.31	0.38	0.31	0.33
Mn	0.01	0.01	0.01	0.01	0.01	0.00	0.01	0.01	0.01	0.01	0.01	0.01	0.01	0.01	0.01	0.01	0.01	0.01	0.01	0.01	0.01	0.01	0.01	0.01	0.01
Mg	0.92	0.92	0.91	0.92	0.93	0.91	0.86	0.87	0.90	0.88	0.93	0.89	0.82	0.77	0.91	0.92	0.92	0.92	0.90	0.80	0.83	0.83	0.75	0.81	0.80
Ca	0.89	0.88	0.91	0.82	0.79	0.84	0.85	0.71	0.83	0.82	0.83	0.81	0.81	0.79	0.75	0.74	0.82	0.77	0.78	0.75	0.78	0.78	0.78	0.80	0.77
Na	0.02	0.02	0.01	0.02	0.02	0.02	0.01	0.02	0.02	0.02	0.01	0.01	0.02	0.02	0.02	0.01	0.02	0.01	0.02	0.02	0.02	0.02	0.02	0.02	0.02
Mg #	0.88	0.87	0.88	0.82	0.80	0.82	0.80	0.70	0.80	0.78	0.83	0.79	0.74	0.68	0.77	0.76	0.80	0.78	0.76	0.69	0.73	0.73	0.66	0.72	0.71

Table A3.1 (continued)

Rocktype	*Quibiján volcanics (Q2)*																		*Moa-Baracoa crustal gabbro*										
Sample	Q 209																Q 210		CY 200										
SiO_2 (wt%)	52.06	51.75	51.34	51.03	51.93	51.47	52.02	52.61	52.46	52.19	51.81	52.31	51.48	52.05	52.34	50.32	51.08	51.03	50.94	51.80	51.09	51.74	52.00	52.18	53.13	52.15	51.14	52.49	52.33
TiO_2	0.31	0.35	0.45	0.34	0.38	0.49	0.38	0.32	0.34	0.29	0.38	0.39	0.44	0.39	0.36	0.70	0.51	0.52	0.71	0.46	0.80	0.65	0.60	0.53	0.31	0.73	0.72	0.60	0.53
Al_2O_3	2.02	1.93	2.85	2.18	2.09	2.90	2.61	1.86	2.17	1.71	1.96	1.95	2.08	2.13	1.98	3.60	2.48	2.88	2.32	1.65	2.23	2.15	2.11	2.22	1.36	1.95	2.56	1.55	1.85
FeO	8.06	8.84	9.44	8.44	8.28	8.45	7.77	8.04	8.83	8.80	11.21	9.09	9.28	9.51	8.34	10.59	7.52	6.54	9.01	9.41	9.40	9.24	9.60	9.02	8.98	8.94	9.13	9.31	8.81
MnO	0.22	0.28	0.29	0.21	0.28	0.34	0.28	0.23	0.29	0.33	0.43	0.33	0.33	0.31	0.22	0.31	0.44	0.38	0.22	0.28	0.24	0.21	0.27	0.25	0.23	0.35	0.30	0.29	0.31
MgO	16.25	16.57	15.11	16.35	16.38	15.46	15.51	16.56	16.25	16.46	15.25	16.22	16.03	16.25	16.22	14.87	15.69	15.89	14.06	14.22	14.19	14.16	14.33	14.37	14.65	14.04	14.54	14.32	14.23
CaO	20.26	19.48	19.62	20.33	19.88	20.25	20.61	20.23	19.36	19.65	18.19	19.72	19.25	18.74	19.90	18.65	21.19	21.31	21.69	21.11	21.22	20.88	21.18	21.28	21.45	21.51	20.48	20.93	21.24
Na_2O	0.25	0.22	0.28	0.23	0.24	0.26	0.21	0.18	0.19	0.18	0.27	0.19	0.28	0.20	0.20	0.28	0.44	0.57	0.34	0.34	0.34	0.37	0.34	0.34	0.39	0.42	0.31	0.26	0.29
Total	99.43	99.42	99.38	99.11	99.46	99.62	99.39	100.03	99.89	99.61	99.50	100.20	99.17	99.58	99.56	99.32	99.34	99.12	99.28	99.27	99.51	99.40	100.43	100.19	100.50	100.09	99.18	99.75	99.59
Structural formula																													
Si	1.93	1.92	1.91	1.90	1.92	1.91	1.93	1.94	1.94	1.93	1.94	1.93	1.92	1.93	1.94	1.88	1.89	1.89	1.91	1.94	1.91	1.94	1.93	1.94	1.96	1.94	1.92	1.96	1.96
Ti	0.01	0.01	0.01	0.01	0.01	0.01	0.01	0.01	0.01	0.01	0.01	0.01	0.01	0.01	0.01	0.02	0.01	0.01	0.02	0.01	0.02	0.02	0.02	0.01	0.01	0.02	0.02	0.02	0.01
Al	0.09	0.08	0.13	0.10	0.09	0.13	0.11	0.08	0.09	0.07	0.09	0.08	0.09	0.09	0.09	0.16	0.11	0.13	0.10	0.07	0.10	0.09	0.09	0.10	0.06	0.09	0.11	0.07	0.08
Fe^{2+}	0.25	0.27	0.29	0.26	0.26	0.26	0.24	0.25	0.27	0.27	0.35	0.28	0.29	0.30	0.26	0.33	0.23	0.20	0.28	0.30	0.29	0.29	0.30	0.28	0.28	0.28	0.29	0.29	0.28
Mn	0.01	0.01	0.01	0.01	0.01	0.01	0.01	0.01	0.01	0.01	0.01	0.01	0.01	0.01	0.01	0.01	0.01	0.01	0.01	0.01	0.01	0.01	0.01	0.01	0.01	0.01	0.01	0.01	0.01
Mg	0.90	0.92	0.84	0.91	0.90	0.85	0.86	0.91	0.89	0.91	0.85	0.89	0.89	0.90	0.90	0.83	0.87	0.88	0.78	0.79	0.79	0.79	0.79	0.79	0.81	0.78	0.81	0.80	0.79
Ca	0.80	0.77	0.78	0.81	0.79	0.80	0.82	0.80	0.77	0.78	0.73	0.78	0.77	0.75	0.79	0.75	0.84	0.84	0.87	0.85	0.85	0.84	0.84	0.85	0.85	0.86	0.82	0.84	0.85
Na	0.02	0.02	0.02	0.02	0.02	0.02	0.02	0.01	0.01	0.01	0.02	0.01	0.02	0.01	0.01	0.02	0.03	0.04	0.02	0.02	0.02	0.03	0.02	0.02	0.03	0.03	0.02	0.02	0.02
Mg #	0.78	0.77	0.74	0.78	0.78	0.77	0.78	0.79	0.77	0.77	0.71	0.76	0.75	0.75	0.78	0.71	0.79	0.81	0.74	0.73	0.73	0.73	0.73	0.74	0.74	0.74	0.74	0.73	0.74

Table A3.2 Representative EPMA of (albitized) plagioclase in igneous rocks spatially-related with the Mayarí-Baracoa Ophiolitic Belt

Rocktype	*Guamuta dyke*			*L. Bandera dyke*	*Téneme volcanics*				*Quibiján volcanics (Q1)*				*Quibiján volcanics (Q2)*	
Sample	GUA 205			LB 204	T 201	T 202	TEN 1	TM 21	Q 206	Q 208			Q 209	
SiO_2 (wt%)	49.40	48.87	49.06	49.50	65.12	63.67	63.28	64.60	53.30	67.36	67.46	66.91	64.98	63.96
Al_2O_3	31.21	31.84	31.62	32.39	21.18	22.15	22.90	21.64	28.63	20.40	20.58	20.19	21.98	22.80
FeO	0.59	0.42	0.40	0.31	0.40	0.09	0.12	0.15	0.35	0.08	0.07	0.11	0.09	0.08
CaO	14.37	15.42	14.73	15.13	2.57	3.31	2.32	2.20	13.23	0.71	0.84	0.65	3.00	3.82
Na_2O	3.56	2.77	3.40	2.99	10.16	9.92	9.78	10.39	3.37	11.69	11.43	11.44	10.51	10.18
K_2O	0.02	0.02	0.02	0.03	0.06	0.07	0.97	0.13	0.41	0.08	0.05	0.06	0.05	0.04
Total	99.15	99.33	99.23	100.35	99.49	99.21	99.37	99.12	99.44	100.31	100.42	99.37	100.61	100.88
Structural formula														
Si	2.28	2.25	2.26	2.25	2.88	2.83	2.82	2.87	2.43	2.94	2.94	2.95	2.85	2.81
Al	1.70	1.73	1.72	1.74	1.11	1.16	1.20	1.13	1.54	1.05	1.06	1.05	1.14	1.18
Fe^{2+}	0.02	0.02	0.02	0.01	0.01	0.00	0.00	0.01	0.01	0.00	0.00	0.00	0.00	0.00
Ca	0.71	0.76	0.73	0.74	0.12	0.16	0.11	0.10	0.65	0.03	0.04	0.03	0.14	0.18
Na	0.32	0.25	0.30	0.26	0.87	0.86	0.84	0.89	0.30	0.99	0.97	0.98	0.89	0.87
K	0.00	0.00	0.00	0.00	0.00	0.00	0.06	0.01	0.02	0.00	0.00	0.00	0.00	0.00
An (wt%)	69	75	70	74	12	16	11	10	67	3	4	3	14	17

Table A3.3 Representative LA-ICP-MS analyses of clinopyroxene and plagioclase in eastern Cuba volcanics

Sample	Q 206 clinopyroxene	Q 206 plagioclase
Rb (ppm)	0.4	127
Sr	27	706
Y	10	1.8
Zr	7	2
Nb	*bdl*	0.1
La	0.3	0.9
Ce	1.5	2.0
Nd	2.6	1.2
Sm	1.2	0.3
Eu	0.4	0.3
Gd	1.7	0.3
Tb	0.3	0.04
Dy	2.0	0.2
Ho	0.4	0.1
Er	1.3	0.3
Tm	0.2	0.02
Yb	1.2	*bdl*
Lu	0.2	0.03
Hf	0.4	0.1
Pb	0.2	1.1
Th	*bdl*	*bdl*
U	*bdl*	*bdl*

bdl = below detection limit

APPENDIX 4

WHOLE ROCK COMPOSITION OF THE CRETACEOUS IGNEOUS ROCKS SPATIALLY-RELATED WITH THE MAYARÍ-BARACOA OPHIOLITIC BELT

Table A4.1 Whole rock major and trace element data of studied igneous rocks spatially-related with the Mayarí-Baracoa Ophiolitic Belt

Group	Group 1									Group 2											
Type	*Morel volcanics*				*La Melba volcanics*		*Centeno volcanics*			*Guamuta dykes*						*Loma de la Bandera dykes*					*Cerrajón dyke*
Sample	M 200	M 201	M 202	MOREL 1*	MEL 200	MEL 201	CEN 200	CEN 201	CEN 202	GUA 200	GUA 201	GUA 202	GUA 203	GUA 205	GUA 206	LB 200	LB 201	LB 202	LB 203	LB 204	FA 202
Latitude N	20º 29' 19"				20º 28' 03"		20º 38' 33"		20º 37' 53"	20º34'49"	20º34'41"	20º34'44"	20º34'21"	20º33'57"	20º32'56"	20º35'31"	20º35'23"	20º35'08"	20º35'54"	20º35'47"	20º 31' 10"
Longitude W	74º 38' 06"				74º 47' 43"		74º 59' 42"		75º 00' 34"	75º48'29"	75º48'20"	75º48'19"	75º48'28"	75º48'04"	75º47 46"	75º43'14"	75º43'16"	75º43'16"	75º43'10"	75º43'08"	75º 01' 23"
SiO_2 (wt%)	49.59	51.12	49.08	47.35	49.83	49.11	52.66	51.05	49.23	51.75	49.19	51.64	50.69	50.83	52.12	50.64	50.50	56.33	50.35	43.05	51.65
TiO_2	1.95	1.87	1.88	1.77	1.21	2.17	2.33	2.17	2.87	1.04	0.94	0.89	0.82	0.82	1.41	0.78	0.89	0.70	0.84	1.41	0.80
Al_2O_3	14.35	14.16	14.38	14.01	14.87	13.64	12.79	13.54	13.11	16.28	16.63	15.84	16.81	16.22	16.49	16.37	16.40	16.23	15.75	16.64	15.93
FeO*	10.91	10.67	11.04	10.12	9.67	13.19	12.78	11.60	14.31	8.56	9.44	8.88	8.20	7.71	10.33	8.08	8.62	9.50	8.38	6.21	7.71
MnO	0.20	0.18	0.22	0.19	0.14	0.26	0.21	0.21	0.28	0.15	0.18	0.18	0.14	0.14	0.18	0.16	0.16	0.16	0.15	0.14	0.16
MgO	7.91	7.98	8.16	7.20	8.37	7.20	4.79	6.58	6.90	7.74	7.86	8.08	8.45	8.36	5.87	8.30	8.39	5.47	9.09	12.83	8.92
CaO	9.54	8.33	9.77	12.25	10.83	9.09	7.88	8.20	8.12	11.51	10.63	9.82	12.80	13.04	9.65	12.54	11.47	8.49	12.33	15.59	11.13
Na_2O	3.07	3.06	2.82	1.71	3.22	3.79	3.71	4.51	2.93	2.90	3.65	3.29	1.78	2.18	2.96	2.30	2.65	2.89	2.37	0.67	2.91
K_2O	0.79	0.94	1.24	0.50	0.40	0.16	0.36	0.21	0.59	0.08	0.04	0.36	0.02	0.06	0.54	0.12	0.14	0.17	0.12	0.05	0.07
P_2O_5	0.19	0.17	0.18	0.16	0.10	0.20	0.44	0.21	0.29	0.08	0.08	0.07	0.06	0.06	0.10	0.06	0.07	0.06	0.06	0.67	0.07
Total	98.50	98.48	98.77	95.26	98.64	98.81	97.96	98.26	98.64	100.09	98.63	99.04	99.78	99.42	99.66	99.36	99.29	100.00	99.45	97.26	99.37
Sc (ppm)	45	46	45	*n.a.*	40	44	36	42	44	38	40	41	38	41	37	39	40	34	41	35	32
V	380	364	375	359	271	394	279	399	486	248	277	257	229	240	369	237	253	305	236	227	215
Cr	144	166	167	161	386	125	67	125	85	253	184	153	318	170	12.8	167	210	26	406	99	324
Ni	56	57	59	58	89	52	32	57	42	76	70	62	102	82	35	75	73	22	111	289	141
Rb	8.5	9.9	10.7	5.1	1.80	0.77	1.9	2.1	2.7	0.30	0.20	1.84	0.12	0.47	3.6	0.87	1.21	0.98	1.18	0.36	0.77
Sr	97	111	107	58	181	133	93	67	122	128	80	164	109	117	173	145	198	164	151	59	179
Y	45	40	42	37	28	48	100	49	64	25	23	20	20	19.7	29	19.4	22	17.4	20	53	21
Zr	116	108	110	108	64	130	348	134	187	62	46	40	43	42	64	37	44	35	41	54	46
Nb	3.2	2.9	2.9	3.0	1.39	3.6	8.3	3.6	5.7	0.57	0.64	0.63	0.48	0.48	0.98	0.47	0.53	0.38	0.56	1.32	0.40
Cs	0.18	0.19	0.36	0.15	0.06	0.01	0.02	0.01	0.031	*bdl*	*bdl*	0.0003	*bdl*	0.008	0.02	0.01	0.03	0.03	0.09	0.02	0.03
Ba	11.0	11.8	13.6	8.0	14.4	6.5	8.5	15.0	18.6	15.7	5.7	43	8.7	17.0	54	26	42	62	25	5.5	8.1
La	4.1	3.9	3.8	3.7	2.4	4.9	12.0	5.0	7.4	2.2	2.0	1.74	1.62	1.59	2.7	1.43	1.80	1.82	1.50	5.6	1.56
Ce	12.3	11.6	11.4	11.9	7.2	14.4	35	14.8	21	6.8	5.6	4.9	4.8	4.8	7.7	4.3	5.2	4.5	4.5	17.3	5.0
Pr	2.1	1.9	1.9	2.1	1.21	2.3	5.6	2.4	3.3	1.17	0.94	0.83	0.83	0.83	1.30	0.73	0.89	0.72	0.77	3.0	0.88
Nd	11.7	10.7	10.6	11.3	6.9	13.1	31	13.5	18.3	6.5	5.4	4.8	4.8	4.7	7.3	4.4	5.2	4.1	4.6	17.7	5.3
Sm	4.7	4.2	4.3	4.1	2.7	5.0	11.0	5.2	6.8	2.6	2.2	2.0	2.0	1.9	3.0	1.89	2.1	1.69	2.0	6.5	2.1
Eu	1.69	1.54	1.54	1.37	1.12	1.70	3.3	1.79	2.3	1.01	0.88	0.81	0.82	0.79	1.16	0.77	0.80	0.69	0.81	1.68	0.87
Gd	6.3	5.6	5.8	5.3	3.8	6.7	14.2	7.0	8.9	3.5	3.1	2.8	2.8	2.7	4.1	2.6	3.0	2.3	2.7	8.1	2.9
Tb	1.20	1.09	1.11	0.91	0.72	1.27	2.7	1.32	1.70	0.66	0.59	0.54	0.53	0.52	0.77	0.51	0.56	0.44	0.53	1.46	0.56
Dy	7.9	7.3	7.5	6.2	4.9	8.5	17.9	8.7	11.3	4.4	4.1	3.6	3.6	3.4	5.1	3.4	3.8	2.9	3.6	9.6	3.8
Ho	1.68	1.52	1.58	1.37	1.05	1.82	3.8	1.88	2.4	0.93	0.88	0.78	0.77	0.75	1.13	0.74	0.81	0.65	0.77	2.0	0.80
Er	4.6	4.2	4.4	3.8	2.9	5.0	10.6	5.2	6.7	2.6	2.4	2.2	2.1	2.1	3.1	2.0	2.3	1.90	2.1	5.5	2.2
Tm	0.65	0.59	0.63	0.57	0.42	0.73	1.54	0.73	0.96	0.37	0.35	0.31	0.31	0.30	0.44	0.30	0.32	0.27	0.30	0.77	0.32
Yb	4.1	3.8	3.9	3.6	2.6	4.5	9.6	4.6	5.9	2.3	2.2	1.9	1.9	1.87	2.8	1.80	2.0	1.74	1.90	4.6	2.0
Lu	0.64	0.60	0.62	0.49	0.41	0.70	1.50	0.71	0.93	0.37	0.35	0.30	0.31	0.30	0.44	0.29	0.32	0.29	0.30	0.69	0.31
Hf	3.3	3.1	3.1	3.0	1.88	3.7	9.4	3.8	5.2	1.89	1.43	1.26	1.30	1.29	2.0	1.16	1.37	1.24	1.26	2.1	1.45
Ta	0.24	0.21	0.23	*n.a.*	0.11	0.27	0.61	0.27	0.43	0.051	0.048	0.051	0.042	0.037	0.077	0.035	0.041	0.029	0.043	0.085	0.033
Pb	0.55	0.48	0.59	0.38	0.074	0.20	0.53	0.49	0.98	0.26	0.22	0.15	0.24	0.20	0.45	0.56	0.17	0.21	0.21	0.15	0.22
Th	0.19	0.18	0.18	0.17	0.091	0.23	0.63	0.24	0.38	0.10	0.15	0.13	0.076	0.09	0.17	0.064	0.12	0.26	0.077	0.084	0.11
U	0.32	0.30	0.44	0.27	0.032	0.078	0.24	0.15	0.14	0.041	0.051	0.046	0.025	0.035	0.068	0.030	0.046	0.11	0.027	0.16	0.034
U/Pb	0.58	0.62	0.74	0.72	0.43	0.40	0.45	0.31	0.14	0.16	0.23	0.31	0.10	0.17	0.15	0.05	0.27	0.53	0.13	1.03	0.15
La/Sm	0.9	0.9	0.9	0.9	0.9	1.0	1.1	1.0	1.1	0.8	0.9	0.9	0.8	0.8	0.9	0.8	0.8	1.1	0.8	0.9	0.7

*n.a. = not analysed; bdl = below detection limit. * Data from Proenza et al. (2006); † major element data from Proenza et al. (2006) and trace elements analysed here;§ data from Table A2.2. MTZ = Moho transition zone*

Table A4.1 (continued)

Group	Group 3																
Subgroup	3T																
Type	*Téneme volcanics*										*Téneme volcanics with boninitic affinity*				*Téneme intrusive*	*Loma Estrella de Mayarí dykes*	
Sample	T 200	T 201	T 202	TEN 1*	TEN 2†	TEN 3*	TM 12†	TM 13†	TM 20†	TM 21*	TM 1*	TM 8†	TM 14†	TM 15†	DT 200	CAR 4	LEM 5
Latitude N	20º38'50"	20º39'07"			20º 38' 50"				20º 40' 10"		20º 39' 35"		20º 39' 10"		20º 35' 58"	20º 27' 46"	20º 30' 49"
Longitude W	75º25'43"	75º25'32"			75º 25' 43"				75º 23' 05"		75º 25' 55"		75º 25' 45"		75º 22' 31"	75º 50' 16"	75º 42' 04"
SiO_2 (wt%)	55.64	55.20	58.59	55.45	57.63	67.27	68.61	66.78	58.19	50.51	55.95	59.75	54.53	56.09	61.01	51.76	51.15
TiO_2	0.43	0.92	0.42	0.46	0.40	0.73	0.76	0.76	0.45	0.83	0.28	0.39	0.37	0.35	0.49	0.62	0.63
Al_2O_3	18.33	16.47	16.69	18.86	15.73	13.51	13.60	13.34	14.55	17.68	12.77	15.39	14.23	13.18	17.38	19.81	18.87
FeO*	8.05	9.88	7.07	6.33	6.16	6.14	4.99	6.16	6.71	9.39	6.69	5.94	7.20	6.98	6.92	7.91	8.56
MnO	0.04	0.18	0.09	0.11	0.11	0.07	0.08	0.08	0.12	0.19	0.13	0.08	0.13	0.13	0.17	0.15	0.15
MgO	5.41	3.88	5.28	4.27	5.15	0.89	0.87	1.12	5.59	4.88	9.17	7.73	8.00	8.24	2.88	3.38	3.73
CaO	6.69	8.11	8.69	7.84	9.05	2.34	2.80	2.86	10.06	8.04	8.32	0.49	9.24	8.85	7.25	7.18	10.44
Na_2O	1.70	3.56	2.03	2.79	1.69	5.96	6.00	5.37	1.51	3.29	2.69	4.49	1.42	1.42	2.52	4.36	2.47
K_2O	1.05	0.81	0.53	0.50	0.25	1.44	0.66	1.02	0.22	0.85	0.28	0.22	0.71	0.65	0.51	1.00	0.64
P_2O_5	0.05	0.13	0.06	0.08	0.06	0.20	0.21	0.19	0.06	0.10	0.03	0.07	0.05	0.07	0.11	0.15	0.13
Total	97.38	99.14	99.44	96.69	96.23	98.55	98.58	97.68	97.46	95.76	96.31	94.55	95.88	95.96	99.24	96.32	96.78
Sc (ppm)	28	34	34	*n.a.*	*n.a.*	*n.a.*	*n.a.*	*n.a.*	*n.a.*	*n.a.*	*n.a.*	*n.a.*	*n.a.*	*n.a.*	27	*n.a.*	*n.a.*
V	189	316	204	190	170	70	81	80	199	325	185	218	187	175	139	268	318
Cr	65	15	109	45	171	27	59	90	194	51	500	94	293	296	3.9	25	31
Ni	56	11	34	27	49	11	21	34	58	22	113	22	59	62	6.2	20	14
Rb	7.1	9.7	6.5	5.4	4.3	*n.a.*	7.8	12.9	3.0	8.4	3.2	2.2	8.3	8.4	10.2	10.9	5.4
Sr	307	259	238	582	334	*n.a.*	97	110	279	324	292	63	348	248	112	496	494
Y	12.1	23	14.6	15.6	13.0	*n.a.*	38	33	13.8	19.8	13.1	17.1	8.9	10.3	16.1	12.0	9.7
Zr	51	61	37	59	47	*n.a.*	116	116	50	40	28	48	42	52	45	28	29
Nb	0.69	0.62	1.50	1.19	1.02	*n.a.*	1.84	1.70	0.60	1.31	1.16	0.61	0.64	0.71	1.46	1.15	1.03
Cs	0.36	0.15	0.20	0.30	0.13	*n.a.*	0.036	0.08	0.065	0.22	0.17	0.19	0.094	0.14	0.60	0.10	0.09
Ba	5157	307	284	627	223	*n.a.*	247	312	67	421	116	78	137	311	258	339	217
La	3.8	5.0	3.7	7.6	6.3	*n.a.*	12.1	11.6	4.8	4.1	1.60	10.5	3.5	6.3	6.0	4.4	4.2
Ce	8.2	12.2	7.6	17.4	12.9	*n.a.*	27	26	10.9	11.6	4.8	20	7.6	14.2	11.8	10.4	10.0
Pr	1.11	1.83	1.01	2.3	1.63	*n.a.*	3.8	3.7	1.55	1.73	0.65	2.6	1.02	1.9	1.49	1.55	1.40
Nd	5.2	9.5	4.6	9.7	7.2	*n.a.*	18.5	17.7	7.6	8.5	2.8	11.4	4.9	8.7	6.7	7.9	6.9
Sm	1.69	3.2	1.50	2.3	1.89	*n.a.*	5.4	5.2	2.3	2.5	0.95	2.8	1.47	2.2	1.97	2.1	1.8
Eu	0.54	1.10	0.54	0.98	0.64	*n.a.*	1.54	1.44	0.79	0.91	0.39	1.08	0.50	0.76	0.73	0.79	0.69
Gd	1.76	3.6	1.9	2.4	2.1	*n.a.*	5.9	5.6	2.4	2.9	1.35	3.0	1.53	2.1	2.23	2.4	2.0
Tb	0.31	0.61	0.36	0.38	0.35	*n.a.*	0.99	0.94	0.40	0.50	0.23	0.46	0.26	0.32	0.40	0.37	0.33
Dy	2.0	4.0	2.4	2.4	2.3	*n.a.*	6.3	5.9	2.5	3.0	1.45	2.8	1.61	1.89	2.7	2.6	2.2
Ho	0.45	0.85	0.55	0.53	0.49	*n.a.*	1.35	1.23	0.52	0.64	0.33	0.58	0.34	0.39	0.58	0.55	0.48
Er	1.29	2.4	1.55	1.49	1.39	*n.a.*	3.7	3.4	1.40	1.76	0.95	1.60	0.95	1.08	1.70	1.54	1.33
Tm	0.20	0.35	0.24	0.24	0.21	*n.a.*	0.56	0.50	0.21	0.27	0.15	0.24	0.14	0.16	0.26	0.23	0.20
Yb	1.33	2.2	1.56	1.51	1.40	*n.a.*	3.4	3.2	1.38	1.71	1.01	1.49	0.90	1.02	1.77	1.48	1.30
Lu	0.22	0.34	0.26	0.25	0.23	*n.a.*	0.55	0.51	0.22	0.26	0.16	0.25	0.15	0.16	0.30	0.25	0.22
Hf	1.72	2.0	1.27	1.83	1.54	*n.a.*	3.8	3.8	1.56	3.3	3.1	1.46	1.33	1.62	1.58	1.05	1.07
Ta	0.044	0.047	0.11	*n.a.*	0.05	*n.a.*	0.10	0.093	0.042	*n.a.*	*n.a.*	0.041	0.039	0.044	0.11	0.092	0.084
Pb	3.2	1.13	2.4	3.6	3.0	*n.a.*	3.6	1.50	3.1	2.4	1.90	2.4	2.0	2.7	1.13	1.4	2.1
Th	0.77	0.57	0.53	0.87	0.76	*n.a.*	1.52	1.54	0.57	0.58	0.46	0.70	0.55	1.07	1.17	0.42	0.45
U	0.96	0.42	0.45	0.65	0.57	*n.a.*	1.07	1.01	0.41	0.38	0.38	0.44	0.24	0.50	0.50	0.24	0.29
U/Pb	0.30	0.37	0.19	0.18	0.19	-	0.30	0.67	0.13	0.16	0.20	0.19	0.12	0.18	0.44	0.17	0.14
La/Sm	2.2	1.6	2.4	3.3	3.3	-	2.2	2.2	2.1	1.6	1.7	3.7	2.4	2.8	3.0	2.1	2.3

Table A4.1 (continued)

Group	Group 3																Moa-Baracoa ophiolitic gabbros		
Subgroup	3Q																Crustal gabbros		MTZ sill
Type	*Quibiján volcanics (Q1)*												*Quibiján volcanics (Q2)*				*Cayo Grande*	*Quemado del Negro*	*Cayo Guam*
Sample	Q 200	Q 201	Q 203	Q 204	Q 205	Q 206	Q 207	Q 208	Q 212	Q 213	Q 214	Q 215	Q 202	Q 209	Q 210	Q 211	CY 200	QN 4[§]	CG 17[§]
Latitude N	20º 20' 41"		20º 20' 35"		20º 20' 40"		20º 20' 41"		20º 21' 05"	20º 20' 49"			20º 20' 41"	20º 20' 41"		20º 20' 59"	20º 35' 15"	20º 35' 30"	20º 35' 45"
Longitude W	74º 39' 29"		74º 39' 59"		74º 39' 58"		74º 39' 46"		74º 39' 19"	74º 39' 35"			74º 39' 29"	74º 39' 39"		74º 39' 23"	74º 46' 34"	74º 49' 10"	74º 51' 23"
SiO_2 (wt%)	46.40	51.84	47.56	58.28	46.93	51.59	44.67	46.88	51.70	47.30	50.84	48.51	50.53	50.60	55.05	52.62	50.65	50.00	41.06
TiO_2	0.65	0.55	0.69	0.69	0.73	0.67	0.54	0.56	0.85	0.60	0.73	0.69	0.57	0.57	0.85	0.66	0.66	0.29	0.21
Al_2O_3	18.54	18.01	18.74	17.12	18.47	17.70	17.72	18.07	17.12	17.28	20.00	19.24	14.60	17.29	18.08	16.54	16.40	16.85	6.30
FeO*	8.29	7.30	8.89	7.26	7.93	10.48	9.21	7.54	9.53	8.18	8.35	8.42	8.63	8.53	8.26	9.14	8.14	5.49	11.46
MnO	0.16	0.13	0.15	0.12	0.17	0.12	0.16	0.17	0.12	0.17	0.10	0.14	0.17	0.16	0.12	0.18	0.16	0.11	0.19
MgO	5.92	6.02	5.88	3.84	5.07	6.94	5.23	4.43	5.03	6.11	4.97	5.13	9.71	7.06	3.99	6.18	7.59	11.05	27.59
CaO	13.18	9.74	11.38	6.83	13.67	7.26	15.12	17.92	8.80	12.64	9.52	11.69	11.46	11.59	6.70	9.85	12.88	15.71	5.19
Na_2O	2.31	4.82	1.99	3.02	2.00	1.23	2.24	2.77	4.50	2.31	2.28	2.04	1.80	1.80	5.49	3.21	2.75	1.37	0.45
K_2O	0.88	0.17	1.03	1.29	0.86	1.35	0.31	0.27	0.65	0.72	0.69	0.81	0.83	1.36	0.35	0.84	0.11	*bdl*	*bdl*
P_2O_5	0.07	0.09	0.07	0.20	0.08	0.06	0.07	0.07	0.11	0.08	0.08	0.08	0.06	0.06	0.14	0.08	0.03	0.01	0.01
Total	96.40	98.68	96.38	98.64	95.91	97.39	95.28	98.67	98.40	95.39	97.57	96.73	98.35	99.01	99.03	99.30	99.37	100.88	92.45
Sc (ppm)	36	37	34	31	35	43	39	38	37	36	32	36	45	39	27	38	44	*n.a.*	*n.a.*
V	253	255	251	210	251	318	266	268	289	232	246	248	250	246	286	277	235	157	108
Cr	64	56	45	17.5	28	37	117	85	62	101	25	54	353	174	13.3	62	515	855	2275
Ni	28	42	38	14.4	14.7	38	46	30	27	34	22	41	91	45	15.7	34	95	243	1400
Rb	11.0	1.69	12.4	17.0	11.2	15.3	6.4	4.1	8.2	8.3	8.7	10.9	10.5	18.8	6.6	15.3	0.57	0.05	0.09
Sr	218	327	168	218	162	294	167	134	309	215	239	220	297	325	394	277	147	78	38
Y	15.2	13.7	16.5	23	17.7	13.3	13.1	13.0	21	15.0	17.1	16.5	16.3	17.0	22	19.9	18.7	7.3	4.4
Zr	35	33	46	53	44	34	33	31	62	36	46	43	35	37	71	47	22	5	3.5
Nb	0.44	0.38	0.59	0.70	0.68	0.36	0.40	0.36	0.78	0.43	0.67	0.58	1.01	1.01	1.62	1.60	0.32	0.05	0.012
Cs	0.34	0.032	0.30	0.33	0.37	0.63	0.14	0.092	0.15	0.29	0.28	0.33	0.12	0.33	0.07	0.20	*bdl*	0.003	0.007
Ba	177	131	203	277	171	709	66	54	152	181	196	208	311	562	109	230	7.6	3.3	2.1
La	3.2	3.0	3.9	5.5	3.9	2.9	3.3	3.1	5.9	3.2	3.6	3.7	4.0	4.6	8.5	4.7	0.88	0.26	0.16
Ce	7.5	7.0	9.3	12.6	9.1	6.9	7.3	7.3	13.7	7.5	8.6	8.6	8.4	9.3	18.0	9.6	2.9	0.9	0.56
Pr	1.13	1.03	1.36	1.82	1.35	1.04	1.08	1.08	1.9	1.11	1.27	1.28	1.16	1.23	2.4	1.30	0.52	0.19	0.11
Nd	5.9	5.5	6.9	9.2	6.9	5.4	5.4	5.5	9.4	5.8	6.6	6.6	5.8	5.9	11.5	6.4	3.3	1.3	0.8
Sm	2.0	1.79	2.2	2.9	2.2	1.79	1.76	1.74	2.9	1.88	2.2	2.1	1.9	2.0	3.3	2.3	1.56	0.59	0.34
Eu	0.75	0.68	0.80	0.88	0.85	0.69	0.68	0.64	0.96	0.64	0.78	0.79	0.71	0.70	1.07	0.81	0.90	0.38	0.21
Gd	2.4	2.2	2.5	3.4	2.7	2.1	2.0	2.0	3.3	2.2	2.5	2.5	2.4	2.3	3.6	2.8	2.4	1.02	0.59
Tb	0.42	0.37	0.45	0.59	0.48	0.37	0.34	0.34	0.58	0.40	0.46	0.45	0.44	0.44	0.60	0.51	0.48	0.19	0.11
Dy	2.7	2.4	3.0	3.8	3.1	2.4	2.2	2.2	3.8	2.6	3.1	2.9	2.9	2.9	3.9	3.4	3.3	1.4	0.9
Ho	0.57	0.51	0.65	0.82	0.67	0.52	0.47	0.48	0.80	0.56	0.66	0.62	0.61	0.63	0.83	0.74	0.72	0.30	0.19
Er	1.58	1.41	1.77	2.3	1.83	1.41	1.36	1.31	2.2	1.56	1.82	1.72	1.74	1.82	2.3	2.1	2.0	0.83	0.56
Tm	0.23	0.21	0.26	0.32	0.27	0.21	0.19	0.19	0.33	0.23	0.26	0.25	0.26	0.26	0.34	0.31	0.29	0.12	0.08
Yb	1.46	1.29	1.62	2.0	1.72	1.30	1.16	1.21	2.0	1.41	1.63	1.56	1.66	1.64	2.1	2.0	1.78	0.75	0.56
Lu	0.23	0.21	0.27	0.32	0.28	0.21	0.19	0.19	0.32	0.22	0.27	0.25	0.26	0.27	0.34	0.31	0.28	0.12	0.09
Hf	1.15	1.08	1.44	1.69	1.39	1.10	1.02	0.99	1.9	1.12	1.42	1.34	1.23	1.25	2.2	1.57	0.79	0.24	0.16
Ta	0.032	0.022	0.037	0.047	0.044	0.027	0.025	0.025	0.055	0.032	0.049	0.041	0.11	0.12	0.15	0.21	0.024	0.013	0.001
Pb	1.81	1.17	1.87	1.73	1.52	1.29	1.32	1.45	4.1	1.21	1.44	1.84	4.7	18.0	6.5	3.5	0.46	0.14	0.11
Th	0.33	0.34	0.52	0.58	0.41	0.32	0.43	0.39	0.70	0.36	0.46	0.44	0.94	1.08	1.64	1.46	0.019	0.003	0.001
U	0.21	0.20	0.33	0.57	0.27	0.19	0.73	0.34	0.60	0.23	0.26	0.28	0.65	0.66	0.91	0.84	0.008	0.001	*bdl*
U/Pb	0.12	0.17	0.17	0.33	0.18	0.15	0.55	0.23	0.15	0.19	0.18	0.15	0.14	0.04	0.14	0.24	0.02	0.01	-
La/Sm	1.6	1.7	1.8	1.9	1.7	1.6	1.9	1.8	2.0	1.7	1.6	1.8	2.1	2.3	2.6	2.0	0.6	0.4	0.5

APPENDIX 5

Nd-Sr-Pb RADIOGENIC ISOTOPIC COMPOSITIONS OF THE CRETACEOUS IGNEOUS ROCKS SPATIALLY-RELATED WITH THE MAYARÍ-BARACOA OPHIOLITIC BELT

Table A5.1 Nd, Sr and Pb radiogenic isotopic compositions of selected igneous rocks from eastern Cuba. Ratios are corrected for radioactive decay since 90 Ma, except for the values in italic that represent present-day compositions

Group	Type	Sample	Material	$^{143}Nd/^{144}Nd$	±	ε_{Nd}	$^{87}Sr/^{86}Sr$	±	$^{206}Pb/^{204}Pb$	±	$^{207}Pb/^{204}Pb$	±	$^{208}Pb/^{204}Pb$	±
Group 1	*Morel volcanics*	M 200	Whole rock	0.513091	8	11.07	0.703971	12	18.4128	7	15.5103	6	37.7169	16
		M 201	Whole rock	0.513010	8	9.49	0.703802	5	18.3714	9	15.5026	8	37.6822	22
	Centeno volcanics	CEN 200	Whole rock	0.513019	4	9.68	0.703836	6	18.2494	5	15.5105	6	37.7450	17
		CEN 201	Whole rock	0.513029	3	9.87	0.704155	6	18.2787	12	15.5046	10	37.7242	27
		CEN 202	Whole rock	0.512990	16	9.10	0.703515	5	18.1938	6	15.4890	6	37.6550	15
Group 2	*Guamuta dykes*	GUA 200	Whole rock	0.513021	6	9.74	0.702918	9	18.1504	15	15.4628	14	37.7388	36
		GUA 201	Whole rock	0.513057	8	10.43	0.704324	3	18.2512	9	15.5226	8	37.9637	20
		GUA 203	Whole rock	0.513014	3	9.59	0.702932	11	18.2480	10	15.6043	9	38.2542	18
		GUA 205	Whole rock	0.513031	15	9.90	0.702936	3	18.2330	4	15.5191	3	37.9939	10
			Cpx	*n.a*			*n.a*		*18.3135*	9	*15.5301*	7	*38.0473*	20
			Pl	0.513086	17	11.00	*n.a*		*n.a*		*n.a*		*n.a*	
	Loma de la Bandera dykes	LB 203	Whole rock	0.513019	3	9.70	0.703495	4	18.2514	7	15.5386	7	38.0512	18
		LB 204	Whole rock	0.513026	16	9.83	0.703262	10	18.1738	3	15.5116	3	37.8233	10
			Pl	0.513025	4	9.82	*n.a*		*18.6014*	9	*15.5261*	9	*37.9085*	20
Group 3														
3T	*Téneme volcanics*	T 201	Whole rock	0.512776	15	4.96	0.703581	20	18.4322	4	15.5477	3	37.9876	12
			Cpx	*n.a*			*n.a*		*18.6634*	13	*15.5542*	10	*38.0754*	29
			Pl	0.512723	53	3.92	*n.a*		*18.5910*	8	*15.5609*	6	*38.0990*	19
		T 202	Whole rock	0.512944	13	8.23	0.703689	20	18.5137	9	15.5733	9	38.1312	27
			Cpx	*n.a*			*n.a*		*18.6779*	11	*15.5747*	9	*38.1654*	29
			Pl	*n.a*			*n.a*		*18.5856*	9	*15.5830*	8	*38.1974*	24
		TEN 1	Whole rock	0.512951	14	8.37	0.703856	10	18.4621	11	15.5566	9	38.0435	25
			Cpx	*n.a*			0.703600	20	*n.a*		*n.a*		*n.a*	
			Pl	0.513001	6	9.33	0.704347	10	*n.a*		*n.a*		*n.a*	
		TM 21	Whole rock	0.512980	17	8.93	0.703391	8	18.5180	9	15.5497	9	38.0147	26
			Cpx	0.512964	4	8.62	*n.a*		*n.a*		*n.a*		*n.a*	
			Pl	*0.513108*	22	*11.44*	*n.a*		*n.a*		*n.a*		*n.a*	
	Téneme boninite	TM 1	Whole rock	0.512927	11	7.89	0.703901	4	18.4278	8	15.5570	9	38.0238	25
			Cpx	0.512947	4	8.29	*n.a*		*18.5371*	17	*15.5617*	12	*38.0368*	35
	Téneme intrusive	DT 200	Whole rock	0.512662	12	2.73	0.704778	4	18.6141	8	15.6248	9	38.3870	15
	Estrella de Mayarí dyke	CAR 4	Whole rock	0.512855	13	6.50	0.703539	10	18.5823	11	15.5631	8	38.2237	28
			Cpx	*n.a*			0.703538	20	*n.a*		*n.a*		*n.a*	
3Q	*Quibiján volcanics (Q1)*	Q 206	Whole rock	0.512911	13	7.64	0.703914	4	18.6205	4	15.5657	4	38.1286	11
			Cpx	*n.a*			*n.a*		*18.7528*	8	*15.5748*	7	*38.2001*	22
		Q 208	Whole rock	0.513002	23	9.41	0.704140	7	18.5679	11	15.5587	10	38.0716	29
			Cpx	*n.a*			0.703806	11	*n.a*		*n.a*		*n.a*	
			Pl	*0.513084*	11	*11.01*	0.704783	10	*n.a*		*n.a*		*n.a*	
	Quibiján volcanics (Q2)	Q 202	Whole rock	0.512693	14	3.38	0.705307	20	18.2889	7	15.5894	8	38.0032	21
			Cpx	*n.a*			*n.a*		*18.4066*	6	*15.5933*	6	*38.0414*	18
		Q 209	Whole rock	0.512700	13	3.52	0.705020	20	18.2429	11	15.5813	8	37.9504	27
			Cpx	*n.a*			0.704097	10	18.2556	16	15.5348	12	*38.0986*	33
			Pl	*n.a*			0.704120	10	18.2380	15	15.5792	11	37.9432	34
		Q 210	Whole rock	0.512792	13	5.32	0.704355	5	18.2715	19	15.5757	15	37.9401	41
			Cpx	0.512802	25	5.52	*n.a*		*18.3103*	7	*15.5776*	7	*37.9701*	21
Moa-Baracoa ophiolitic gabbros														
Crustal gabbros	*Cayo Grande*	CY 200	Whole rock	0.513011	13	9.51	0.703226	10	18.1487	13	15.4851	11	37.6285	33
			Cpx	0.513028	5	9.84	0.702246	20	*n.a*		*n.a*		*n.a*	
	Quemado del Negro	QN 4	Whole rock	0.513086	15	10.98	0.702598	10	18.1641	11	15.4858	10	37.6347	32
			Pl	0.513068	37	10.63	0.702726	40	*n.a*		*n.a*		*n.a*	
Moho transition zone sill	*Cayo Guam*	CG 17	Whole rock	0.512893	37	7.20	0.702826	10	*18.1560*	14	*15.4906*	11	37.6417	33
			Cpx	0.513138	4	12.00	0.702405	50	*n.a*		*n.a*		*n.a*	

n.a. = not analysed